

# Important Notice

This copy may be used only for the purposes of research and private study, and any use of the copy for a purpose other than research or private study may require the authorization of the copyright owner of the work in question.

Responsibility regarding questions of copyright that may arise in the use of this copy is assumed by the recipient

UNIVERSITY OF CALGARY

Time-lapse AVO inversion

by

Abdul-Nassir Saeed

A THESIS

SUBMITTED TO THE FACULTY OF GRADUATE STUDIES  
IN PARTIAL FULFILMENT OF THE REQUIREMENTS FOR THE  
DEGREE OF MASTER OF SCIENCE

DEPARTEMENT OF GEOSCIENCE

CALGARY, ALBERTA

OCTOBER, 2013

© Abdul-Nassir Saeed 2013

UNIVERSITY OF CALGARY  
FACULTY OF GRADUATE STUDIES

The undersigned certify that they have read, and recommend to the Faculty of Graduate Studies for acceptance, a thesis entitled "Time-lapse AVO inversion" submitted by Abdul-Nassir Saeed in partial fulfillment of the requirements for the degree of Master of Science.

---

Supervisor, Dr. Laurence R. Lines  
Department of Geoscience

---

Co-Supervisor, Dr. Gary F. Margrave  
Department of Geoscience

---

Dr. Donald C. Lawton  
Department of Geoscience

---

Dr. Harvey Yarranton  
Department of Chemical and Petroleum Engineering

---

Date

## **Abstract**

A reservoir characterization workflow for time-lapse study requires integrating seismic data vintages and well logs information into a single consistent model to delineate changes of reservoir parameters. The research work in this thesis is divided into four parts: 1) pre-stack inverse problems for time-lapse seismic surveys; 2) prediction of shear sonic logs for wells that are not available; 3) a processing flow for optimum seismic repeatability and imaging of the production related change; 4) interpretation of seismic inversions and seismic differences results from time-lapse seismic surveys.

In this thesis, we present three new time-lapse AVO inversion algorithms: 1) total inversion of the differences; 2) inversion of seismic differences only; 3) sequential reflectivity-constrained inversion. The proposed methods were implemented using synthetic data that simulate reservoir conditions at pre- and post-production of a heavy oil reservoir after depletion. The time-lapse AVO inversion schemes simultaneously invert the P-P & P-S seismic data of the baseline and monitor line surveys to estimate the change of elastic impedances and density model parameters. The proposed algorithms have proven their robustness in terms of computation time and stability in the presence of noise.

Predictions of shear-wave logs in wells that do not have dipole sonic are challenging, particularly in heavy oil reservoirs. The linear-regression, robust locally weighted scattering and smoothing (LOWESS), and several other approaches of iteratively re-weighted linear least-squares inversion (IRLS) techniques were implemented to estimate shear-wave sonic logs. The developed computer codes were applied using well logs from three different types of reservoirs (conventional oil, heavy oil, and tight shale oil) in WCSB. The proposed methods guard against

outliers, and have shown improvements in predicting shear-wave sonic logs compared to empirical linear relationships.

The time-lapse processing and imaging flow designed for seismic data vintages of Pikes-Peak oil field has overcome many difficulties related to differences in acquisition parameters and seismic noise. The proposed flow managed to track production related changes in the reservoir and clearly imaged induced amplitude changes at the Waseca reservoir channel.

The dimming zones observed in the stack section of the monitor line reveal that the steam pressures have caused fluid move through the top seal into the overlying formation. This finding also correlates with the cloud of amplitude change in colony formation shown in the amplitude differences of the time-lapse stack section. The impedances differences show that the interbedded silty sands provide a pathway for steam movements within the Waseca sand channel.

The elastic attributes from the AVO inversion of time-lapse seismic surveys successfully map the hydrocarbon movement at the Waseca reservoir channel.

Conditioning of pre-stack seismic migrated gathers of the Pikes Peak time-lapse surveys remains a challenge and is not covered in this dissertation. Therefore the implementation of proposed time-lapse inversion schemes is left as future research work.

## **Acknowledgements**

I would like to thank my thesis advisers, Dr. Larry Lines and Dr. Gary Margrave, for their support and guidance given to me throughout my graduate studies. I am fortunate to have the opportunity to conduct research work under their guidance, and also grateful for their encouragements and patience. Thanks to Dr. Brian Russell for encouragements and constructive suggestions that have shaped up many parts in this thesis. Many thanks are due to Dr. Helen Isaac for her kind help and support throughout my research studies. In addition, I wish to thank Ken Hedlin and David Gray for constant support, and also for interesting discussions about some aspects in this study. I also acknowledge the supports and help offered by my colleagues at work, Albert Scutt, Mark Ng, Brent Sato and Sam Green.

I wish to thank CREWES faculty, staff and student, particularly, Dr. Don Lawton, Dr. Kris Innanen, Kevin Hall, Rolf Maier, Laura Baird, Faranak Mahmoudian, Mahdi Al-Mutlaq, Oliver Lahr, Steve Kim and Khalid Al-Dulaijan for their assistance and excellent discussions. Thanks to CREWES sponsors, Husky Energy for providing seismic data and well logs, Divestco for allowing me to process seismic data used in this study, Hampson-Russell software for inverting of seismic data, and Ikon Science for financial supports.

Thanks to all my family and friends for being so supportive.

Finally, I wish to thank my wife Tanya, daughters Nadia and Mariam for their love and patience.

This work would have not been possible without their supports.

## **Dedication**

*To my wife Tanya and daughters, Nadia and Mariam.*

## Table of Contents

Abstract .....	iii
Acknowledgements .....	v
Dedication .....	vi
Table of Contents .....	vii
List of Tables .....	x
List of Figures .....	xi
List of Symbols, Abbreviations .....	xix
CHAPTER ONE: INTRODUCTION .....	1
1.1 Amplitude variations with offset (AVO) .....	1
1.2 Time-lapse reservoir monitoring .....	3
1.3 The Pikes Peak heavy oil field.....	4
1.3.1 Survey area and enhancements oil recovery .....	4
1.3.2 Well log analysis .....	7
1.3.3 Previous research work at Pikes Peak .....	7
1.4 Thesis contributions .....	11
1.5 Outline of thesis .....	12
CHAPTER TWO: PREDICTION OF SHEAR-WAVE SONIC LOGS IN THE WESTERN CANADIAN SEDIMENTARY BASIN (WCSB).....	14
2.1 Introduction.....	14
2.2 Empirical Relations for Mudrock Line Estimation.....	14
2.3 Inverse Problem for Predicting of Shear Sonic log .....	15
2.3.1 Formulating of Least-squares Inversion.....	16
2.3.2 Setting up the Regularization Parameter of the Inversion Scheme .....	17
2.4 IRLS Inversion of the shear-sonic log .....	18
2.4.1 Minimization using $\ell_1$ measures of $R_d$ and $R_m$ .....	20
2.4.1.1 Building the L-curve.....	22
2.4.1.2 The curvature of the L-curve .....	24
2.4.2 Smoothness constraint of the model regularization operator $Wm$ .....	25
2.4.3 Compactness constraint of the model regularization operator $Wm$ .....	26
2.4.3.1 Modified total variation method .....	27
2.4.3.2 Minimum support method .....	29
2.4.3.3 Minimum gradient support .....	32
2.4.4 Constrained weight matrix $Wd$ .....	32
2.4.4.1 Standard deviation of residual .....	34
2.4.4.2 Robustness normalized by the standard deviation .....	35
2.4.4.3 Hybrid $\ell_1\ell_2$ norms.....	35
2.4.4.4 Huber constraint.....	37
2.4.4.5 The Annealing M-Estimator .....	40
2.4.5 Analysis of IRLS results from model and data constraints .....	42
2.4.5.1 Diagnosing the RMS error curve .....	42
2.4.5.2 Cross plots of residuals .....	43
2.4.5.3 Simultaneous application of model and data misfit norms.....	47
2.5 Mud-rock line estimation via the locally weighted scattering smoothing method ..	49

2.5.1 Robust locally weighted smoothing scattering (LOWESS) .....	49
2.5.2 Application of LOWESS to Mudrock line estimation in the WCSB .....	52
2.5.2.1 Conventional oil reservoir (Blackfoot field).....	52
2.5.2.2 Tight shale oil reservoir (NW Alberta).....	55
2.5.2.3 Heavy oil reservoirs .....	57
2.6 Conclusions.....	62
<b>CHAPTER THREE: TIME-LAPSE AVO INVERSION OF SEISMIC SURVEYS.....</b>	<b>63</b>
3.1 Introduction.....	63
3.2 Time-lapse modelling .....	63
3.2.1 Building of time-lapse model of Pikes Peak heavy oil.....	65
3.2.2 Synthetic seismic data .....	67
3.2.3 AVA Reflectivity analysis.....	72
3.3 Linear approximation of Zoeppritz equations .....	74
3.4 Practical techniques for time-lapse AVO inversion .....	79
3.4.1 Total inversion of differences.....	81
3.4.1.1 Inversion for elastic attributes of monitor line ( <b>m1</b> ) and time-lapse changes ( <b><math>\Delta m</math></b> ).....	81
3.4.1.2 Inversion for elastic attributes of base line ( <b>m0</b> ) and time-lapse changes ( <b><math>\Delta m</math></b> ).....	87
3.4.2 Inversion of seismic differences data <b><math>\Delta d</math></b> only .....	90
3.4.3 Sequential reflectivity-constrained inversion .....	93
3.5 Conclusions.....	100
<b>CHAPTER FOUR: SEISMIC DATA PROCESSING OF THE PIKES PEAK TIME-LAPSE SURVEYS .....</b>	<b>101</b>
4.1 Introduction.....	101
4.2 Time-lapse seismic surveys for the Pikes Peak heavy oil field .....	101
4.3 Seismic data processing flow for time-lapse and imaging .....	104
4.3.1 Amplitude recovery and correction .....	107
4.3.2 Five-component surface consistent deconvolution .....	108
4.3.3 Noise attenuation by modelling.....	114
4.3.4 Refraction statics calculation and application .....	117
4.3.5 Velocity Analysis and seismic imaging .....	118
4.4 Conclusions.....	123
<b>CHAPTER FIVE: QUANTITATIVE INTERPRETATION OF THE PIKES PEAK TIME- LAPSE SEISMIC SURVEYS .....</b>	<b>124</b>
5.1 Introduction.....	124
5.2 Interpretation of time-lapse seismic data .....	125
5.2.1 Analysis of time-lapse seismic differences .....	127
5.2.2 Analysis of Isochron ratio .....	132
5.3 Interpretation of post-stack impedance inversion.....	135
5.3.1 Post-stack impedance inversion of individual survey line .....	136
5.3.2 Time-lapse post stack impedance inversion.....	138
5.4 AVO inversion of time-lapse survey .....	140
5.5 Conclusions.....	149

CHAPTER SIX: CONCLUSIONS AND FUTURE WORK .....	150
6.1 Conclusions.....	150
6.2 Future work.....	152
REFERENCES .....	154

## List of Tables

Table 1.1 Summary of the reservoir properties at Waseca Channel (after Wong. at al., 2003). ....	6
Table 2.1: The slope, intercept, number of iteration and RMS values for the final iteration of different weighted matrices used in predicting of shear sonic log of well 1A15-6, Pikes Peak heavy oil field.....	47
Table 4.1: Field acquisition parameters for the 2D time-lapse seismic surveys of Pikes Peak heavy-oil field. ....	104

## List of Figures

Figure 1.1: Location map for the Pikes Peak oil field. The honeycomb pattern represents locations of produced well while injected steam is drilled in the centre of the hexagonal shape (after Wong et al., 2003; Watson 2004).....	5
Figure 1.2: Stratigraphic chart for the Pikes Peak area (after Core laboratories; Watson, 2004). .....	5
Figure 1.3: Map of location of time-lapse seismic surveys (baseline H1991 and monitor line H2000) along with wells that are used in this study that are closely located to the time lapse seismic survey lines for the Pikes Peak area. Red dots indicate wells drilled after the baseline survey was carried out (after Watson, 2004). .....	8
Figure 1.4: Log curves of well 1A15-6, Pikes Peak oil field. Note the drop in the Vp/Vs curve commencing at the Colony formation.....	9
Figure 1.5: LambdaRho versus Lambda / Mu for Well 15A-6, Pikes Peak field colored by gamma ray values. Estimated elastic rock properties for the upper Quaternary, Viking, and Waseca formations are superimposed and colored in solid green, black and magenta respectively. ....	10
Figure 1.6: The shallow, mid and deep resistivity logs along with the SP log for Well D2-6, Pikes Peak field.....	10
Figure 2.1: The Lagrange multiplier, $\lambda$ for the $i^{\text{th}}$ iterations during inversion of shear sonic log using one of the proposed inverse schemes. ....	18
Figure 2.2: The L-curve plot of log values of residual and solution norms.....	23
Figure 2.3: The optimum maximum curvature $\epsilon$ . ....	25
Figure 2.4: The measured Vp and Vs, Vp/Vs ratio and density logs of the Pikes Peak heavy oil field. ....	28
Figure 2.5: The measured and inverted shear sonic logs of Well 1A15-6, Pikes Peak using the modified total variant method. ....	28
Figure 2.6: The measured versus inverted shear sonic logs colored by residual of Well 1A15-6, Pikes Peak, using a modified total variant method. The color bar represents the absolute difference between measured and inverted shear sonic logs values. Velocity unit is in Km/sec. ....	29
Figure 2.7: The measured and inverted shear sonic logs of Well 1A15-6, Pikes Peak area using the minimum support method. ....	31
Figure 2.8: The RMS error during IRLS inversion of inverted shear sonic logs of Well 1A15-6, Pikes Peak, using the minimum support method. ....	31

Figure 2.9: The measured and inverted shear sonic logs of Well 1A15-6, Pikes Peak using the minimum gradient support method. ....	33
Figure 2.10: Plot of the damping factor during IRLS inversion of shear sonic logs of Well 1A15-6, Pikes Peak area, using the minimum gradient support method. ....	33
Figure 2.11: The measured and inverted shear sonic logs of Well 1A15-6, Pikes Peak, using the standard deviation of the weight matrix method. ....	34
Figure 2.12: The measured and inverted shear sonic logs of Well 1A15-6, Pikes Peak using robustness normalized by the standard deviation method. ....	36
Figure 2.13: The RMS error during IRLS inversion of shear sonic log of Well 1A15-6, Pikes Peak, using robustness normalized by the standard deviation method. ....	36
Figure 2.14: The measured and inverted shear sonic logs of Well 1A15-6, Pikes Peak, using a hybrid l1l2 norms method. ....	38
Figure 2.15: The measured and inverted shear sonic logs of Well 1A15-6, Pikes Peak, using the Huber constraint. ....	39
Figure 2.16: The measured and inverted shear sonic logs of Well 1A15-6, Pikes Peak, using the annealing M-Estimator. ....	41
Figure 2.17: The RMS error during IRLS inversion of shear sonic logs of Well 1A15-6, Pikes Peak, using the annealing M-Estimator. ....	41
Figure 2.18: The measured and inverted shear sonic logs of Well 1A15-6, Pikes Peak. (A): inversion at the first iteration. (B) Inversion at the second iteration, while (C) the inversion of the shear sonic log at the final solution. ....	44
Figure 2.19: Measured versus inverted shear sonic logs of Well 1A15-6, Pikes Peak, color coded by the residual. Constraint applied in data space. ....	46
Figure 2.20: Measured versus inverted shear sonic logs of Well 1A15-6, Pikes Peak, color coded by the residual. Constraint applied in model space. ....	46
Figure 2.21: The measured and inverted shear sonic logs of Tight Shale Montney, WCSB using a combination of hybrid l1l2 and minimum gradient support weighted matrices. ....	48
Figure 2.22: Scatter plot of P-wave velocity versus S-wave velocity using LOWESS for mapping of Mudrock line. (A): smooth curve factor, $f=0.2$ , while (B), smooth curve factor, $f=0.8$ . ....	50
Figure 2.23: Cross-plot of P-wave velocity versus S-wave velocity of well log from conventional oil reservoir area. The scatter points are colored using Gamma ray API (color bar). $V_p$ - $V_s$ values from the productive sand channel reservoir (black dots) are superimposed. ....	53

Figure 2.24: Plots for measured (red color) and inverted shear-wave logs of a well from a conventional oil reservoir area using linear regression (green curve), the LOWESS method (blue curve) and the ARCO Mudrock equation (black curve)..... 54

Figure 2.25: Plots for percentage of residual of shear-wave logs using a well log from a conventional oil reservoir..... 54

Figure 2.26: Cross- plot for S-wave velocity versus P-wave velocity of well log from conventional oil reservoir area. The scatter points are colored using Gamma ray values API (color bar). Velocity values from the productive sand channel reservoir (black dots) are superimposed. The LOWESS fit line curves as it maps the channel reservoir..... 55

Figure 2.27: Plots for P-wave, S-wave, density and Gamma ray logs of a well from tight shale reservoir area..... 56

Figure 2.28: Plots for measured (red color) and inverted shear-wave logs of well log from a tight shale oil reservoir area using linear regression (green curve), the LOWESS method (blue curve), the ARCO Mudrock equation (black curve), and Han’s equation (magenta curve). Col Color bar represents Gamma ray API. .... 57

Figure 2.29: Cross- plot for S-wave velocity versus P-wave velocity of well 1A15-6, from a heavy oil reservoir area. The scatter points are coloured using Gamma ray, and velocity values from the productive Waseca sand reservoir (black dots) are superimposed. (A) for a smoothing factor,  $f = 0.25$ , (B) is for  $f = 0.95$ . The color bar represents Gamma ray API. .... 59

Figure 2.30: Plots for measured (red color) and inverted shear-wave logs of a well log from the heavy oil reservoir area using linear regression (green curve), the LOWESS method (blue curve), and the ARCO Mudrock equation (black curve). (A) for a smoothing factor,  $f = 0.25$ , while (B) is for  $f = 0.95$ . .... 61

Figure 3.1: Neutron- and density- porosity logs for Well D2-6, Pikes Peak field. Arrows shows location of crossover of Neutron and density porosity logs as indicative of gas accumulation. .... 64

Figure 3.2: Time-lapse model to simulate heavy oil reservoir, Pikes Peak field. The color bar represents P-wave velocity. Note the increase of blue color of the reservoir layer (mid layer) in the monitor model as a result of decreasing P-wave velocity. .... 66

Figure 3.3: Synthetic logs to simulate pre- and post-steam injection in heavy oil reservoir. .... 67

Figure 3.4: Synthetic P-P seismic data for the base (A) and the monitor (B) models. .... 68

Figure 3.5: Synthetic P-S seismic data for the base (A) and the monitor (B) models. .... 69

Figure 3.6: Properties of heavy oil sand (after Han et. al., 2008). (A) shows classification of heavy oil phases depending on temperature. (B) shows changes in  $V_p$  and  $V_s$  velocities

with temperature. $V_p$ decreases at a higher rate compared to $V_s$ as temperature increases.....	71
Figure 3.7: Difference of synthetic P-P seismic data for the base and the monitor models. ....	73
Figure 3.8: Difference of synthetic P-S seismic data for the base and the monitor models. ....	73
Figure 3.9: AVA analysis for the P-P and P-S reflectivities of the top and reservoir layers of time-lapse model of the Pikes Peak area.....	74
Figure 3.10: A schematic diagram shows reflected and transmitted waves generated at a welded solid-solid interface by an incident P-wave.....	75
Figure 3.11: Estimated model parameters ( $\Delta I/I$ , $\Delta J/J$ and $\Delta R/R$ ) for the <i>monitor</i> model before adding low-frequency models.....	84
Figure 3.12: Estimated model parameters changes [ $\Delta(\Delta I/I)$ , $\Delta(\Delta J/J)$ and $\Delta(\Delta R/R)$ ] for the <i>time-lapse</i> model before adding low-frequencies from logs.....	84
Figure 3.13: Estimated model parameters ( $\Delta I/I$ , $\Delta J/J$ and $\Delta R/R$ ) for the <i>base</i> model before adding low- frequencies from logs.....	85
Figure 3.14: Elastic parameters (IP, IS and $\rho$ ) of the base model after adding low frequencies. Embedded graphs in bold black dotted lines represent actual (IP, IS and $\rho$ ) calculated from logs. ....	85
Figure 3.15: Elastic parameters (IP, IS and $\rho$ ) of the monitor model after adding low frequency. Embedded graphs in bold black dotted lines represent actual (IP, IS and $\rho$ ) calculated from logs.....	86
Figure 3.16: Elastic parameter changes ( $\Delta IP$ , $\Delta IS$ and $\Delta \rho$ ) of the time-lapse model after adding low frequency. Embedded graphs in bold black dotted lines represent actual elastic parameter changes calculated from logs.....	86
Figure 3.17: Elastic parameters (IP, IS and $\rho$ ) of the <i>base</i> survey model using equation (3.17) after adding low frequency. Embedded graphs in bold black dotted lines represent actual (IP, IS and $\rho$ ) calculated from logs.....	88
Figure 3.18: Elastic parameters (IP, IS and $\rho$ ) of the <i>monitor</i> survey model using equation (3.17) after adding low frequency. Embedded graphs in bold black dotted lines represent actual (IP, IS and $\rho$ ) calculated from logs.....	89
Figure 3.19: Elastic parameters changes ( $\Delta IP$ , $\Delta IS$ and $\Delta \rho$ ) of the <i>time-lapse</i> survey model using equation (3.17) after adding low frequency. Embedded graphs in bold black dotted lines represent actual (IP, IS and $\rho$ ) calculated from logs.....	89
Figure 3.20: Estimated model parameters changes [ $\Delta(\Delta I/I)$ , $\Delta(\Delta J/J)$ and $\Delta(\Delta R/R)$ ] from an inversion of data differences (equation 3.21) before adding low-frequencies from logs. ....	91

Figure 3.21: Estimated attribute changes [ $\Delta(\text{IP})$ , $\Delta(\text{IS})$ and $\Delta\rho$ ] from inversion of data differences (equation 3.21) after adding low-frequencies from logs. ....	92
Figure 3.22: P-P synthetic seismic data for the base model with 0.1% random noise added. ....	94
Figure 3.23: P-S synthetic seismic data for the base model with 0.1% random noise added. ....	94
Figure 3.24: P-P synthetic seismic data for the monitor model with 1% random noise added. ...	95
Figure 3.25: P-S synthetic seismic data for the monitor model with 1% random noise added. ...	95
Figure 3.26: Elastic parameters (IP, IS and $\rho$ ) using sequential reflectivity-constrained inversion of the noisy (0.01) monitor model after adding low frequencies from logs. ....	98
Figure 3.27: Regularization parameter during a reflectivity-constrained Inversion. ....	98
Figure 3.28: The RMS error during reflectivity- constrained Inversion scheme. ....	99
Figure 3.29: Elastic parameters (IP, IS and $\rho$ ) using sequential reflectivity-constrained inversion of the noisy (10 times amount of noise in Figure 22) monitor model after adding low frequency. ....	99
Figure 4.1: Base map view for the 2D time-lapse survey lines of the Pikes Peak oil field. ....	103
Figure 4.2: A shot gather from monitor line survey (H-2000) show noises related to pump jacks, ground-roll and air blast during seismic data acquisition of the 2D time-lapse survey lines of Pikes Peak oil field. ....	106
Figure 4.3: Correlation analysis window to determine operator length for time-domain deconvolution. (A) Window length of 60msec, while (b) has an operator length of 85msec. ....	110
Figure 4.4: (A) Spectral analysis form using four component surface-consistent spike deconvolution, while (B) from using five component surface-consistent deconvolution. .	111
Figure 4.5: Spectral analysis of a shot gather- from the baseline H-1991. Left: Spectral analysis before Decon. Right: Spectral Analysis after applying five-component surface consistent deconvolution. ....	113
Figure 4.6: Spectral analysis for a shot gather- from the monitor line H-2000. Left: Spectral analysis before Decon. Right: Spectral analysis after applying five-component surface consistent deconvolution. ....	113
Figure 4.7: (A) Original shot gather from monitoring line (H-2000), while (B) is for the same shot after deconvolution. The pump-jack noise and ground-roll noise that masked reflectors at the central and eastern part of the shot gather are partially attenuated after deconvolution. Notice the continuity of reflectors at the middle and east sides of the shot gather after deconvolution. ....	114

Figure 4.8: A shot gather from the monitor line survey before applying the noise attenuation procedure.....	115
Figure 4.9: A shot gather from the monitor line survey after applying a noise attenuation procedure. The ground-roll noise is successfully removed, while preserving reflection amplitudes. Air blast noises with frequencies above 120Hz are also removed. ....	116
Figure 4.10: A shot gather from the monitor line survey. Left: Shot gather before applying refraction statics. Right: Same shot gather after applying refraction statics using DRM method.....	117
Figure 4.11: Second pass of velocity analysis. (A) for the baseline 1991, while (B) is for the monitor line 2000. ....	119
Figure 4.12: Left: Structure stack-section. Right: PSPI migrated stack-section for the 2D baseline (H-1991) survey of Pikes Peak oil field.....	121
Figure 4.13: Left: Structure stack-section. Right: PSPI migrated stack-section for the 2D monitor line (H-2000) survey of Pikes Peak oil field. ....	122
Figure 4.14: PSPI migrated stack-sections for the 2D time-lapse survey of Pikes Peak oil field. Left: Baseline (H-1991) survey. Right: monitor line (H-2000) survey. Time horizons: yellow for BFS, cyan for Colony, red for Top Waseca, blue for Sparky and green for PCU. Note the change in amplitude at the Waseca channel, and below Formations due to steam injection effect. ....	123
Figure 5.1: Well to seismic tie for dipole sonic well 1A15-6, Pikes Peak oil field. ....	125
Figure 5.2: Stack sections for the time-lapse survey of Pikes Peak oil field. Top: stack of the baseline H1991. Bottom: stack of the monitor line H2000. Inserted curves are P-wave curve. Note the amplitude build up due to steam injection at the Waseca channel, base of Waseca channel (blue color horizon) and below formations.....	126
Figure 5.3: Common image gathers of time-lapse survey of Pikes Peak oil field. Top: CIG of the baseline. Bottom: CIG of the monitor line. Note the induced-amplitude changes for the gathers of the monitor line survey due to steam effect at reflectors close to steam chamber (around 450 -550 ms). ....	129
Figure 5.4: Seismic difference between the baseline H1991 and monitor line H2000 of the time-lapse survey of Pikes Peak oil field. A) for time window designed to be above, within and below the Waseca reservoir zone. B) for time window designed to be above the Waseca reservoir zone.....	130
Figure 5.5: Volume, pore saturation, neutron and density porosity and resistivity/SP logs of well D2-6, Pikes Peak oil field. Note the crossover of NPHI and DPHI curves at Colony formation and subsequent formation that are colored by oil saturation (So).....	132
Figure 5.6: Isochron ratio of the Waseca interval travel time, Pikes Peak oil field.....	134

Figure 5.7: Isochron ratio of the extension Waseca interval travel time to start from the Colony formation as top of the reservoir at Pikes Peak oil field. ....	134
Figure 5.8: The low frequency (1-8 Hz) background model of P-impedance used in the post-stack acoustic impedance inversion of the Pikes Peak time-lapse survey. ....	136
Figure 5.9: The post-stack acoustic impedance (AI) inversion sections of the Pikes Peak oil field from inverting time lapse seismic data individually using a sparse spike impedance inversion scheme. Left: impedance section of the base line H1991. Right: impedance section of the monitor line H2000. ....	137
Figure 5.10: Schematic diagram depicting facies of the Waseca incised valley channel at Pikes Peak oil field. The Waseca reservoir is comprised of a shale unit, an interbedded silty sand unit and a homogenous sand unit (after Van Hulten 1984; Watson, 2004).....	139
Figure 5.11: The time-lapse P-impedance difference section of the Pikes Peak oil field. The section shows the difference between monitor line and baseline surveys. The negative values in impedance difference section are indicative of impedance decreases due to steam effects.....	140
Figure 5.12: Correlating and QC of inverted and actual $Z_p$ , $Z_s$ and density attributes around well D15-6. The second track represents synthetic while the third panel is extracted gathers around the well. The fourth panel shows residual (difference between seismic and synthetic traces).....	141
Figure 5.13: Cross-correlation measurement of inverted synthetic along the wells.....	141
Figure 5.14: P-Impedance sections of the baseline H1991 (top) and monitor line H2000 (bottom) from AVO inversion of the Pikes Peak time-lapse surveys. Inserted curves are AI logs. Color bar for P-impedance is within a range of (4000 – 7600 ((m/s) *(g/cc))). ...	143
Figure 5.15: S-Impedance sections of the baseline H1991 (top) and monitor line H2000 (bottom) from AVO inversion of the Pikes Peak time-lapse surveys. Inserted curves are density logs. Color bar for S-impedance is within a range of (1500 – 3750 ((m/s) *(g/cc)))......	144
Figure 5.16: Density sections of the baseline H1991 (top) and monitor line H2000 (bottom) from AVO inversion of the Pikes Peak time-lapse surveys. Inserted curves are density logs.....	145
Figure 5.17: P-wave velocity sections of the baseline H1991 (top) and monitor line H2000 (bottom) from AVO inversion of the Pikes Peak time-lapse surveys. Inserted curves are P-wave logs.....	146
Figure 5.18: S-wave velocity sections of the baseline H1991 (top) and monitor line H2000 (bottom) from AVO inversion of the Pikes Peak time-lapse surveys. Inserted curves are S-wave logs.....	147

Figure 5.19:  $V_p/V_s$  ratio sections of the baseline H1991 (top) and monitor line H2000 (bottom) from AVO inversion of the Pikes Peak time-lapse surveys. Inserted curves are  $V_p/V_s$  logs. .... 148

## List of Symbols, Abbreviations

$\Delta I/I$	Estimated model parameter from AVO inversion for P-impedance before adding low frequency model
$\Delta J/J$	Estimated model parameter from AVO inversion for S-impedance before adding low frequency model
$\Delta R/R$	Estimated model parameter from AVO inversion for density before adding low frequency model
$d$	Measured data
$G$	Forward operator
$I$	Identity matrix
$\ell_1$	L <sub>1</sub> norm
$\ell_2$	L <sub>2</sub> norm
$m$	inverse model parameter
PP	P-wave seismic data. Seismic waves travelling down as $P$ waves, reflecting from an interface, and travelling up as $P$ waves.
PS	Converted-wave seismic data. Seismic waves travelling down as $P$ waves, reflecting and converting from an interface, and travelling up as $S$ waves.
$Rd$	Weighted matrix in data space
$Rm$	Weighted matrix in model space
$V_p$	P-wave sonic log
$V_s$	S-wave dipole-sonic log
$Wd$	Weighted matrix of data-misfit norm
$Wm$	Regularization operator or weighted matrix of model norm

$\lambda$	regularization parameter (damping factor)
$J(m)$	Objective function of inverse problem
$m1$	Inverse model parameter of monitor line survey
$m0$	Inverse model parameter of baseline survey
$\Delta d$	Difference of the measured data between the baseline and monitor line surveys
$\Delta m$	Change or difference in the inverse model parameter between baseline and monitor line surveys
AVA	Amplitude variation with angle of incidence
AVAZ	Amplitude variation with angle and azimuth
AVO	Amplitude variation with offset
CDP	Common depth point
CIG	Common image gather
DHI	Direct hydrocarbon indicator
EOR	Enhancement oil recovery
IRLS	Iteratively re-weighted least squares inversion
LOWESS	Robust locally weighted scattering smoothing method
NMO	Normal move out
PSPI	Phase-shift plus interpolation migration
RMS	Root mean square

## Chapter One: **INTRODUCTION**

### **1.1 Amplitude variations with offset (AVO)**

In early 1970s, the first use of amplitude information as a hydrocarbon indicator was made by Hammond, (1974) when it was found that “bright-spot” amplitude anomalies are associated with the gas-filled sand of a hydrocarbon trap. However, post-stack impedance inversion (Lindseth, 1979; Oldenburg et al., 1983) and more discoveries indicated that these bright spots are due to rapid lithology changes, such as igneous intrusion, carbonate and coal seams in clastic sequences (Allen and Peddy, 1993). Avseth et. al.,(2005) have also shown that gas-filled sands sometimes cause "dim spots", not only bright spots. Therefore, AVO analysis should be conducted to identify potential hydrocarbon accumulations particularly in sand/shale impedance crossovers in an over-pressured zone.

The Zoeppritz equation (Zoeppritz, 1919) forms the basis of AVO methodology by estimating reflected amplitude as a function of angle of incidence at a welded elastic interface. The amplitude variations with offset provide the link between rock physics properties and seismic observations along offsets (Mavko et al., 1998). Simplification of the Zoeppritz equation in a linearized AVO form (Bortfeld, 1961; Aki and Richards, 1980) has assisted many researchers to reformulate the linear AVO equations (such as using the empirical relationship of Gardner et al., 1974 for two-term AVO reflectivities) to estimate different elastic reflectivities and petrophysical attributes (Shuey, 1985; Smith and Gidlow, 1987; Fatti et al., 1994; Goodway et. al., 1997; Connolly 1999 and Whitcombe et al., 2002).

The above literatures, as well as the research work in this thesis, assume that the half-spaces across welded contacts are elastic and isotropic. However, extension of AVO theory to

amplitude variation with azimuth (AVAZ) in the anisotropic media demonstrated its successful application in determining fracture density and orientation in the unconventional tight reservoirs (Thomson, 1986 and 1988; Tsvankin 2001 and Rugure, 2002).

With the aid of the AVO classifications (Rutherford and William, (1989); Verm and Hilterman (1995), and Castagna and Swan, (1997)) the developed AVO methodologies have improved capabilities of amplitude variation with offset in discriminating against lithology and pore fluid contents. As such, AVO has become a direct hydrocarbon indicator tool, (DHI) that has been used extensively in hydrocarbon explorations.

A number of authors have used AVO for lithology classifications and pore fluid type identifications. For example, Ostrander (1982) was the first to introduce applications of AVO in hydrocarbon explorations, and showed the anomalous behavior of the reflected amplitudes of gas-filled sand as a function of offset. Since then, AVO has become a standard quantitative interpretation method used by explorationists in the oil and gas industry. Moreover, Ostrander (1984) published case studies for the successful application of AVO in gas reservoir mapping. Allen and Peddy (1993) used AVO on Gulf Coast data to show its usefulness and limitations in mapping hydrocarbon traps. Goodway et al. (1997) used AVO for lithology and fluid discrimination in clastics. Li et al., (2003) show successful applications of AVO in carbonates, while Xu (2012) used AVO to characterise the heterogeneity of oil sand.

The rapid developments in seismic acquisition and data processing software have elevated the simultaneous AVO inversion by incorporating multicomponent (PP and PS) seismic data in order to improve estimates of elastic and density parameters (Stewart, 1990). Larsen et al. (1999) presented a successful PP-PS inversion for mapping a sand reservoir channel at Blackfoot, Alberta. Russell et al. (2005) applied joint PP-PS inversion to delineate areas of best sand

development in oil sand reservoirs. Mahmoudian (2006) implemented PP-PS inversion for VSP studies. Ronholt et al, (2010) proved the reliability of the use of the Vp/Vs attribute, as a result of joint PP-PS inversion, in hydrocarbon explorations in the North Sea.

## **1.2 Time-lapse reservoir monitoring**

Lumley (1995) established a framework for seismic time-lapse monitoring of subsurface fluid flow, while Altan (1997) has improved the repeatability of processing time-lapse seismic data for reservoir monitoring. In time-lapse reservoir monitoring, the ultimate goal is to estimate changes in elastic and density attributes of a reservoir after hydrocarbon recovery processes. Estimations of these elastic differences assist in tracking fluid saturation and pressure changes in the reservoir after depletion (LandrØ, 2001).

Pullin et. al., (1987) have applied seismic imaging to map heat zones at an Athabasca tar sands thermal project. Eastwood et. al., (1994) have used seismic monitoring for steam-based recovery of bitumen while Isaac (1996) has used seismic methods for monitoring heavy oil reservoirs. Time-lapse seismic monitoring has also proven its effectiveness in planning drilling programs by identifying bypassed reservoirs and performing pore pressure prediction (Carcione and Gangi, 2000). The literature also shows excellent case studies about the successful application of time-lapse monitoring of steam flood movements and CO<sub>2</sub> sequestrations (Waite and Sigit, 1997; Ma et al., 2009). In reservoir characterization, the time-lapse seismic monitoring has been successfully applied to estimating pore pressure and saturation changes after hydrocarbon recovery processes (Tura and Lumley, 1999; LandrØ, 2001). The goal of this thesis is to establish time-lapse AVO inversion schemes to become standard industry tools for heavy oil monitoring using time-lapse seismic surveys.

### **1.3 The Pikes Peak heavy oil field**

#### ***1.3.1 Survey area and enhancements oil recovery***

Watson, (2004) has provided excellent reviews of the geology and engineering studies at the Pikes Peak oil field. The Pikes Peak heavy-oil field is located in the western Canadian heavy oil basin, approximately 40 km east of Lloydminster (Figure 1.1), border of Alberta/ Saskatchewan (Township 55, Range 23W3). The heavy oil is produced from the sands of the Waseca formation (Figure 1.2) of the lower Cretaceous Mannville group (Van Hulten, 1984).

The Pikes Peak field itself is located on an east-west structural high within an incised valley-fill channel complex that trends north/south (Sheppard et al., 1998). Based on the well logs, the Waseca formation lies at a true vertical depth (TVD) range of 475-510 m. The Waseca channel has an average thickness of 10-30 m, but thickness can locally increase up to 50 m. The channel is made up of shale, interbedded silty sand and homogenous sand facies (Van Hulten, 1984). Table (1.1) summarizes the reservoir properties of the homogenous sand at the Waseca channel reservoir, Pikes Peak oil field.

The Pikes Peak oil field was first discovered in early 1970 with primary hydrocarbon production from the General Petroleum (GP) formation. In 1981, after successful implementation of cyclic steam simulation, CSS, on a pilot project at Waseca channel sand, additional wells were drilled. Since then, the Waseca channel has become a main producing formation at the Pikes Peak.

By the end of 1987, the west side of the Pikes Peak area had undergone thermal recovery, including steam drive processes to optimize heavy oil recovery for wells that have shown thermal interconnections between them after several cycles of CSS processes. After 1992, the CSS process was implemented on the east side of the Pikes Peak oil field (Wong et al., 2003), and since then more wells were drilled and the site expanded more towards the south.

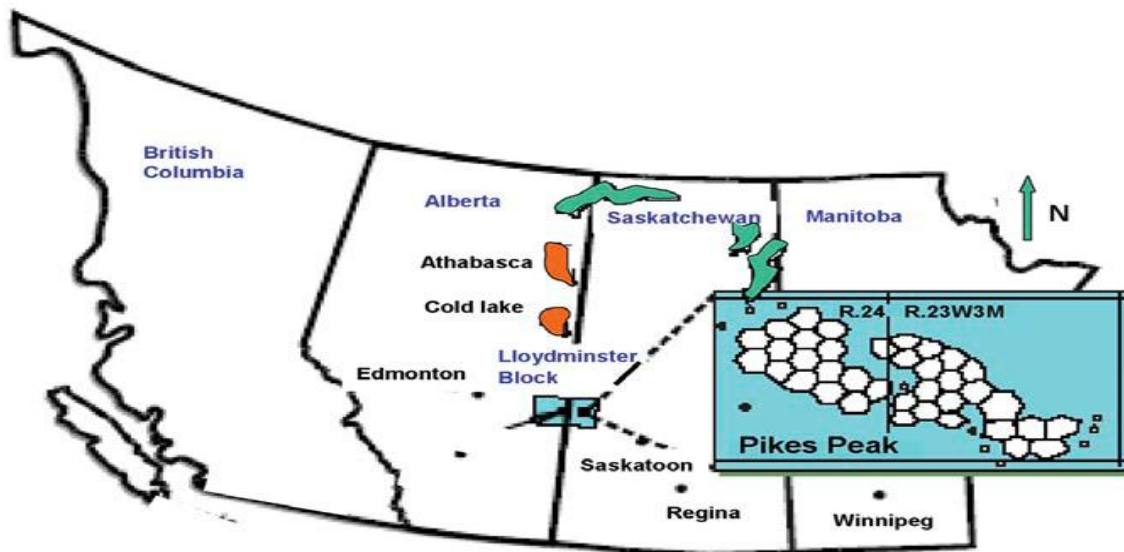


Figure 1.1: Location map for the Pikes Peak oil field. The honeycomb pattern represents locations of produced well while injected steam is drilled in the centre of the hexagonal shape (after Wong et al., 2003; Watson 2004).

AGE / GROUP		FORMATION	LITHOLOGY	APPROX DEPTH
QUATERNARY		GLACIAL DRIFT		
CRETACEOUS	UPPER	JUDITH RIVER		- 150 m -
		LEA PARK		
		COLORADO GROUP	SHALE	- 300 m -
	LOWER	VIKING		
		JOLI FOU COLONY		- 450 m -
		MCLAREN		
		WASECA		- 475 m -
		SPARKY	SANDSTONE & SHALE	- 510 m -
		GENERAL PETROLEUM		
		REX		
		LLOYDMINSTER		- 550 m -
		CUMMINGS		
		DINA		- 650 m -
		DUPEROW	DOLOMITE	
DEVONIAN	SASK. GROUP	SOURIS RIVER		- 825 m -
	MANITOBA GROUP	PRAIRIE EVAPORITE	EVAPORITE	
	ELK POINT GROUP	WINNIPEGOSIS		- 950 m -
		ASHERN		- 1050 m -
CAMBRIAN		DEADWOOD		- 1600 m -
PRECAMBRIAN				

Figure 1.2: Stratigraphic chart for the Pikes Peak area (after Core laboratories; Watson, 2004).

<i>Reservoir properties</i>	<i>Measured values</i>
<b>Depth(TVD)</b>	<b>475 – 500 m</b>
<b>Maximum Dip</b>	<b>4.5°</b>
<b>Net Pay Thickness (m) – Range</b>	<b>5 – 30 m</b>
<b>–Median</b>	<b>15 m</b>
<b>Porosity – Range</b>	<b>32 – 36%</b>
<b>–Median</b>	<b>34%</b>
<b>Permeability – Range</b>	<b>1 – 10 <math>\mu\text{m}^2</math></b>
<b>–Median</b>	<b>5 <math>\mu\text{m}^2</math></b>
<b>Oil Saturation</b>	<b>78 – 92%</b>
<b>Initial Reservoir Pressure</b>	<b>3350 kPa</b>
<b>Initial Reservoir Temperature</b>	<b>18 °C</b>
<b>Oil Formation Volume Factor</b>	<b>1.022 m<sup>3</sup>/ m<sup>3</sup></b>
<b>Oil Density</b>	<b>985 Kg/ m<sup>3</sup></b>
<b>Oil Gravity</b>	<b>12.4 °API</b>
<b>Dead –Oil Viscosity @ 18 °C</b>	<b>25000 mPa.s</b>
<b>Solution GOR</b>	<b>14.5 m<sup>3</sup>/ m<sup>3</sup></b>
<b>Mineralogy</b>	
<b>Quartz</b>	<b>92%</b>
<b>Feldspar</b>	<b>3%</b>
<b>Kaolinite</b>	<b>3%</b>
<b>Other</b>	<b>2%</b>

Table 1.1 Summary of the reservoir properties at Waseca Channel (after Wong. at al., 2003).

### **1.3.2 Well log analysis**

Wells that are located closely to the time-lapse seismic survey lines (Figure 1.3) are used in this study. Figure (1.4) shows different logs for the well 15A-6 that was drilled in February, 2000. Note the substantial drop in  $V_p/V_s$  ratio that starts from the Colony Formation and extends through the Waseca reservoir channel.

The elastic rock properties are computed from the dipole sonic of well 15A-6, of the Pikes Peak area. In the crossplot of  $\Lambda$  Rho versus  $\Lambda/\mu$  given in Figure (1.5), data points are colored by gamma ray values. Furthermore, the estimated elastic rock properties for the upper Quaternary, Viking, and Waseca formations are colored in black, green and magenta colors respectively. The Quaternary facies show distinct, low  $\Lambda$  and  $\mu$  values, while the Viking facies shows smaller  $\Lambda$  Rho values than the Waseca Formation.

The resistivity logs of Well D2-6 (Figure 1.6), which was logged in 1980, shows a spike increase in resistivity at the Waseca reservoir as an indication of increased hydrocarbon content. However, the sharp decrease in resistivity at the base of the Waseca Formation, where the bottomwater layer is manifest, is indicative of brine water content. In general, well log analysis shows distinctive changes in elastic rock properties at the Waseca heavy oil reservoir zone, which assists in building a time-lapse model.

### ***1.3.3 Previous research work at Pikes Peak***

The previous geophysical work at the Pikes Peak oil field includes acquisition and processing of surface and VSP multicomponent data (Hoffe et al., 2000). Downton and Lines (2000) have conducted an early AVO feasibility study using seismic data of the monitor survey line H2000.

The attenuation of high frequency seismic wavelets due to steam injection was thoroughly investigated by Hedlin et al., (2001). On the other hand, Zhang (2003) used PP-PS inversion data as an interpretive tool for the Waseca reservoir channel. The work by Watson (2004), Zou (2005) and Soubotcheva, (2006) demonstrated successful integration of geological, engineering, and geophysical data in interpreting and predicting properties of the Waseca reservoir channel at the Pikes Peak heavy oil field.

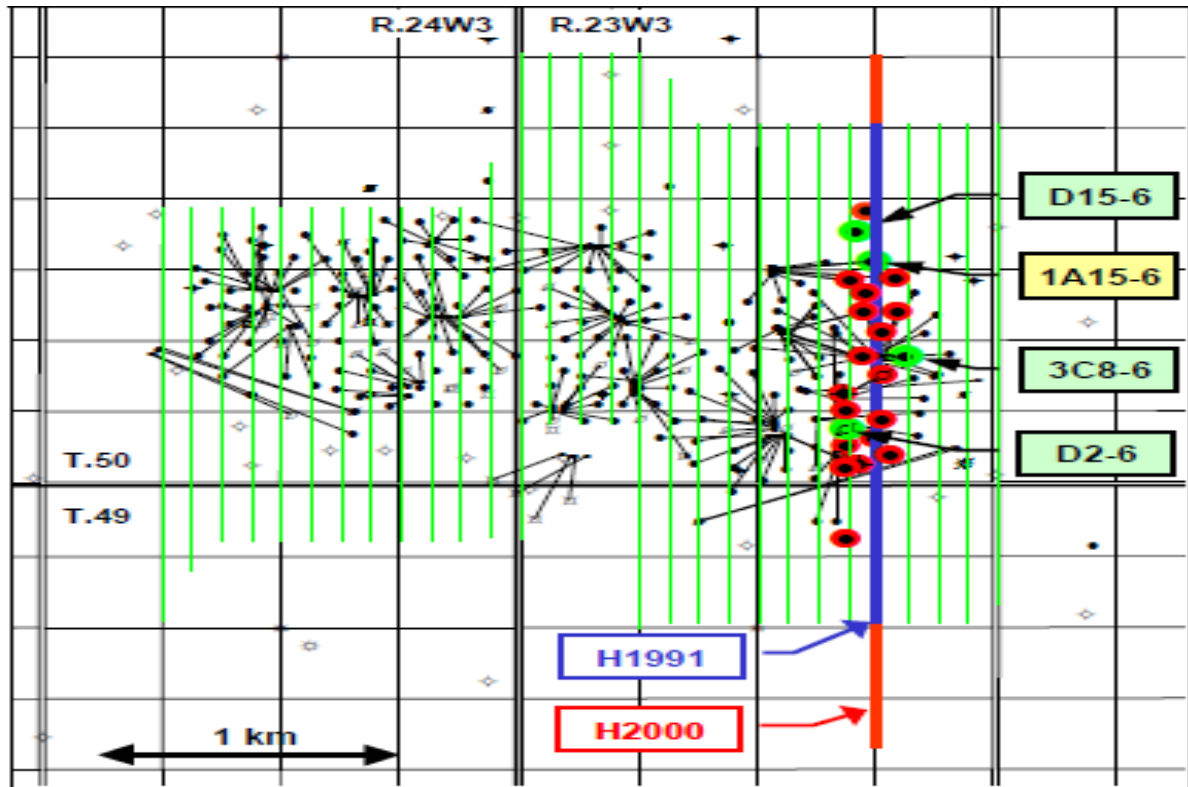


Figure 1.3: Map of location of time-lapse seismic surveys (baseline H1991 and monitor line H2000) along with wells that are used in this study that are closely located to the time lapse seismic survey lines for the Pikes Peak area. Red dots indicate wells drilled after the baseline survey was carried out (after Watson, 2004).

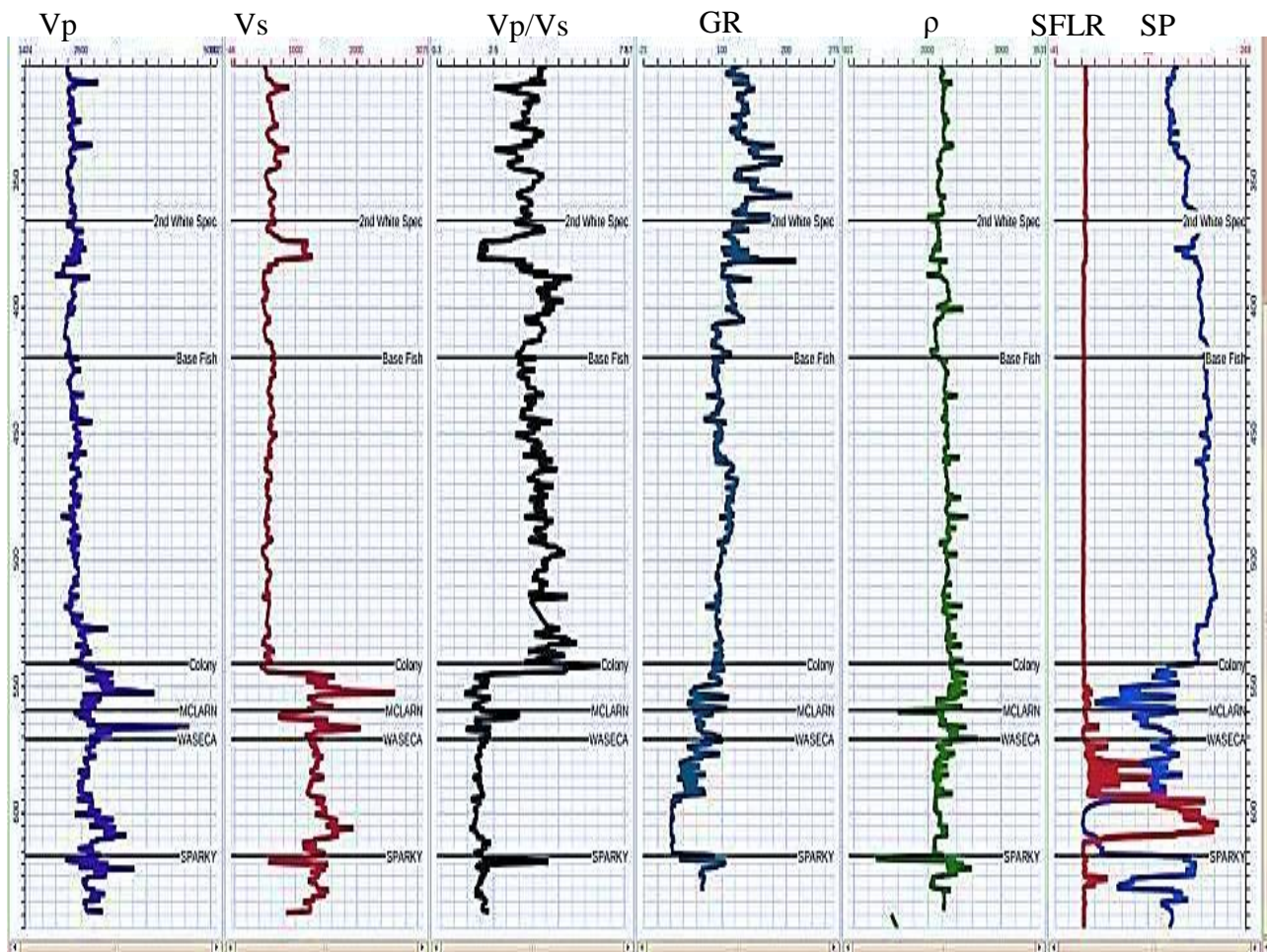


Figure 1.4: Log curves of well 1A15-6, Pikes Peak oil field. Note the drop in the Vp/Vs curve commencing at the Colony formation.

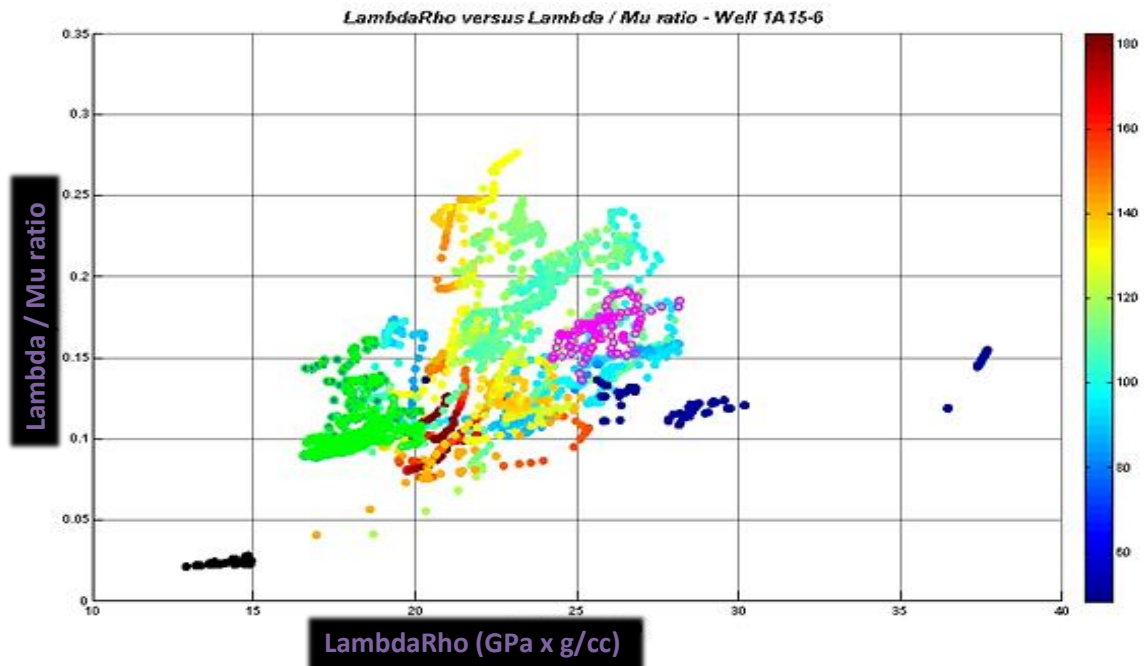


Figure 1.5: LambdaRho versus Lambda / Mu for Well 15A-6, Pikes Peak field colored by gamma ray values. Estimated elastic rock properties for the upper Quaternary, Viking, and Waseca formations are superimposed and colored in solid green, black and magenta respectively.

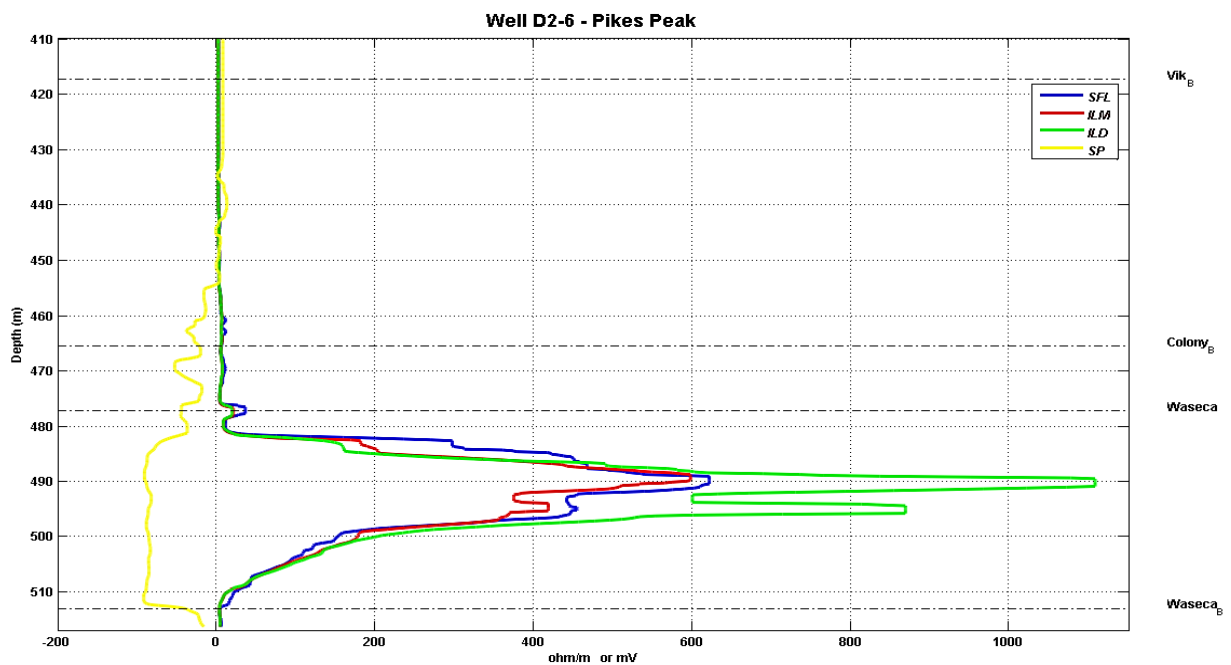


Figure 1.6: The shallow, mid and deep resistivity logs along with the SP log for Well D2-6, Pikes Peak field.

## 1.4 Thesis contributions

In performing the research work for this thesis, several computer codes were developed in MATLAB to generate sections and graphs to support the theory and concepts introduced in this thesis. These codes have also used some CREWES library modules related to ray tracing and the reading of LAS files developed by Dr. Margrave and fellow researchers at CREWES.

The proposed computer codes were developed for:

- Reading, displaying and computing elastic rock properties of well logs
- Implementations of the iteratively re-weighted least square inversion, IRLS, for predicting shear sonic logs include building weighted matrices and L2-curves modules.
- Implementation of the robust locally weighted scattering smoothing, LOWESS, method for the estimation of the mudrock line for predicting shear sonic log
- Three-term simultaneous time-lapse AVO inversion schemes including robust AVO inversion.
- Three-term simultaneous PP-PS AVO inversion to estimate elastic impedances and density model parameters.

The research work has also included the following contributions:

- Complete seismic data processing of the Pikes Peak for AVO compliant and seismic imaging.
- An effective seismic noise attenuation procedure that attenuates noise while preserving reflected amplitude.
- Quantitative interpretation of seismic data including, time-lapse seismic differences, post-stack impedance inversion, and three-term AVO inversion for impedances and density sections for the Pikes Peak time-lapse seismic surveys.

## **1.5 Outline of thesis**

This thesis is organized as follows. The introductory chapter reviewed research objectives, and provided background details regarding elastic rock properties; and their links with lithology and pore-fluid content. In addition, AVO methodology and time-lapse seismic monitoring applications were reviewed to address short comings of applications of time-lapse seismic monitoring including AVO inversion in tracking steam movement in heavy oil reservoirs.

Chapter 2 explains the theory and application of the iteratively re-weighted least-squares inversion, IRLS, in predicting a shear sonic log. Steps to build the  $L_2$  curve function to estimate optimum curvature value to be used in minimizing the objective function of the inverse problem are given in detail. The robust locally weighted scattering smoothing method, LOWESS that further enhances calculating the slope and intercept used in predicting shear sonic log is introduced. The successful implementations of the LOWESS method in predicting shear sonic using wells from different reservoirs (conventional -, heavy oil- and unconventional tight-reservoirs) from the Western Canadian sedimentary basin, WCSB, are presented.

Chapter 3 introduces the theory of time-lapse AVO inversion methods that simultaneously invert the PP-PS data of the baseline and monitor line surveys. Further discussions about building time-lapse survey and generating synthetic data that are used in testing proposed computer codes are given. Chapter 3 further discusses the potential of implementing the proposed time-lapse inversion schemes using noise-free and noisy synthetic data. The robustness of the AVO inversion in the presence of noise, the stability of inversion codes, and the convergence toward a final solution are also investigated. Simultaneous inversion accuracy in estimating elastic parameters, density, and changes in inverted model parameters of the time-lapse surveys are also investigated.

Chapter 4 discusses the seismic data processing of the time-lapse surveys at Pikes Peak heavy oil field. An optimized seismic processing flow that improved seismic repeatabilities and minimized processing differences in time-lapse seismic processing is explored. Noise attenuation procedures adopted in this thesis for attenuating ground-roll, pumpjack and air blast noise effects by modelling are presented. Results of the successful seismic imaging of the Waseca reservoir channel and time-lapse seismic monitoring of the thermal hydrocarbon recovery at the Pikes Peak oil field are also given.

Chapter 5 presents quantitative interpretations of the seismic differences and time-lapse post stack P-impedance inversion. Chapter 5 also discuss the potential of seismic data conditioning and resulting elastic and density attributes from AVO inversion that was conducted individually for the Pikes Peak data set. Hydrocarbon movement through the top seal into overlying formations, as a result of excessive steam injection, are explored. Further discussions about hydrocarbon movements along the interbedded silt/ sand facies, and their correlations with time-lapse seismic stack and seismic differences sections are also presented.

Chapter 6 provides concluding remarks drawn from research work carried in this thesis. Guidelines for the potential expansion of some of the research ideas left in this thesis for possible future work are also given.

## Chapter Two: **PREDICTION OF SHEAR-WAVE SONIC LOGS IN THE WESTERN CANADIAN SEDIMENTARY BASIN (WCSB)**

### **2.1 Introduction**

Dipole sonic logging is an important tool capable of measuring sonic compressional and shear wave transit time of both hard and soft formations. Shear sonic logs are not always available for most wells drilled in explored areas due to the high cost of shear-wave sonic logging as well as the difficulty in obtaining precise shear slowness measurements that are free from mud invasion effects, cycle skipping and other environmental attributes that affect well drilling procedures and data acquisition (Ellis and Singer, 2008).

Recent developments of sonic logging tools have prompted drilling companies to calculate mode-converted shear sonic wave using compressional sonic measurements from several receivers along the probe, as an alternate method of direct shear wave sonic measurement. However, this method of calculation can be applied only to formations or rock layers where the shear wave velocities are faster than the velocity of drilling mud.

The Pikes Peak seismic survey area has only one dipole sonic log, therefore, one of the thesis objectives is to estimate shear sonic log for wells that do not have dipole sonic measurements acquired during well logging. Another goal is to quantify shear sonic logs for those were logged in different (conventional oil, heavy oil and unconventional-tight oil shale) reservoirs in WCSB.

### **2.2 Empirical Relations for Mudrock Line Estimation**

The Castagna's mud-rock line equation (Castagna et al., 1985) is given by

$$V_s = 0.8621 * V_p - 1.1724 \quad 2.1$$

where P-wave sonic velocities are in km/sec.

Han et al., (1986) have also established another empirical relationship used to predict shear-wave log, and it is written as:

$$V_s = 0.7936 * V_p - 0.7868 \quad 2.2$$

The most common empirical S-wave estimation formula is the relation developed by Greenberg and Castagna, (1992). The  $V_s$ -estimation equation is given by

$$V_s = \alpha_2 V_p^2 + \alpha_1 V_p + \alpha_0 \quad 2.3$$

Where  $\alpha_0, \alpha_1$  and  $\alpha_2$  coefficients are global and are defined for each lithology.

While the general approach for estimating shear-wave log is to use one of the empirical relationships above, our goal is to derive these empirical parameters locally, since the classical approach often neglects specific lithology of geological markers, reservoir pressure and temperature conditions, as well as drilling and other circumstances that affect specific well bore log during the course of a survey.

### **2.3 Inverse Problem for Predicting of Shear Sonic log**

Linear regression is a classical method that is used to derive empirical Castagna's constants locally. Thus, better approximations of lithology and borehole conditions are maintained. However, the linear regression method is often influenced by the presence of outliers that lead to inaccurate estimates of the slope and intercept points; thus producing erroneous predicted data.

In a linear inverse problem, the objective is to re-calculate measured data, trying to fit the synthetic model or predicted data to measured data, and then estimating data misfit or uncertainty. Producing a model that describes our observed data to a certain degree of confidence is the core subject of the inverse theory (Tarantola, 1987). The shear sonic log can be

posed as an inverse problem and solved accordingly. By writing S-wave estimation as a linear inverse problem, Castagna's equation can be written as follows:

$$V_s = aV_p + b \quad 2.4$$

The forward – inverse pair can be written as follows:

$$m = \mathbf{G}^T d \quad 2.5$$

$$d = \mathbf{G}m + \varepsilon \quad 2.6$$

where  $m$  is the model parameters,  $\mathbf{G}$  is the forward operator,  $d$  is measured data and  $\varepsilon$  noise.

### 2.3.1 Formulating of Least-squares Inversion

In least-squares inversion, we solve for a parameter model vector,  $m$ , which fits a model response to data,  $d$ , in a least squares sense (Lines and Treitel, 1984). The error,  $\varepsilon$ , in equation (2.6) is assumed to be white noise (Aster et. al., 2005). Traditional Tikhonov regularization selects solutions by minimizing an objective function of equation (2.7) that combines the  $\ell_2$  norm of data-misfit and semi-norm of model length given in equation (2.8).

$$J = J_d + \lambda J_m \quad 2.7$$

$$J(m) = \|\mathbf{G}m - d\|_2^2 + \lambda \|m\|_2^2 \quad 2.8$$

The Levenberg-Marquardt least-squares inverse equation (Levenberg, 1963) can be written as

$$(\mathbf{G}^T \mathbf{G} + \lambda_i \mathbf{I})m = \mathbf{G}^T d \quad 2.9$$

where  $\mathbf{G}$  is the forward operator,  $\mathbf{I}$  is identity matrix, and  $\lambda$  is the regularization parameter.

### 2.3.2 Setting up the Regularization Parameter of the Inversion Scheme

The regularization parameter or damping factor,  $\lambda$ , is the trade-off parameter between the residual norm and model norm. If  $\lambda$  is a relatively large number, the noise will be attenuated at the expense of a less accurate approximation of the desired output, thus it degrades the resolution of the predicted shear sonic log. On the other hand, if  $\lambda$  is too small, the noise could dominate the predicted shear sonic log, which leads to instabilities in the inversion. Therefore, the addition of a damping factor is a trade-off between accuracy and instabilities in the inverse algorithm.

There are many approaches for selecting a proper value of the regularization parameter. The L-curve method (Hansen and O'Leary, 19993) is based on maximum curvature. On the other hand, the discrepancy principle or generalized cross-validation method, GCV, (Wahba, 1977) is another approach in determining an optimum regularization parameter. Both techniques require solving equation (2.9) for a different range of the damping factor; a potentially very costly task.

In this study, a damping factor of 0.1 is used in the initial iteration. For subsequent iterations, the damping factor is either increased by 0.25 of  $\lambda_{i-1}$  or decreased by a magnitude of  $\lambda_{i-1}/4$ , as the computed damping factors have produced stable and good convergence for the inverted model. Increasing or decreasing the regularization parameter is bound by the magnitude of the  $\ell_2$  norm of the model length for  $J_m^i$  and  $J_m^{i-1}$ . For the first iteration, we choose the norm of logarithmic measured data as an initial norm condition of model length. Figure (2.1) shows the Lagrange multiplier,  $\lambda_i$  for the  $i^{\text{th}}$  iterations during an inversion to estimate the shear sonic log.

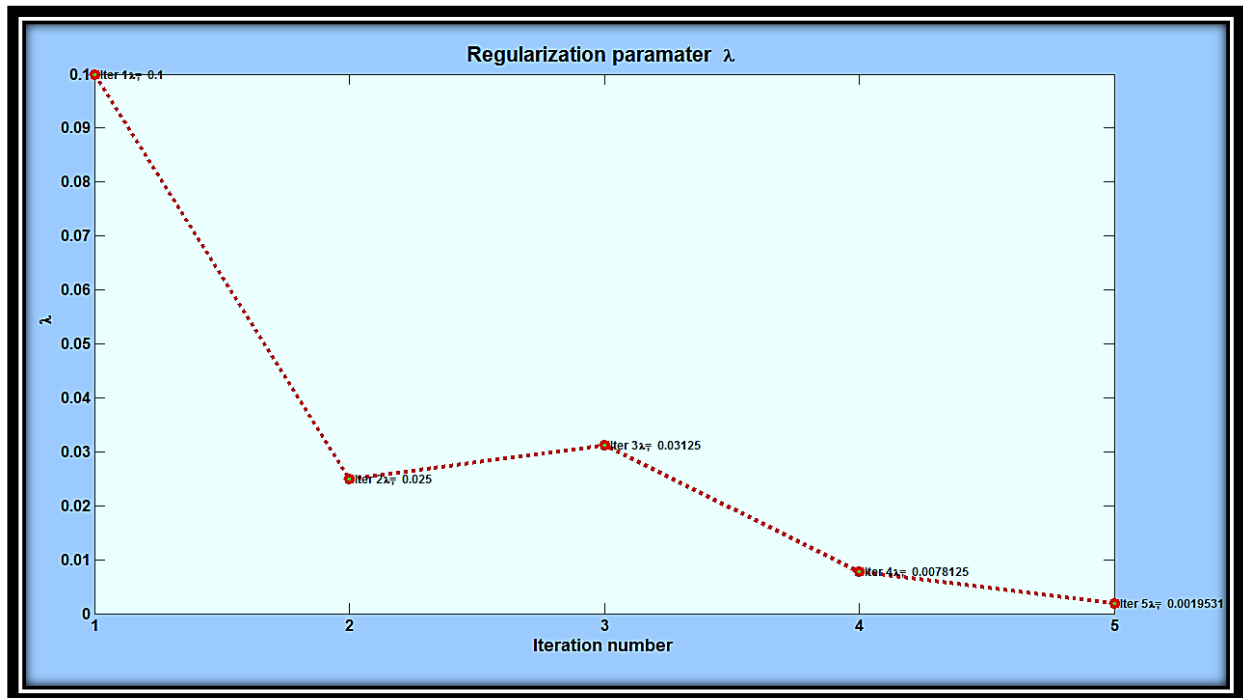


Figure 2.1: The Lagrange multiplier,  $\lambda$  for the  $i^{\text{th}}$  iterations during inversion of shear sonic log using one of the proposed inverse schemes.

## 2.4 IRLS Inversion of the shear-sonic log

In the previous section, it is stated that the linear inverse method is often influenced by the presence of outliers that might give inaccurate estimates of the slope and intercept values. Thus, the presence of outliers prompts us to research for an inverse method that tackles noise in shear sonic logs. Thus, a need for developing new techniques to estimate the uncertainty in shear sonic log becomes imminent in order to quantify the shear sonic log via the Inverse theory, and to produce more interpretive sections of inverted shear log.

The iteratively re-weighted least squares, IRLS, (Wolke and Schwetlick, 1988; Saeed et al., 2010a and 2010b) inverse method is another technique used to estimate shear-wave sonic log that is less influenced by noise, and it guards against outliers.

We formulate the inverse problem using Tikhonov regularization (Tikhonov and Arsenin, 1977) to obtain inverse solution by minimizing the objective function in equation (2.7).

The data misfit is defined as

$$J_d = \|W_d(Gm - d)\|_2^2 \quad 2.10$$

While the model solution is defined as

$$J_m = \|W_m(m)\|_2^2 \quad 2.11$$

A new objective function that incorporates different weights is then expressed as

$$J(m) = \|W_d(Gm - d)\|_2^2 + \lambda \|W_m(m)\|_2^2 \quad 2.12$$

Thus, a new system of equation that provide an estimate of unknown parameters can be written as

$$(G^T W_d^T R_d W_d G + \lambda_i W_m^T R_m W_m) m = G^T W_d^T R_d W_d d \quad 2.13$$

where  $R_d$  and  $R_m$  are data misfit and model-structure weighting matrices (Farquharson and Oldenburg, 1998) introduced so that different elements of the data misfit and model roughness vectors are given equal weights in the inversion process.  $W_d$  is a diagonal weighted matrix in the data space, while  $W_m$  is a weighted or roughness operator in the model space.

In the following subsections, several types of weights (constraints) used in the data-misfit and regularization model norms are given.

### 2.4.1 Minimization using $\ell_1$ measures of $R_d$ and $R_m$

The general form of an objective function to be minimized (Scales et al., 1988) can be written as

$$J(x) = \sum_i |x_i|^p \quad 2.14$$

Traditional least square problems that satisfy  $\ell_2$  are solved for  $p=2$ . If  $\ell_1$  is sought, then  $p=1$ , and the objective function is merely the sum of the absolute values of vector  $x$ . The vector  $x$  represents either data-misfit term (equation 2.15) or the model-length term given by regularization function (equation 2.16).

$$x = W_d(d - Gm) \quad 2.15$$

$$x = W_m m \quad 2.16$$

For the case  $x_i = 0$ , the objective function (equation 2.14) must be modified to avoid a discontinuity in  $\partial j / \partial x$  (Farquharson and Oldenburg, 1998). Thus a small user-specified value  $\varepsilon$  is added to equation (2.14) in order to introduce stability when  $x_i = 0$ . The modified objection function for an  $\ell_1$  measure is then expressed as

$$J(x) = \|x + \varepsilon\|_1^1 \quad 2.17$$

Recall equation (2.13),

$$(G^T W_d^T R_d W_d G + \lambda_i W_m^T R_m W_m)m = G^T W_d^T R_d W_d d \quad 2.18$$

The  $R$  matrix in equation (2.18) can be written as

$$R_{ij} = \begin{cases} (x + \varepsilon)^{-1/2} & , i = j \\ 0 & , i \neq j \end{cases} \quad 2.19$$

Since  $\mathbf{R}$  is a function of an unknown parameter,  $\mathbf{x}$ , this is a non-linear system, and an iterative approach must be used. This is referred to as iteratively re-weighted least squares, IRLS, (Wolke and Schwetlick, 1988).

We followed the approach of Farquharson and Oldenburg (1998), by setting  $\mathbf{R} = \mathbf{I}$  for the first iteration, which results in a traditional least-squares solution. The estimation of  $m^i$  for  $i=1$  is used to calculate  $\mathbf{R}$  in equation (2.19), and then subsequently substituted again in equation (2.18) to calculate a new  $m^{i+1}$ . The procedure is repeated until the convergence condition given in equation (2.20) between successive IRLS iterations is met.

$$J(x) = \frac{\|m^{k+1} - m^k\|_2}{1 + \|m^{k+1}\|_2} < \tau \quad 2.20$$

where  $\tau$  is a tolerance value, and was set equal to 0.001 for research work in this thesis.

There are now two user-defined parameters,  $\lambda$  and  $\varepsilon$ , that control the behavior of the solution of inverse problems. A small value of  $\varepsilon$  is needed to stabilize equation (2.17), but too small a value can introduce instability for any  $x_j \rightarrow 0$ . On the other hand, a large value of  $\varepsilon$  tends to act more like a traditional regularization parameter when  $\varepsilon \gg x$  (Minsley, 1997). The damping parameter,  $\lambda$ , can be chosen either by the L-curve method (Hansen, 1994) or by using a user specified small positive value that is within  $0 < \lambda < 1$  range.

Since the main objective of the inversion algorithm used in this study is to have minimal intervention by the user, it followed the approach of Farquharson and Oldenburg, (1998) and

Zhdanov and Tolstaya, (2004) by plotting  $J(x)$  for a range of  $\varepsilon$  to determine an optimal balance between these two extremes. This is not computationally expensive because it only requires substituting multiple values of  $\varepsilon$  into equation (2.17) using the current value of  $x$ . In the following sub sections, building of the L-curve functional and calculating the maximum curvature to obtain the optimal trade-off parameter  $\varepsilon$  are given.

#### 2.4.1.1 Building the L-curve

The optimal trade-off parameter,  $\varepsilon$ , is calculated based on the L-curve method of Hansen and O'Leary, (1993). The L-curve is a plot, in log-log scale, of corresponding values of the residual and solution norms (Figure 2.2). In this research, the optimal trade-off value of  $\varepsilon$  is chosen to be within the range ( $10^{-5} \leq \varepsilon \leq 1$ ) divided over 150 points of equal spaces. The L-corner is defined either as maximum curvature (Hansen, 1994) or as the point of tangency with a straight line of negative slope (Reginska, 1996; Orintara et. al., 2000).

Note that Hansen, (1994) defined the L-corner as the point of maximum curvature, and the calculation of the inverse problem was repeated for two-hundred different values of regularization parameters to find the L-corner.

In order to construct the L-curve function given in Figure (2.2), define the x- and y-axes as follows:

$$\rho = \log\|x_d + \varepsilon\|_1^1 \tag{2.21}$$

$$\eta = \log\|x_m + \varepsilon\|_1^1 \tag{2.22}$$

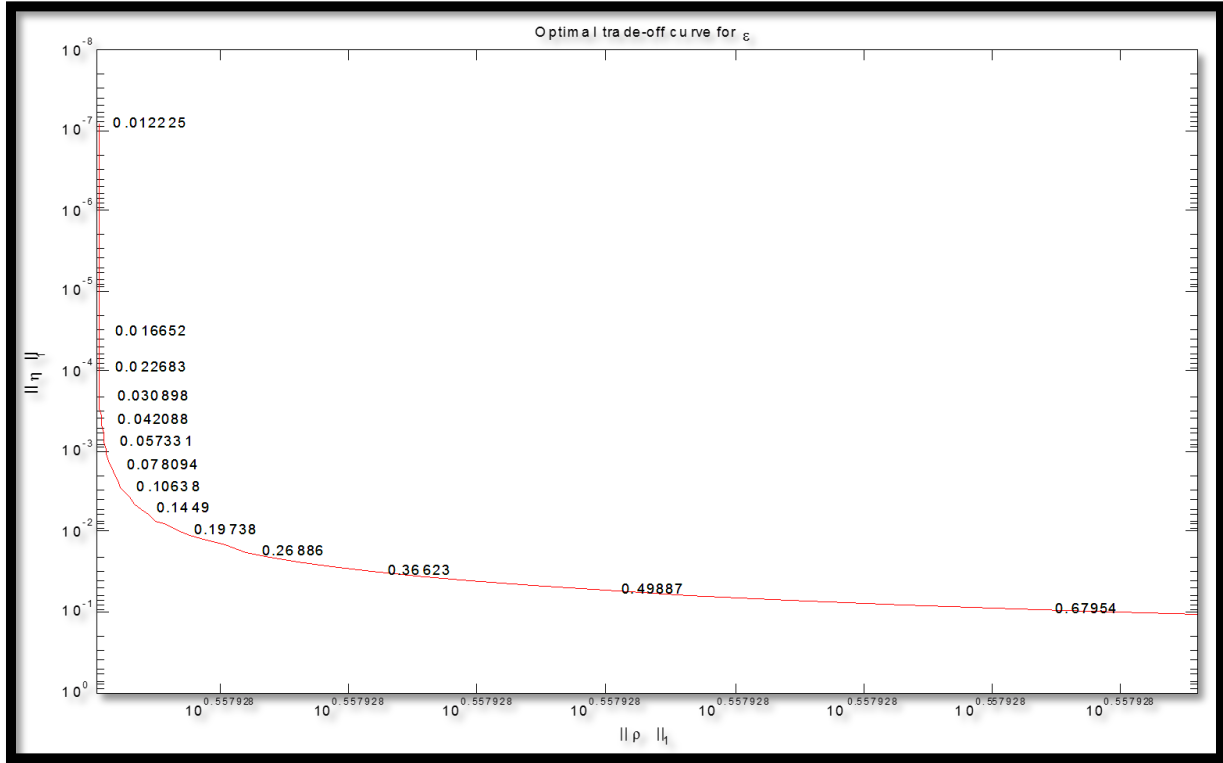


Figure 2.2: The L-curve plot of log values of residual and solution norms.

where  $x_d$  and  $x_m$  represent the data-misfit and model length terms that were calculated from equations (2.15) and (2.16) respectively. The point on the L-curve associated with  $\varepsilon$  is given by  $1/2(\rho, \eta)$ .

In Figure (2.2), when  $\varepsilon$  is very large, the curve is essentially a horizontal line in a region called the over-regularization region (Oraintara et. al., 2000). Conversely, when  $\varepsilon$  is very small (under-regularization), the curve is a near vertical line. The transition between these two regions of under and over-regularization corresponds to the “corner” of the L-curve and the associated value of  $\varepsilon$  at this corner is considered to be an optimal value of the regularization parameter.

### 2.4.1.2 The curvature of the L-curve

The curvature  $k_\varepsilon$  of the L-curve (Calvetti et. al., 2000) is given by

$$k_\varepsilon = 2 \frac{\rho''\eta' - \rho'\eta''}{((\rho')^2 + (\eta')^2)^{3/2}} \quad 2.23$$

where ' and '' denotes the first and second derivative with respect to  $\varepsilon$ . From equations (2.21 and 2.22), and  $\rho' = -\varepsilon\eta'$  (Hansen and O'Leary, 1993), the optimal curvature,  $\widehat{k}_\varepsilon$ , is given by

$$\widehat{k}_\varepsilon = 2 \frac{\eta\rho}{\eta'} \frac{\varepsilon^2\eta'\rho + 2\varepsilon\eta\rho + \varepsilon^4\eta\eta'}{(\varepsilon^2\eta^2 + \rho^2)^{3/2}} \quad 2.24$$

Note that Hansen, (1994) uses the initial  $k_\varepsilon$  obtained in equation (2.23) with few regularization parameters before and after the initial  $k_\varepsilon$  in order to obtain the optimal maximum curvature  $\widehat{k}_\varepsilon$ . The index of the minimum of this maximum curvature is the optimal trade-off parameter  $\hat{\varepsilon}$ . In this study, the associated  $\varepsilon$  to initial  $k_\varepsilon$  curvature estimated in equation (2.23) is substituted into equation (2.24) in order to obtain the optimal  $\widehat{k}_\varepsilon$ . The index of the minimum  $\widehat{k}_\varepsilon$  is then cross-referenced with an array of all  $\varepsilon_i$  values used so as to obtain the associated optimal trade-off parameter  $\hat{\varepsilon}$ . Figure (2.3) shows the maximum curvature calculated from the L-curve function, where the optimal  $\hat{\varepsilon}$  is obtained during the IRLS inversion algorithm.

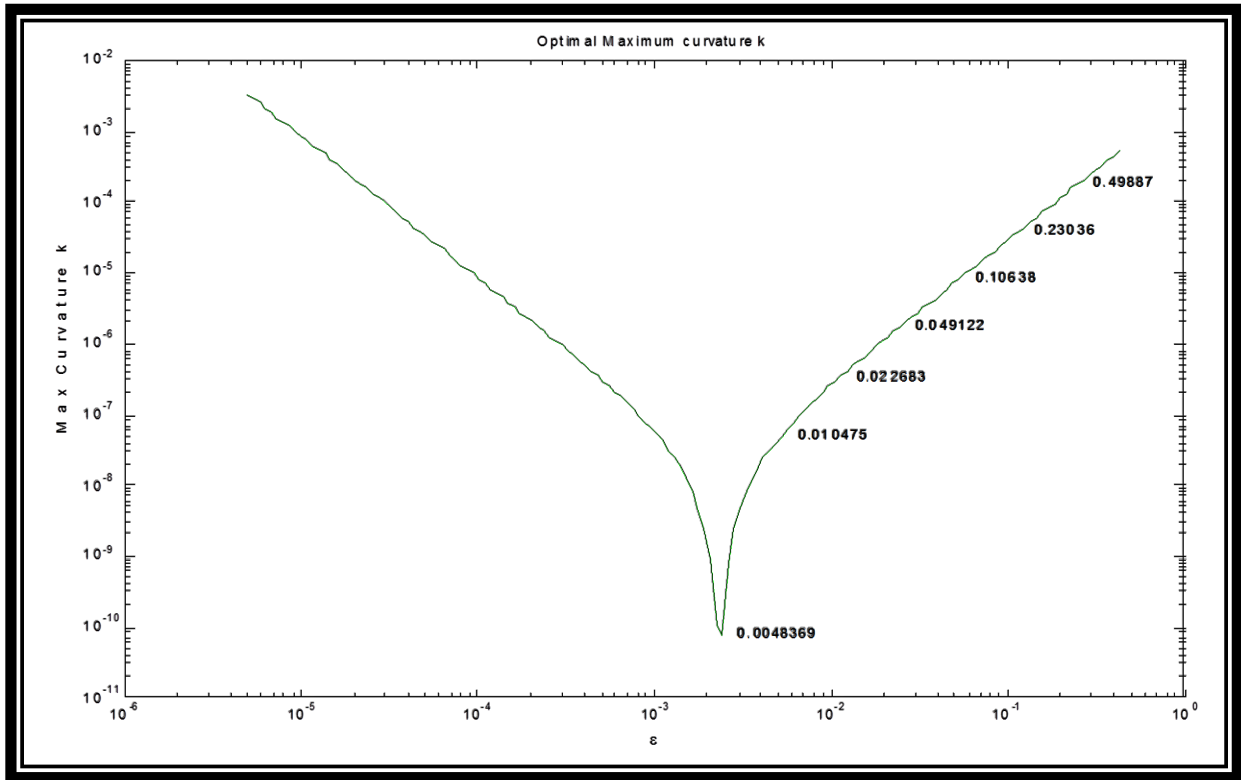


Figure 2.3: The optimum maximum curvature  $\widehat{k}_\varepsilon$ .

#### 2.4.2 Smoothness constraint of the model regularization operator $W_m$

Imposing additional information about the model will constrain the roughness of the inverse operator (Constable et al., 1987) in order to produce a refined model. The purpose of the regularization operator in the inverse problem is to introduce stability while recovering models that do not involve complicated features. The regularization operator can be either smoothness or compactness.

Common forms of regularizations applied to the model space are those developed by Tikhonov and Arsenin, (1977) in order to introduce stability through constraints provided by the regularization operator. When the operator is the identity matrix ( $W_m = I$ , 0<sup>th</sup> order), a

minimum length solution is obtained. If the operator is the gradient ( $\mathbf{W}_m = \nabla$ , 1<sup>st</sup> order), a flat solution is obtained, while a Laplacian operator ( $\mathbf{W}_m = \nabla^2$ , 2<sup>nd</sup> order) leads to a smooth solution (Ajo-Franklin, et. al., 2007).

Although neither flatness nor smoothness are intrinsic properties of the earth, Tikhonov methods have enjoyed remarkable success, particularly in the use of first order finite-difference operators (deGroot-Hedlin, and Constable, 1990). Note that, although these operators introduce stability to inverse algorithm, some resulting model tends to have very smooth sections that may not always be realistic (Silva et al., 2001).

Li and Oldenburg, (2000) advocate selecting regularization operators, which incorporate some constraints that are responsible for observed property variations, such as geological dip or fluid flow in a high permeability zone. The regularization operators can also be the case when a geologic feature such as a dike has material properties that vary over short distances, or where fluid flow occurs along restricted high permeability pathways (Ajo-Franklin et al., 2007).

### ***2.4.3 Compactness constraint of the model regularization operator $\mathbf{W}_m$***

A compactness constraint operator is another stabilizing function that minimizes the area where strong variation in model parameters or discontinuities occur (Portniaguine and Zhdanov, 1999). The compactness constraint operator is non-linear and requires the use of model-space in an iteratively reweighted least squares (IRLS) sense for an effective solution. In the following subsections, three types of compactness constraints are given in some details. The weighted matrix,  $\mathbf{W}_d$  was set as identity matrix during the inversion. Note that due to large numbers of figures generated using different weight methods, we will include only figures that best describe the concept used in this study.

### 2.4.3.1 Modified total variation method

The total variation approach ( $T_v(m) = \|\nabla m\|_1$ ) was used by Rudin et al. (1992) to reconstruct noisy and blurred images. This approach was then modified by Acar and Vogel (1994), to introduce stability when model parameters are non-differentiable. The modified total variation method or cumulative sensitivity (Portniaguine and Zhdanov, 1999) is defined as follows:

$$\Lambda_{ij} = (J^2 + \beta^2)^{1/2} \quad i = 1:N \quad 2.25$$

where  $J$  is the Jacobian matrix of the data with respect to model parameters  $\partial J_m / \partial m$  and  $\beta$  is a small fractional number introduced to provide stability. The operator,  $\Lambda_{ij}$  forms a diagonal weighting matrix that allows for solutions away from measurement locations, where sensitivity decreases (Boulangier and Chouteau, 2001; Li and Oldenburg, 1996).

Figure (2.4) shows measured  $V_p$  (blue in color),  $V_s$  (red in color), the  $V_p/V_s$  ratio (black in color) and the density (green in color) logs from Well 1A15-6 of the Pikes Peak, heavy oil reservoir. The hope is to obtain good estimates of slope and intercept values that are used in equation (2.4) to estimate shear log that is close to the measured shear-sonic log with minimum residual. In Figure (2.5), the inverted shear sonic log has successfully delineated all lithology layers, and was able to discriminate Waseca sandstone reservoir. Note that a spike at a depth of 560m in predicted shear log can be attributed to coal seam in McLaren formation. Figure (2.6) is a scatter plot for both measured and predicted shear sonic log colored by residual. The majority of predicted shear log values falls in the low residual area.

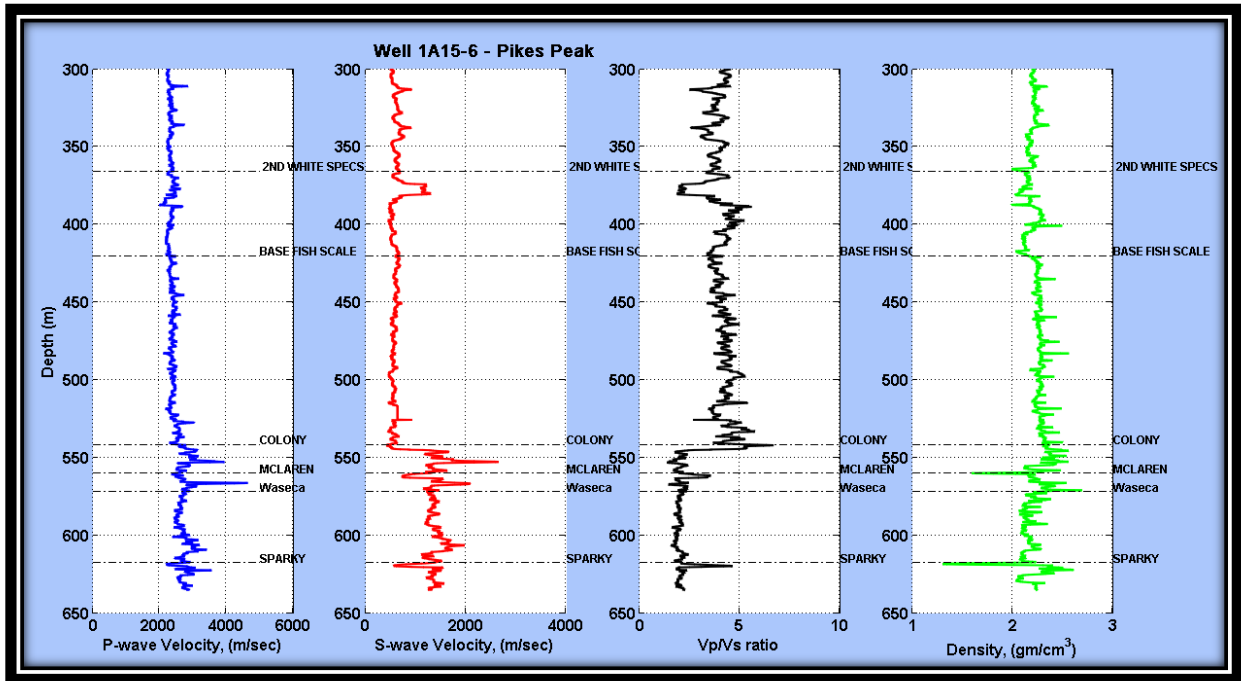


Figure 2.4: The measured  $V_p$  and  $V_s$ ,  $V_p/V_s$  ratio and density logs of the Pikes Peak heavy oil field.

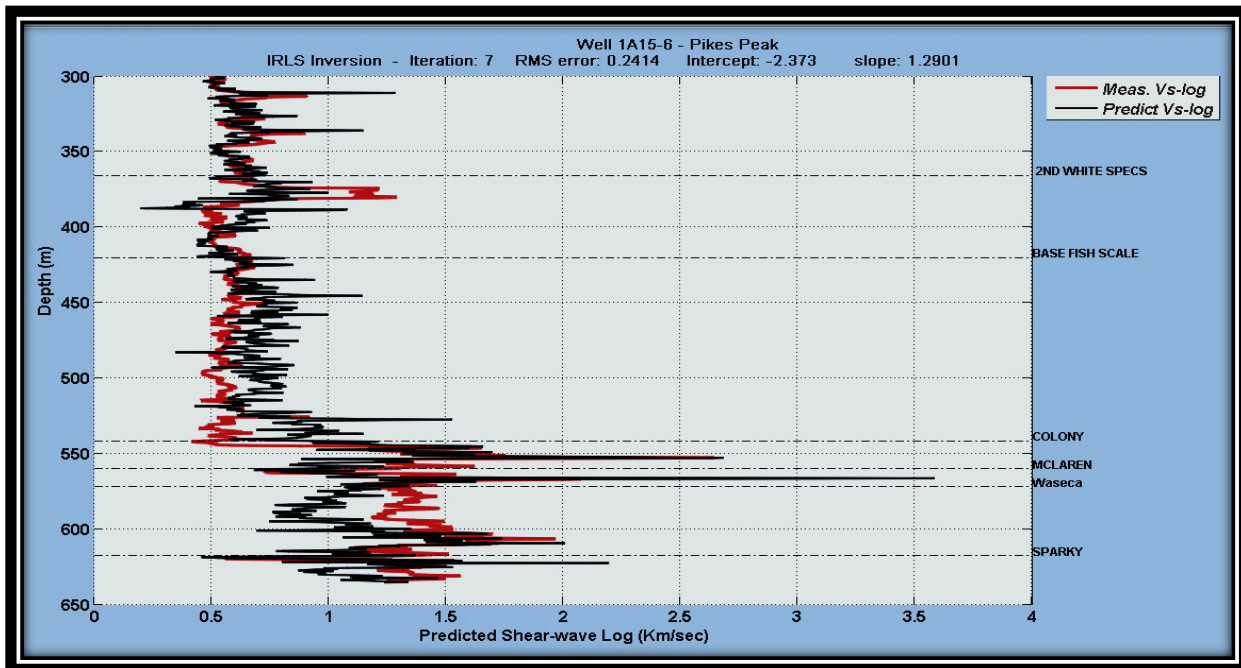


Figure 2.5: The measured and inverted shear sonic logs of Well 1A15-6, Pikes Peak using the modified total variant method.

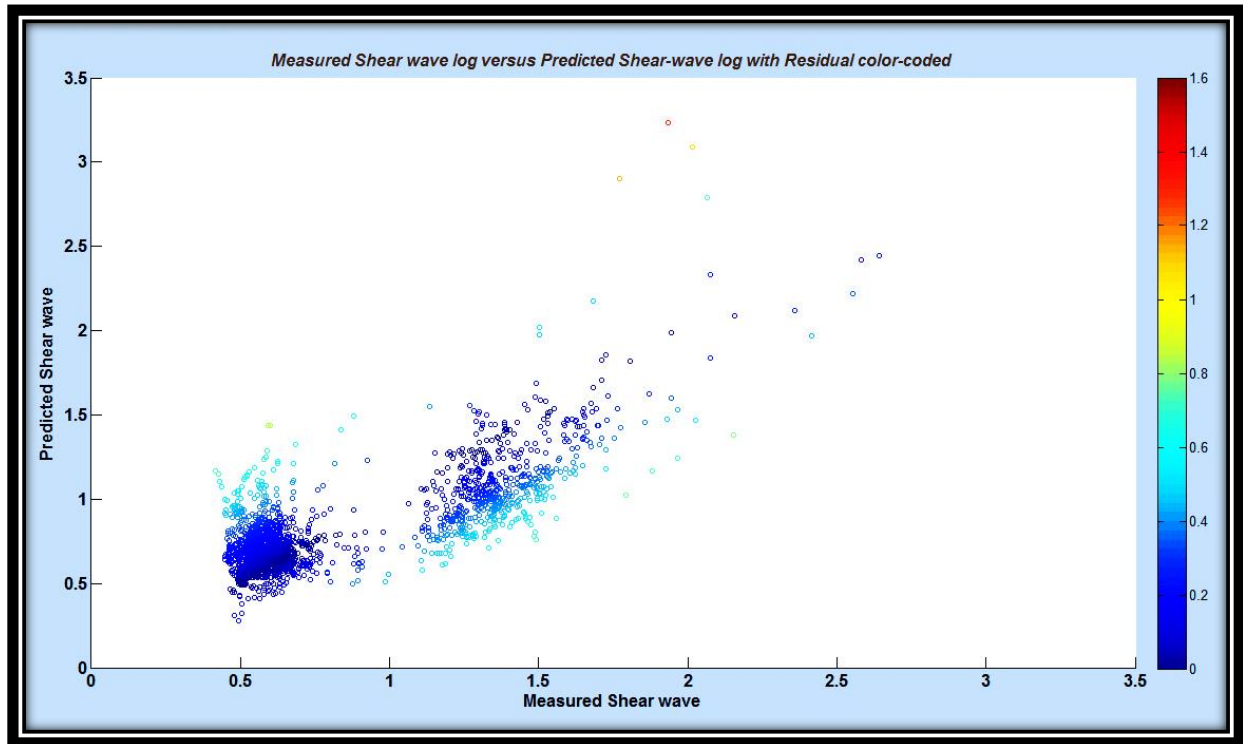


Figure 2.6: The measured versus inverted shear sonic logs colored by residual of Well 1A15-6, Pikes Peak, using a modified total variant method. The color bar represents the absolute difference between measured and inverted shear sonic logs values. Velocity unit is in Km/sec.

#### 2.4.3.2 Minimum support method

Compact body inversion, developed by Last and Kubik (1983), has been used in potential fields (Portniaguine and Zhdanov, 1999) as well as in seismic tomography (Ajo-Franklin, 2007) inverse problems, and usually produces a blocky image model (Claerbout and Muir, 1973). The minimum support function, often referred to as compactness, is based on the minimization of an area (or volume in three-dimensions) metric of the anomaly. Last and Kubik (1983) introduced an area metric,  $A(m)$  that is expressed as follows:

$$A(m) = a_{\mathcal{E}} \lim_{\beta \rightarrow 0} \sum_{i=1}^N \frac{m_i}{m_i^2 + \beta} \quad 2.26$$

where  $a_{\mathcal{E}}$  is the area of a single element,  $m_i$  is the  $i^{\text{th}}$  model parameters, and  $\beta$  is a small fraction introduced to provide stability as  $m_i \rightarrow 0$ . In the limit of  $\beta \rightarrow 0$ , the term on the right hand side of equation (2.26) evaluates to 1 when  $m_i \neq 0$ , and they become 0 when  $m_i = 0$ . This metric approximate the area of the anomalous region.

A new objective function that incorporates the measure of the area, is given by

$$J_d + \lambda J_m = \|\mathbf{G}m - d\|_2^2 + \lambda \sum_{i=1}^N \frac{m_i}{m_i^2 + \beta} \quad 2.27$$

Minimization of the objective function yields a least-square problem that is now dependent on model estimates. The new diagonal weighted matrix,  $\mathbf{W}_c$ , that incorporates compactness, can be written in explicit form as

$$\mathbf{W}_c = \left( \frac{m_i}{m_i^2 + \beta} \right)^{-1/2} \quad 2.28$$

The  $\mathbf{W}_c$  matrix can be viewed as a spatially variable damping matrix with high values in regions where the prior model estimate has a small absolute magnitude (Ajo-Franklin, 2007). The inverted shear sonic log (Figure 2.7), using compactness constraint, has converged to the final solution after the 7<sup>th</sup> iteration. The plot of RMS errors during the inversion (Figure 2.8) shows slight decrease change in RMS compared to the cumulative index in Figure (2.5).

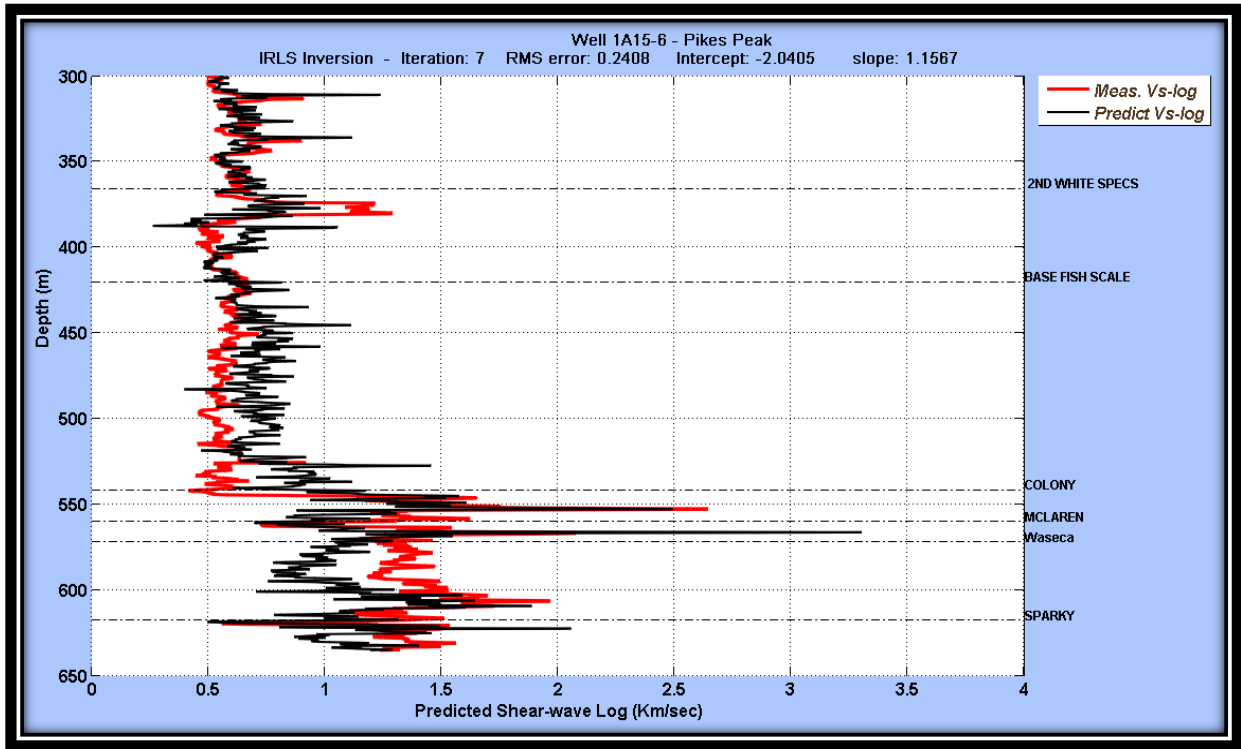


Figure 2.7: The measured and inverted shear sonic logs of Well 1A15-6, Pikes Peak area using the minimum support method.

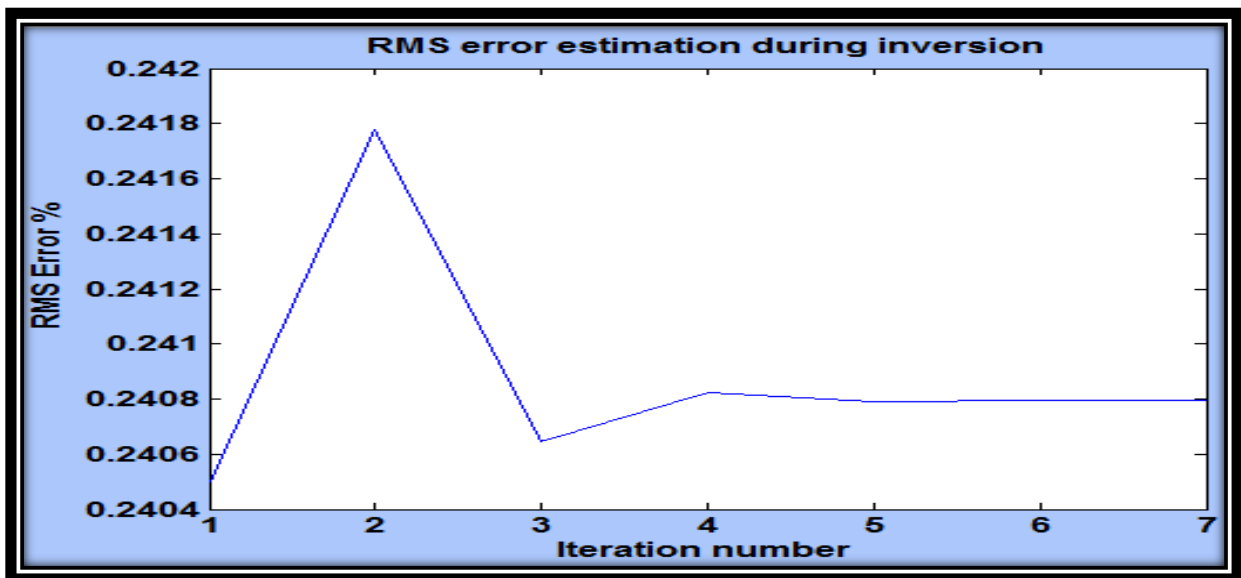


Figure 2.8: The RMS error during IRLS inversion of inverted shear sonic logs of Well 1A15-6, Pikes Peak, using the minimum support method.

### 2.4.3.3 Minimum gradient support

A new constraint that can also be implemented in model space is defined by equation (2.29), where the cumulative constraint (sensitivity weight) is scaled by model parameters.

$$\mathbf{\Omega}_{ii} = \left(\frac{m_i \cdot m_i}{\Lambda_{ii}^2}\right)^{-1/2} \quad 2.29$$

Incorporating of new weight function into traditional least square inverse problem leads to a new objective function that can be expressed as,

$$J_d + \lambda J_m = \|\mathbf{G}m - d\|_2^2 + \lambda \|\mathbf{\Omega}m\|_2^2 \quad 2.30$$

Figure (2.9) shows the inverted shear sonic log using the minimum gradient support constraint. There is a slight change in the slope and intercept calculated after converging to the final solution in the 7<sup>th</sup> iteration. The damping factor graph in Figure (2.10) starts to showing increasing in magnitude at 5<sup>th</sup> iteration before the program reached the final solution.

### 2.4.4 Constrained weight matrix $\mathbf{W}_d$

Several methods to estimate the weighted matrix  $\mathbf{W}_d$  that can be incorporated in the data misfit domain have been tested. These weighted matrices have size of M x M, where zeros take up much spaces of the matrices sizes. One can utilize the sparse matrix technique (Varga, 1962) where only non-zero values with their indices are saved in disk memory. In the following subsections, explanations for each of weight method used are given.

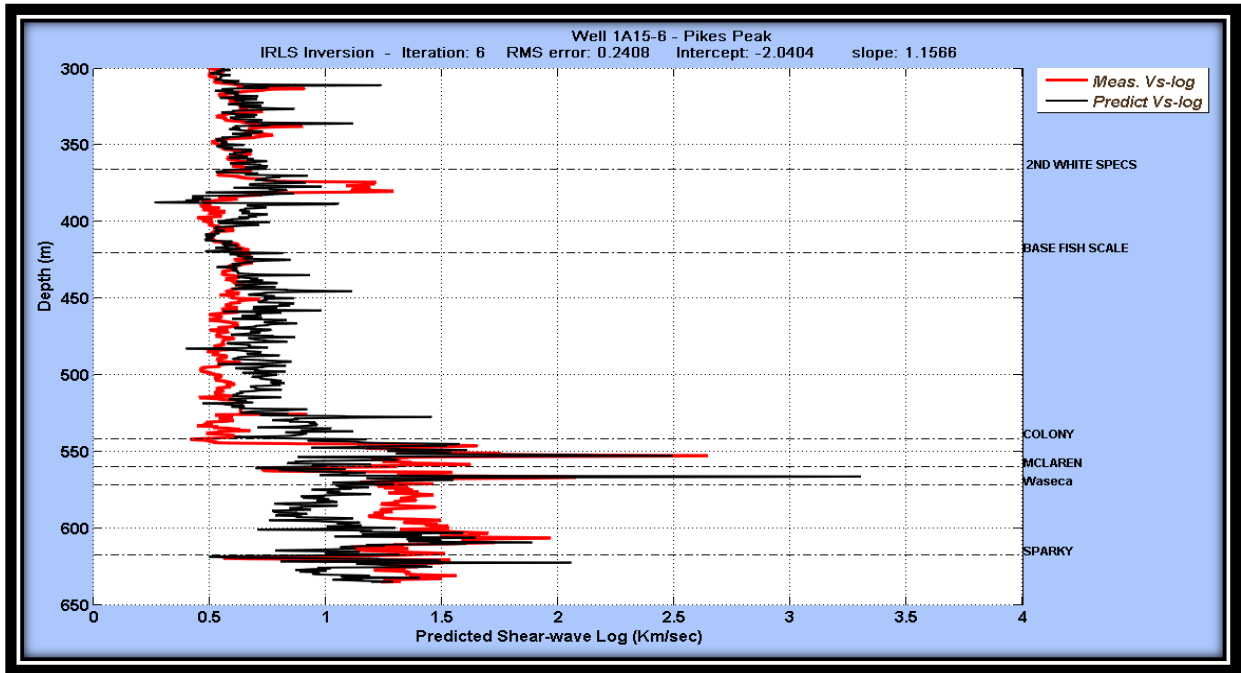


Figure 2.9: The measured and inverted shear sonic logs of Well 1A15-6, Pikes Peak using the minimum gradient support method.

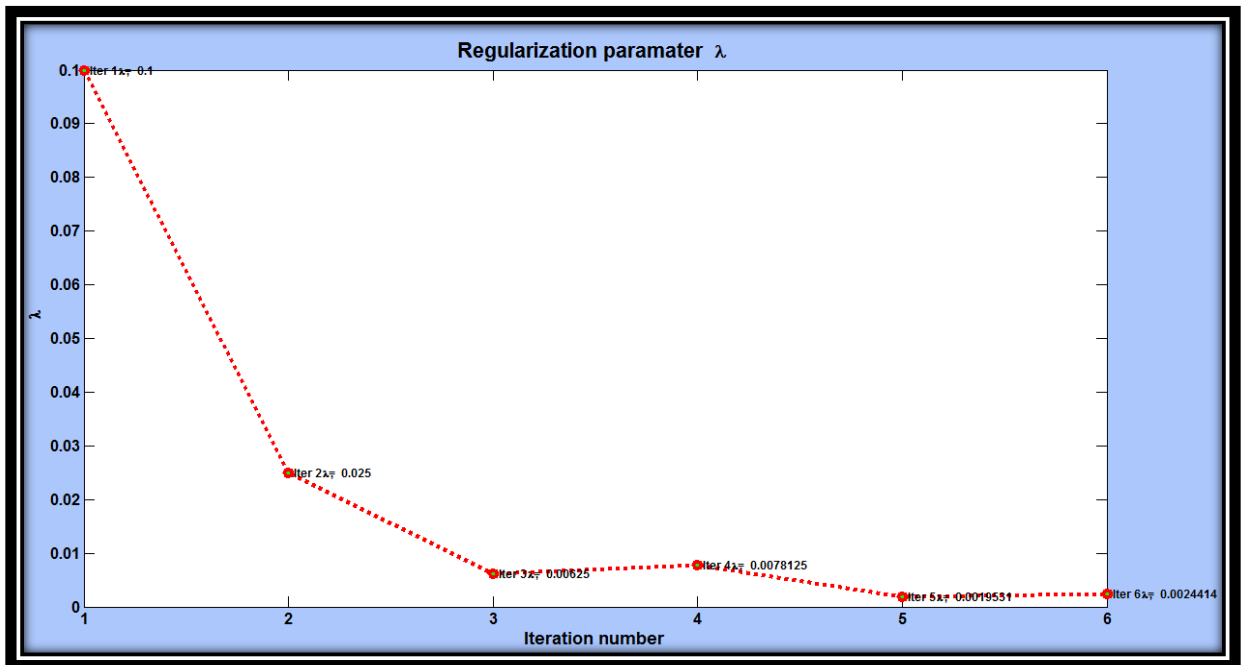


Figure 2.10: Plot of the damping factor during IRLS inversion of shear sonic logs of Well 1A15-6, Pikes Peak area, using the minimum gradient support method.

#### 2.4.4.1 Standard deviation of residual

In geophysical inversion, it is assumed that the model parameter errors are independent and normally distributed (Aster et. al., 2005). Typically,  $\mathbf{W}_d$  contains information about the standard deviation of measurement errors. For the first iteration,  $\mathbf{W}_d$  in equation (2.13) was set to be the identity matrix, and for subsequent iterations, the standard deviation is calculated by

$$\sigma = \sqrt{\frac{1}{m-n} \sum_{i=1}^m r_i^2} \quad 2.31$$

Note that in equation (2.31), the weighted matrix,  $\mathbf{W}_d$ , is scaled by the measured shear sonic log,  $d^{obs}$ , in order to test the stability of the algorithm. Figure (2.11) shows the measured and the inverted shear log. Note that the residual in the Waseca zone is less compared to predicted logs obtained using the constraints in model space. Contrarily, the residual from Base fish scale is increased until we reach the Colony formation where a better approximation is achieved.

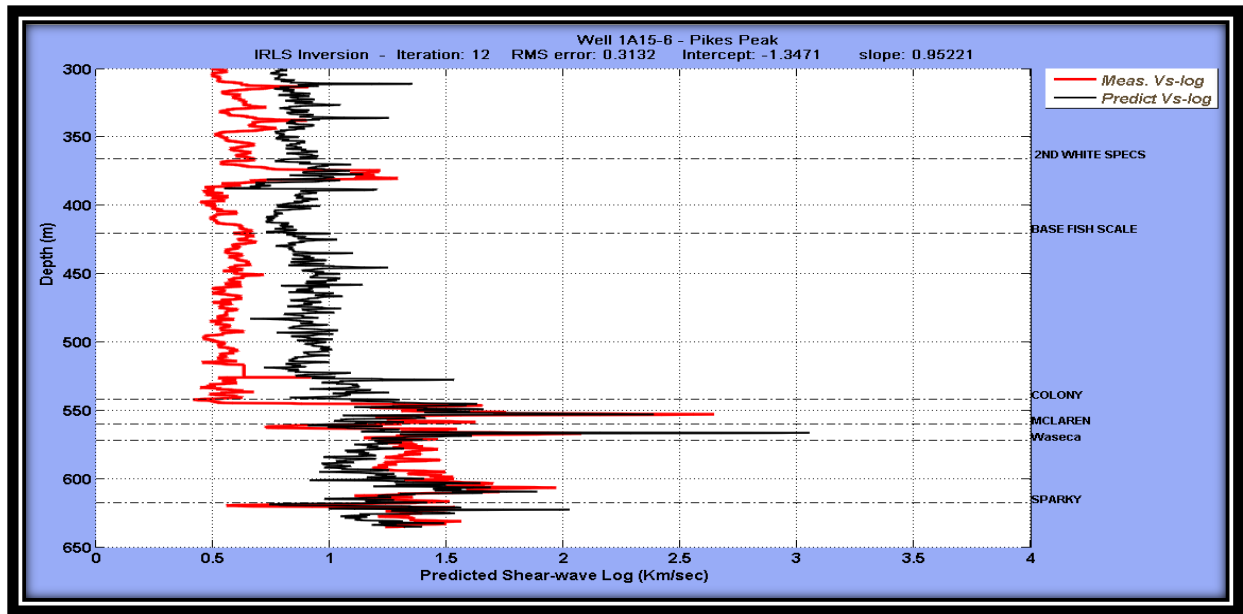


Figure 2.11: The measured and inverted shear sonic logs of Well 1A15-6, Pikes Peak, using the standard deviation of the weight matrix method.

#### 2.4.4.2 Robustness normalized by the standard deviation

The fractional  $\ell_1 - \ell_2$  norms, scaled by the standard deviation (Rücker and Günther, 2006) are another weighted matrix form that can be implemented in data misfit space. The weighted function is written as,

$$\mathbf{\kappa} = \frac{\frac{|e_i|}{\|e\|_1}}{\frac{|e_i|^2}{\|e\|_2^2}} = \frac{\frac{|e_i|}{\sum |e_i|}}{\frac{e_i^2}{\sum e_i^2}} = \frac{\sum e_i^2}{|e_i| \sum |e_i|} \quad 2.32$$

Further improvement in terms of time computation is made by scaling robustness given in equation (2.32) by the standard deviation. Scaling  $\mathbf{\kappa}/\sigma$  leads the program to converge to a final solution after 14 iterations compared to the 17 iterations required if equation (2.32) is used alone. Figure (2.12) show the inverted shear sonic log, while Figure (2.13) shows an associated *RMS* error during inversion. In general, the inverted log better predicts the measured shear sonic log with a clearly smaller residual compared to the constraint method given in the previous section.

#### 2.4.4.3 Hybrid $\ell_1/\ell_2$ norms

The hybrid  $\ell_1/\ell_2$  norms are introduced by (Bube and Langan, (1997) to incorporate desirable geological characteristic in to the inverse problem. The hybrid  $\ell_1/\ell_2$  norm is written as

$$W_{ii} = [1 + (r_i/\tau)^2]^{-0.25} \quad 2.33$$

The norms were scaled by the Darche (1989) tuning constant,  $\tau = \max(d) / 100$ .

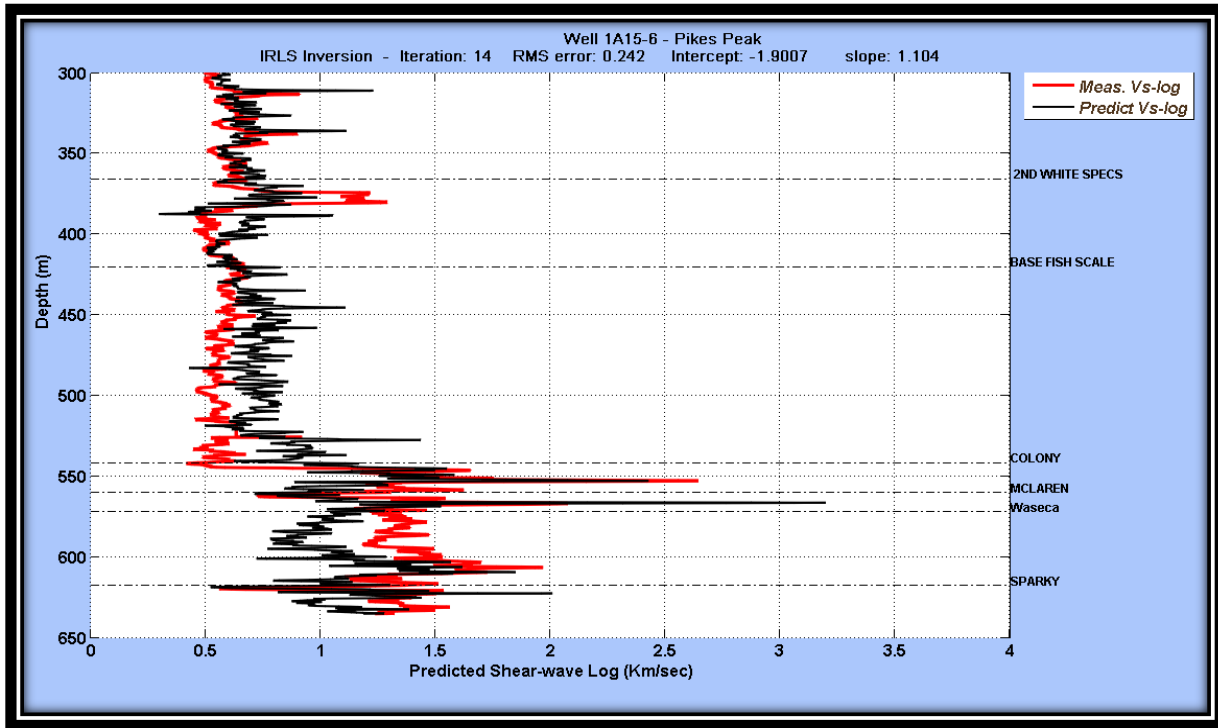


Figure 2.12: The measured and inverted shear sonic logs of Well 1A15-6, Pikes Peak using robustness normalized by the standard deviation method.

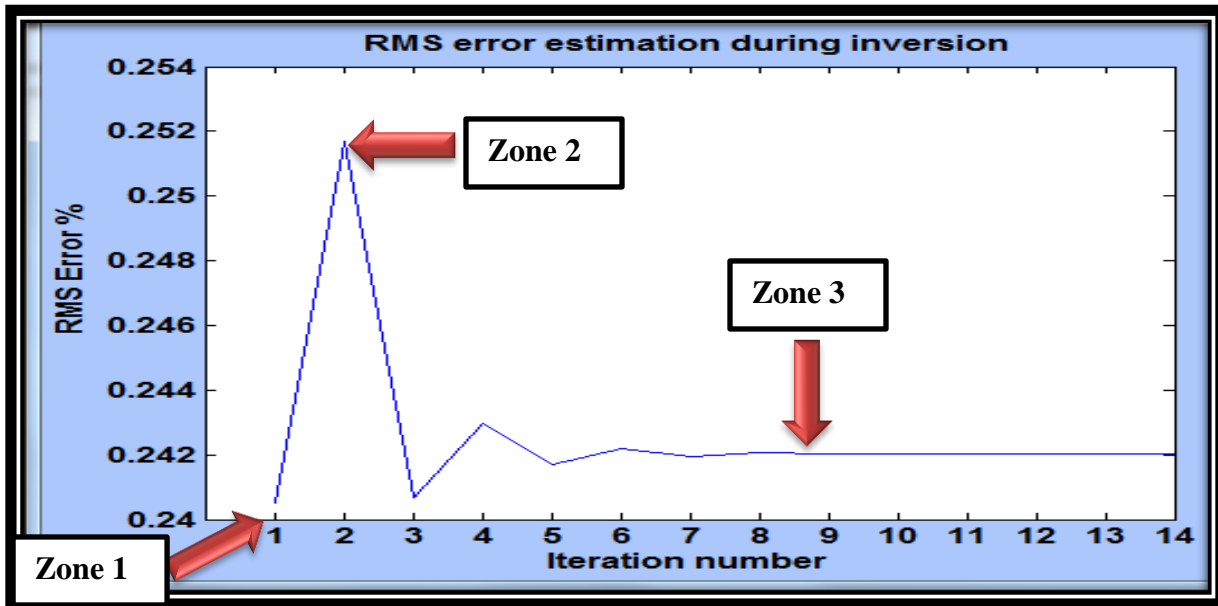


Figure 2.13: The RMS error during IRLS inversion of shear sonic log of Well 1A15-6, Pikes Peak, using robustness normalized by the standard deviation method.

The use of the maximum value of observed data in Darche's tuning factor implies scaling the weighted matrix by a global constant scale, which leads to an increase in the number of iterations required for the program to converge towards the final solution.

The objective is to optimize the inverse scheme in terms of accuracy and computation time, and therefore, by using the absolute maximum of residual in Darche's threshold,  $= \max|r|/100$ , the tuning scale varies at every iteration. The modified tuning factor reduced number of iterations required to converge to final solution significantly, and has also reduced RMS error.

The inverted shear sonic log is given in Figure (2.14). Note that, the final predicted shear sonic converges after nine iterations compared to the robustness normalized by standard deviation previous method that required 14 iterations. The final predicted shear sonic log is close to the measured shear sonic log with a smaller residual.

#### 2.4.4.4 Huber constraint

The maximum likelihood estimator, often referred as the M-estimator, has been widely used in linear regression problems (Hong and Chen, 2005) to reduce the influence of outliers. The M-estimator is defined as the solution of the minimization cost function, which can be expressed as

$$g(x) = \sum_{i=1}^N \rho \frac{(r_i(x))}{s} \quad 2.34$$

Where  $\rho$  is an even, continuously differentiable function (Wolke and Schwetlick, 1988), and  $S$  is a scaling factor of the residual,  $r_i$ . The scaling parameter,  $S$ , used in this study, is the median absolute deviation, MAD (Holland and Welsch, 1977). The most common M-estimators are the *Huber* estimators (Huber, 1981), and these are written as follows:

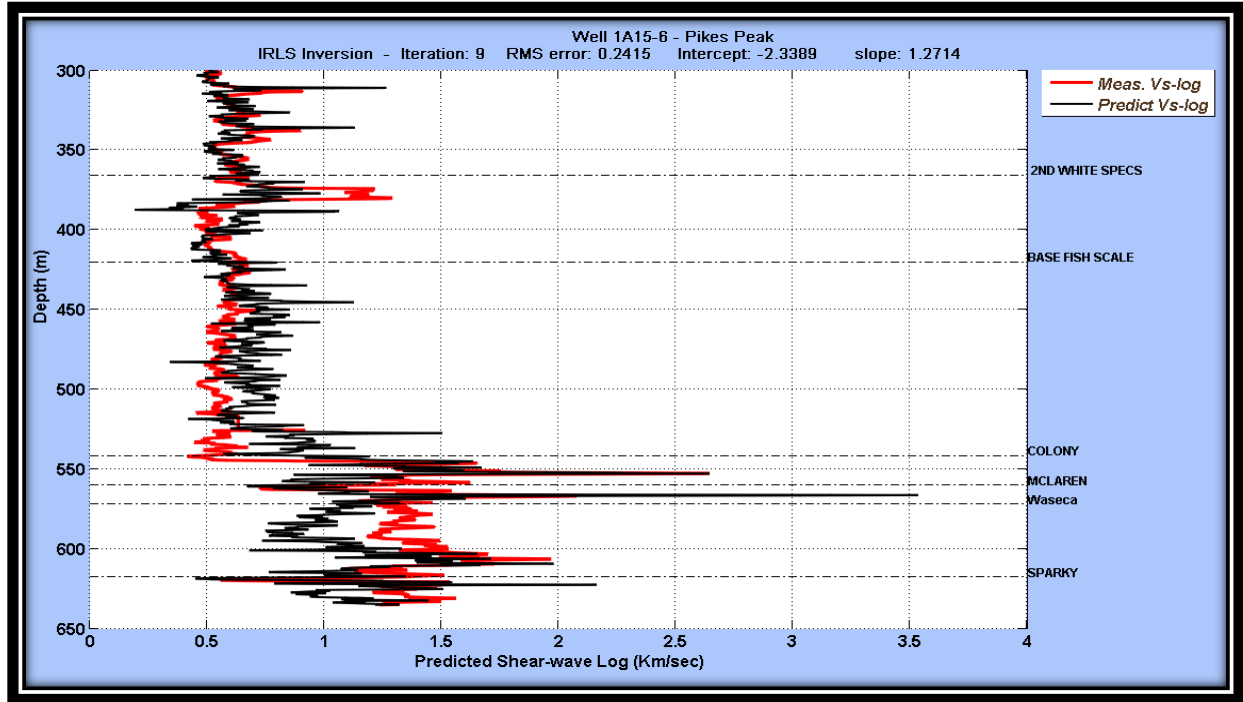


Figure 2.14: The measured and inverted shear sonic logs of Well 1A15-6, Pikes Peak, using a hybrid  $\ell_1/\ell_2$  norms method.

$$\rho_H(r) = \begin{cases} \frac{1}{2}r^2 & \text{for } |r| \leq \xi \\ \xi|r| - \frac{1}{2}r\xi^2 & \text{for } |r| > \xi \end{cases} \quad 2.35$$

where  $\xi$  is a tuning constant.

It is common to choose  $\xi = 1.345\sigma$  for a *Huber* estimator, since it offers robustness against outliers, yet produces 95% efficiency when the error are normally distributed (Huber, 1981). For the  $k$  th iteration step, the weight function for Huber constraints are defined as follows:

$$\omega_H^{(k)} = \begin{cases} 1 & \text{for } |r^{(k-1)}| \leq \xi \\ \frac{\xi}{|r^{(k-1)}|} & \text{for } |r^{(k-1)}| > \xi \end{cases} \quad 2.36$$

Since  $\varpi$  is a prior unknown, an iteratively reweighted least-square (IRLS) inversion is required. Note that the tuning constant given earlier did not produce a converged solution for equation (2.13). Therefore a modification for the tuning constant is needed to stabilize the IRLS inverse algorithm. In this study, a modification of Huber's and Darce's tuning constant is established. The new tuning constant for the Huber weight function is written as follows:

$$\xi_H = 1.345 \frac{\max|r|}{100} \quad 2.37$$

The new tuning constant in equation (2.37) is used, and has improved convergence and accuracy for resulting models. In Figure (2.15), the inverted shear sonic log using the Huber weight function fairly matches the measured shear sonic log.

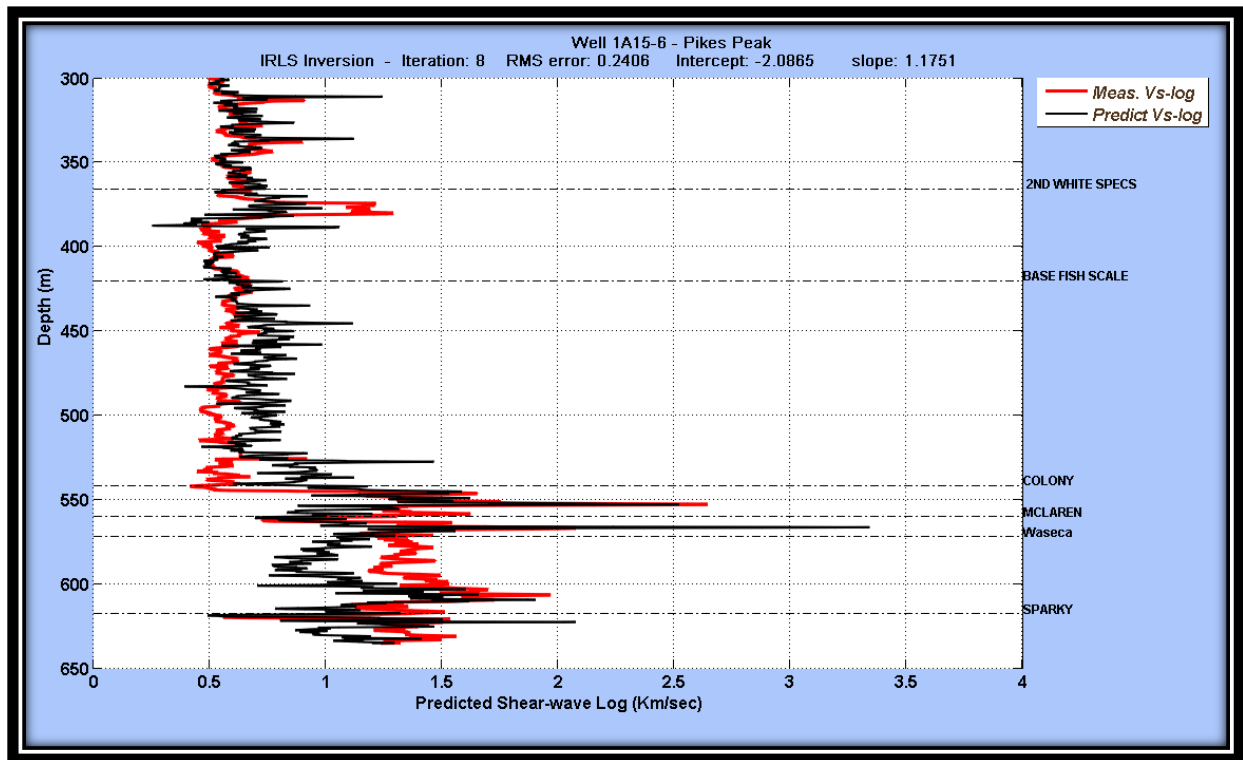


Figure 2.15: The measured and inverted shear sonic logs of Well 1A15-6, Pikes Peak, using the Huber constraint.

#### 2.4.4.5 The Annealing M-Estimator

Li, (1996) presented a modified robust M-estimator called annealing M-estimator, often referred to as an **AM**-Estimator, in order to stabilize convergence towards the final solution. The AM-estimator gives a global solution, is very stable, and has good behavior with regards to percentage of outliers and noise variance.

The scale,  $s$ , in the M-function is replaced by the parameter  $\gamma$  in the AM-estimator that is approaching  $0^+$  during the processing. The AM-estimator under  $\gamma$  is defined by

$$f_{\gamma} = \frac{\sum_i h_{\gamma}(\eta_i) r_i}{\sum_i h_{\gamma}(\eta_i)} \quad 2.38$$

where  $h_{\gamma}(\eta_i)$  is an adaptive interaction function parameterized by  $\gamma$  (Li, 1996).

The adaptive interaction function is given by

$$h_{\gamma}(\eta_i) = \frac{1}{1+(\eta^2/\gamma)} \quad 2.39$$

where  $h_{\gamma}$  acts as interaction weighting function, and  $\eta_i = r_i$ .

In the inversion algorithm, the parameter  $\gamma$  was initially set equal to the Huber tuning constant,  $\xi = 1.345\sigma$  and then minimized after the first iteration by  $\xi_{i+1} = \xi_i - \xi_i/4$ . Figure (2.16) shows the inverted shear log, while in Figure (2.17) the RMS error reached a minimum magnitude after 6<sup>th</sup> iteration.

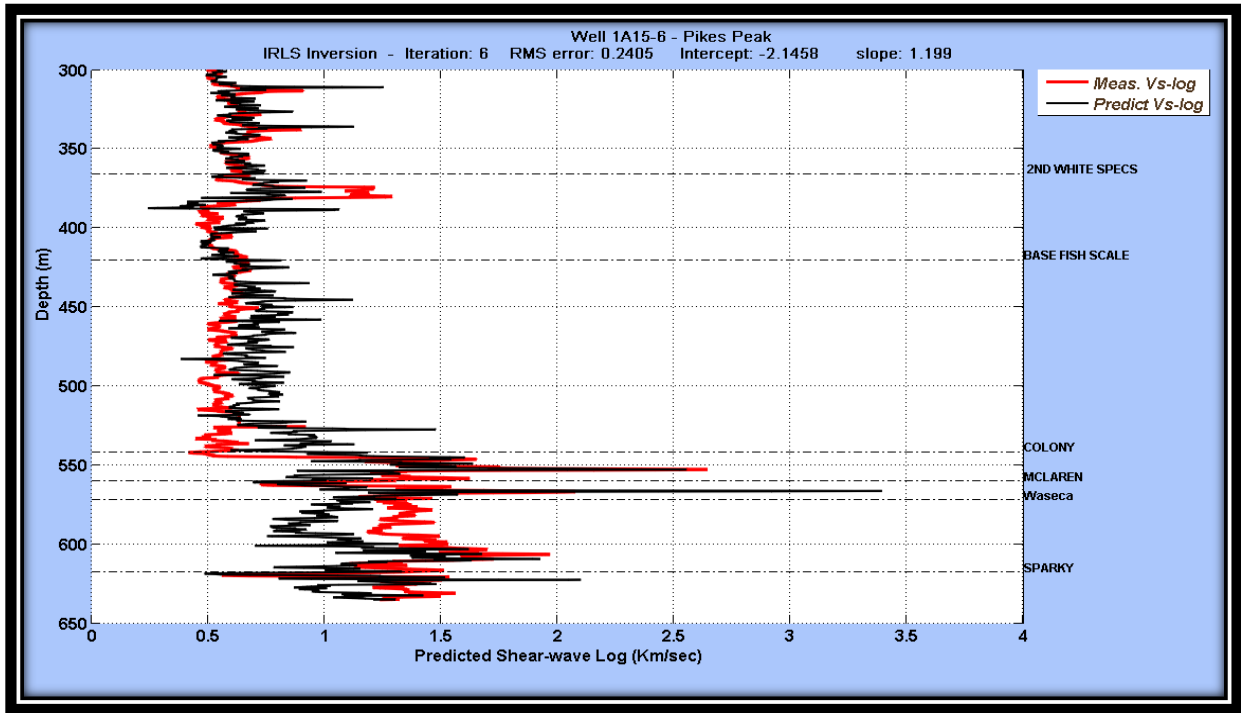


Figure 2.16: The measured and inverted shear sonic logs of Well 1A15-6, Pikes Peak, using the annealing M-Estimator.

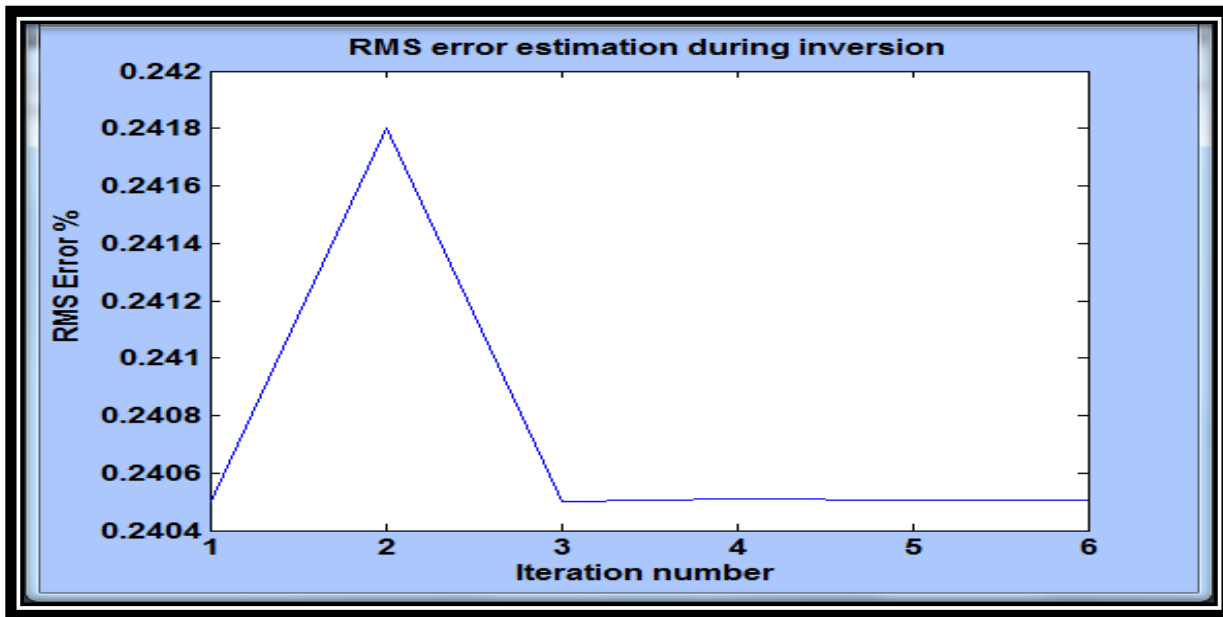


Figure 2.17: The RMS error during IRLS inversion of shear sonic logs of Well 1A15-6, Pikes Peak, using the annealing M-Estimator.

#### ***2.4.5 Analysis of IRLS results from model and data constraints***

Saeed et al., (2012) used the iteratively re-weighted least-square inversion, IRLS, to improve prediction of shear sonic logs in the western Canadian sedimentary basin, as proposed inverse schemes give confidence for estimating the regression line in the presence of outliers. In the following subsections, further analysis for the residual, simultaneous utilization for the weighted matrices of both model and data domains, and application of proposed inverse schemes to predict shear sonic log in the tight shale Montney reservoir are explained.

##### **2.4.5.1 Diagnosing the RMS error curve**

A successful inverse algorithm is achieved when its residual follows a Gaussian error distribution (Claerbout and Muir, 1973). The RMS error curve (Figure 2.13) during IRLS inversion of the shear sonic log characterizes three RMS areas of interest that need to be investigated in some detail. The first zone of interest is of the first iteration, where no constraint(s) applied in the inversion; thus a simple damped least-square (equation 2.9) inversion is used. The second RMS area, which is the zone in the second iteration of IRLS inversion, whereby constraints are first introduced into the inverse algorithms (equation 2.18). A noticeable spike increase in RMS error is detected. The third RMS zone of interest is the area after the third iteration, leading towards the final solution where convergence is achieved. In this zone, constraints have stabilized the RMS curve towards minimum error estimated during inversion.

The plot in Figure (2.18a) shows shear sonic inversion in the first iteration where no constraint was applied, and the inversion algorithm used is merely a damped least-square inversion. Note that the inverted shear sonic log resembles the measured shear sonic log. The hope is to

minimize the residual between measured and inverted logs. The inverted shear log shows small residual from depth 300m through to the second White Specs geological marker. At the Waseca reservoir there is a gap between predicted and measured logs where a best fit line relation is not totally adequate. The spike in the predicted log in the McLaren formation is indicative of a coal seam, and is expected since the p-wave velocity is twice the shear wave velocity in coal.

In Figure (2.18b), the predicted shear sonic at the second iteration where the constraint is just introduced into the inversion algorithm, matches the measured shear sonic log. However the residual has grown large, and this is expected since error norms are just introduced in the inverse algorithm. The plot in Figure (2.18c) shows the result at the last iteration. Note that after a few iterations, the incorporated constraint has stabilized the RMS, reduced the residual, and has also reduced the magnitudes of spikes that indicative of over estimations of predicted log values at various depths in the shear sonic log.

In other words, introduced constraints reduce the effect of outliers in best fit line estimation. Nevertheless, introducing these soft constraints lead to refining estimated slope and intercept values in best fit linear relation.

#### 2.4.5.2 Cross plots of residuals

Figure (2.19) shows the cross plot for the measured shear sonic log versus the inverted shear sonic (where weighted constraint was embedded into the data space) colored by the residual.

Figure (2.20) shows same plot but for a weighted matrix embedded in the model-space. Note that the residual in model-space is slightly higher than the residual resulting from the weight imposed on the data-space.

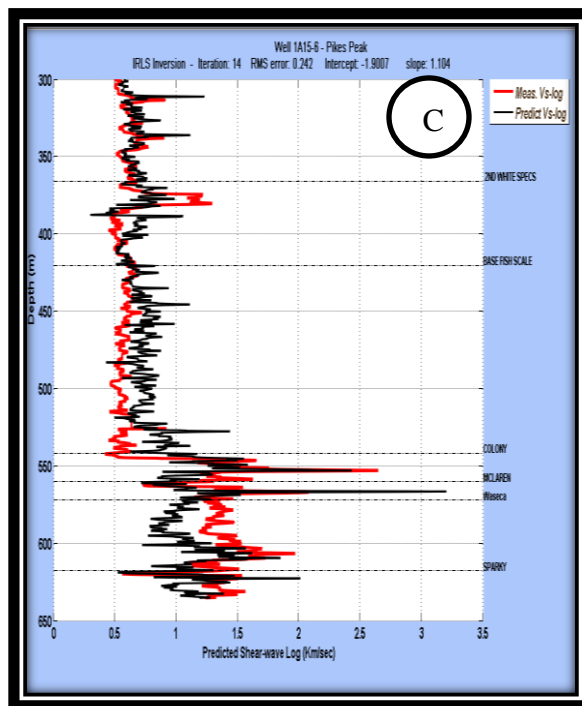
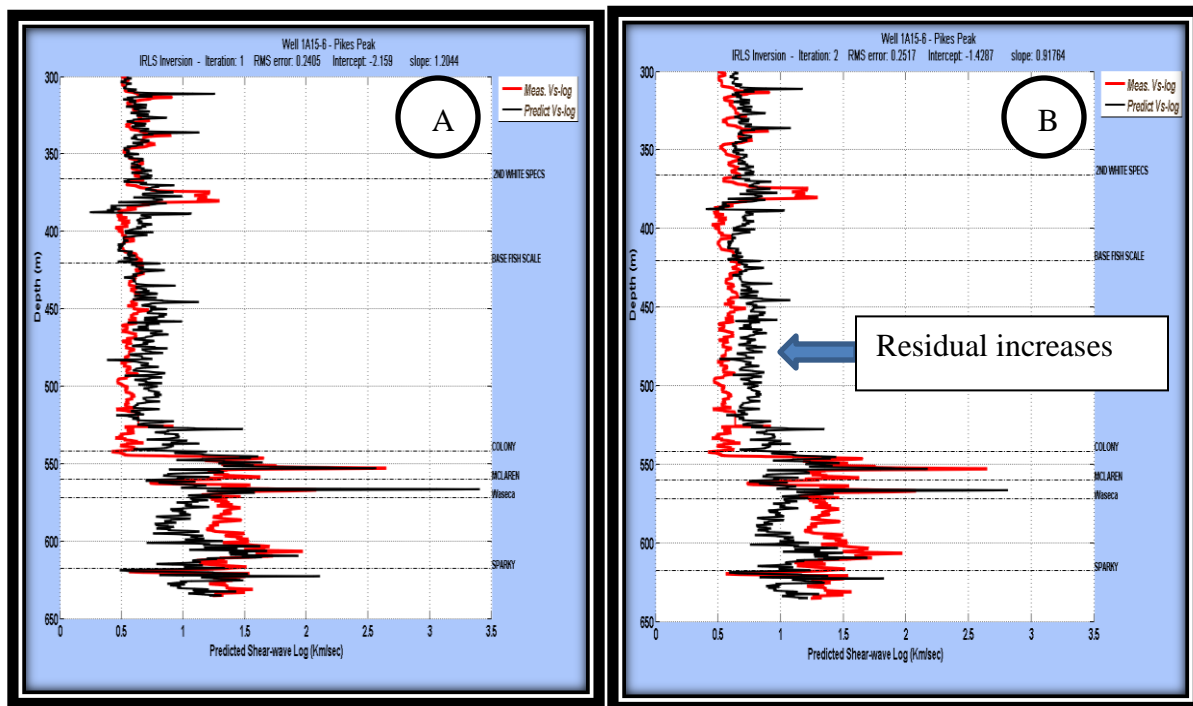


Figure 2.18: The measured and inverted shear sonic logs of Well 1A15-6, Pikes Peak. (A): inversion at the first iteration. (B) Inversion at the second iteration, while (C) the inversion of the shear sonic log at the final solution.

The majority of inverted shear sonic values in both figures have small residuals. Furthermore, the cross plots allow user to examine points with high residual that are substantially having high error percentage. Hence, one can either adjust or trim these outliers to improve the overall prediction of sonic logs. In terms of computation time required to converge to a final solution, it has been noticed that embedding constraint in model space leads to reduce in number of iterations compared to constraints involve in data space.

Table (2.1) shows values of slope, intercept, number of iteration and RMS values for the final iteration of different weighted matrices used in predicting a shear sonic log of Well 1A15-6, from a heavy oil reservoir of the Pikes Peak oil field. Note that all sonic velocities are in km/sec. Table (2.1) can serve as a QC tool for estimated slope and intercept. It will also assist in selecting the right inverse scheme for the prediction of a shear sonic log.

In terms of computation time, the study shows that the type of the used constraint, tuning factors, and the amount of outliers would control the number of calculation cycles required to converge towards final solution model. For weighted matrices that are embedded in data-misfit space, it has been found that the annealing M-estimator method is the fastest inverse scheme in terms of time computation required to converge to a final solution. On the contrary, the minimum gradient support constraint applied in model space considers a fast inverse scheme compared to the other constraints techniques applied in model norm space.

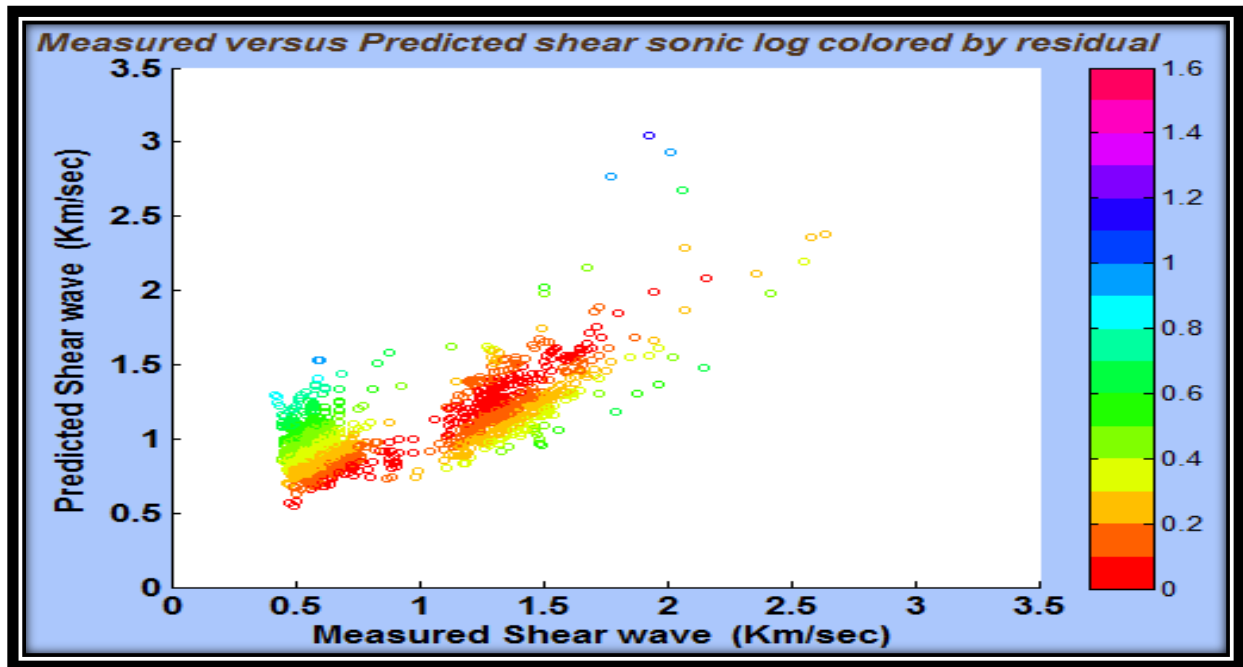


Figure 2.19: Measured versus inverted shear sonic logs of Well 1A15-6, Pikes Peak, color coded by the residual. Constraint applied in data space.

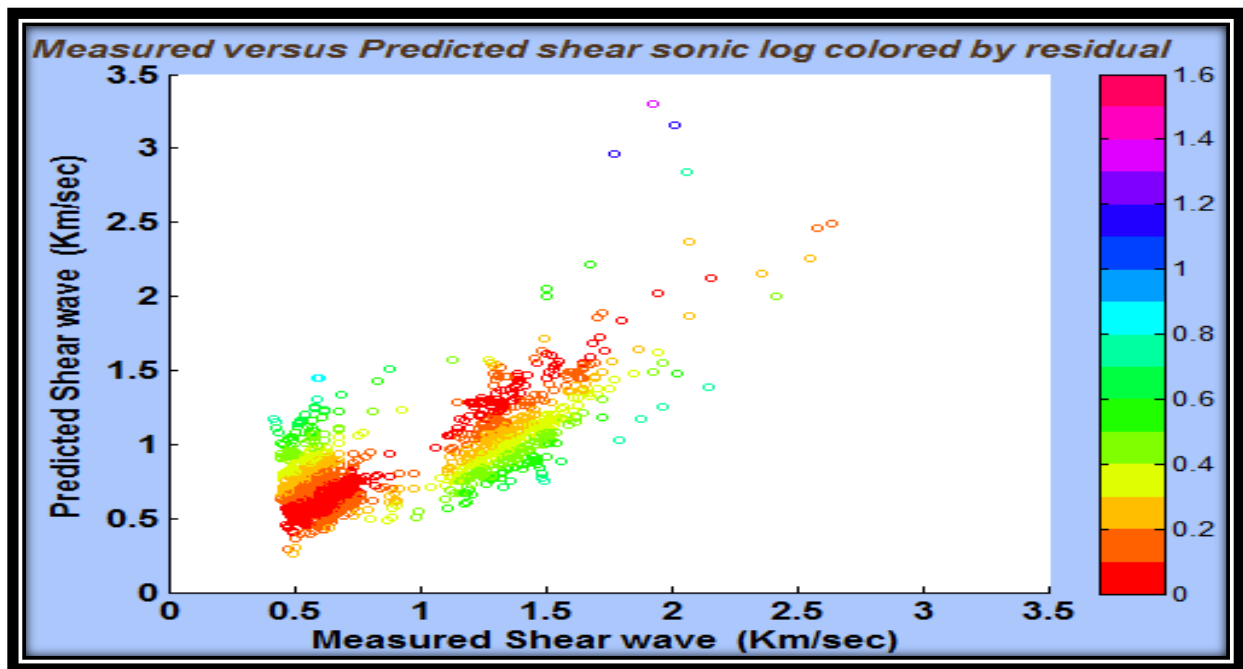


Figure 2.20: Measured versus inverted shear sonic logs of Well 1A15-6, Pikes Peak, color coded by the residual. Constraint applied in model space.

<b>Type of applied Constraint</b>	<b>Slope</b>	<b>Intercept</b>	<b>RMS error %</b>	<b>No. of Iterations</b>
No constraint applied	1.2044	-2.159	0.2405	1
Modified total variation	1.1247	-1.9593	0.2413	8
Minimum support	1.1567	-2.0405	0.2408	7
Minimum gradient support	1.1566	-2.0404	0.2408	6
Std. Deviation of measured error	0.9522	-1.3471	0.3132	12
Robustness normalized by Std. deviation	1.104	-1.9007	0.242	14
Hybrid $\ell_1/\ell_2$ norms	1.2714	-2.3389	0.2415	9
Huber constraint	1.1751	-2.0865	0.2406	8
The Annealing M-Estimator	1.199	-2.1458	0.2405	6

Table 2.1: The slope, intercept, number of iterations and RMS values for the final iteration of different weighted matrices used in predicting of shear sonic log of well 1A15-6, Pikes Peak heavy oil field.

#### 2.4.5.3 Simultaneous application of model and data misfit norms

Further experiments were carried out to study effect of simultaneously applying constraints in both model-space and data-misfit. The results from inverting shear sonic log using this approach lead to further tuning the estimated slope and intercepts values. In terms of computation time, it has been found that type of constraint used in data-misfit domain controls number of computation iterations. On the other hand, the type of constraint used in the model space may reduce the number of iterations required to converge to final solution.

Figure (2.21) shows a zoomed section of an inverted shear sonic log from the tight-shale Montney reservoir in the WCSB. A combination of data misfit (hybrid  $\ell_1/\ell_2$ ) and model space

(minimum gradient support) weighted matrices were incorporated in the inversion algorithm, and have led to reduced cycles of calculation iterations, yet improved best fit line estimation. The inverted shear log is consistent with measured shear sonic log where the minimum residual is achieved.

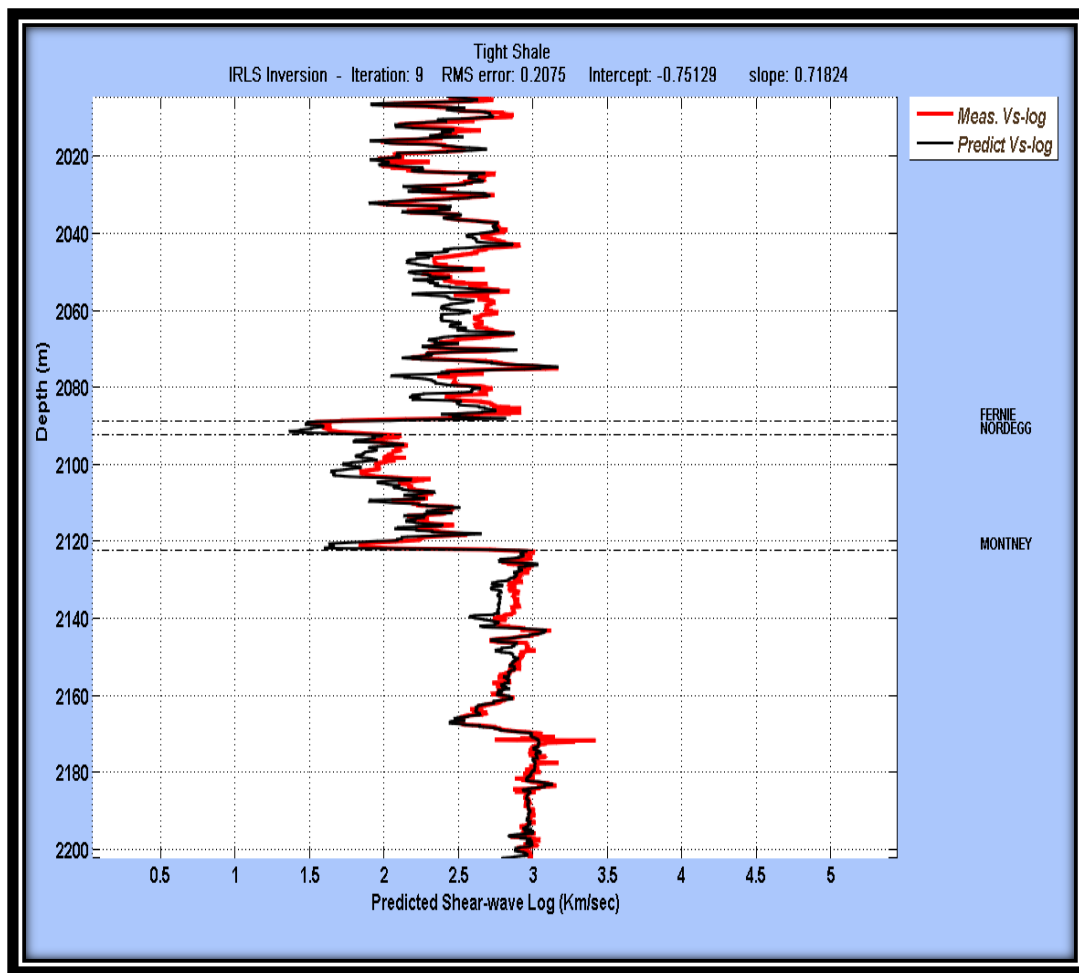


Figure 2.21: The measured and inverted shear sonic logs of Tight Shale Montney, WCSB using a combination of hybrid  $\ell_1/\ell_2$  and minimum gradient support weighted matrices.

## **2.5 Mud-rock line estimation via the locally weighted scattering smoothing method**

A classical procedure for noisy data usually requires some editing before performing linear regression in order to reduce influences of outliers on estimating slope and intercept points used in a best fit-line equation. Another approach is to fit a polynomial of a higher degree, such as quadratic equation, where the curvature of line is included in the best fit-line equation. Thus, to map the mud-rock line more precisely, we should look for another regression method that takes into consideration the effect of neighbor points in the scattering graph, and prove it is robustness against the outliers as well.

### ***2.5.1 Robust locally weighted smoothing scattering (LOWESS)***

Cleveland, (1979) has introduced the robust locally weighted scattering smoothing (LOWESS) method. This is another regression method that not only smoothes the scatter plot but also guards against outliers that distort the smoothed points in the scattering plot. Given  $(x_i, y_i)$  points, let  $d_i$  be the distance between  $x_i$  and its  $b^{\text{th}}$  nearest neighbors along the X-axis. The value of  $b$  is the nearest integer to  $(f \cdot n/2)$ , where  $n$  is the number of data points and  $f$  is the smoothing factor ( $0 < f < 1$ ). A small value of  $f$  produces rough curve (Figure 2.22a), while greater value of  $f$  tends to smooth the curve line (Figure 2.22b). However, for a general scatter graph, a practical value for  $f$  is usually between 0.2 and 0.8.

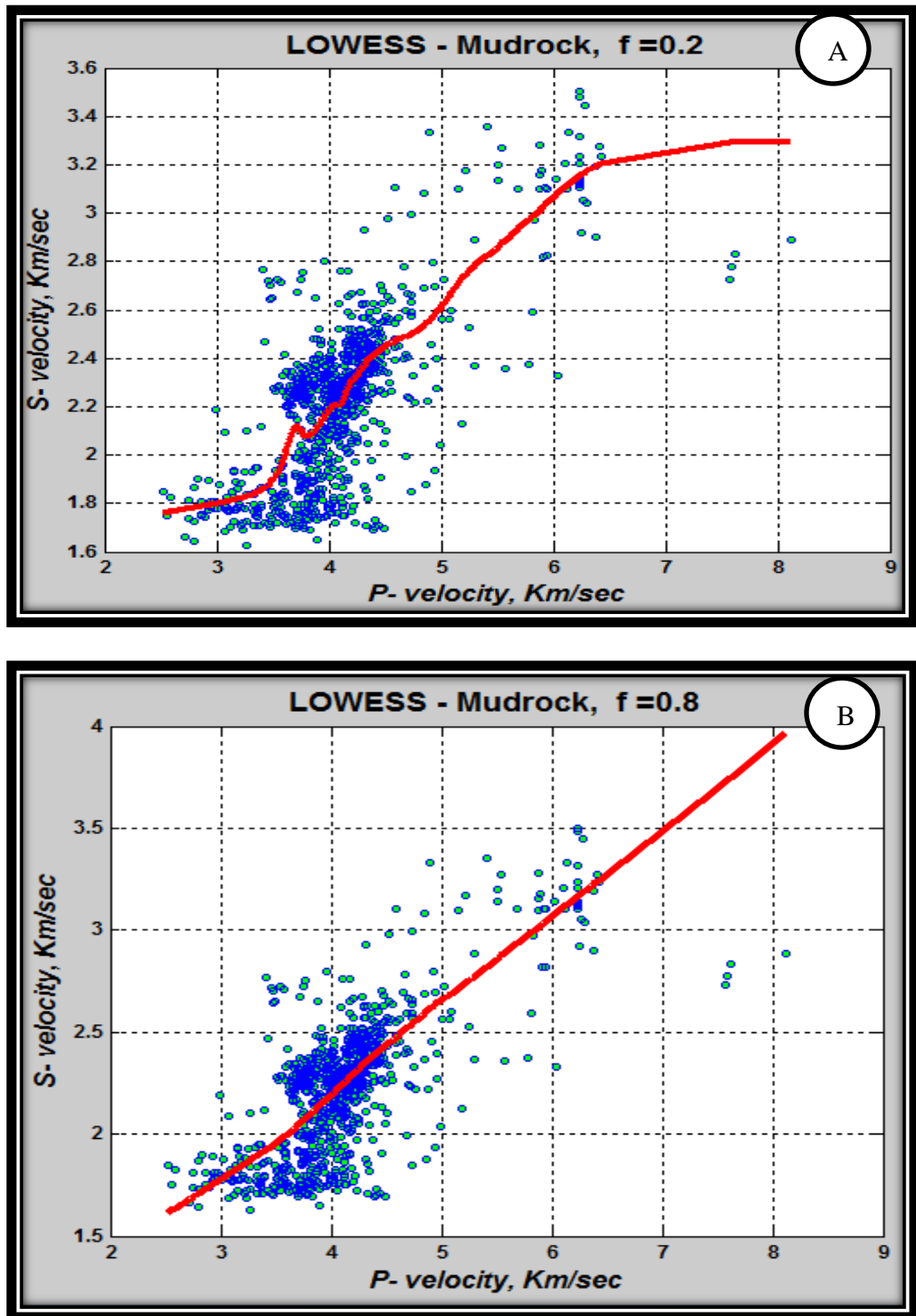


Figure 2.22: Scatter plot of P-wave velocity versus S-wave velocity using LOWESS for mapping of Mudrock line. (A): smooth curve factor,  $f=0.2$ , while (B), smooth curve factor,  $f=0.8$ .

The weighted slope ( $b_{estimate}$ ) and the intercept ( $a_{estimate}$ ) of the line derived from the robust locally weighted regression method can be written as,

$$b_{est} = \frac{\sum W_k^2 (x_i - \bar{x}) (y_i - \bar{y})}{\sum W_k^2 (x_i - \bar{x})^2} \quad 2.40$$

$$a_{est} = \bar{y} - b_{est} \cdot \bar{x} \quad 2.41$$

where  $\bar{x}$  and  $\bar{y}$  are weighted mean values, and

$$W_k = \varpi \left( \frac{x_i - x_k}{d_i} \right), \quad \varpi(x) = \begin{cases} (1 - |x|^p)^p, & \text{for } |x| < 1 \\ 0, & \text{for } |x| \geq 1 \end{cases} \quad 2.42$$

The best fit line equation is then written as

$$y_W = a_{est} + b_{est} \cdot \bar{x} \quad 2.43$$

The weight function,  $\varpi$ , can be either a bi-weight function (p=2), or a tri-cube weight function (p=3). In this study, a tri-cube weight function is applied. Note that the size of the weight depends on the magnitude of residual. Large residuals results in small weights and small residuals result in large weights (Cleveland, 1979).

### ***2.5.2 Application of LOWESS to Mudrock line estimation in the WCSB***

The robust locally weighted smooth scattering, LOWESS, method has been used to map the mud-rock line using well logs from three different types of reservoirs (conventional oil, tight shale oil and heavy oil,) in the WCSB. The optimum choice of a smoothing curve factor  $f$  varies among different types of reservoirs, and plays a key control of the magnitude of the residual. It has been found that  $f$  is a trade-off between consistency of matching log curves for different lithology intervals and residuals, particularly in the zone of interest. Although, it is solely a user choice, it would be meaningful to set  $f$  to be related to best expected shear sonic values, with a minimum residual, in the zone of interest rather than assigning an average  $f$  value to the complete log.

#### **2.5.2.1 Conventional oil reservoir (Blackfoot field)**

The Blackfoot field represents a common style of stratigraphic trap in the western Canadian basin (Pendrel et. al, 1999). The producing formation is from a channel sand (Glaucconitic of the lower Cretaceous age) deposited as incised valley-fill sediments above the Mississippian carbonates (Wood and Hopkins 1992).

Figure (2.23) shows a cross-plot of  $V_p$  versus  $V_s$  logs where Mudrock lines calculated from using different methods are superimposed. The scatter points are colored by Gamma values where sand usually has low gamma ray values. The s-wave values of the dipole sonic logs for the productive sand channel reservoir are superimposed (black dots) in the section as well. Figure (2.24) shows measured and predicated shear logs using the ARCO line equation, linear regression, and the weighted regression method (LOWESS) respectively.

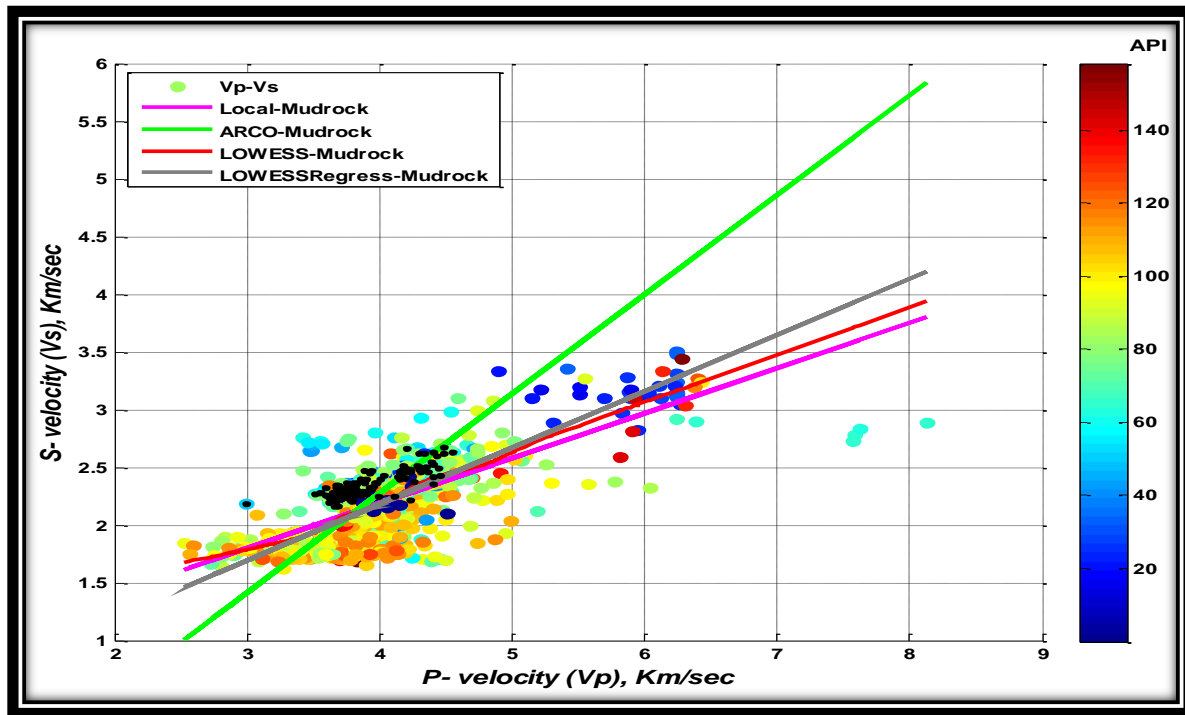


Figure 2.23: Cross-plot of P-wave velocity versus S-wave velocity of well log from conventional oil reservoir area. The scatter points are colored using Gamma ray API (color bar).  $V_p$ - $V_s$  values from the productive sand channel reservoir (black dots) are superimposed.

The predicted curves using the linear and LOWESS methods match well the measured shear-wave log. Figure (2.25) shows percentages of residuals for the three methods used in predicting the shear-wave log of a well from a conventional oil reservoir. Notice that the residual is higher for ARCO compared to regression methods.

In Figure (2.26), the Mudrock line calculated by the robust locally weighted scattering smoothing (LOWESS) method can be used as a direct indicator of hydrocarbon (Saeed et al, 2010c). The mud-rock line estimated by the LOWESS method has successfully delineated channel sand, whereas linear regression and the ARCO mud-rock equation did not. Furthermore, the carbonate zone can be easily distinguished by the LOWESS method, where it starts from the intersection point of  $V_s$  (around 2.8 km) and  $V_p$  of 4.8 km/sec and above.

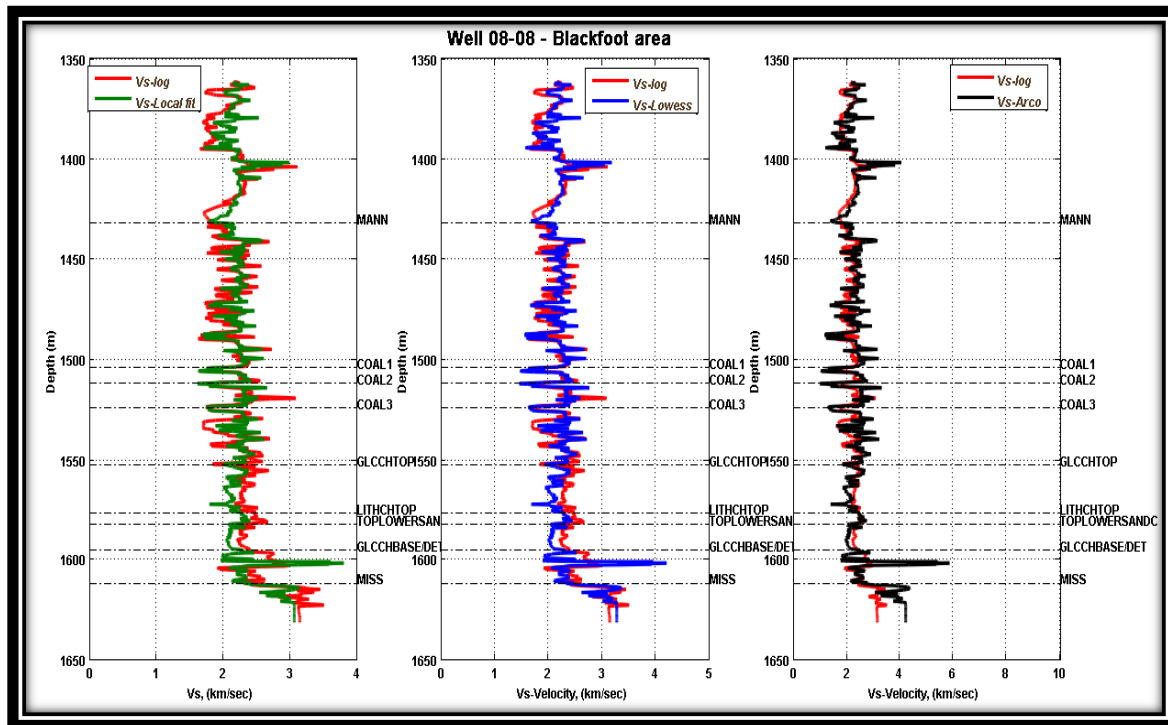


Figure 2.24: Plots for measured (red color) and inverted shear-wave logs of a well from a conventional oil reservoir area using linear regression (green curve), the LOWESS method (blue curve) and the ARCO Mudrock equation (black curve).

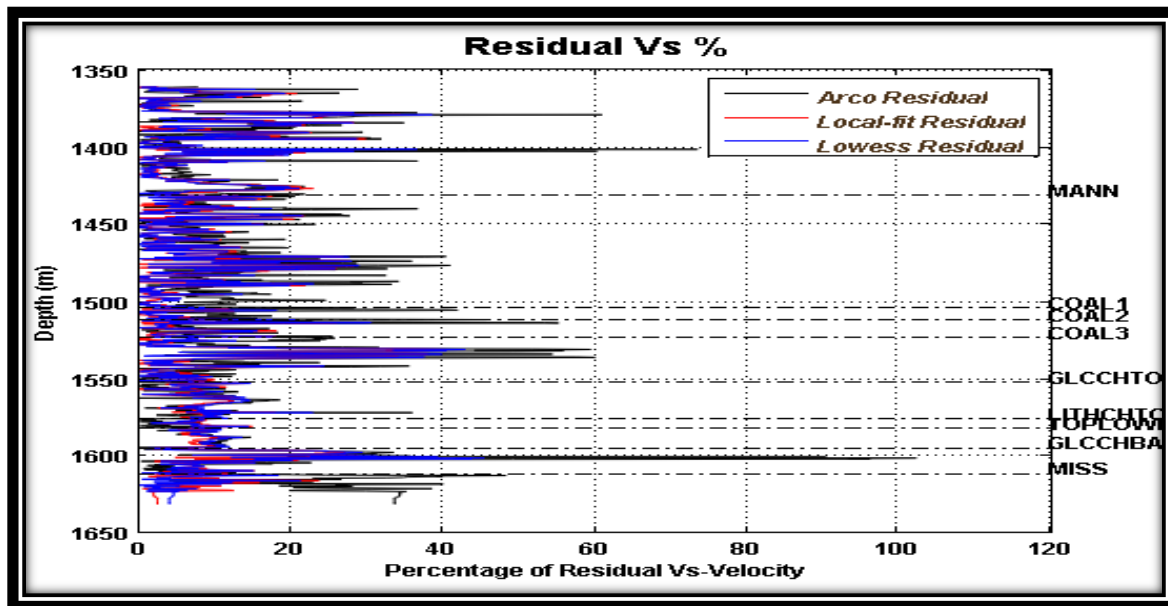


Figure 2.25: Plots for percentage of residual of shear-wave logs using a well log from a conventional oil reservoir.

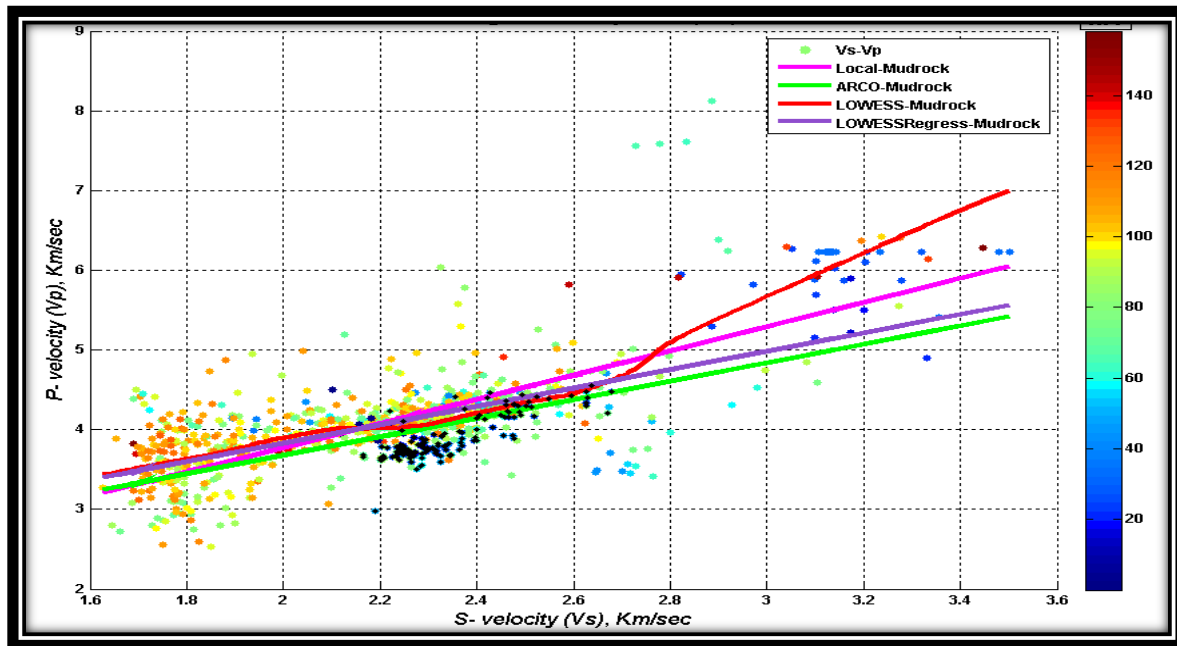


Figure 2.26: Cross- plot for S-wave velocity versus P-wave velocity of well log from conventional oil reservoir area. The scatter points are colored using Gamma ray values API (color bar). Velocity values from the productive sand channel reservoir (black dots) are superimposed. The LOWESS fit line curves as it maps the channel reservoir.

### 2.5.2.2 Tight shale oil reservoir (NW Alberta)

Figure (2.27) shows P-wave velocity, S- wave velocity, density and Gamma ray of a well from a tight shale reservoir in northern Alberta. Several oil companies have been actively targeting the Montney Formation as well as the Duvernay shale. The tight light oil of shale reservoirs is emerging as an important new source of energy in North America. With successful development of fracturing techniques applied to unconventional shale reservoirs, attention has now been shifted to the Montney and Duvernay shale in Alberta.

Figure (2.28) shows measured and predicted shear-wave logs using linear best fit, LOWESS method, ARCO and Han's empirical equations. Note that LOWESS method is in excellent agreement with the actual measured shear-wave log with minimum residuals, compared to estimated shear sonic logs using empirical relationship.

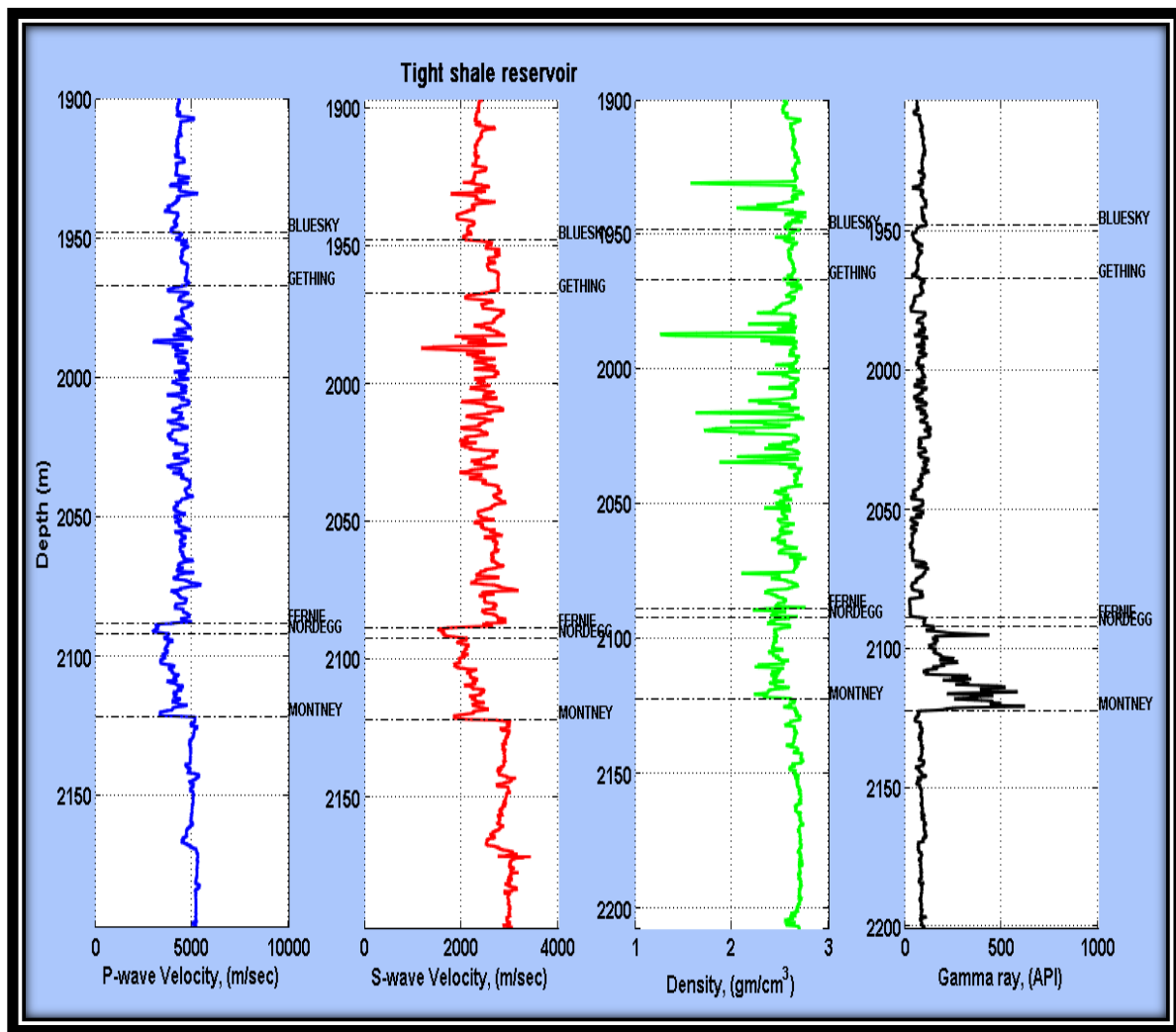


Figure 2.27: Plots for P-wave, S-wave, density and Gamma ray logs of a well from tight shale reservoir area.

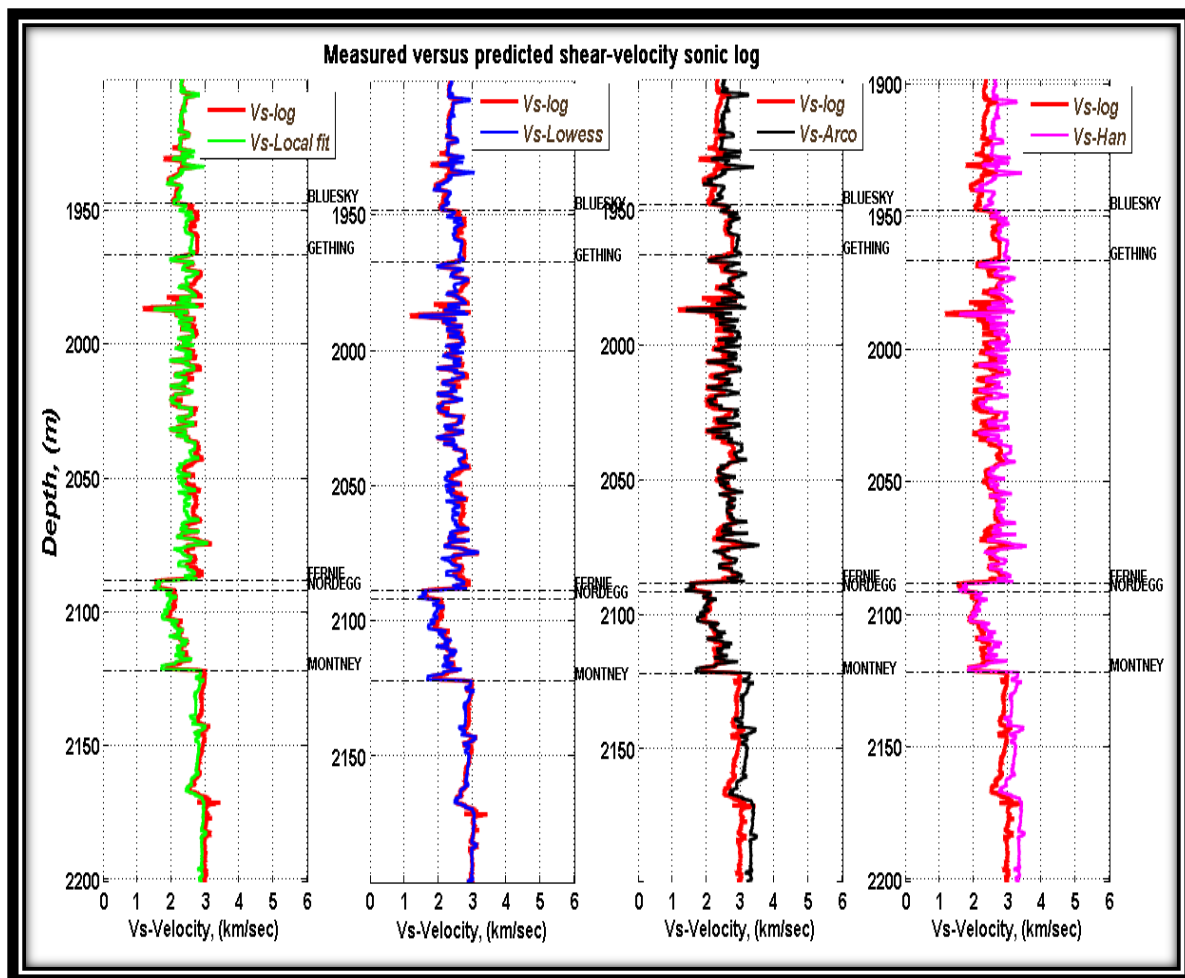


Figure 2.28: Plots for measured (red color) and inverted shear-wave logs of well log from a tight shale oil reservoir area using linear regression (green curve), the LOWESS method (blue curve), the ARCO Mudrock equation (black curve), and Han's equation (magenta curve). Col Color bar represents Gamma ray API.

### 2.5.2.3 Heavy oil reservoirs

The heavy oil in the Pikes Peak area, Saskatchewan, is produced from the sands of the Waseca Formation of the Lower Cretaceous Mannville Group (Watson, 2004). For heavy oil, it is understood that the physical properties of reservoirs are considerably affected by the pressure

and temperature of steam injected as part of reservoir production process. Well 1A15-6 was drilled in 2000, after the reservoir has already been put in cycle of steam injection, soaked period, and then production. Therefore, prediction of shear sonic log in steam injected heavy oil reservoir poses great challenges that need to be investigated in more detail.

It was stated earlier that the smoothing factor,  $f$ , weighs the accuracy of inverted shear sonic, and extra attention is needed in assigning an optimal  $f$  value. Figure (2.29a) is a cross plot of dipole sonic velocities, where local linear, Arco and LOWESS methods used for calculating Mudrock lines are superimposed. The smoothing factor,  $f$  was set to be 0.2 for the LOWESS method. Figure (2.29b) is the same plot but with  $f$  set to be 0.95 to produce a very smooth curve.

The objective is to examine the effect of the  $f$  value in calculating a best fit line. The red and brown lines, which represent the best fit line using the LOWESS method, in both Figures give an indication of the precise  $f$  be used in order to guard against outliers in the logs. Note that the brown line of LOWESS-regression is estimated by taking mean values of slope and intercept that are calculated during the LOWESS calculation procedure. When  $f = 0.25$  (set to be an extremely rough curve), the estimated best fit line deviates from being a correct estimation of the Mudrock line, and outliers now add more weight to the calculated slope and intercept. The LOWESS regression line is projected in the outlier's territory. In contrary, when  $f = 0.95$  (set to yield an extremely smooth curve), the estimated best fit line of Mudrock line becomes more realistic, and outliers have less effect to the calculated slope and intercept. The mudrock line is now better representative of lithology areas and less affected by outliers that could have come from cycle skipping or a washout zone.

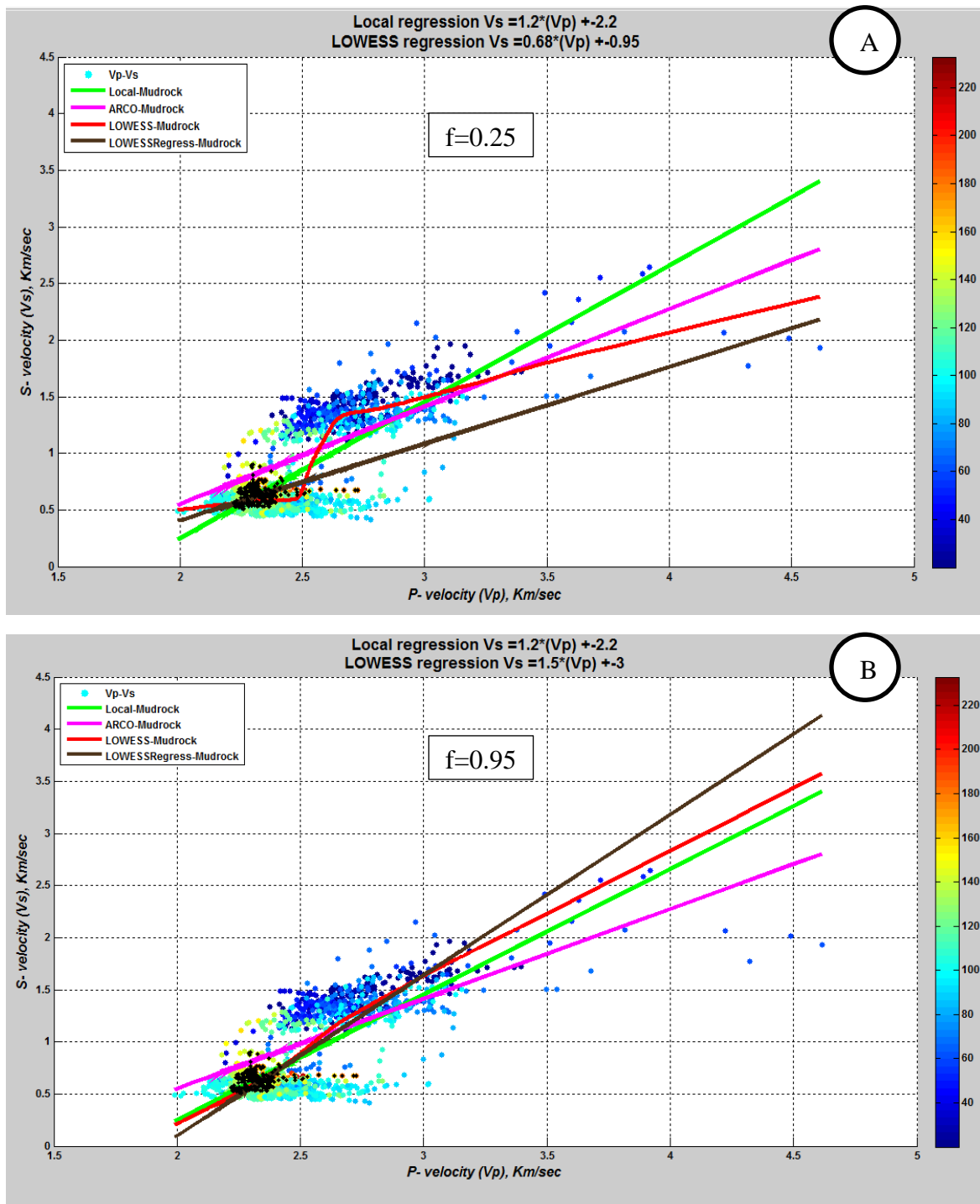


Figure 2.29: Cross- plot for S-wave velocity versus P-wave velocity of well 1A15-6, from a heavy oil reservoir area. The scatter points are coloured using Gamma ray, and velocity values from the productive Waseca sand reservoir (black dots) are superimposed. (A) for a smoothing factor,  $f = 0.25$ , (B) is for  $f = 0.95$ . The color bar represents Gamma ray API.

Figure (2.30a) shows a zoomed section of measured and predicted shear-wave logs using linear regression, the LOWESS method and the empirical ARCO mudrock relationship. The smoothing factor,  $f$ , for LOWESS was set to be 0.25 as in Figure (2.29a). Note that, although the predicted curve of the LOWESS method (middle track) has matched measured log fairly well for the Base fish-scale marker through to the Colony geological marker, the residual between the two curves is noticeable at the McLaren formation, and more at the Waseca formation, compared to the local regression and ARCO method.

In Figure (2.30b),  $f$  was set be very smooth (0.95) as in Figure (2.29b). As expected, LOWESS become more close to linear regression, but with better tuning for estimated slope and intercept values. The predicted shear sonic log shows good matching to the measured sonic log, with less residual compared to the linear regression method. By far, the ARCO empirical equation shows quite obvious residuals (where the gap between measured and estimated shear sonic logs increases) compared to the other methods.

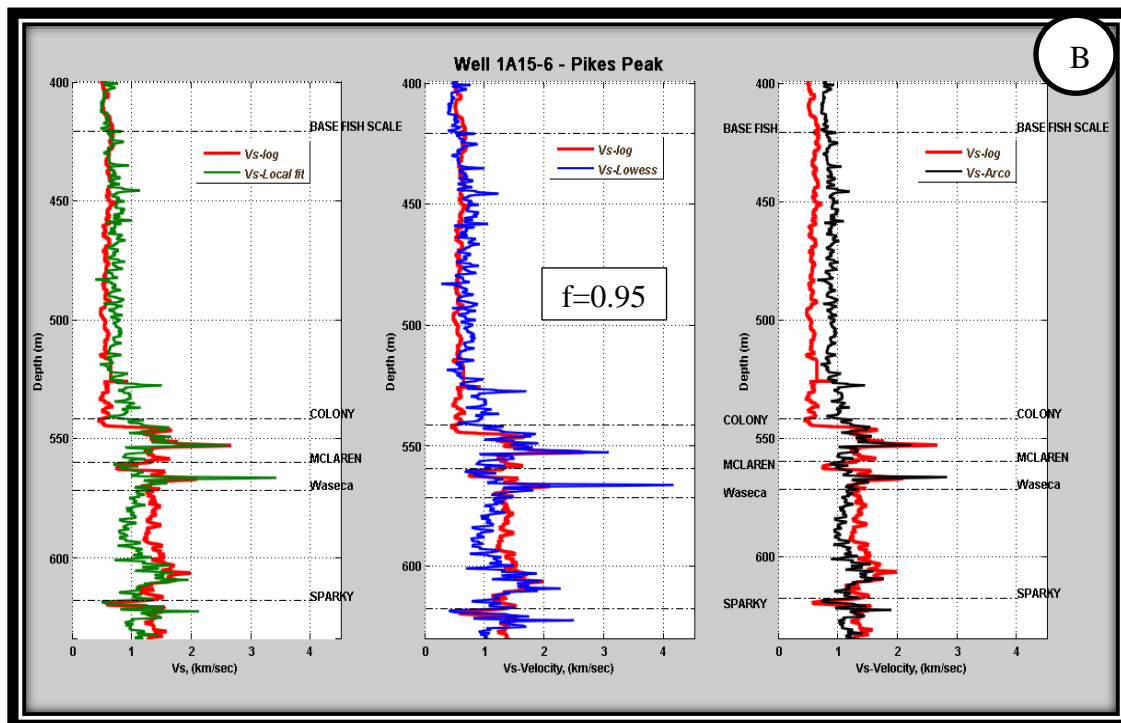
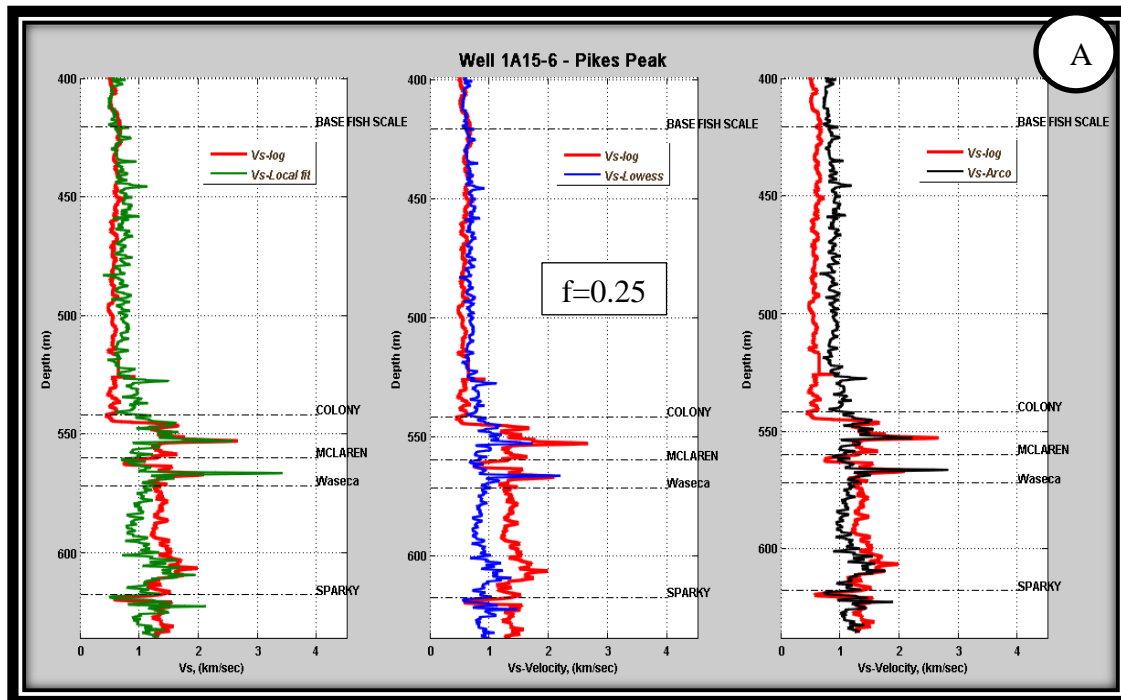


Figure 2.30: Plots for measured (red color) and inverted shear-wave logs of a well log from the heavy oil reservoir area using linear regression (green curve), the LOWESS method (blue curve), and the ARCO Mudrock equation (black curve). (A) for a smoothing factor,  $f = 0.25$ , while (B) is for  $f = 0.95$ .

## 2.6 Conclusions

Sonic measurements make important contributions to our knowledge of a potential hydrocarbon field in every phase of reservoir drilling, evaluation and exploitation. The linear regression method is noticeably influenced by the presence of noise or outliers that might give an inaccurate prediction of a shear sonic log. The constraints used in the iteratively re-weighted least-squares inversion further refine the estimated slope and intercept values used in the best fit line equation. Thus it improves the inverted shear-wave log, and helps in model convergence towards the final solution in a few iterations.

The robust locally weighted smoothing scattering method, LOWESS, successfully maps the productive sand reservoir in conventional oil reservoirs. It proves to be a good interpretive tool to be used in hydrocarbon and lithology discrimination.

The choice of an optimal smoothing factor,  $f$ , used in the LOWESS method to map the mudrock line, depends mainly on the percentage of outliers in the used logs, lithology of logs, and type of hydrocarbon reservoir. While small values  $0.25 < f < 0.35$  have produced good results in predicting shear sonic logs in conventional and tight shale reservoirs, it has been found that  $0.88 < f < 0.95$  range give better estimation of shear sonic in heavy oil reservoirs.

In terms of residuals, the study has found that the minimum residual between the measured and predicted shear sonic is accomplished by using the LOWESS method, while the ARCO empirical relation shows a high residual for different lithology in the predicted well log.

## Chapter Three: **TIME-LAPSE AVO INVERSION OF SEISMIC SURVEYS**

### **3.1 Introduction**

AVO analysis is a direct diagnostic tool in hydrocarbon detection. In reservoir monitoring, the changes in seismic attributes are often associated to the change in rock fluid properties. The differences in seismic attributes of the base and monitor surveys are then used in evaluating the spatial change of reservoir attributes (LandrØ, 2001) after reservoir depletion due to the production process.

A common method used in time-lapse seismic inversion is to invert seismic data of base and monitor surveys individually (Watson and Lines, 2001; Zou, 2005) and to then calculate the difference or percentage changes in estimated elastic attributes of time-lapse surveys. Another approach used by in-house developed software is to perform simultaneous inversion of base and monitor seismic data, and then estimate the change in model parameters in order to reduce computation time. The latter depends on the size of seismic data vintages.

In this chapter, more practical and non-conventional inverse techniques for time lapse AVO inversion are introduced. The objectives of proposed inverse techniques are to enhance elastic parameters estimations, in the presence of noise, and also to prove their efficacy in terms of accuracy and computation time.

### **3.2 Time-lapse modelling**

Zou et al. (2006), have attributed the amplitude build-up in the seismic migrated section of monitor line for the Pikes Peak survey to the gas accumulating due to the cyclic steam stimulation (CSS) process used by Husky Energy for extracting the heavy oil. When the heavy

oil is depleted after being heated during the CSS process, it draws the gas out of oil-phase. The reservoir simulation work by Zou, et al., (2006) has shown that seismic response is significantly affected by the evolved of gas from the oil-phase. The gas saturation increases at the top of the reservoir, and this is confirmed by the cross-over of neutron and porosity logs in Figure (3.1).

The goal is to build a time lapse model to study the effect of cycle steam simulation on generated synthetic P-P and P-S seismic data for the Pikes Peak area, based on available well logs and seismic data that were acquired at two different times.

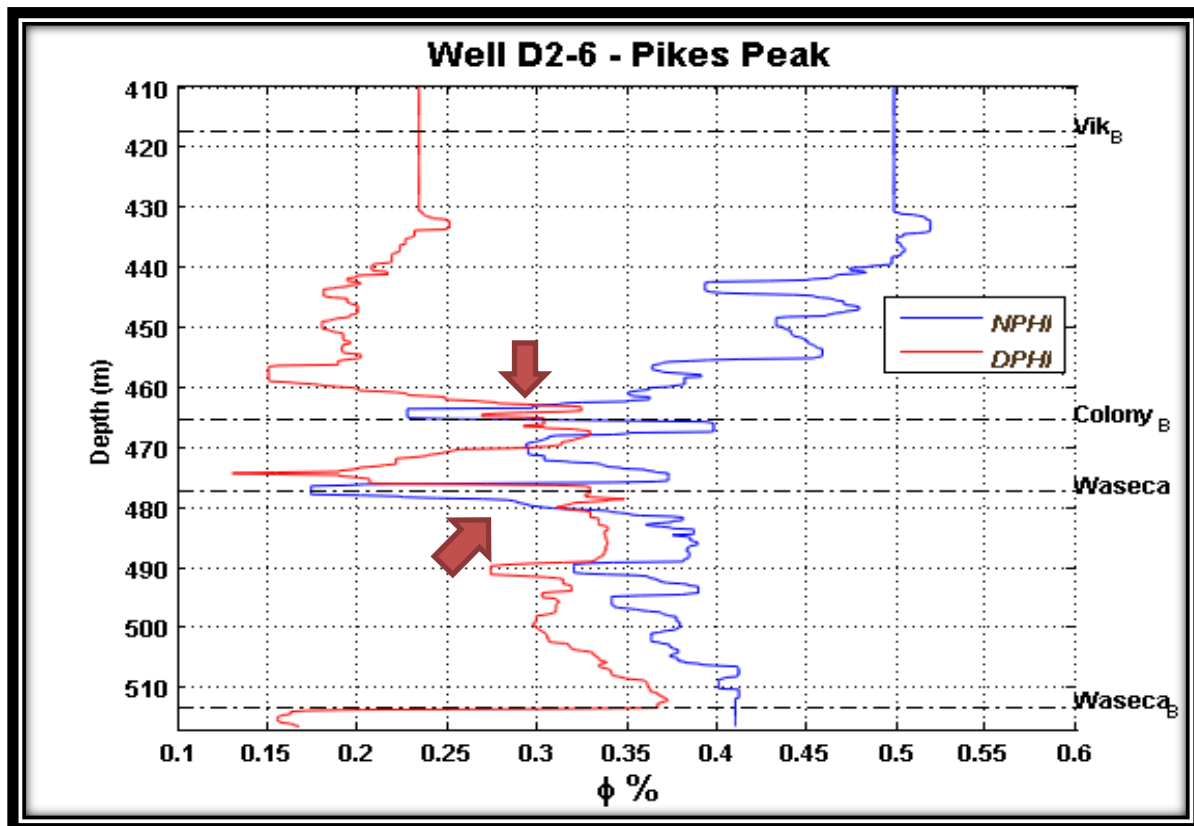


Figure 3.1: Neutron- and density- porosity logs for Well D2-6, Pikes Peak field. Arrows shows location of crossover of Neutron and density porosity logs as indicative of gas accumulation.

### ***3.2.1 Building of time-lapse model of Pikes Peak heavy oil***

AVO modeling is a practical aspect in seismic acquisition design, processing and interpretation of pre-stack seismic data (Li., et al., 2007). In this study, many assumptions are made in building up the time-lapse model. The model consists of three layers, where the second layer represents the reservoir. We assume that the Waseca reservoir is made up of a horizontal homogenous sand interval. The elastic physical parameters (P-wave velocity, S-wave velocity and density) for the top and bottom layers were held constant in the base and monitor surveys, while elastic attributes of the middle layer were allowed to vary over the lapsed time.

The P-wave velocity, S-wave velocity, and density values of the top layer are set to be 3500 m/sec, 1750 m/sec and 2.7 gm/cm<sup>3</sup> respectively, while for the bottom layer, these physical attributes were set to be 4000 m/sec, 2250 m/sec and 2.900 gm/cm<sup>3</sup> respectively. For the base survey, the P-wave velocity, S-wave velocity, and density values of the reservoir (middle) layer were set respectively to 3000 m/sec, 1500 m/sec and 2.65gm/cm<sup>3</sup>, while for the monitor model, these attributes were set at 2500 m/sec, 1450 m/sec and 2.5gm/cm<sup>3</sup>.

Note that we set the change in P-wave velocity by 500 m/sec over the lapsed time, while the S-wave velocity and density values were changed by small amounts compared to the P-wave velocity, because the P-wave velocity is significantly reduced by steam injection due to the CSS process. The assumption of a large P-wave rate of change is in consistent with previous work by Watson and Lines, (2001) for the same survey area, where the V<sub>p</sub>/V<sub>s</sub> ratio was decreased at a high rate over time-lapse surveys.

Figure (3.2) shows the time-lapse model. The thickness of the reservoir layer is slightly exaggerated in order to avoid tuning effects on seismic resolution and AVO responses (Downton, 2005). The bottom layer was terminated at a depth of 850m where Pre-Cambrian unconformity

manifests itself (Watson 2004). The far offset of the model is set to be at 1200m, and the geophone interval is 20m so as to simulate time-lapse seismic surveys that were carried out for the time-lapse lines (H1990 and H2000). Figure (3.3) shows synthetic logs generated for the time-lapse model to simulate pre- and post-steam injection response in a heavy oil reservoir.

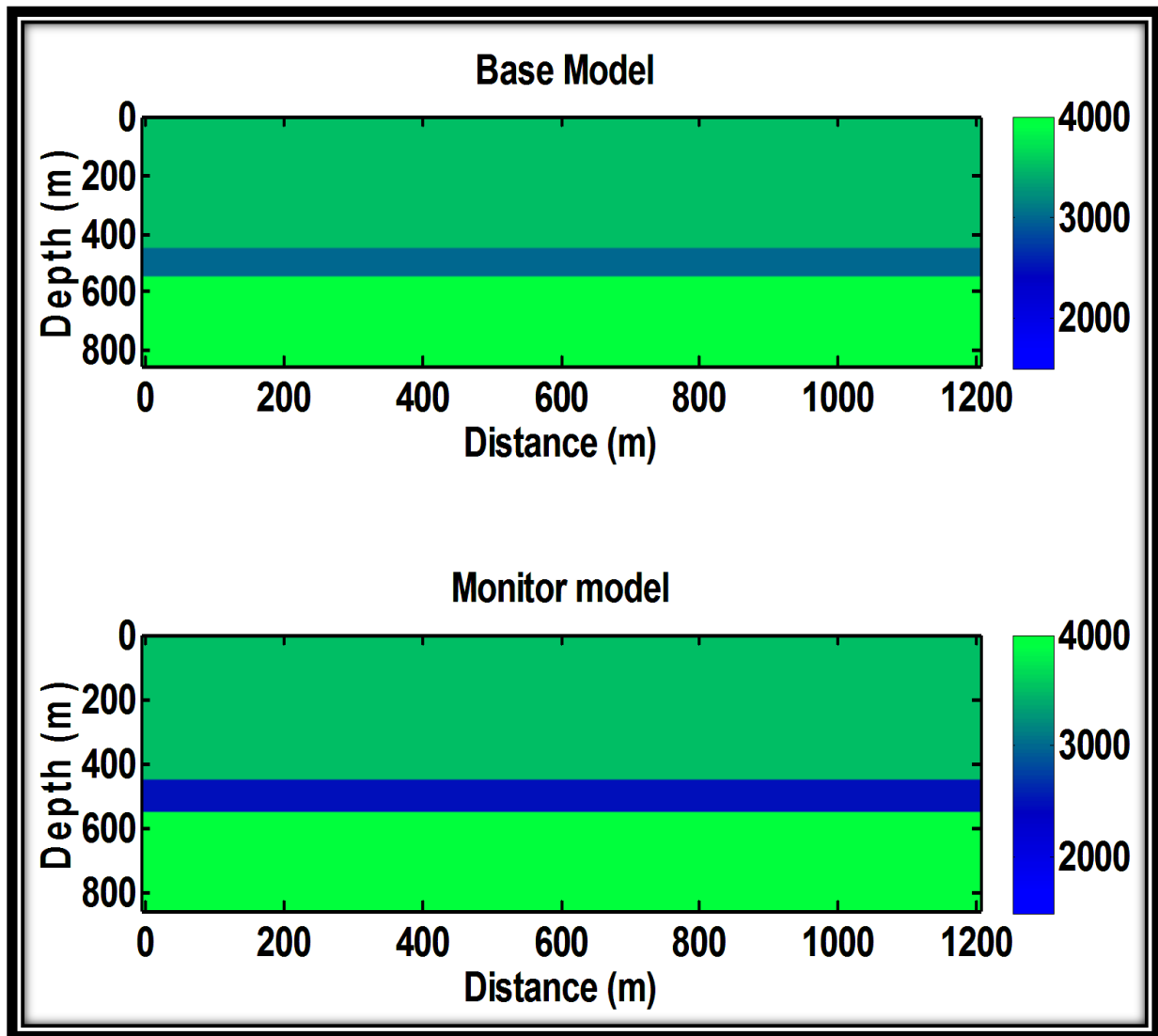


Figure 3.2: Time-lapse model to simulate heavy oil reservoir, Pikes Peak field. The color bar represents P-wave velocity. Note the increase of blue color of the reservoir layer (mid layer) in the monitor model as a result of decreasing P-wave velocity.

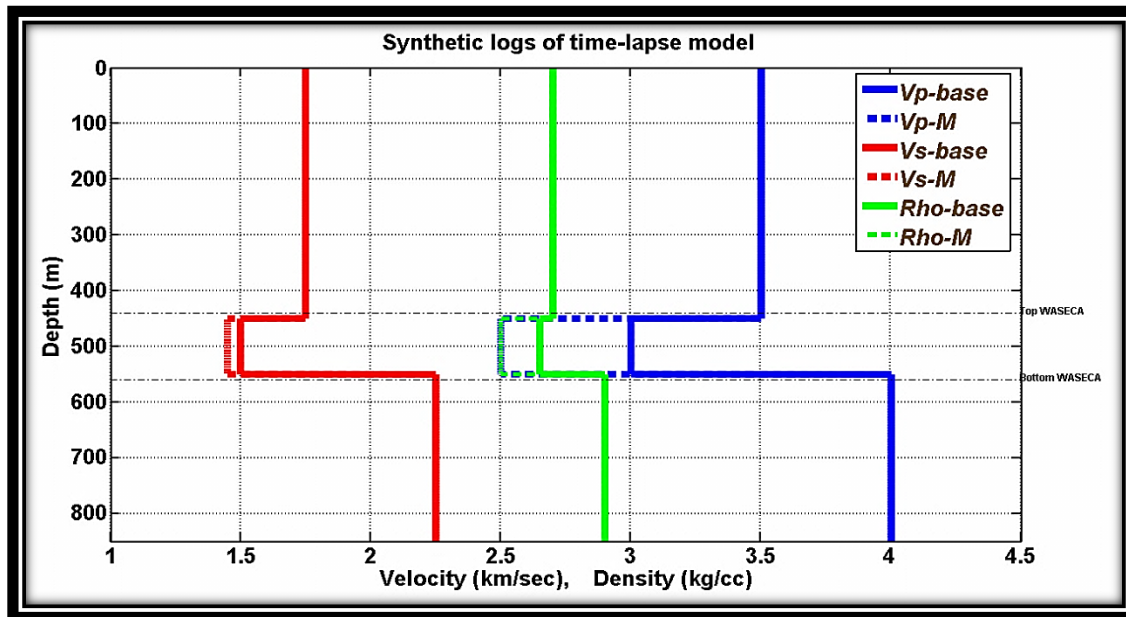


Figure 3.3: Synthetic logs to simulate pre- and post-steam injection in heavy oil reservoir.

### 3.2.2 Synthetic seismic data

The synthetic P-P and P-S data were generated using a multi-offset synthetic seismogram, SYNGRAM, (Lawton and Howell, 1992; Margrave and Foltinek, 1995) CREWES software. The Vp, Vs and density models are ray-traced for P-P and P-S incidence angles, and reflectivity amplitudes were calculated using the Zoeppritz equations. The PP- and PS- reflectivities are then convolved with a source wavelet, which is a zero-phase Ricker wavelet of dominant frequency of 35Hz, to generate synthetic seismic gathers. Figure (3.4) shows P-P synthetic data of baseline and monitoring models respectively, while Figure (3.5) represents P-S synthetic data of the baseline and monitoring models. The seismic amplitudes for the gathers of the monitoring survey are scaled relative to the seismic amplitude of baseline survey. Note the amplitude builds up and contrasts increase for the monitor model survey compared to the gathers of the base model.

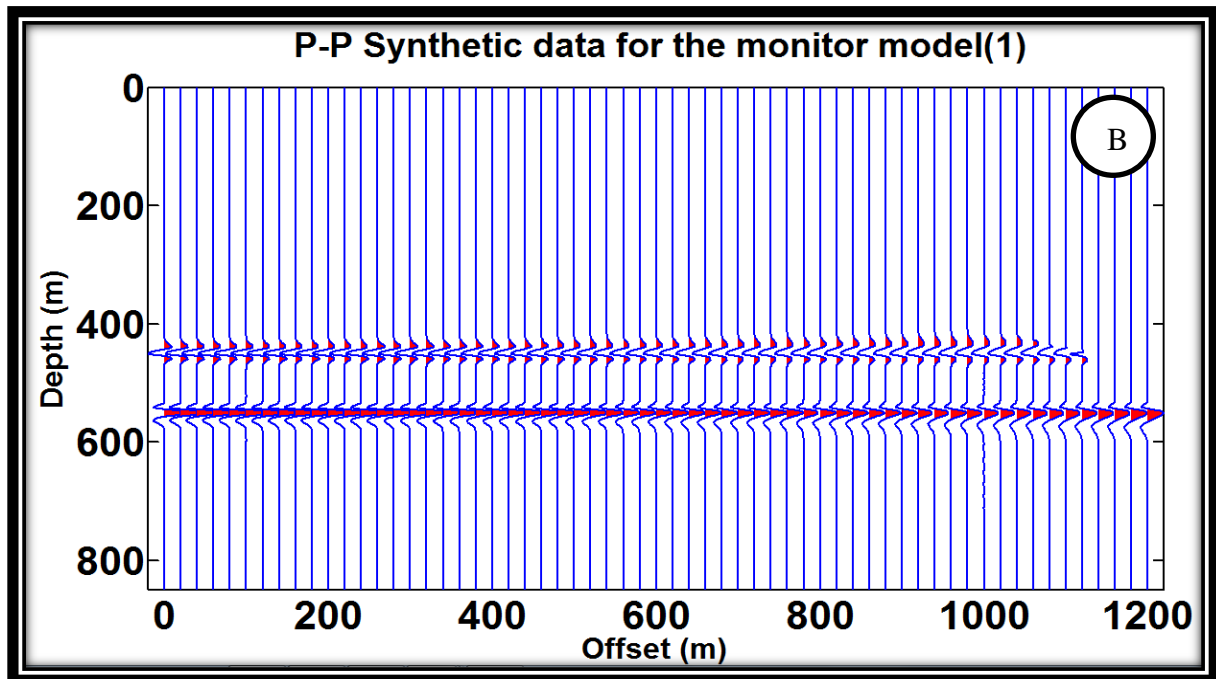
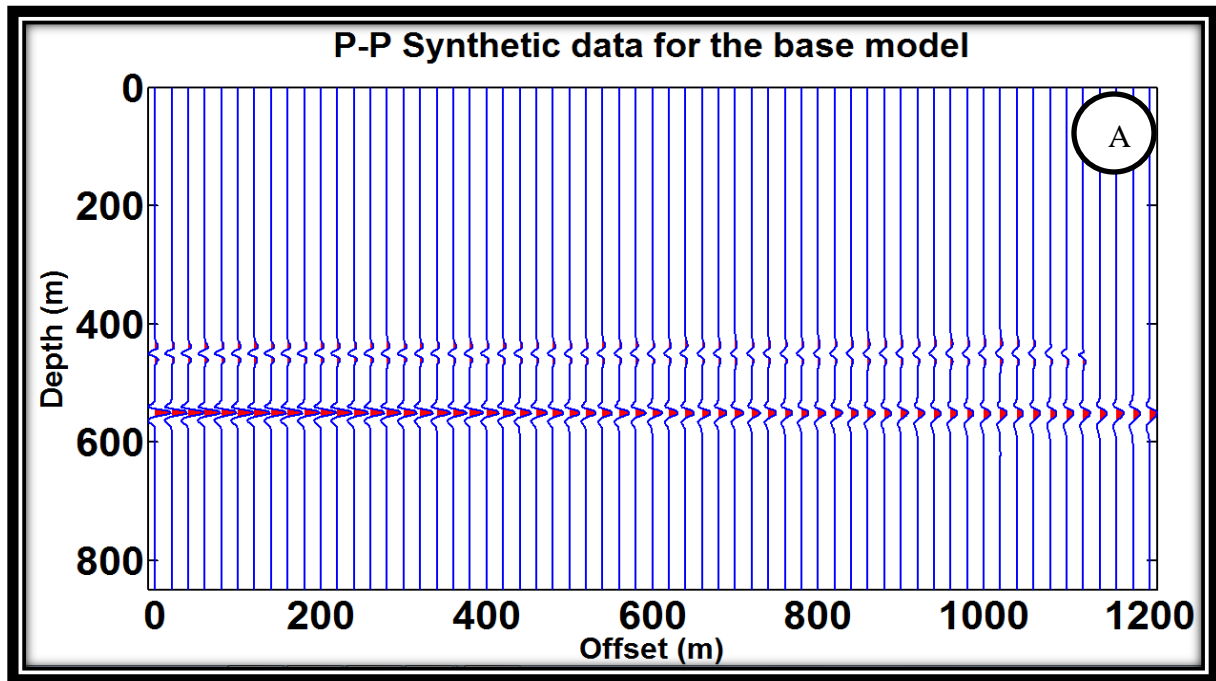


Figure 3.4: Synthetic **P-P** seismic data for the base (A) and the monitor (B) models.

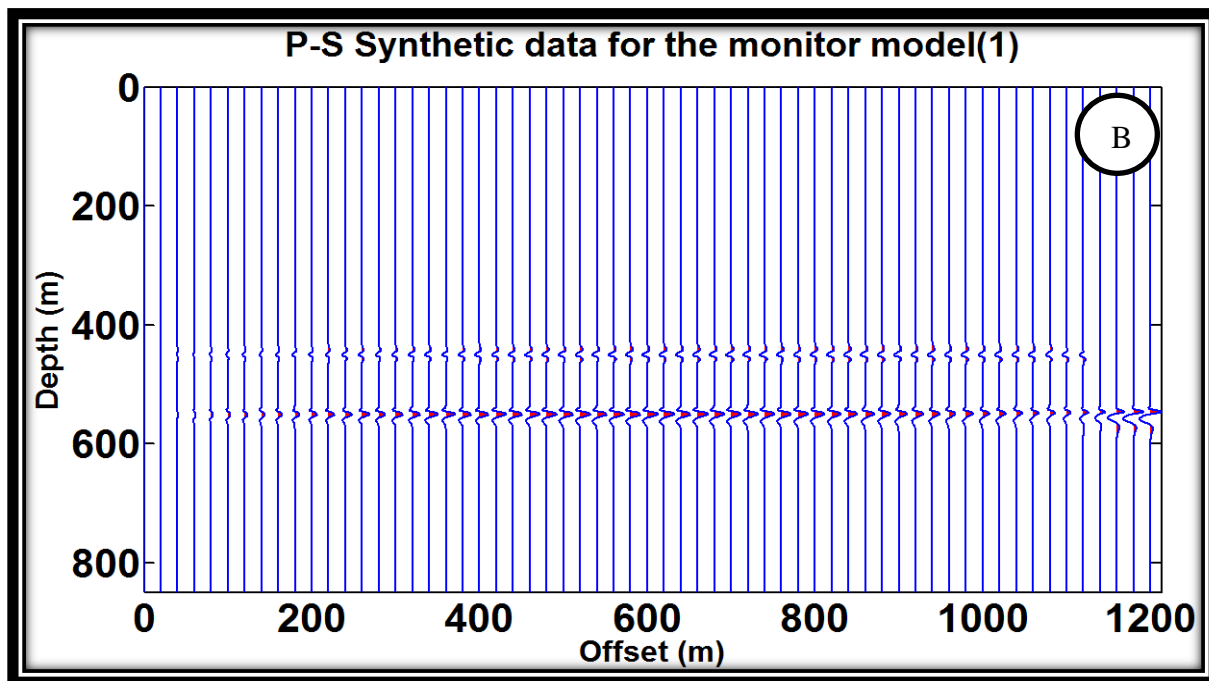
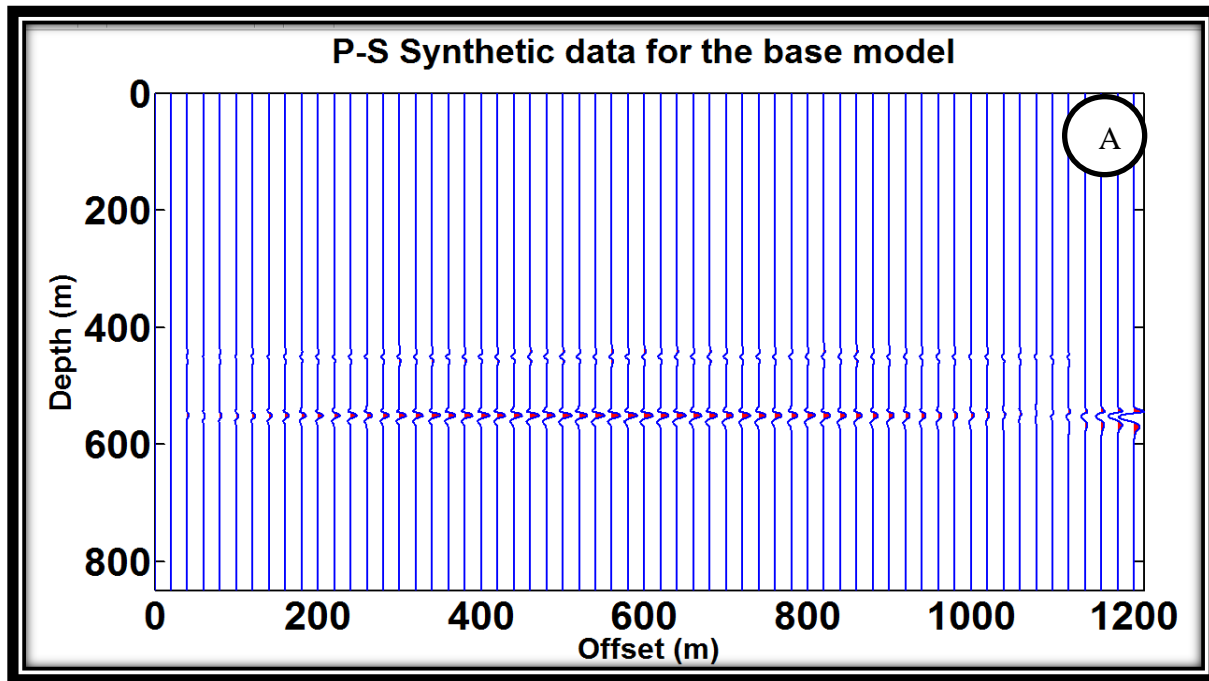


Figure 3.5: Synthetic **P-S** seismic data for the base (A) and the monitor (B) models.

The magnitudes of S-wave and density in building a time-lapse model were set to decrease at a small rate compared to the P-wave velocity. In theory, and specifically for conventional oil reservoirs, the shear wave velocity is inversely proportional to density ( $V_s = \sqrt{\mu/\rho}$ ). In order to investigate this theoretic assumption for a heavy oil model, the density of the second layer (reservoir layer) for the monitoring survey model was let to increase in magnitude compared to the density value of the same reservoir layer in the baseline survey (i.e., swapped the density values of monitoring survey from original setting). Although, the resulting gathers are not shown in this thesis, it was discovered that the amplitude contrast decreased as density increased. Thus, the results are in conflict with seismic sections of previous work (Zou et al., 2006).

Han et. al., (2008) studied elastic properties of heavy oil under the effect of temperature and pressure from steam injection in a heavy oil reservoir. In the study, they have categorized three areas in the heavy oil graph (Figure 3.6a) based on temperature. At low temperature, the heavy oil is merely in glass solid-phase, and then it changes to quasi-liquid all the way to liquid phases as temperature increases. The graph represents pre-steam and post-steam stages, which simulates the soaking period. If the pressure is allowed to decrease, as in the production stage, then heavy oil evolves to gas-phase as a result from an exsolution process from liquids. Note that both P-wave and S-wave velocities in Han's work (Figure 3.6b) show decreases in their magnitudes as temperature increases. Furthermore, it has also been found that the P-wave velocity decreases at high rate compared to the S-wave velocity (Eastwood, 1993).

In practice, injecting steam during the cycle steam simulation (CSS) process reduces the viscosity of the heavy oil and decreases the density. The CSS process will also lead to a decrease in the shear modulus of the heavy oil. As a result, an increase in the gas accumulation due to the evolution of gas from the oil-phase, will affect seismic amplitude responses.

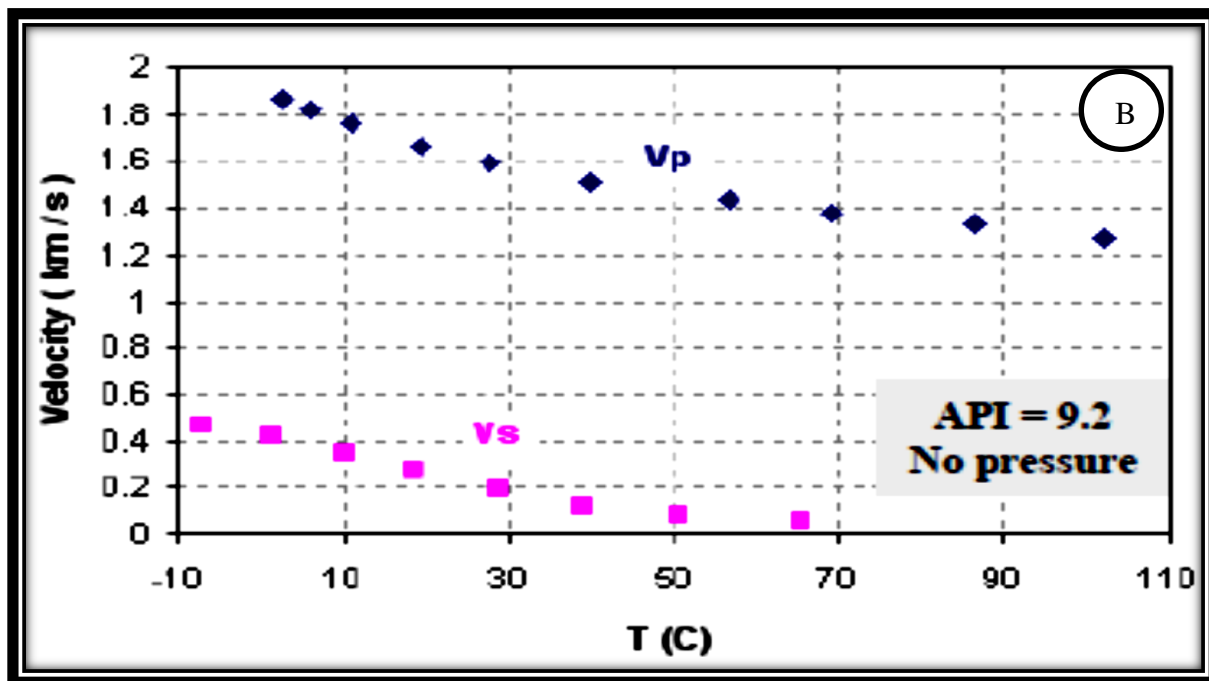
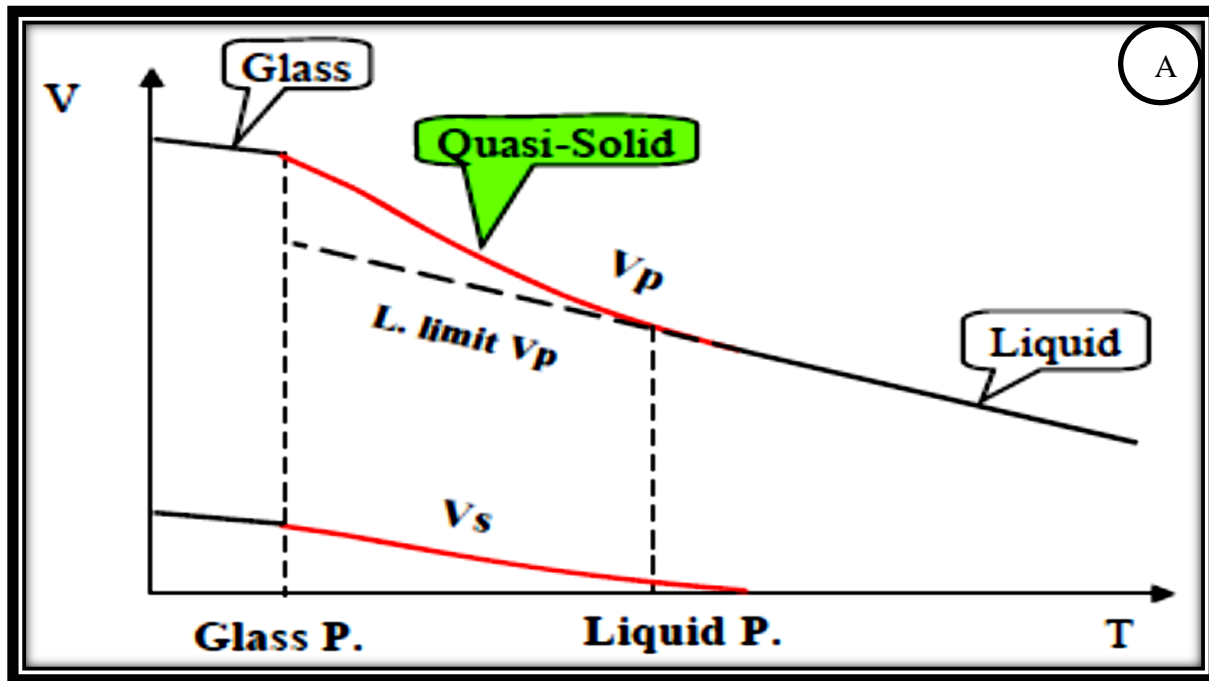


Figure 3.6: Properties of heavy oil sand (after Han et. al., 2008). (A) shows classification of heavy oil phases depending on temperature. (B) shows changes in  $V_p$  and  $V_s$  velocities with temperature.  $V_p$  decreases at a higher rate compared to  $V_s$  as temperature increases.

Therefore, we concluded that density values of the reservoir layer of the time-lapse model should be decreasing with time due to the steam injection (Saeed et al., 2013a) to be consistent with Han's study as well as processed seismic sections given in Chapter Four of this thesis.

Figure (3.7) shows the difference of synthetic P-P data between baseline and monitoring models, while Figure (3.8) displays the difference of synthetic P-S data between base and monitor models. In terms of changes in amplitude magnitude, it is obvious that change in P-wave data is responds more to the change in fluid properties at the reservoir zone.

### **3.2.3 AVA Reflectivity analysis**

The elastic properties of the time-lapse model of heavy oil are used in combination with the Zoeppritz equations to numerically model the changes in P-P and P-S reflectivities with incidence angle at the Waseca formation. Reflectivity analysis is performed only for the top and reservoir layers, where the interface is a *shale/sand*.

Figure (3.9) shows that the P-P reflectivity steadily decreases in magnitude with increasing angle until a critical angle is reached, and then the amplitudes dive towards the end of the curves. Note that there is no change in terms of amplitude polarities for the base and monitoring curves. The amplitudes of P-S reflectivity for the base and monitoring models are showing a scenario reverse to that of the P-P reflectivity. The magnitude of P-S reflection amplitudes is increasing but at small magnitudes compared to the P-P reflectivity. Note that the increase in amplitudes as angle of incidence increases is in consistent with synthetic P-S data shown in Figure (3.5).

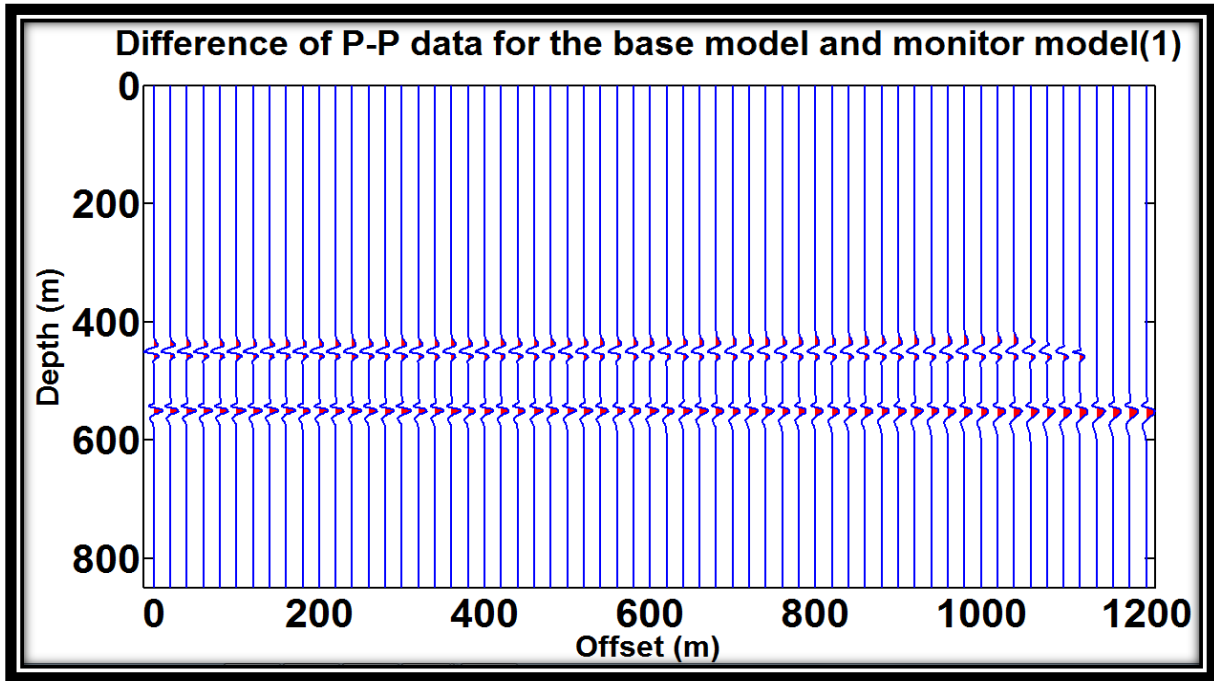


Figure 3.7: Difference of synthetic **P-P** seismic data for the base and the monitor models.

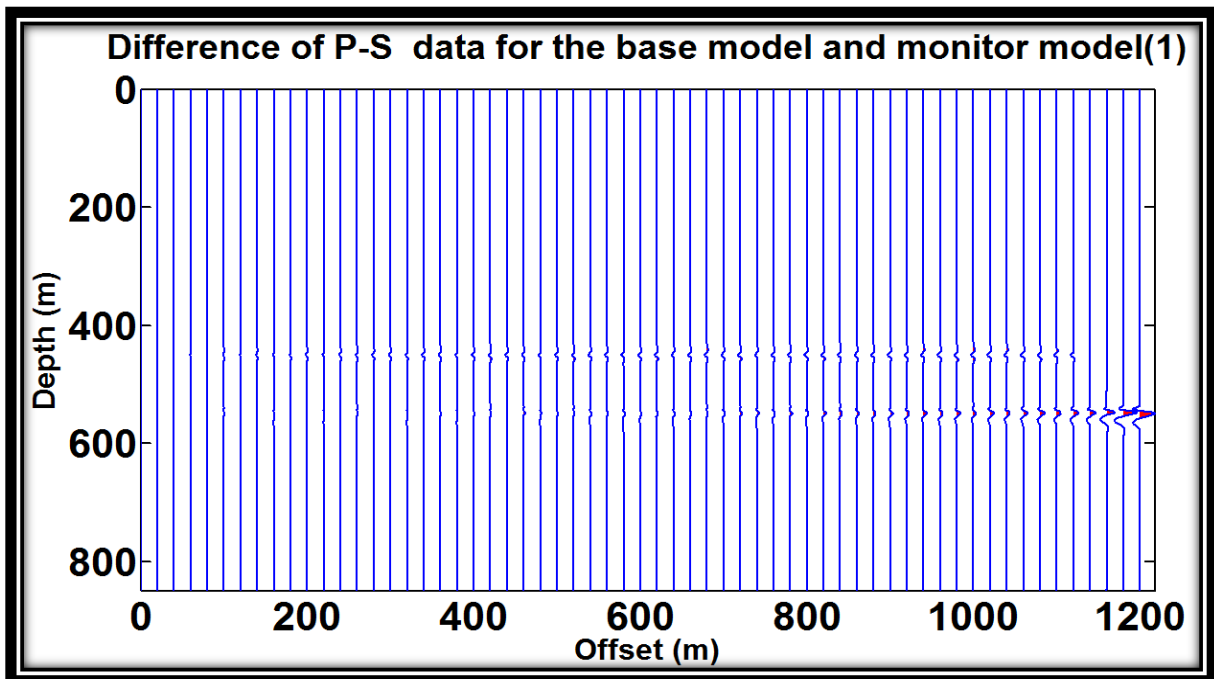


Figure 3.8: Difference of synthetic **P-S** seismic data for the base and the monitor models.

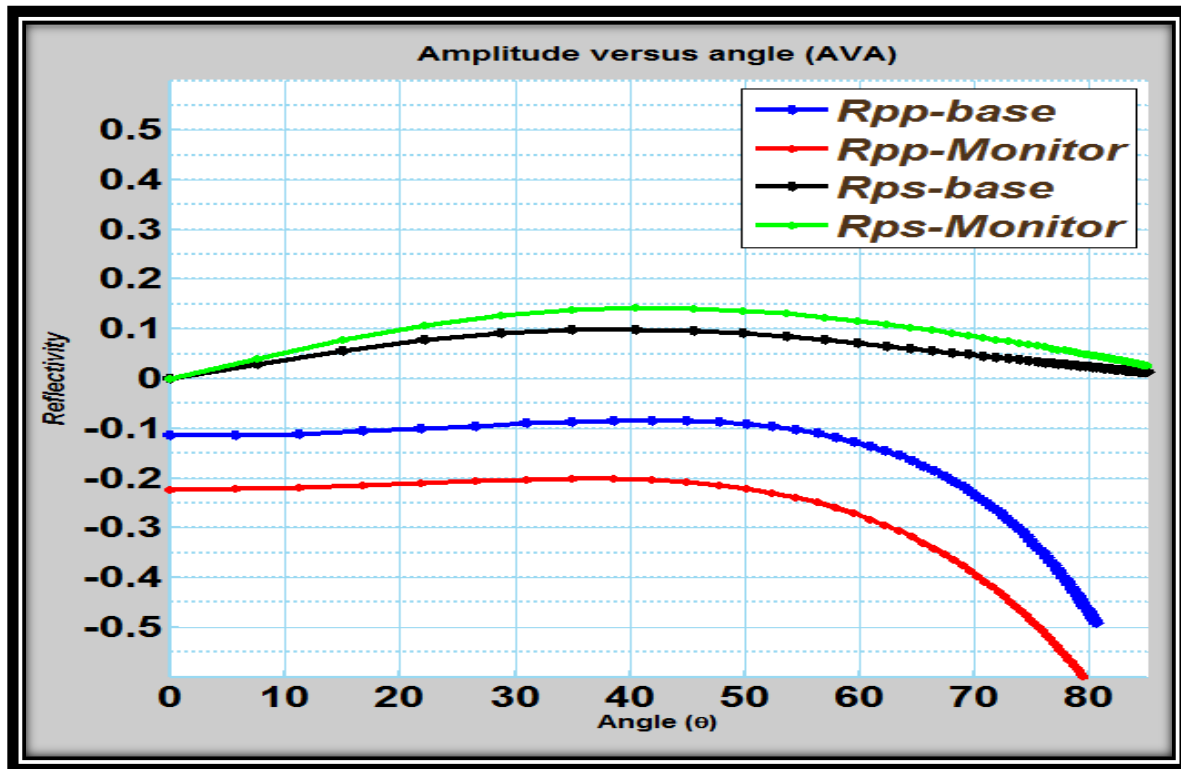


Figure 3.9: AVA analysis for the **P-P** and **P-S** reflectivities of the top and reservoir layers of time-lapse model of the Pikes Peak area.

The analysis of amplitude variation with angle of incidences for the P-P and P-S reflectivity curves assist in designing some of field survey parameters, such as defining appropriate geophone spacing and maximum offset.

### 3.3 Linear approximation of Zoeppritz equations

The Knott-Zoeppritz equations (Zoeppritz, 1919) describe the partitioning of seismic wave energy for plane waves at a welded elastic interface that is typically a boundary between two different layers of rock and fluid content (Sheriff and Geldart, 1995). The equations relate the

amplitudes of the incident, reflected and transmitted waves to the angle of incidence, for plane waves at a welded interface (Figure 3.10).

Although the boundary conditions set for Knott-Zoeppritz equations varies subject to elastic media across the interface (Larsen, 1999), boundary conditions for a solid-solid interface are commonly used in seismic reflection surveys. These boundary conditions include continuity for the normal and tangential stress and displacement across the welded interface and the incident angle does not approach the critical angle (Aki and Richards, 1980).

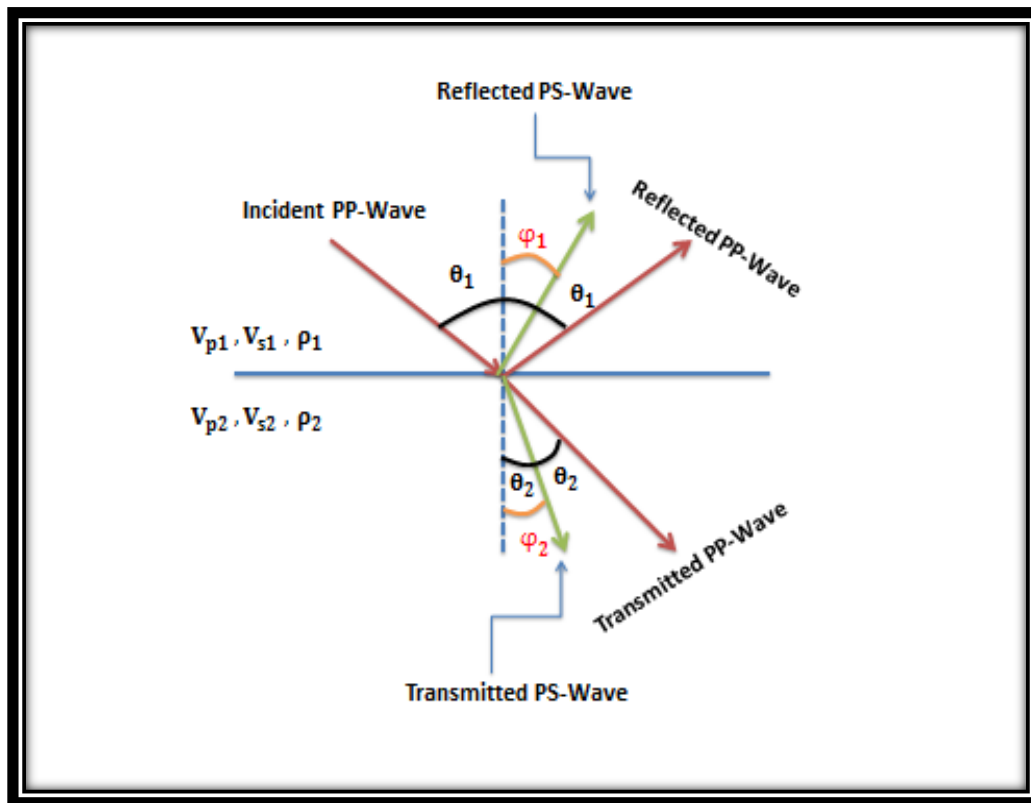


Figure 3.10: A schematic diagram shows reflected and transmitted waves generated at a welded solid-solid interface by an incident P-wave.

The Knott-Zoeppritz equations are described in details by Aki and Richards (1980). While Zoeppritz equations are widely used in AVO modelling to provide exact solutions for reflection varying with angle or offset, however the Zoeppritz equations are not practically applied to actual seismic data, due to the complexity of their algebraic solution with too many unknowns. Also, due to the complex nature of the subsurface, the recorded seismic wavefield is not typically composed of ideal reflected plane waves (Xu, 1999).

Aki and Richards (1980) have simplified the Zoeppritz equations into first order approximations of reflection and transmission coefficients of a plane-wave at a welded interface, between two elastic half-spaces. The linearized approximations for the P-P and P-S reflection coefficients,  $R_{pp}$  and  $R_{ps}$ , as functions of P-wave and S-wave velocity reflectivities, are written as follows:

$$R_{pp}(\theta) = \frac{1}{2} \left( 1 - 4 \frac{\beta^2}{\alpha^2} \sin^2 \theta \right) \frac{\Delta \rho}{\rho} + \frac{1}{2 \cos^2 \theta} \frac{\Delta \alpha}{\alpha} - 4 \frac{\beta^2}{\alpha^2} \sin^2 \theta \frac{\Delta \beta}{\beta} \quad 3.1$$

$$R_{ps}(\theta, \varphi) = \frac{-\alpha \tan \varphi}{2\beta} \left[ \left( 1 - 2 \frac{\beta^2}{\alpha^2} \sin^2 \theta + 2 \frac{\beta}{\alpha} \cos \theta \cos \varphi \right) \frac{\Delta \rho}{\rho} - \left( 4 \frac{\beta^2}{\alpha^2} \sin^2 \theta - 2 \frac{\beta}{\alpha} \cos \theta \cos \varphi \right) \frac{\Delta \beta}{\beta} \right] \quad 3.2$$

where elastic properties used in equations 3.1 and 3.2 are related to those at each side of the interface shown in Figure (3.10) and are given:

$$\Delta \alpha = (\alpha_2 - \alpha_1) \quad 3.2a$$

$$\alpha = (\alpha_1 + \alpha_2)/2 \quad 3.2b$$

$$\Delta\beta = (\beta_2 - \beta_1) \quad 3.2c$$

$$\beta = (\beta_1 + \beta_2)/2 \quad 3.2d$$

$$\Delta\rho = (\rho_2 - \rho_1) \quad 3.2e$$

$$\rho = (\rho_1 + \rho_2)/2 \quad 3.2f$$

The angle  $\theta$  is the average of P-wave angle of incidence and transmission across the interface, while  $\varphi$  is the average of the S-wave angle of reflection and transmission across the interface:

$$\theta = (\theta_1 + \theta_2)/2 \quad 3.2g$$

$$\varphi = (\varphi_1 + \varphi_2)/2 \quad 3.2h$$

In equations (3.1 and 3.2), it is assumed the fractional changes of reflectivity attributes  $(\frac{\Delta\alpha}{\alpha}, \frac{\Delta\beta}{\beta}, \frac{\Delta\rho}{\rho})$  are sufficiently small, and both  $\theta$  and  $\varphi$  angles do not approach the critical angle or 90 degrees (Aki and Richards, 1980).

In equations (3.1 and 3.2), reflectivity attributes are expressed as functions of P-wave and s-wave velocities and density. These equations can be reformulated as function of P-wave and S-wave impedances (Fatti et. al., 1994). By using impedances relationships,  $I = \alpha\rho(\frac{\Delta I}{I} = \frac{\Delta\alpha}{\alpha} + \frac{\Delta\rho}{\rho})$ , and  $J = \beta\rho(\frac{\Delta J}{J} = \frac{\Delta\beta}{\beta} + \frac{\Delta\rho}{\rho})$ , Snell's law, and trigonometry relationships, equations (3.1 and 3.2) are further re-arranged as functions of elastic impedances as follows:

$$R_{pp}(\theta) = \frac{(1+\tan^2\theta) \Delta I}{2} \frac{\Delta I}{I} - 4 \frac{\beta^2}{\alpha^2} \sin^2\theta \frac{\Delta J}{J} - \left(\frac{1}{2}\tan^2\theta - 2 \frac{\beta^2}{\alpha^2} \sin^2\theta\right) \frac{\Delta\rho}{\rho} \quad 3.3$$

$$R_{ps}(\theta, \varphi) = \frac{-\alpha \tan\varphi}{2\beta} \left[ \left(1 + 2 \sin^2\varphi - 2 \frac{\beta}{\alpha} \cos\theta \cos\varphi\right) \frac{\Delta\rho}{\rho} - \left(4 \sin^2\varphi - 4 \frac{\beta}{\alpha} \cos\theta \cos\varphi\right) \frac{\Delta J}{J} \right] \quad 3.4$$

Equations (3.3 and 3.4) are simultaneously inverted for elastic impedances and density using both P-P and P-S seismic data that are scaled to reflectivity amplitudes. In matrix notation, simultaneous P-P and P-S AVO inversion at specific depth or time sample interval are explicitly written for different ranges of  $\mathbf{M}$  offsets as:

$$\begin{bmatrix} R_{pp_1} \\ \vdots \\ R_{pp_M} \\ R_{ps_1} \\ \vdots \\ R_{ps_M} \end{bmatrix} = \begin{bmatrix} \frac{(1+\tan^2\bar{\theta}_1)}{2} & -4 \frac{\beta^2}{\alpha^2} \sin^2\bar{\theta}_1 & -\left(\frac{1}{2}\tan^2\bar{\theta}_1 - 2 \frac{\beta^2}{\alpha^2} \sin^2\bar{\theta}_1\right) \\ \vdots & \vdots & \vdots \\ \frac{(1+\tan^2\bar{\theta}_M)}{2} & -4 \frac{\beta^2}{\alpha^2} \sin^2\bar{\theta}_M & -\left(\frac{1}{2}\tan^2\bar{\theta}_M - 2 \frac{\beta^2}{\alpha^2} \sin^2\bar{\theta}_M\right) \\ 0 & \frac{-\alpha \tan\bar{\varphi}_1}{2\beta} \left[ -\left(4 \sin^2\bar{\varphi}_1 - 4 \frac{\beta}{\alpha} \cos\bar{\theta}_1 \cos\bar{\varphi}_1\right) \right] & \frac{-\alpha \tan\bar{\varphi}_1}{2\beta} \left[ \left(1 + 2 \sin^2\bar{\varphi}_1 - 2 \frac{\beta}{\alpha} \cos\bar{\theta}_1 \cos\bar{\varphi}_1\right) \right] \\ \vdots & \vdots & \vdots \\ 0 & \frac{-\alpha \tan\bar{\varphi}_M}{2\beta} \left[ -\left(4 \sin^2\bar{\varphi}_M - 4 \frac{\beta}{\alpha} \cos\bar{\theta}_M \cos\bar{\varphi}_M\right) \right] & \frac{-\alpha \tan\bar{\varphi}_M}{2\beta} \left[ \left(1 + 2 \sin^2\bar{\varphi}_M - 2 \frac{\beta}{\alpha} \cos\bar{\theta}_M \cos\bar{\varphi}_M\right) \right] \end{bmatrix} \begin{bmatrix} \frac{\Delta I}{I} \\ \frac{\Delta J}{J} \\ \frac{\Delta\rho}{\rho} \end{bmatrix} \quad 3.5$$

where  $\bar{\theta}$  and  $\bar{\varphi}$  are respectively, the averages of the P-wave angle of incident and S-wave reflected angle across the interface.

Different authors have re-arranged Aki-Richards approximation equations to solve for different reflectivity attributes, such as Poisson ratio (Shuey, 1985; Hilterman, 1989), fluid factor (Smith and Gidlow, 1987) and for Lamé's parameters (Goodway et. al., 1997; Xu and Bancroft, 1997; Gray et. al., 1999 and Gray, 2002). Due to inversion stability reasons and lacking of large offsets, AVO inversion equations are often solved for the first two terms only.

The simultaneous AVO inversion codes for time-lapse P-P and P-S seismic data developed in this thesis use three-term reflectivity attributes given in equations (3.3 and 3.4). Nevertheless, the developed AVO inverse schemes can be easily modified to obtain reflectivity model parameters as functions of velocities, Poisson ratio or Lamé's attributes.

### 3.4 Practical techniques for time-lapse AVO inversion

Practical inversion techniques that simultaneously invert seismic data of different vintages (Saeed et al., 2013b) are used in this study. The objectives from proposed inverse techniques are to improve model parameter estimations in the presence of noise, and to prove their robustness in terms of accuracy and computation time.

For two given data sets, say (base,  $d_0$ , and a monitor,  $d_1$ ), reflectivity data can be written as:

$$d_0 = G_0 m_0 \quad \text{for baseline survey} \quad 3.5$$

$$d_1 = G_1 m_1 \quad \text{for monitor line survey} \quad 3.6$$

where  $\mathbf{d}$  is seismic data,  $\mathbf{G}$  is the forward operator, and  $\mathbf{m}$  represent the unknown model parameters.

The least-squares inverse problems of time-lapse seismic surveys requires minimization of the cost functions below

$$J(\mathbf{m}_0) = \|\mathbf{G}_0\mathbf{m}_0 - \mathbf{d}_0\|^2 + \lambda^2\|\mathbf{R}_0\mathbf{m}_0\|^2 \quad 3.7$$

$$J(\mathbf{m}_1) = \|\mathbf{G}_1\mathbf{m}_1 - \mathbf{d}_1\|^2 + \lambda^2\|\mathbf{R}_1\mathbf{m}_1\|^2 \quad 3.8$$

Equations (3.7 and 3.8) are then solved to give the solutions

$$\mathbf{m}_0 = (\mathbf{G}_0^T\mathbf{G}_0 + \lambda^2\mathbf{R}_0^T\mathbf{R}_0)^{-1}\mathbf{G}_0^T\mathbf{d}_0 \quad 3.9$$

$$\mathbf{m}_1 = (\mathbf{G}_1^T\mathbf{G}_1 + \lambda^2\mathbf{R}_1^T\mathbf{R}_1)^{-1}\mathbf{G}_1^T\mathbf{d}_1 \quad 3.10$$

where,  $\mathbf{R}_i$  and  $\lambda$  are the regularization operator and parameter (Constable et al., 1987) respectively.

The low frequency models are then integrated with estimated model parameters using the band-limited impedance, BLIMP, module (Ferguson and Margrave, 1996). The estimated model parameters ( $\mathbf{m}_0$  and  $\mathbf{m}_1$ ) resulting for inverting seismic data vintages separately, are then manipulated to be expressed either as differences between estimated base and monitor model parameters ( $\Delta\mathbf{m} = \mathbf{m}_1 - \mathbf{m}_0$ ) or as percentages of changes between base and monitoring model parameters ( $\Omega_{m\%} = \frac{\Delta\mathbf{m}}{\mathbf{m}_0} \cdot \mathbf{100}$ ).

In the following sections, we introduce three different time-lapse AVO inversion schemes: 1) total inversion of the differences; 2) inversion of seismic differences only; 3) sequential reflectivity-constrained inversion that simultaneously invert baseline and monitor seismic data surveys to estimate the change of model parameters. The obtained model parameters can also be presented as percentages of changes.

### 3.4.1 Total inversion of differences

The total inversion of differences for estimating model parameter changes of time-lapse data is carried out by simultaneously inverting baseline and monitor data. Equations (3.5) and (3.6) are then re-arranged to represent elastic parameter changes as follows:

$$\mathbf{G}_1 \mathbf{m}_1 - \mathbf{G}_0 \mathbf{m}_0 = \mathbf{d}_1 - \mathbf{d}_0 \quad 3.11$$

Note that different re-arrangement and simplification of total inversion of difference in equation (3.11) yields two sub inverse schemes that can be implemented in time-lapse AVO inversion.

#### 3.4.1.1 Inversion for elastic attributes of monitor line ( $\mathbf{m}_1$ ) and time-lapse changes ( $\Delta\mathbf{m}$ )

By using ( $\Delta\mathbf{G} = \mathbf{G}_1 - \mathbf{G}_0$ ), and then substituting for  $\mathbf{G}_1$  in equation (3.11) yields the following:

$$(\Delta\mathbf{G} + \mathbf{G}_0)\mathbf{m}_1 - \mathbf{G}_0\mathbf{m}_0 = \Delta\mathbf{d} \quad 3.12$$

Then, by further re-arranging equation (3.12), the time-lapse AVO inversion for estimating model parameters of monitor line ( $\mathbf{m}_1$ ) and model parameter changes ( $\Delta\mathbf{m}$ ) is written as follows:

$$\Delta\mathbf{G}\mathbf{m}_1 + \mathbf{G}_0\Delta\mathbf{m} = \Delta\mathbf{d} \quad 3.13$$

In augmented matrix notation, the cost functions of equations (3.7) and (3.8) can be jointly-inverted, and written as follows:

$$J(\mathbf{m}_1, \Delta\mathbf{m}) = \left\| \begin{bmatrix} \Delta\mathbf{G} & \mathbf{0} \\ \mathbf{0} & \mathbf{G}_0 \end{bmatrix} \begin{bmatrix} \mathbf{m}_1 \\ \Delta\mathbf{m} \end{bmatrix} - \begin{bmatrix} \mathbf{d}_1 \\ \mathbf{d}_0 \end{bmatrix} \right\|^2 + \left\| \begin{bmatrix} \lambda^2 \mathbf{R}_1^T \mathbf{R}_1 & \mathbf{0} \\ \mathbf{0} & \lambda^2 \mathbf{R}_0^T \mathbf{R}_0 \end{bmatrix} \begin{bmatrix} \mathbf{m}_1 \\ \Delta\mathbf{m} \end{bmatrix} \right\|^2 \quad 3.14$$

$\Delta G$  represents the difference in ray traced coefficients of equations (3.5 and 3.6) of both baseline and monitor surveys. The differences of ray-traced angles between monitor and base surveys [i.e.,  $\Delta\bar{\theta}_i = (\bar{\theta}_{i_{monitor}} - \bar{\theta}_{i_{base}})$  and  $\Delta\bar{\varphi}_i = (\bar{\varphi}_{i_{monitor}} - \bar{\varphi}_{i_{base}})$ ] are used as follows:

$$\Delta G = \begin{bmatrix} \frac{(1+\tan^2(\Delta\bar{\theta}_1))}{2} & -4\frac{\beta^2}{\alpha^2}\sin^2(\Delta\bar{\theta}_1) & -\left(\frac{1}{2}\tan^2(\Delta\bar{\theta}_1) - 2\frac{\beta^2}{\alpha^2}\sin^2(\Delta\bar{\theta}_1)\right) \\ \vdots & \vdots & \vdots \\ \frac{(1+\tan^2(\Delta\bar{\theta}_M))}{2} & -4\frac{\beta^2}{\alpha^2}\sin^2(\Delta\bar{\theta}_M) & -\left(\frac{1}{2}\tan^2(\Delta\bar{\theta}_M) - 2\frac{\beta^2}{\alpha^2}\sin^2(\Delta\bar{\theta}_M)\right) \\ 0 & \frac{-\alpha\tan(\Delta\bar{\varphi}_1)}{2\beta}\left[-\left(4\sin^2\bar{\varphi}_1 - 4\frac{\beta}{\alpha}\cos(\Delta\bar{\theta}_M)\cos(\Delta\bar{\varphi}_1)\right)\right] & \frac{-\alpha\tan(\Delta\bar{\varphi}_M)}{2\beta}\left[\left(1 + 2\sin^2(\Delta\bar{\varphi}_1) - 2\frac{\beta}{\alpha}\cos(\Delta\bar{\theta}_M)\cos(\Delta\bar{\varphi}_1)\right)\right] \\ \vdots & \vdots & \vdots \\ 0 & \frac{-\alpha\tan(\Delta\bar{\varphi}_M)}{2\beta}\left[-\left(4\sin^2(\Delta\bar{\varphi}_M) - 4\frac{\beta}{\alpha}\cos\bar{\theta}_M\cos(\Delta\bar{\varphi}_M)\right)\right] & \frac{-\alpha\tan(\Delta\bar{\varphi}_M)}{2\beta}\left[\left(1 + 2\sin^2(\Delta\bar{\varphi}_M) - 2\frac{\beta}{\alpha}\cos(\Delta\bar{\theta}_M)\cos(\Delta\bar{\varphi}_M)\right)\right] \end{bmatrix} \quad 3.14a$$

$m_1$  and  $\Delta m$  are, respectively, reflectivities model parameters for the monitor line and change of model parameters attributes between baseline and monitor surveys,

$$m_1 = \left[ \left(\frac{\Delta I}{I}\right)_{monitor}, \left(\frac{\Delta J}{J}\right)_{monitor} \text{ and } \left(\frac{\Delta \rho}{\rho}\right)_{monitor} \right] \quad 3.14b$$

$$\Delta m = \left[ \Delta\left(\frac{\Delta I}{I}\right), \Delta\left(\frac{\Delta J}{J}\right) \text{ and } \Delta\left(\frac{\Delta \rho}{\rho}\right) \right] \quad 3.14c$$

The forward operator  $G_0$  is identical to  $\Delta G$  given in equation (3.14a) except that ray-traced coefficients of baseline survey are used in building the matrix  $G_0$ . The regularization operators ( $R_i$ ) were set to be first-order derivative (Tikhonov and Arsenin, 1977).

Since the outputs from equation (3.13) are  $m_1$  and  $\Delta m$  respectively, then model parameters for the baseline survey model can also be estimated as

$$m_0 = m_1 - \Delta m \quad 3.15$$

Figures (3.11 and 3.12) are the inverted model parameters ( $\frac{\Delta I}{I}$ ,  $\frac{\Delta J}{J}$  and  $\frac{\Delta \rho}{\rho}$ ) for the *monitor model* and model parameters changes [ $\Delta(\frac{\Delta I}{I})$ ,  $\Delta(\frac{\Delta J}{J})$  and  $\Delta(\frac{\Delta \rho}{\rho})$ ] for the *time-lapse survey* before adding low frequency components from well logs. Figure (3.13) shows estimated model parameters ( $\frac{\Delta I}{I}$ ,  $\frac{\Delta J}{J}$  and  $\frac{\Delta \rho}{\rho}$ ) for the *baseline model*, using equation (3.14), before adding low frequency components. The low frequency components of the background models are added using the band-limited impedance module, BLIMP (Ferguson and Margrave, 1996).

Figures (3.14 and 3.15) show inverted elastic parameters (**IP**-impedance, **IS**-impedance and  **$\rho$** ) for the baseline and monitor surveys respectively, while Figure (3.16) represents change in elastic parameters ( $\Delta$ **IP**-impedance,  $\Delta$ **IS**-impedance and  $\Delta$  **$\rho$** ), after adding low frequency background models, as a result of an inversion of total differences using equation (3.14).

Note that actual elastic parameters estimated from well logs are also calculated and superimposed as a bold black dashed-line. The inverted elastic parameters coincide with actual elastic parameters calculated from well logs shown in graphs.

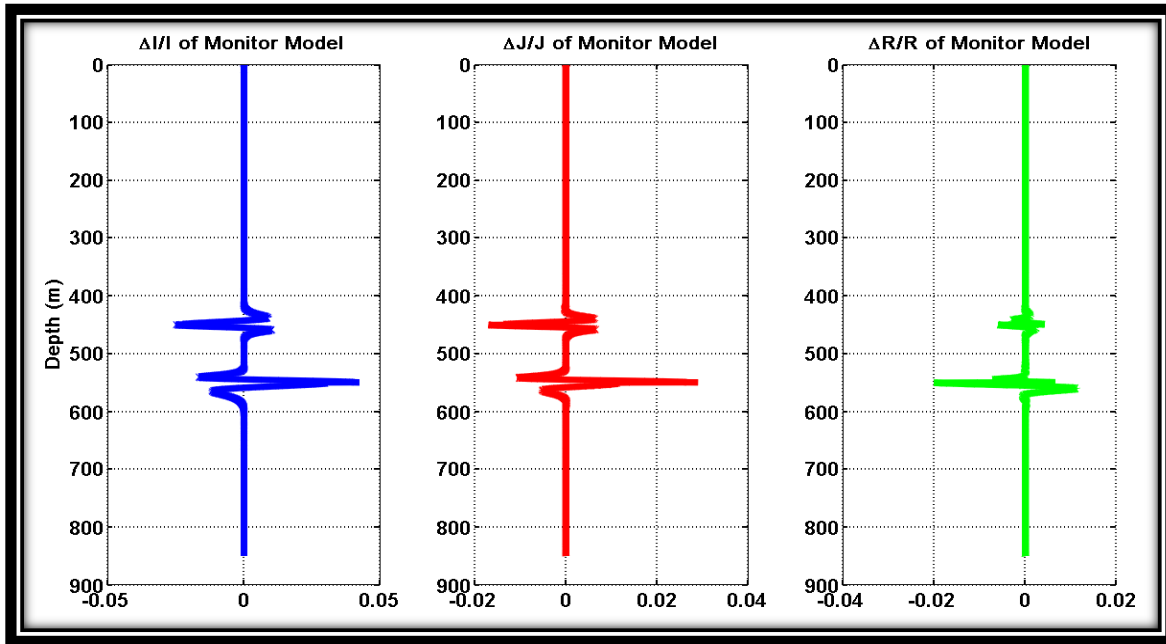


Figure 3.11: Estimated model parameters ( $\frac{\Delta I}{I}$ ,  $\frac{\Delta J}{J}$  and  $\frac{\Delta R}{R}$ ) for the *monitor* model before adding low-frequency models.

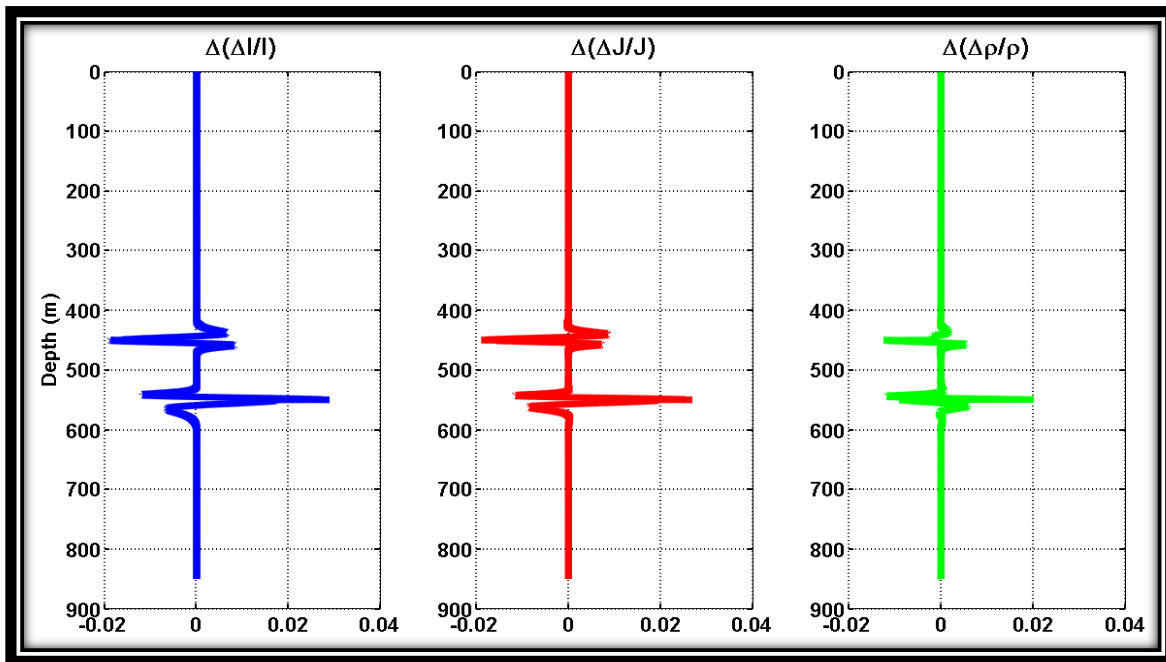


Figure 3.12: Estimated model parameters changes [ $\Delta(\frac{\Delta I}{I})$ ,  $\Delta(\frac{\Delta J}{J})$  and  $\Delta(\frac{\Delta R}{R})$ ] for the *time-lapse* model before adding low-frequencies from logs.

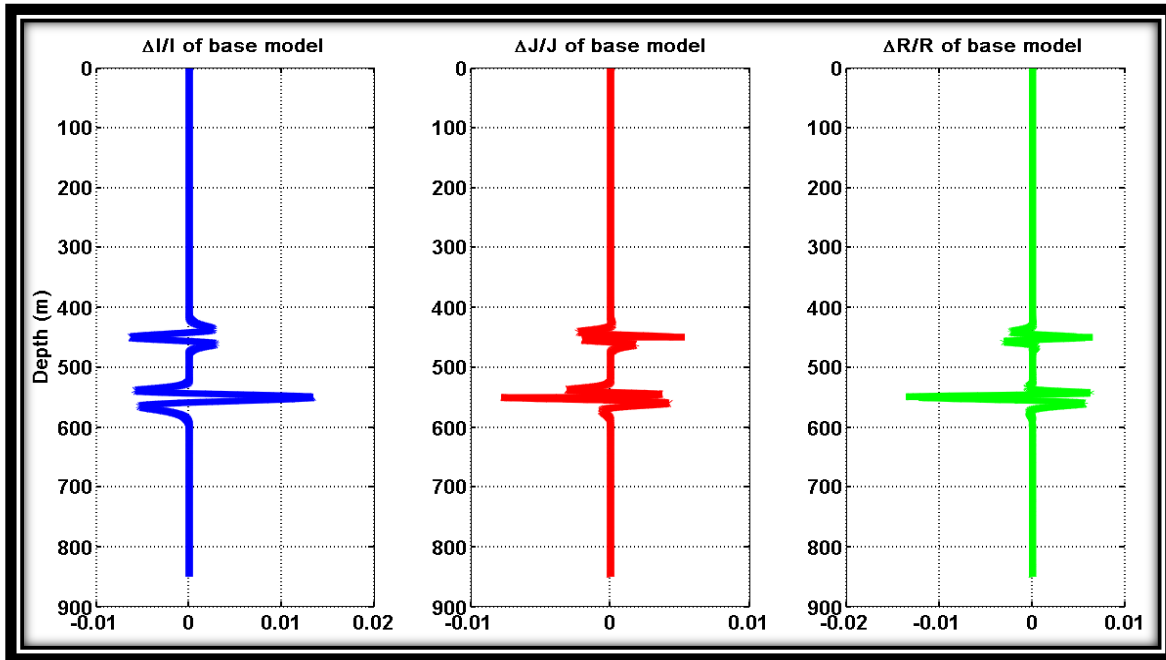


Figure 3.13: Estimated model parameters ( $\frac{\Delta I}{I}$ ,  $\frac{\Delta J}{J}$  and  $\frac{\Delta R}{R}$ ) for the *base* model before adding low-frequencies from logs.

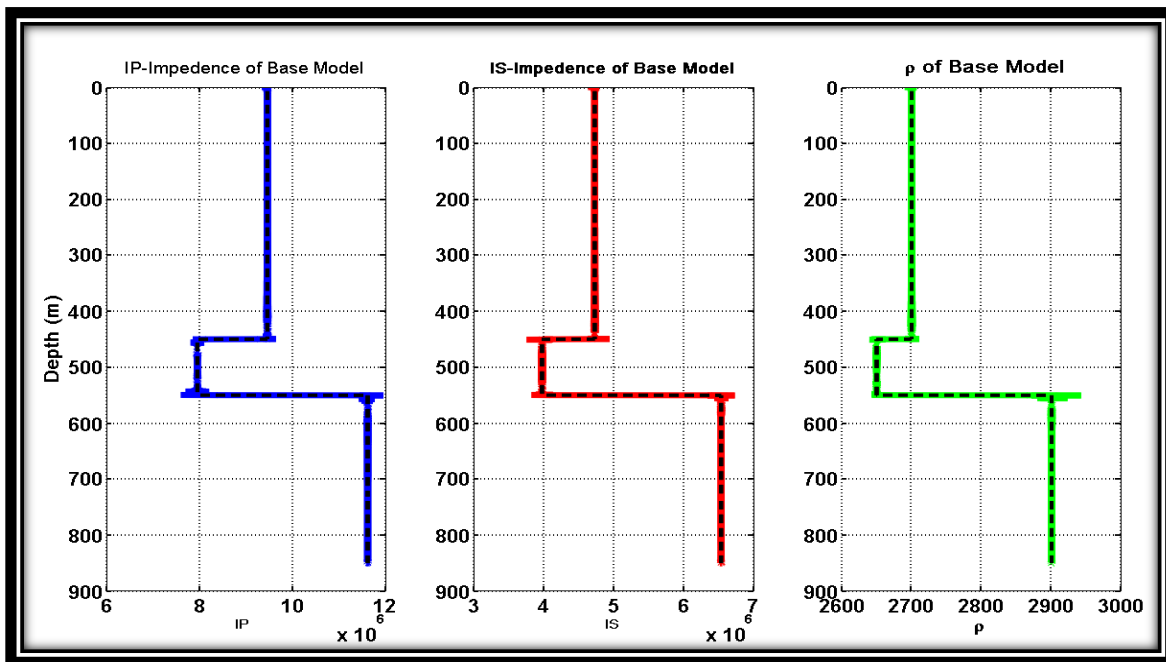


Figure 3.14: Elastic parameters (IP, IS and  $\rho$ ) of the base model after adding low frequencies. Embedded graphs in bold black dotted lines represent actual (IP, IS and  $\rho$ ) calculated from logs.

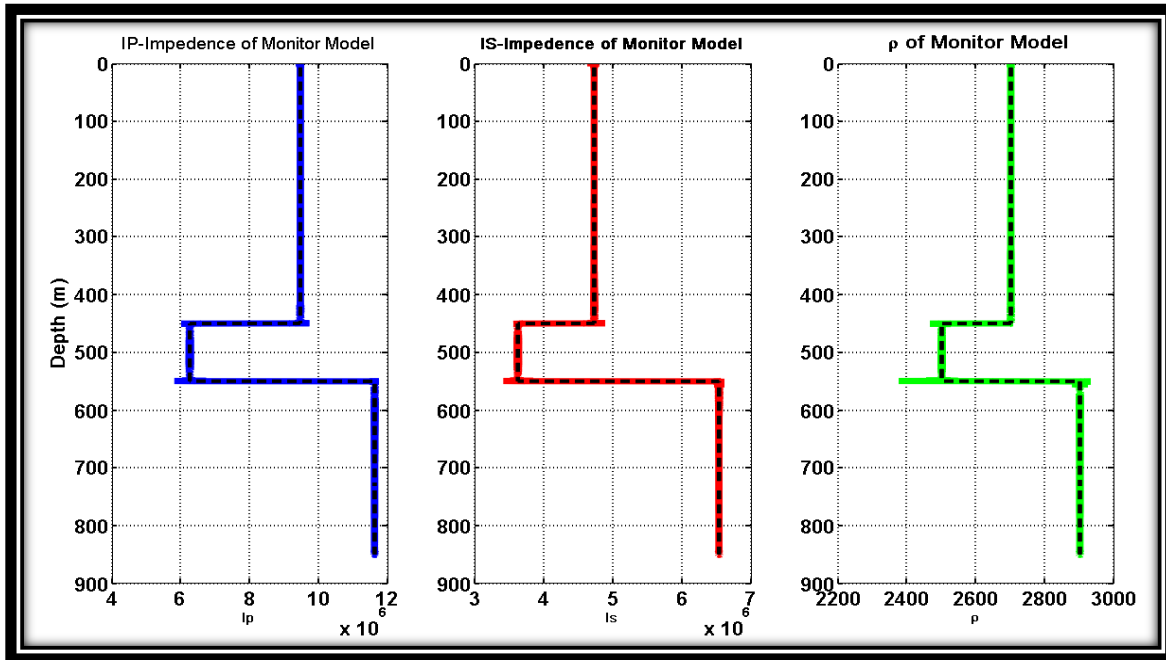


Figure 3.15: Elastic parameters ( $IP$ ,  $IS$  and  $\rho$ ) of the monitor model after adding low frequency. Embedded graphs in bold black dotted lines represent actual ( $IP$ ,  $IS$  and  $\rho$ ) calculated from logs.

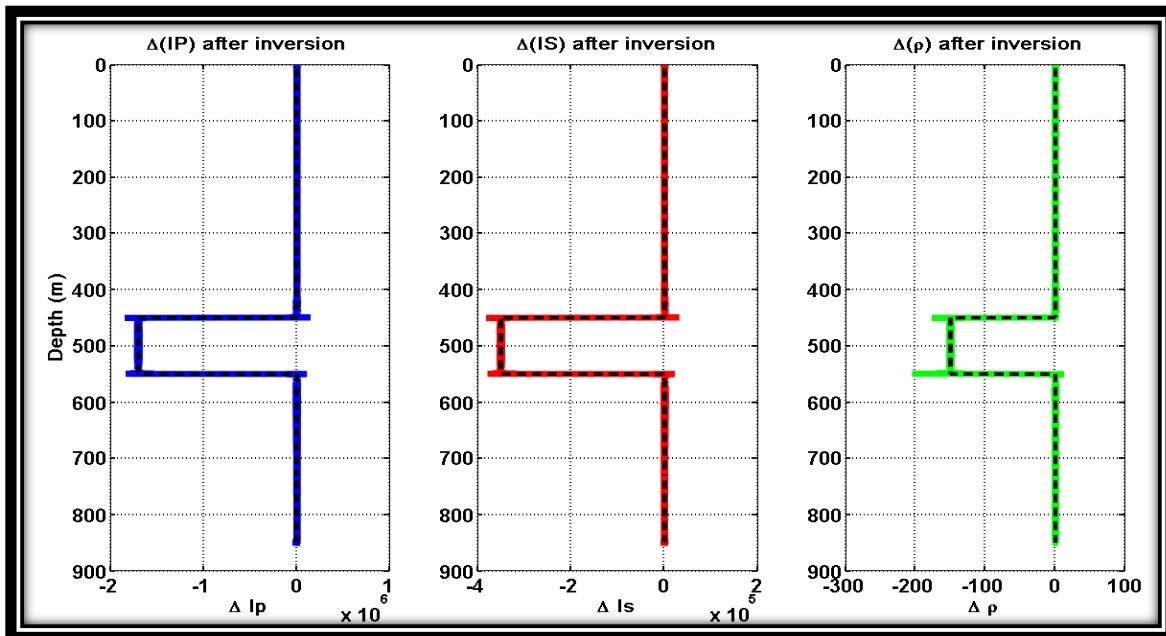


Figure 3.16: Elastic parameter changes ( $\Delta IP$ ,  $\Delta IS$  and  $\Delta \rho$ ) of the time-lapse model after adding low frequency. Embedded graphs in bold black dotted lines represent actual elastic parameter changes calculated from logs.

### 3.4.1.2 Inversion for elastic attributes of base line ( $\mathbf{m}_0$ ) and time-lapse changes ( $\Delta\mathbf{m}$ )

Inverting for the elastic model parameters of base line,  $\mathbf{m}_0$ , and time-lapse reflectivity changes ( $\Delta\mathbf{m}$ ) requires that model parameters of the monitor survey,  $\mathbf{m}_1$ , be expressed as ( $\mathbf{m}_1 = \Delta\mathbf{m} + \mathbf{m}_0$ ), and then substitute into equation (3.11) yields the following:

$$G_1(\Delta\mathbf{m} + \mathbf{m}_0) - G_0\mathbf{m}_0 = \Delta\mathbf{d} \quad 3.16$$

By re-arranging the above equation, the inverse equation used to invert for base model parameters and time-lapse change can be written as follows:

$$\Delta G\mathbf{m}_0 + G_1\Delta\mathbf{m} = \Delta\mathbf{d} \quad 3.17$$

In augmented matrix notation, the cost functions of equations (3.7) and (3.8) to jointly invert for the model parameters of base line,  $\mathbf{m}_0$ , and time-lapse reflectivity parameters changes,  $\Delta\mathbf{m}$ , is written as follows:

$$J(\mathbf{m}_0, \Delta\mathbf{m}) = \left\| \begin{bmatrix} \Delta G & 0 \\ 0 & G_1 \end{bmatrix} \begin{bmatrix} \mathbf{m}_0 \\ \Delta\mathbf{m} \end{bmatrix} - \begin{bmatrix} \mathbf{d}_0 \\ \mathbf{d}_1 \end{bmatrix} \right\|^2 + \left\| \begin{bmatrix} \lambda^2 R_0^T R_0 & 0 \\ 0 & \lambda^2 R_1^T R_1 \end{bmatrix} \begin{bmatrix} \mathbf{m}_0 \\ \Delta\mathbf{m} \end{bmatrix} \right\|^2 \quad 3.18$$

$G_1$  is the forward operator for ray-traced coefficients of the monitor survey,  $\Delta G$  and is same operator explained earlier in equation 3.14a. Note the difference in laying out seismic data of baseline and monitoring surveys compared to the arrangement of input seismic data vintages given in equation 3.14.

The  $\mathbf{m}_0$  and  $\Delta\mathbf{m}$ , are respectively, reflectivity model parameters for the baseline line and change of model parameters attributes between baseline and monitor surveys, and are given by:

$$m_1 = [(\frac{\Delta I}{I})_{base}, (\frac{\Delta J}{J})_{base} \text{ and } (\frac{\Delta \rho}{\rho})_{base}] \quad 3.18a$$

$$\Delta m = [\Delta(\frac{\Delta I}{I}), \Delta(\frac{\Delta J}{J}) \text{ and } \Delta(\frac{\Delta \rho}{\rho})] \quad 3.18b$$

Figures (3.17) and (3.18) show inverted elastic parameters (**IP**-impedance, **IS**-impedance and  $\rho$ ) for the baseline and monitor surveys, while Figure (3.19) shows the change in elastic parameters  $[\Delta(\text{IP}), \Delta(\text{IS}) \text{ and } \Delta\rho]$  as a result of the inversion of total differences using equation (3.17) after adding low frequency components from well logs. The resulting graphs from the time-lapse AVO inversions match the actual elastic parameters estimated from well logs.

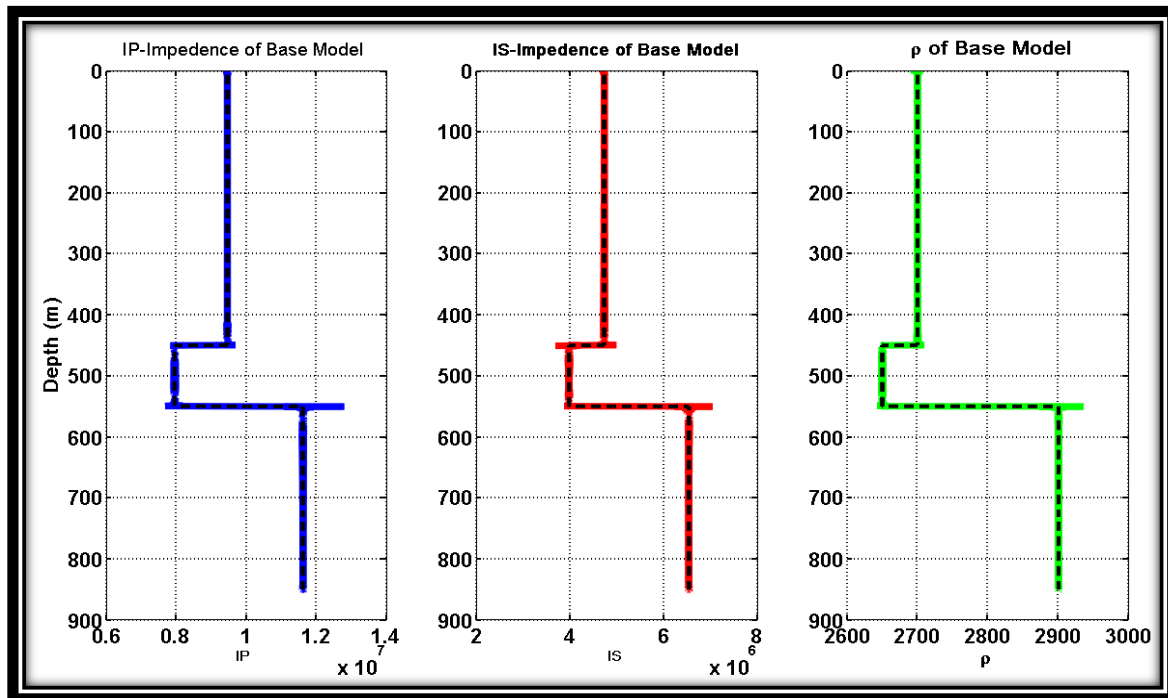


Figure 3.17: Elastic parameters (IP, IS and  $\rho$ ) of the *base* survey model using equation (3.17) after adding low frequency. Embedded graphs in bold black dotted lines represent actual (IP, IS and  $\rho$ ) calculated from logs.

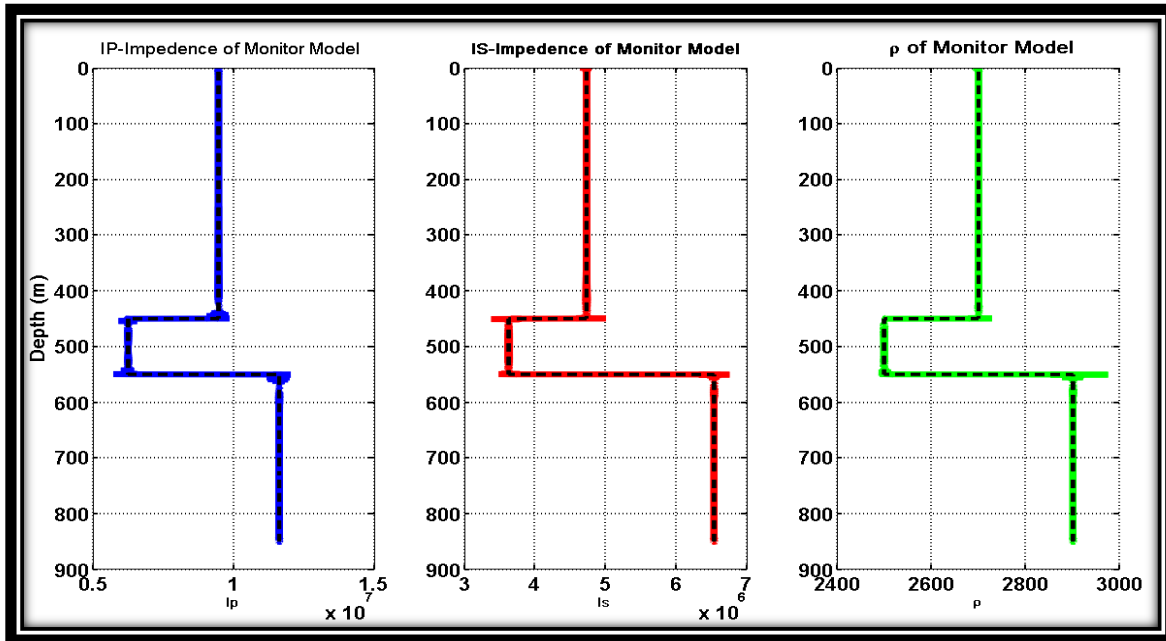


Figure 3.18: Elastic parameters (IP, IS and  $\rho$ ) of the *monitor* survey model using equation (3.17) after adding low frequency. Embedded graphs in bold black dotted lines represent actual (IP, IS and  $\rho$ ) calculated from logs.

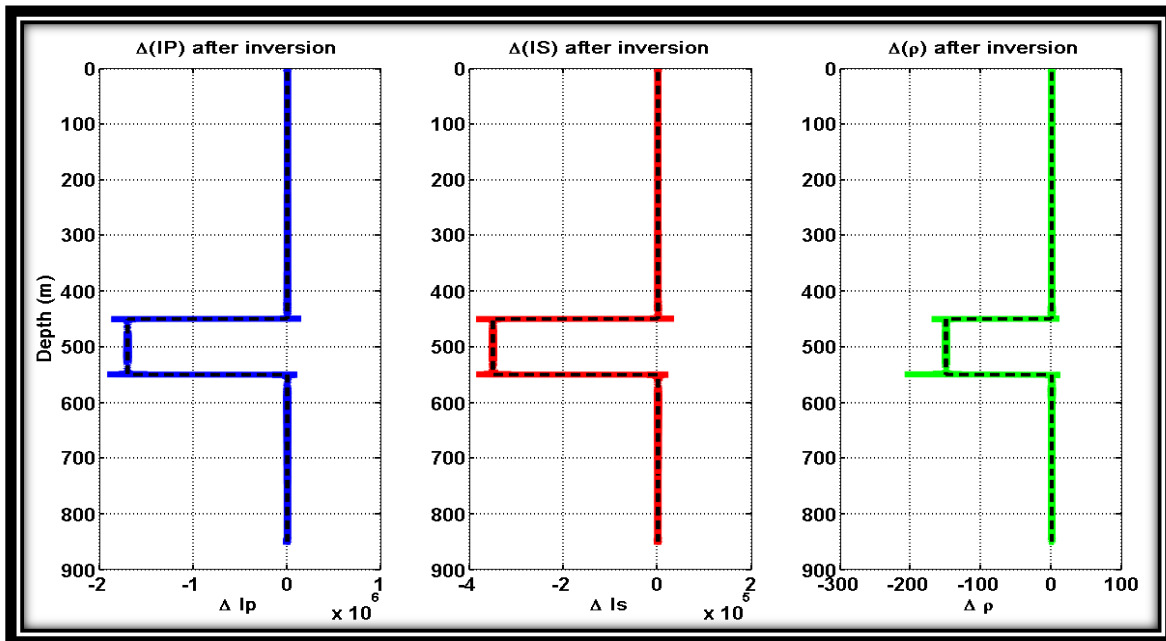


Figure 3.19: Elastic parameters changes ( $\Delta IP$ ,  $\Delta IS$  and  $\Delta \rho$ ) of the *time-lapse* survey model using equation (3.17) after adding low frequency. Embedded graphs in bold black dotted lines represent actual (IP, IS and  $\rho$ ) calculated from logs.

### 3.4.2 Inversion of seismic differences data ( $\Delta d$ ) only

When  $\Delta \mathbf{G} \approx \mathbf{0}$ , the time-lapse inversion equations (3.13) and (3.17) of total inversion of differences given in the previous section reduce to:

$$\mathbf{G}_0 \Delta \mathbf{m} = \Delta \mathbf{d} \quad 3.19$$

$$\mathbf{G}_1 \Delta \mathbf{m} = \Delta \mathbf{d} \quad 3.20$$

Thus, we are inverting for  $\Delta \mathbf{m}$  using difference of data  $\Delta \mathbf{d}$ . Time-lapse inversion of differences data only is a quick inverse scheme used to estimate the change in elastic model parameters. This method is based on the assumption that, at a specific depth interval, if there is a change in time-lapse seismic amplitude  $\Delta d$ , this will yield a change in the estimated  $\Delta \mathbf{m}$ . However, if there is no change in  $\Delta d$ , then  $\Delta \mathbf{m} = \mathbf{0}$ . The least-squares inversion equation for inverting of seismic differences only can be written as

$$(\mathbf{G}_i^T \mathbf{G}_i + \lambda \mathbf{W}_i^T \mathbf{W}_i) \Delta \mathbf{m} = \Delta \mathbf{d} \quad 3.21$$

where  $\Delta \mathbf{m} = \Delta(\frac{\Delta I}{I})$ ,  $\Delta(\frac{\Delta J}{J})$  and  $\Delta(\frac{\Delta \rho}{\rho})$  and  $\Delta \mathbf{d}$  is the difference in seismic data vintages. Note that the forward operator,  $\mathbf{G}_i$  can be either ray-trace coefficients of base or monitor surveys. Figure (3.20) shows model parameter changes  $[\Delta(\frac{\Delta I}{I})$ ,  $\Delta(\frac{\Delta J}{J})$  and  $\Delta(\frac{\Delta \rho}{\rho})]$  from inverting time-lapse seismic data using equation (3.21), while Figure (3.21) shows elastic model changes ( $\Delta(\text{IP})$ ,  $\Delta(\text{IS})$  and  $\Delta \rho$ ) after adding low frequency components of elastic models. Note that inverted

elastic parameter changes are consistent with actual parameter changes calculated from well logs.

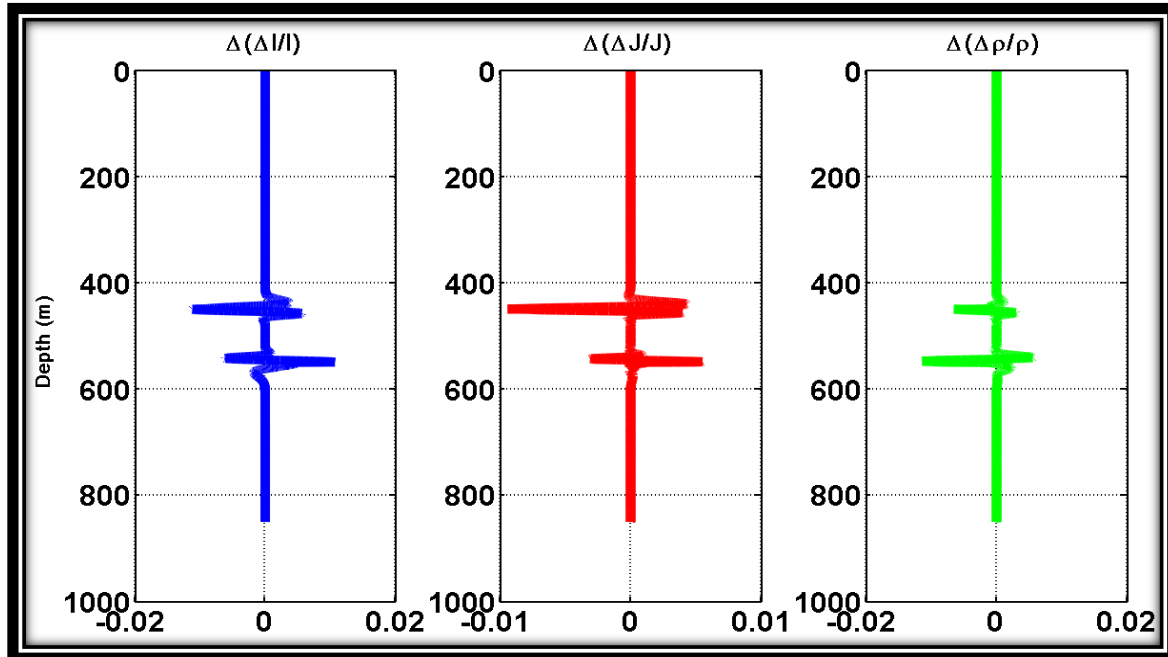


Figure 3.20: Estimated model parameters changes  $[\Delta(\frac{\Delta I}{I}), \Delta(\frac{\Delta J}{J})$  and  $\Delta(\frac{\Delta R}{R})]$  from an inversion of data differences (equation 3.21) before adding low-frequencies from logs.

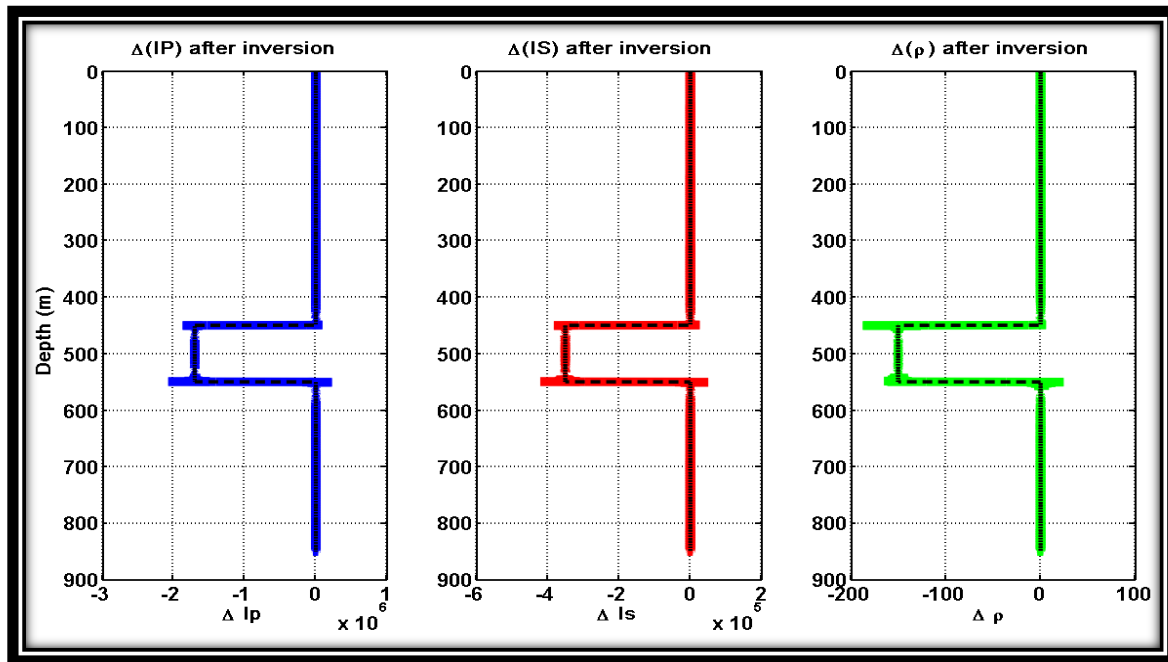


Figure 3.21: Estimated attribute changes [ $\Delta(IP)$ ,  $\Delta(IS)$  and  $\Delta\rho$ ] from inversion of data differences (equation 3.21) after adding low-frequencies from logs.

In real time-lapse seismic data, it is almost impossible to get seismic differences  $\Delta d = 0$  at a specific depth interval. However, we would rather have very slight changes in amplitude that are not necessarily related to changes in fluid properties.

The unexpected small changes in amplitudes in time-lapse seismic sections can be attributed to geometry difference between time-lapse surveys, random noise, or even processing and conditioning differences. Therefore, a *cut-off* point can be set such that seismic differences,  $\Delta d$ , falling below that *cut-off* point will be set to zero. Thus, manipulated differences of seismic amplitudes,  $\Delta d$ , would be more representative of fluid change.

### ***3.4.3 Sequential reflectivity-constrained inversion***

In geophysical inversion, constraints can be included into inversion problems so as to refine estimated model parameters; thus producing more realistic inverted earth models. Geophysical constraints can be incorporated in either data space (Bube and Langan, 1997; Saeed et. al., 2010b) or in model spaces (Ajo-Franklin et. al., 2007; Saeed et al., 2010a) or in both space domains, which is often called blocky inversion (Claerbout, and Muir, 1973).

In the Pikes Peak seismic surveys, noise is noticeable and affects most shot gathers of the monitoring seismic survey (H-2000), compared to the baseline seismic survey, (H-1991). The source of noise is due to jack pumps that were operating during the course of seismic data acquisition. Therefore, In order to simulate the effect of jack pump noise in a time-lapse model, small random noise of 0.1% were added to synthetic data of the base line (Figures 3.22 and 3.23), while 1% of random noise was also added to the monitoring model (Figures 2.24 and 2.25).

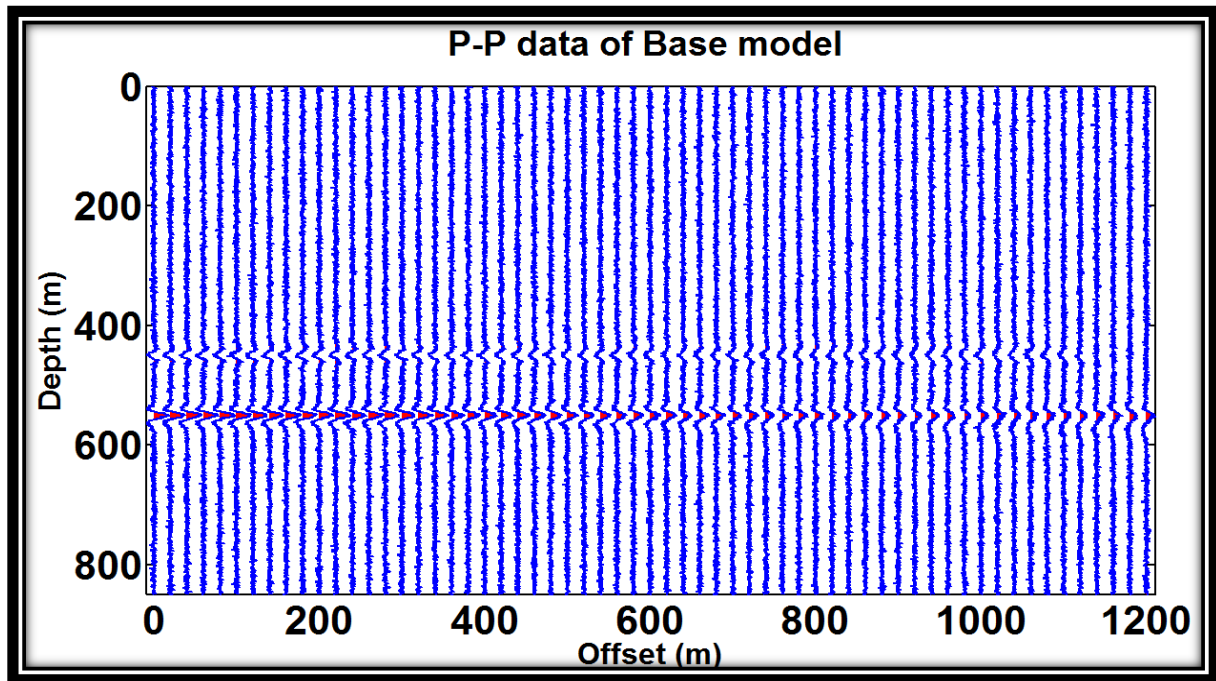


Figure 3.22: **P-P** synthetic seismic data for the base model with 0.1% random noise added.

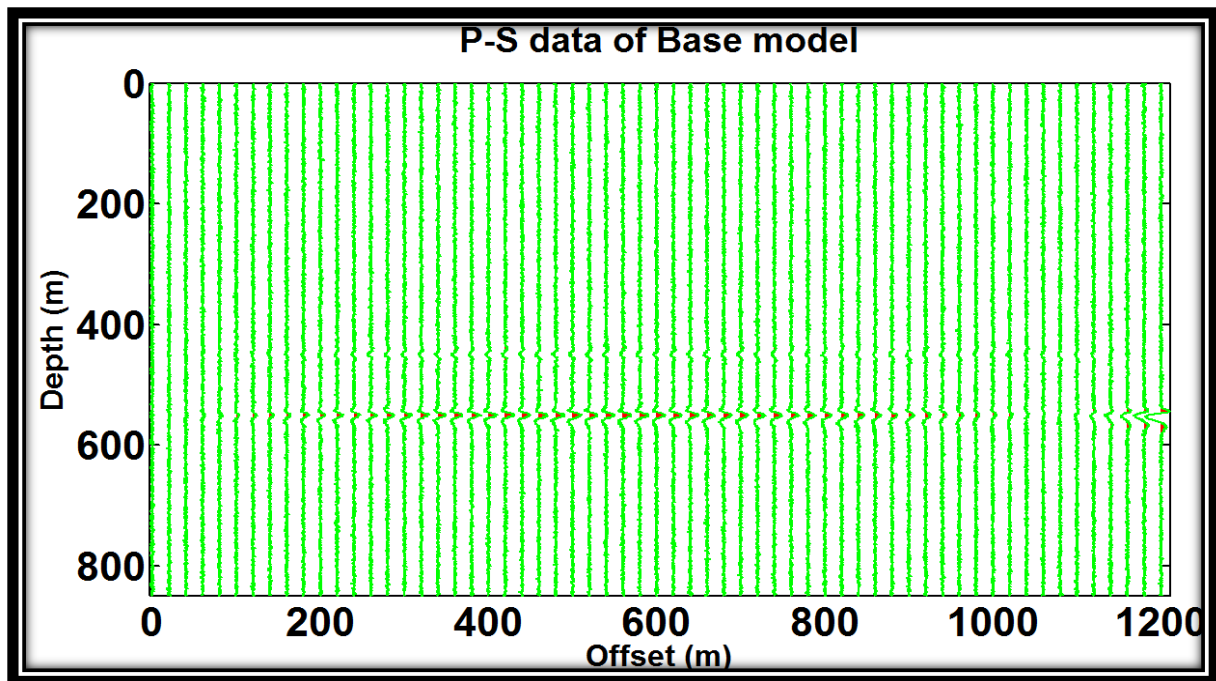


Figure 3.23: **P-S** synthetic seismic data for the base model with 0.1% random noise added.

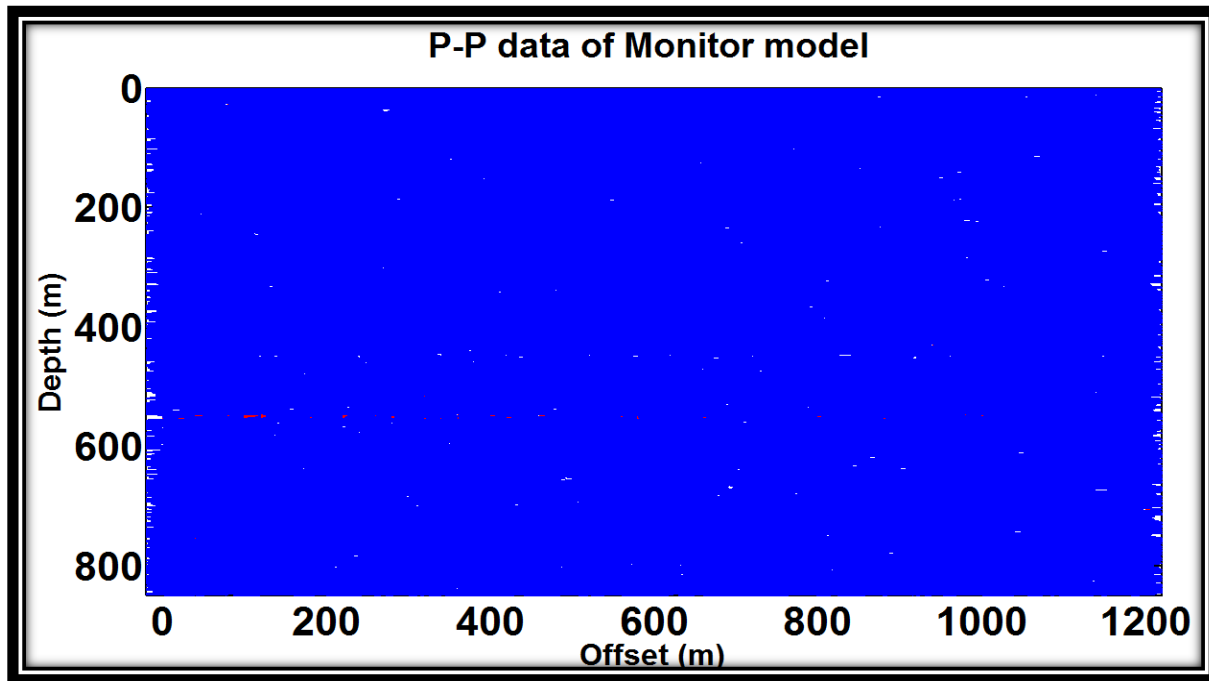


Figure 3.24: P-P synthetic seismic data for the monitor model with 1% random noise added.

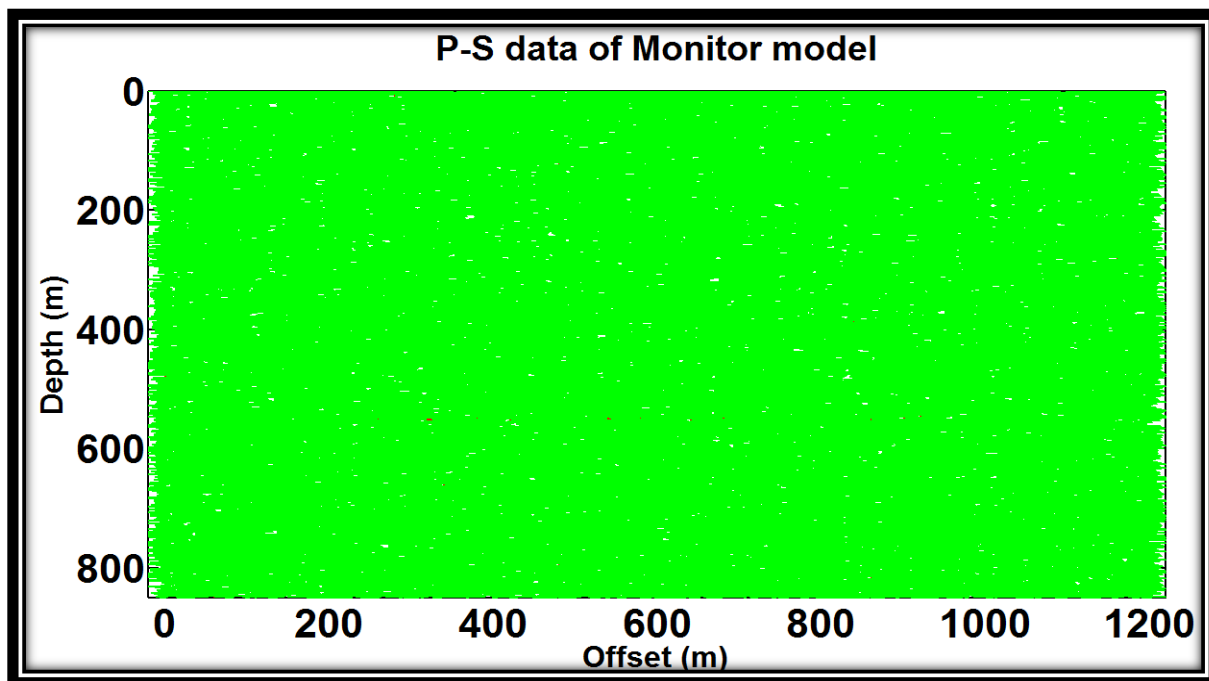


Figure 3.25: P-S synthetic seismic data for the monitor model with 1% random noise added.

The *sequential reflectivity-constrained inversion* given in equation (3.22) is one form of a robust time-lapse inversion method whereby estimated model parameters of a base survey are used to constrain inversion of a monitoring model to ensure smooth variation in estimated elastic parameters of the monitoring model. The inverse problem is given by:

$$[(G^T G + \lambda_1 W_m^T W_m + \lambda_2 V^T V)]m_i = [G^T d + \lambda_2 V^T V(m_{i-1}^M - m_0^B)^T] \quad 3.22$$

where  $V_{monit.} = diag[abs(m_{i-1}^M - m_0^B)]$

The estimated model parameters of the baseline survey will act as prior information in the inversion of the monitoring survey. Because  $V$  and  $(m_{i-1}^M - m_{i-1}^B)^T$  are functions of unknown *base- and monitor- model parameters*, an iterative approach must be used. This is referred to as iteratively re-weighted least squares, IRLS, (Wolke and Schwetlick, 1988).

In equation (3.22), we set  $V$  and  $(m_{i-1}^M - m_{i-1}^B)^T = \mathbf{I}$  for the first iteration, which resulted in a traditional least squares solution. The estimation of  $m_i^B$  for  $i=1$  is then subsequently substituted in equation (3.22) to obtain new  $m_{i+1}^M$ . The procedure is repeated until the estimated model parameters of the monitoring survey between successive IRLS iterations become less than tolerance value,  $\tau$  given in convergence limit equation (3.23)by:

$$J(m) = \frac{\|m^{k+1} - m^k\|_2}{1 + \|m^{k+1}\|_2} < \tau \quad 3.23$$

Note that equation (3.22) can be implemented using two other scenarios that require more time computation and cycles of iteration calculations. These implementation options are:

- Perform IRLS inversion for the baseline survey first where elastic attributes are further refined. Then the final refined model parameters are used as prior information in equation (3.23).
- Implement sequential IRLS inversion for both the baseline and monitor surveys where refined model parameters are used as prior information in equation (3.23).

In Figure (3.26), inverted elastic impedances for the monitoring model using reflectivity-constrained inverse scheme is matching actual impedances fairly well in the presence of noise. Figure (3.27) shows regularization parameter during the inversion, while the RMS error (Figure 3.28) during inversion shows convergence of the program towards the final solution after 5 iterations.

In order to test the stability and reliability of the resulting elastic parameters in the presence of a high percentage of noise, random noise of a magnitude that is 10 fold the noise used before for the monitoring survey is added. Figure (3.29) shows elastic impedances of the monitoring model after inversion. As expected, P-impedance is less affected by noise, while S-impedance and density are influenced by excessive added noise. This experiment assists in deciding which reflectivity attribute is to be constrained, and also what percentage use of a reflectivity attribute of the base survey should be utilized in constraining inverted model parameters of the monitor model.

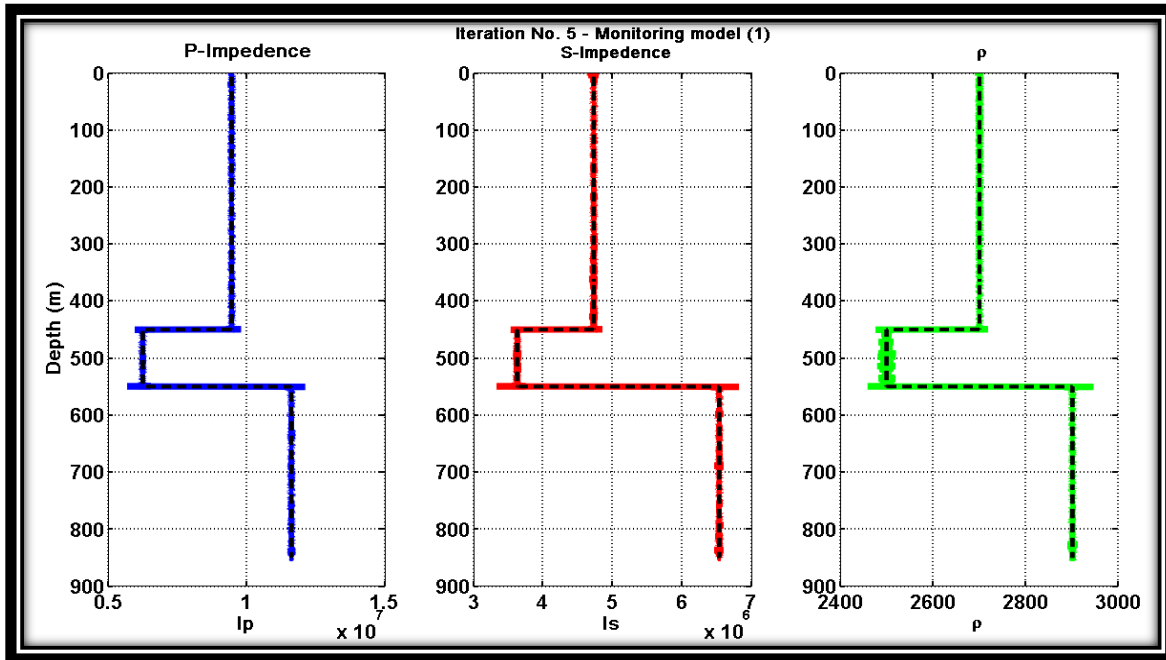


Figure 3.26: Elastic parameters ( $I_p$ ,  $I_s$  and  $\rho$ ) using sequential reflectivity-constrained inversion of the noisy (0.01) monitor model after adding low frequencies from logs.

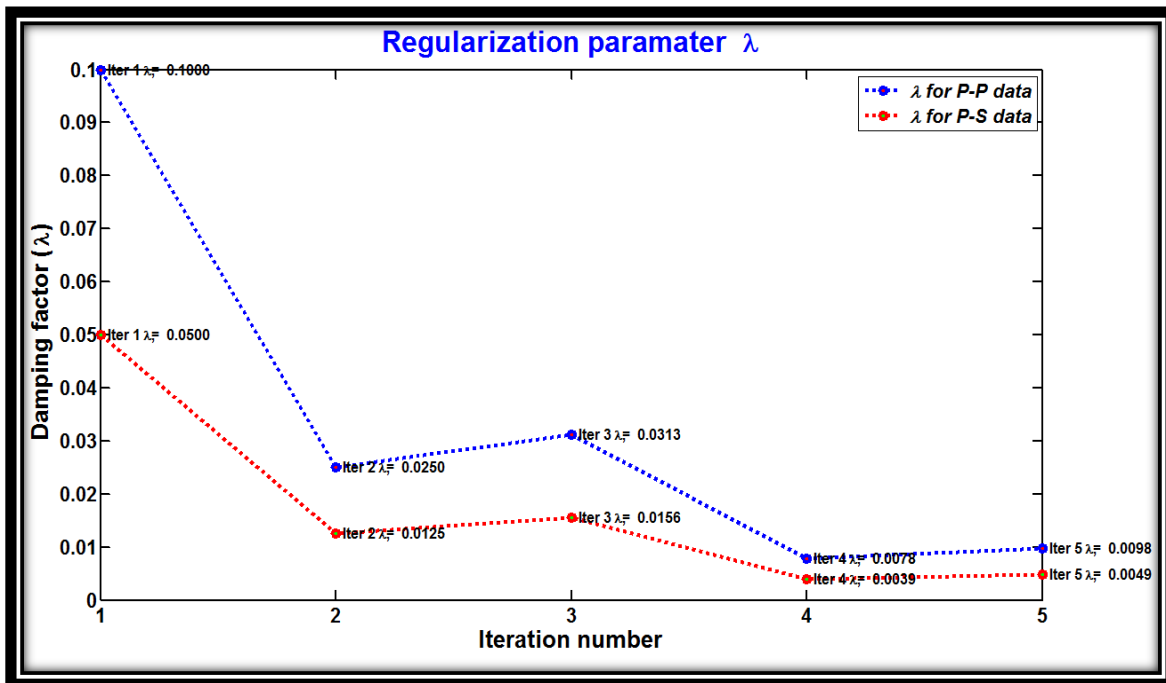


Figure 3.27: Regularization parameter during a reflectivity-constrained Inversion.

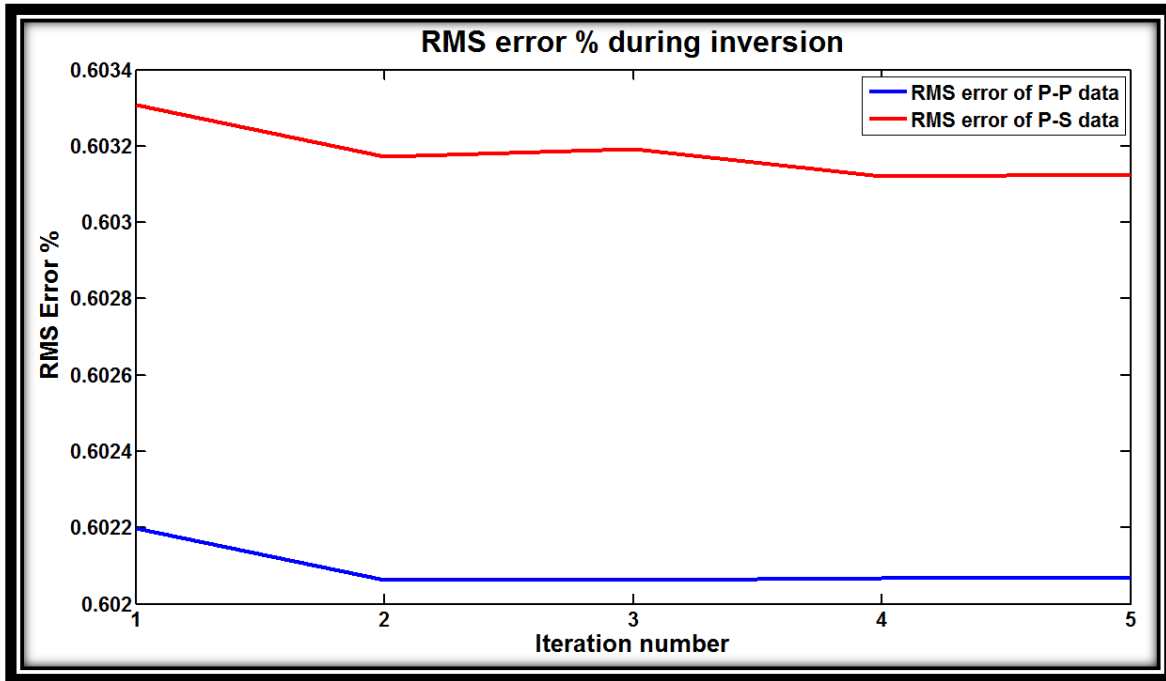


Figure 3.28: The RMS error during reflectivity- constrained Inversion scheme.

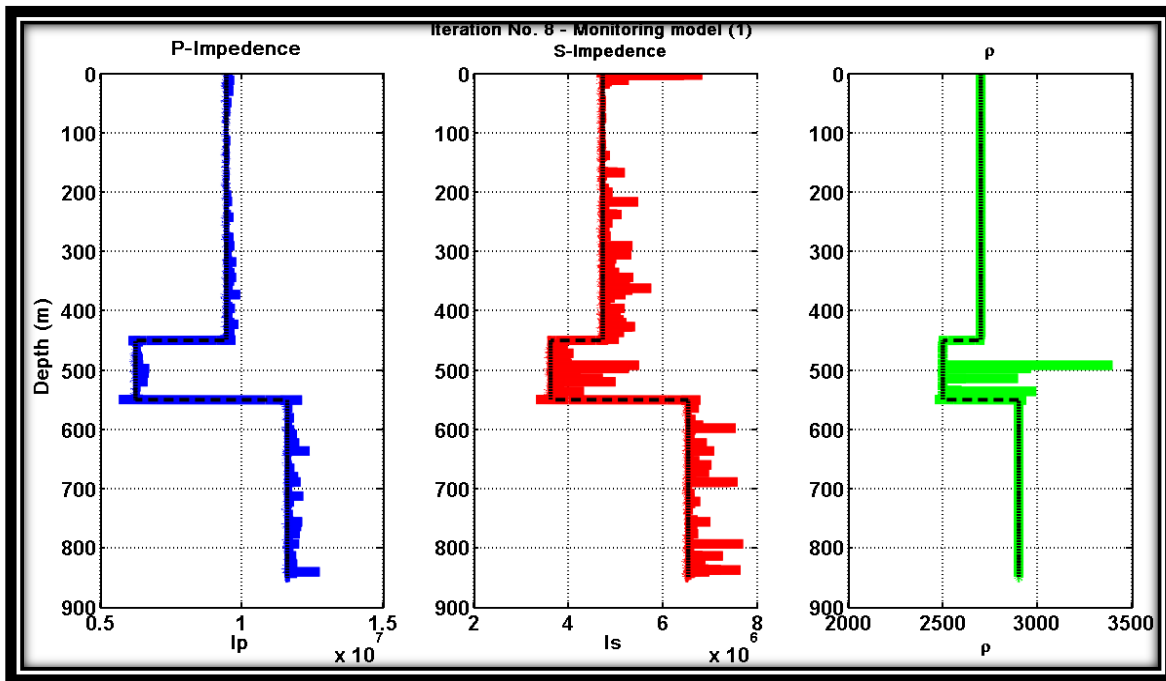


Figure 3.29: Elastic parameters ( $I_P$ ,  $I_S$  and  $\rho$ ) using sequential reflectivity-constrained inversion of the noisy (10 times amount of noise in Figure 22) monitor model after adding low frequency.

### **3.5 Conclusions**

The amplitude variation with angle produces information about rock interfaces only, and assists in setting survey parameters for field data acquisition, and deciding the volume of synthetic data to be used in seismic inversion as well. Analysis of amplitude variation with angle (AVA) does not experience polarity reversal for a given angle range of a time-lapse model.

Three different inverse schemes for time-lapse AVO inversion are developed in this thesis. Inverted elastic impedances from proposed inverse schemes are in agreement with actual elastic impedances calculated from well logs. Although the total inversion of difference and inversion of seismic differences data ( $\Delta d$ ) only have given same result, however, total inversion of difference scheme would provide more accurate result when implemented using real seismic data. The sequential reflectivity-constrained inversion was introduced as form of robust AVO inversion. Therefore, it cannot be compared with other two inversion schemes.

The developed codes were optimized to perform inversion in less time, and have shown fast convergence with a minimal number of iterations for robust time-lapse AVO inversion. Results from inverting noisy data can assist in choosing appropriate reflectivity attributes of a base model to be used in constraining the inversion of a monitor survey.

## Chapter Four: **SEISMIC DATA PROCESSING OF THE PIKES PEAK TIME-LAPSE SURVEYS**

### **4.1 Introduction**

Time-lapse seismic surveys, often referred as “4D seismic”, involve repeated 3D seismic surveys carried out periodically over a reservoir to image the movement of hydrocarbon fluids (Lumley, 1995). Other application include the optimization of production by precise placement of injector wells, monitoring of CO<sub>2</sub> flooding and sequestration (Kendall et al., 2003), identification of bypassed reserves and diagnosing inefficiencies in the reservoir production process.

A good time-lapse processing of seismic vintages is essential to eliminate noise, and enhance 4D repeatability (Johnston et. al., 1998). As a result, time-lapse models for the reservoir are constructed and updated using time-lapse seismic surveys along with other engineering data from well logs. The model is often updated using reservoir production history to calibrate unpredicted changes in reservoir attributes using forward modeling and seismic inversion results.

In the following sections, a description of the time-lapse survey for the Pikes-Peak oil field is given. This is followed by a detailed seismic data processing flow designed for time-lapse and imaging purposes. Noise attenuation by modelling that was implemented to attenuate pump-jack noise, ground roll and air blast is also given. Comparisons between surface consistent deconvolution in time and frequency domains are provided. Seismic images from pre-stack time imaging using phase shift plus interpolation are explained.

### **4.2 Time-lapse seismic surveys for the Pikes Peak heavy oil field**

Time-lapse seismic surveys are usually categorized, based on objectives, as a legacy survey, re-shoot survey, and 4D surveys (Lumley et. al., 2003). Optimum time-lapse seismic surveys

require using the same field data acquisition geometry over lapsed time to eliminate spurious artifacts in seismic images due to differences in used source wavelet and acquisition geometry parameters. However, such acquisition conditions are not often the ideal scenario for which a legacy seismic survey was carried out. Indeed, this is the case for the Pikes Peak time-lapse surveys, as a baseline survey was acquired after twelve years of reservoir production, using different acquisition geometry parameters.

The time-lapse seismic surveys conducted at the Pikes Peak heavy oil field can be considered as a re-shoot survey. The two 2D seismic vintages used in this study were acquired nine years apart using different field seismic data equipment, sources and acquisition parameters. The 2D seismic line, H91-76S, which will be referred to in this thesis, as the baseline survey line, is one of several 2D swath lines acquired by Husky Energy in 1991. In order to study steam-driven effects in heavy oil over lapsed time, the University of Calgary and Husky Oil Energy, in 2000, acquired a repeat high resolution 3C-2D line, H00-131 (Hoffe et al., 2000). This line will be referred to as the monitor line survey.

The shot and receiver coordinates (Figure 4.1) shows that the 2D-lines from time-lapse surveys are approximately 8 m apart, but more importantly, they are different in length. The acquisition geometry parameters are also different for the time lapse surveys. Table 4.1 summarizes field survey acquisition parameters that are extracted from survey notes and EBCDIC headers of seismic raw gathers of the time-lapse survey for the Pikes Peak oil field.

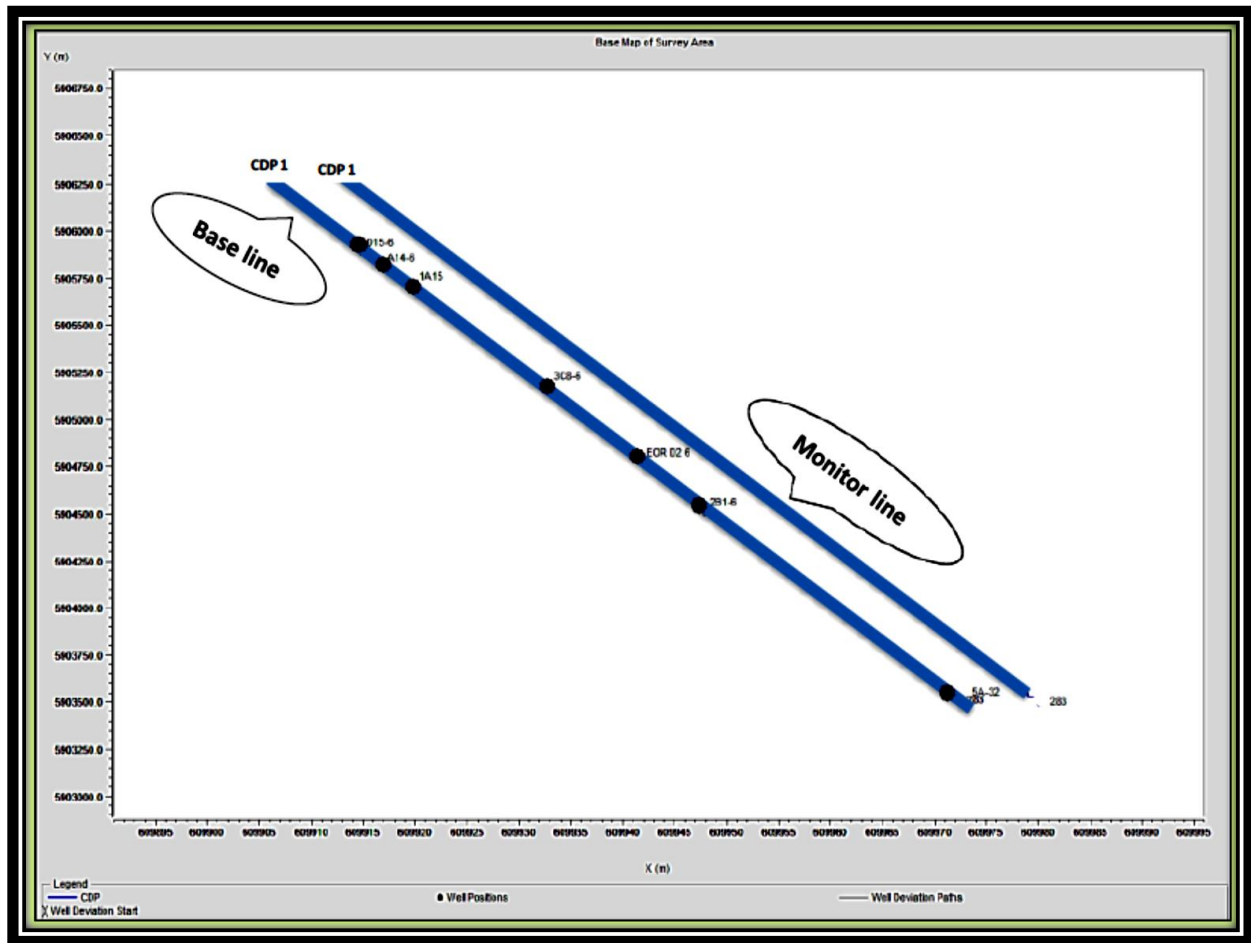


Figure 4.1: Base map view for the 2D time-lapse survey lines of the Pikes Peak oil field.

<b>Field data parameters</b>	<b>Base line survey ( H-1991)</b>	<b>Monitor line survey (H-2000)</b>
<b>Acquisition data</b>	<b>February 1991</b>	<b>March 2000</b>
<b>2D line length</b>	<b>2.8 Km</b>	<b>3.8 km</b>
<b>Source array</b>	<b>3 Vibes over 20m</b>	<b>2 Vibes over 20m</b>
<b>Sweep drag length</b>	<b>10 m</b>	<b>No drag</b>
<b>Sweep length</b>	<b>6 sec</b>	<b>16 sec</b>
<b>Sweep bandwidth</b>	<b>8-110 Hz</b>	<b>8-150 Hz</b>
<b>Field filter</b>	<b>8-110 Hz</b>	<b>3-164 Hz</b>
<b>Geophone array</b>	<b>9 geophones over 20m</b>	<b>6 geophones over 20m</b>
<b>Source interval</b>	<b>40 m</b>	<b>20 m</b>
<b>Geophone Interval</b>	<b>20 m</b>	<b>20 m</b>
<b>CDP Fold</b>	<b>30</b>	<b>66</b>
<b>Maximum offset</b>	<b>1200 m</b>	<b>1320 m</b>

Table 4.1: Field acquisition parameters for the 2D time-lapse seismic surveys of the Pikes Peak heavy-oil field.

### **4.3 Seismic data processing flow for time-lapse and imaging**

A carefully designed time-lapse seismic processing and imaging flow for the Pikes Peak survey lines was established in order to remove spurious differences related to seismic acquisition, processing and near surface changes. The processing flow was calibrated and tested to meet AVO and time-lapse repeatability compliance. The key measures for the parallel processing flow lie in maximizing the repeatability of the 2D vintages, while improving temporal and spatial

resolution of pre-stack image sections of time-lapse surveys to monitor steam-related amplitude variations. The processing flow used for Pikes Peak is given as follows:

- Reformat (full data length & data integrity)
- Geometry assignment (verify 2D geometry database)
- Trace and shot edits
- Pre-decon noise attenuation
- Amplitude recovery (Gain recovery & spherical divergence correction)
- Refraction Statics calculation (GLI,GRM,DRM)
- Pre-decon Surface Consistent Amplitude Correction
- Deconvolution (Surface Consistent Five component Deconvolution)
- Noise suppression by modeling (Monitor line, H-2000 only)
- Post-decon Surface Consistent Amplitude Correction
- Apply datum and refraction statics (DRM)
- First pass of velocity analysis
- Surface Consistent Residual Statics (32ms correlation window)
- Second pass of velocity analysis (half the spacing of first pass for baseline, H-1991 only)
- Second Pass of Surface Consistent Residual Statics (16ms correlation window)
- Final Normal move out
- Trace and shot edits
- PSTM gathers preparation
- Pre Stack Time Migration (Phase Shift Plus Interpolation)
- Mute & Stack
- Filter & Scale (Stack sections only)

Note the time-lapse surveys of the Pikes Peak Oil field were processed using different processing software (Promax, Paradigm, and Divestco propriety software). After assigning geometries of both surveys, initial trace and shot editing were applied to remove dead traces, and clip abnormal amplitudes due to bad coupling and equipment malfunction.

The shot gathers of monitor survey line H-2000 are considerably affected by pump jack noise, as seismic data was acquired while oil production was in progress. Figure (4.2) shows a shot gather from the monitor line survey where noise from pump jacks affect a good part of the gather.

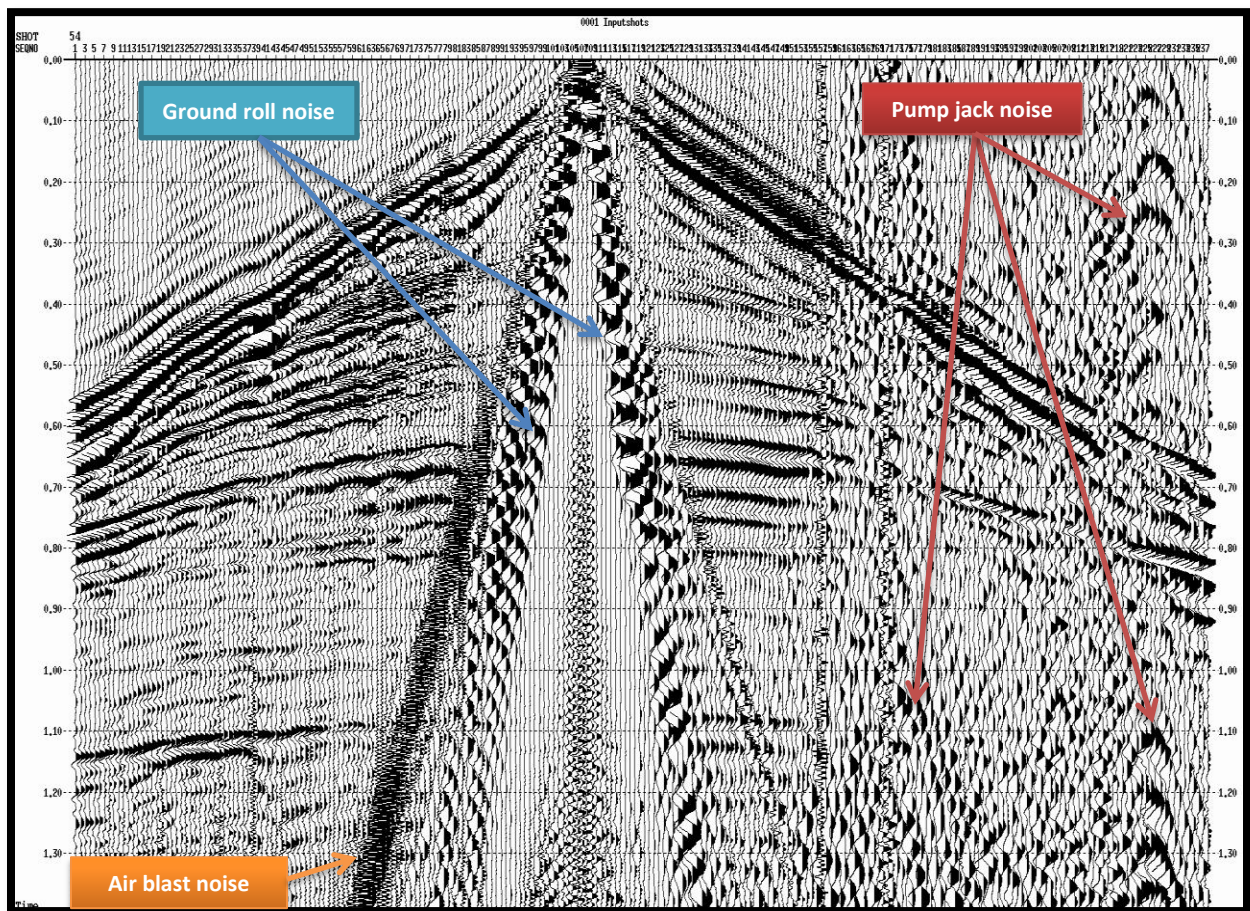


Figure 4.2: A shot gather from monitor line survey (H-2000) show noises related to pump jacks, ground-roll and air blast during seismic data acquisition of the 2D time-lapse survey lines of Pikes Peak oil field.

In the following subsections, descriptions of major steps are given. Note that some of processing steps will be grouped for an easier explanation and brevity.

#### ***4.3.1 Amplitude recovery and correction***

Amplitude recovery processes including gain correction and spherical spreading compensation (Ursin, 1990) were applied to raw data to compensate for noticeable energy loss at deeper parts of the shot gather. The main objective in this processing step is to move seismic energy from the shallow section of the raw gather, and then spread and balance the energy evenly across the shot gathers of the survey lines.

In order to meet the AVO compliance, surface consistent amplitude corrections are applied to raw data to compensate for acquisition geometry effects and near surface variation (which are non-geological amplitude anomalies) at the source and receiver locations. Furthermore, the surface consistent amplitude corrections remove stripe zones from shot gathers by spatially applying relative amplitude compensation that smooth sudden changes in amplitude, and produces a consistent amplitude-look for full offset in the shot gathers.

The surface-consistent amplitude correction is applied before and after deconvolution for the time-lapse survey of the Pikes Peak seismic data. The amplitude spectrum is decomposed into source, receiver, CDP and offset spectrum during the analysis stage. Surface consistent amplitude scaling is then applied to shot gathers using source and receiver spectrum components only. As expected, the magnitude of surface-consistent amplitude scaling is more visible before deconvolution compared to the same processing step after deconvolution.

### 4.3.2 Five-component surface consistent deconvolution

Surface-consistent processing of seismic data is normally applied in amplitude scaling, deconvolution, and residual statics. The basic concept behind surface-consistent processing for seismic data surveys is that any shot-related effects, in principle should affect all traces within a shot gather in the same way and are independent of their receiver position. In the same manner, receiver-related effects should also affect all traces within a receiver gather in the same way, and independent of their shot position.

In order to preserve relative amplitudes of reflectors while de-convolving seismic data, the five-component adaptive surface consistent deconvolution (Wang, 1992) is used in the processing of time-lapse seismic surveys of the Pikes Peak data. The algorithm is implemented in the frequency domain and compensates for the distortion in amplitude and phase spectra due to the presence of near surface irregularities and source –receiver coupling problem.

In the surface consistent five-component deconvolution, individual traces are decomposed into five components (assuming white reflectivity and noise is zero) in the least-square sense as:

$$x(t) = l(t) * s(t) * g(t) * h(t) * c(t) \quad 4.1$$

where  $l$  is the average survey line component spectrum,  $s/g/h/c$  are respectively, shot, geophone, offset and CMP component spectra.

In order to linearize the problem, component spectra are transformed to the frequency domain and by taking logarithm of amplitude spectra, equation (4.1) can be written as follows:

$$\ln[X(f)] = a_L \ln[L(f)] + a_S \ln[S(f)] + a_G \ln[G(f)] + a_H \ln[H(f)] + a_C \ln[C(f)] \quad 4.2$$

where  $a_L, a_G, a_H, a_C$  are the adaptive factors for the seismic trace. When the conventional surface consistency holds true, adaptive factors are all very close to unity (Wang, 1992).

The industry standard procedure for surface consistent deconvolution involves three stages:

- Spectral estimation
- Surface consistent analysis to compute decomposed components
- Operator application

The algorithm is a minimum phase spike-deconvolution which gives whiter spectra than the parametric auto regressive model deconvolution. For the sake of comparison, the four component surface consistent deconvolution (Cary and Lorentz, 1993) that was implemented in the time domain is also used. In this algorithm, a seismic wavelet is broken down into source, receiver, CMP and offset components.

The Pikes Peak seismic data were initially processed by Matrix Geo-services processing company (Hoffe et al., 2000). As a standard procedure in time domain deconvolution, a correlation analysis window was used to determine operator length. Figure (4.3) shows two experimental correlation analysis windows for the monitor line survey (H-2000); one with an operator length of 60 msec to match the same operator length used by Matrix Geo-services processing company, while the another window is for an operator length of 85 msec. In designing operator length, amplitude spectra and brute stacks resulted from deconvolution test are also used as key guides for determining optimum operator length. In this study, an operator length of 85 msec is used, and the resulting amplitude spectra were then compared with amplitude spectra of five-component surface consistent deconvolution.

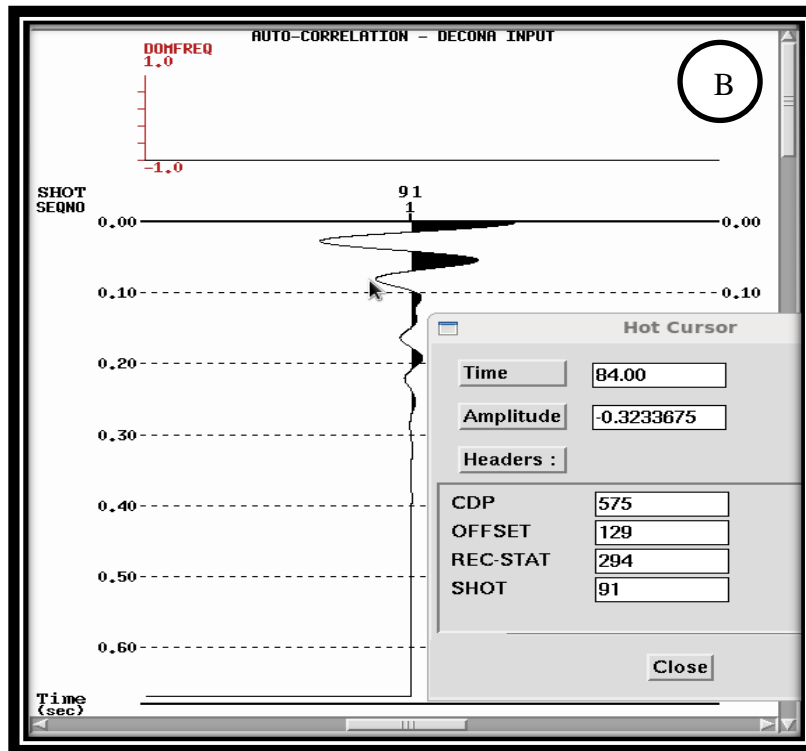
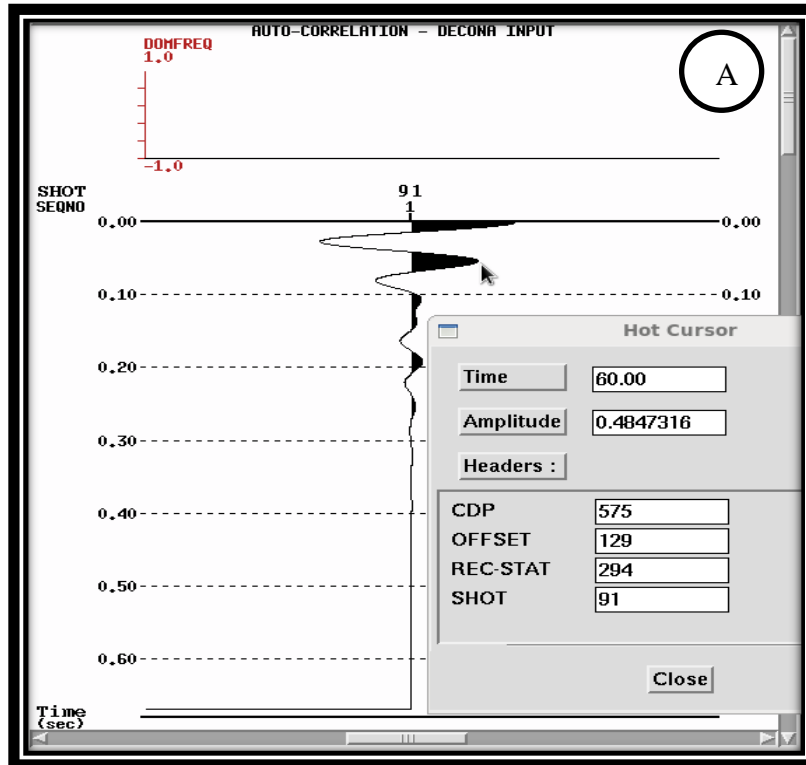


Figure 4.3: Correlation analysis window to determine operator length for time-domain deconvolution. (A) Window length of 60msec, while (b) has an operator length of 85msec.

Figure (4.4a) shows the amplitude spectrum of four-component surface-consistent deconvolution that is implemented in the time-domain for the monitor line (H-2000), while Figure (4.4b) is for the five component surface-consistent deconvolution, which is implemented in the frequency domain. The five-component decon has produced a broad amplitude spectrum compared to the four-component surface consistent deconvolution.

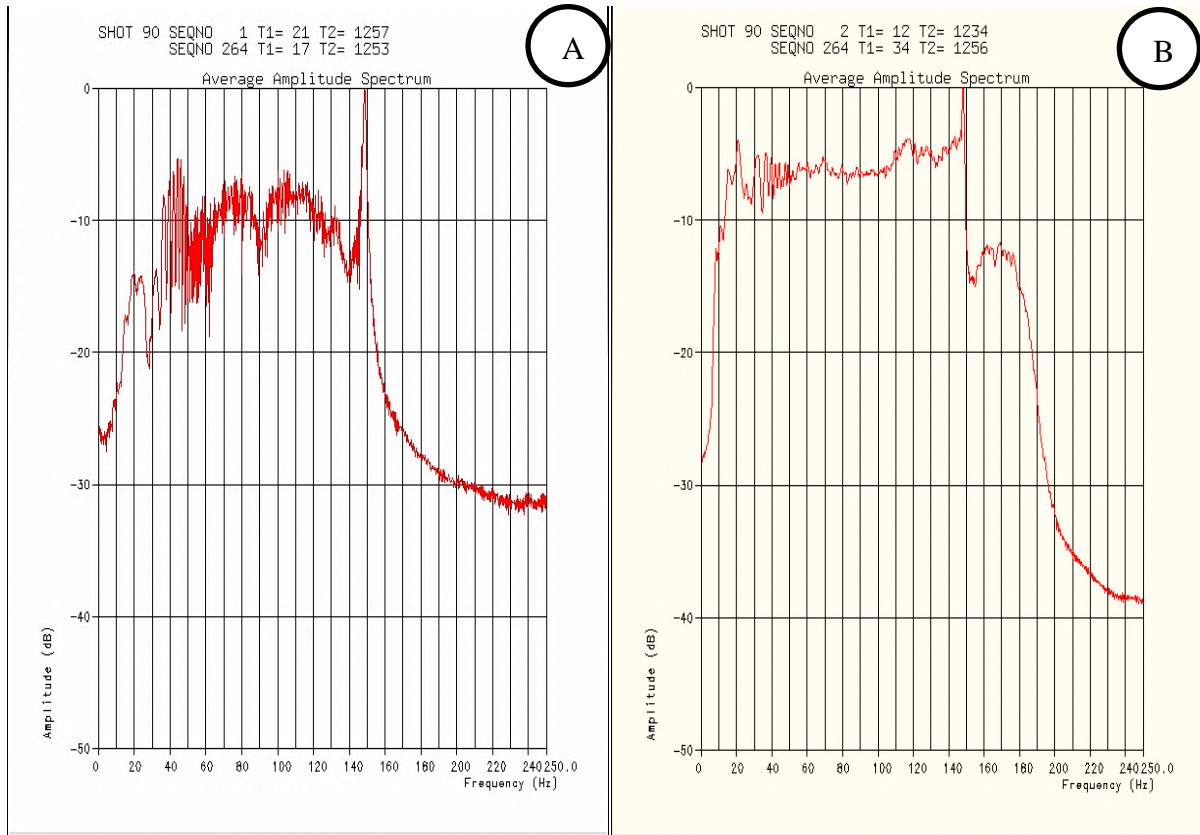


Figure 4.4: (A) Spectral analysis form using four component surface-consistent spike deconvolution, while (B) from using five component surface-consistent deconvolution.

Thus, the five components surface-consistent deconvolution is used in deconvolving time-lapse seismic data of the Pikes Peak. In the analysis stage, seismic traces are decomposed to five components, while application of the operator involved the line, source and receiver components only. The deconvolution algorithm has improved lateral wavelet stability in stack sections and has also increased frequency bandwidth of the deconvolved data.

Figures (4.5) and (4.6) respectively, show spectral analyses for a shot, before and after, applying five components surface-consistent deconvolution for the base and monitor lines of the time-lapse survey of Pikes Peak. The frequency contents in both figures have been broadened in both surveys. Note that, the red curve represents average amplitude spectra for the displayed shot gather, while spectra in magenta colors in the background are for all traces in the shot gather. The spike at the end of the frequency spectrum of the shot gather of the monitor survey is related to the design of a taper zone of the sweep during field data acquisition. Furthermore, the deconvolution operator did also boost noise signal beyond sweep frequency limit (i.e., at 175Hz). However, the frequency content of monitor line will be balanced to match frequency content of base line survey in the time-lapse regularization process.

Another advantage of the five component surface-consistent deconvolution is to leverage against noise. The surface consistent noises are identified in the analysis of surface consistent spectral solutions stage and isolated by their corresponding noise spectra (Wang et. al., 2000). These statistical noise components are then removed from the spectra of the input data.

Figure (4.7a) shows an original shot gather from the monitor line survey where pump jack noise, ground-roll and air blast mask reflectors in the middle of the gather. These noises are further attenuated after deconvolution (Figure 4.7b) where the continuity of reflectors can be clearly recognized in the middle of the deconvolved shot gather.

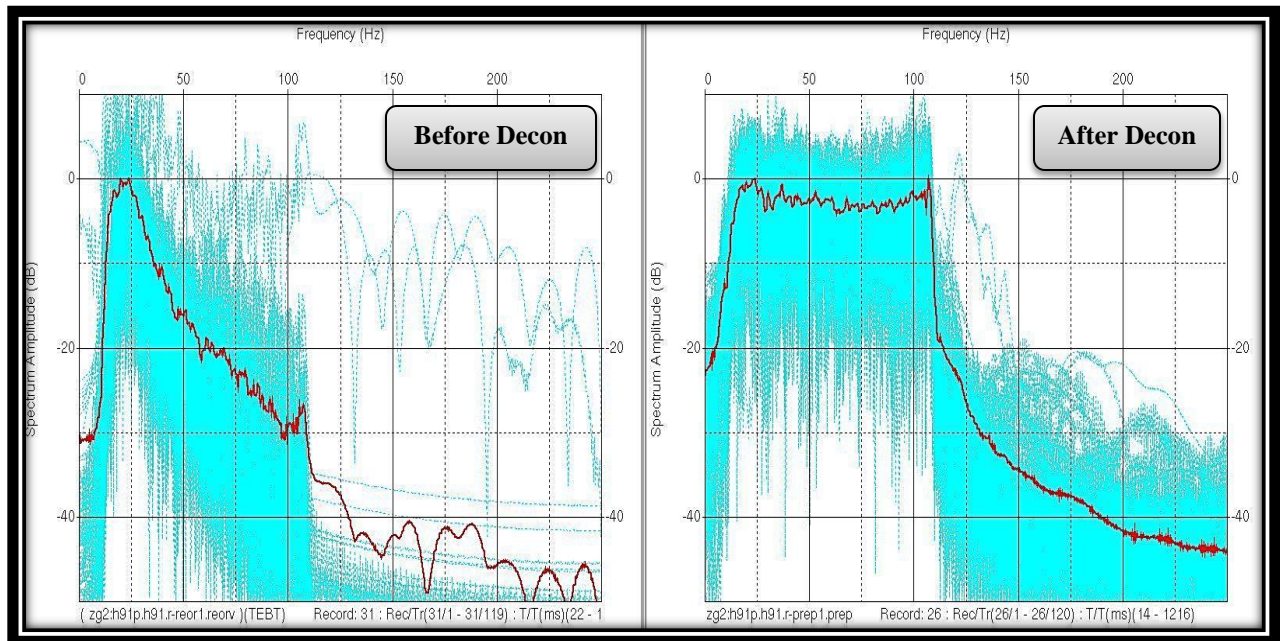


Figure 4.5: Spectral analysis of a shot gather- from the **baseline H-1991**. Left: Spectral analysis before Decon. Right: Spectral Analysis after applying five-component surface consistent deconvolution.

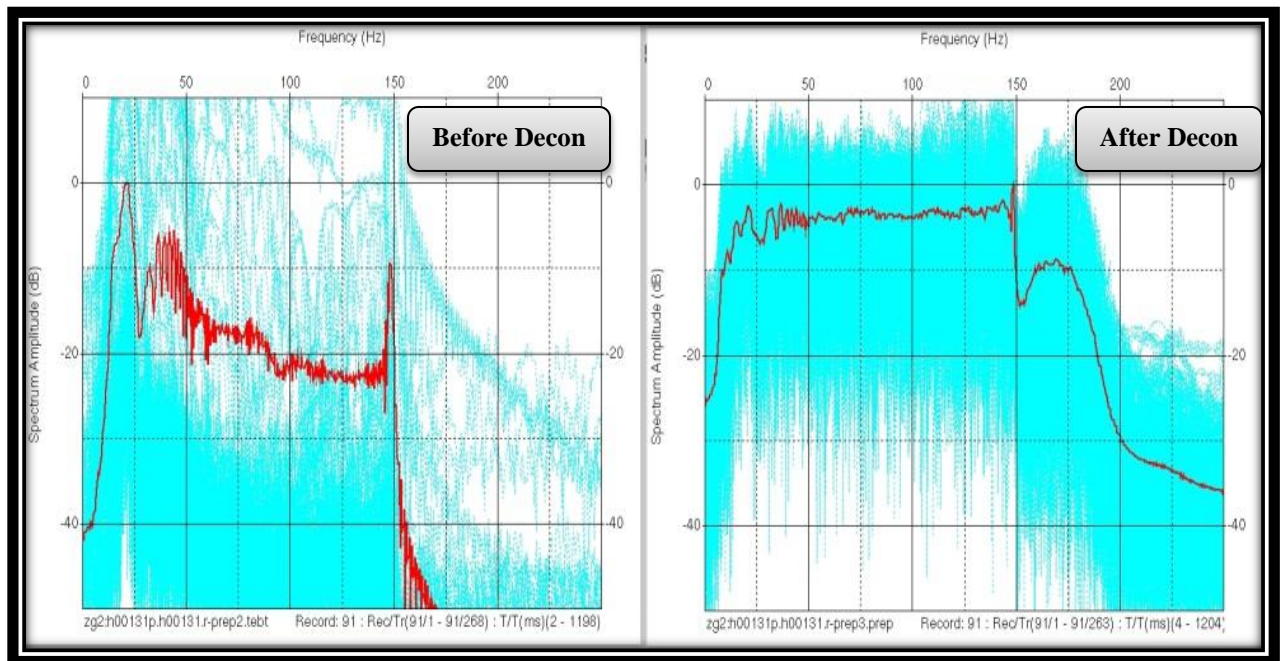


Figure 4.6: Spectral analysis for a shot gather- from the **monitor line H-2000**. Left: Spectral analysis before Decon. Right: Spectral analysis after applying five-component surface consistent deconvolution.

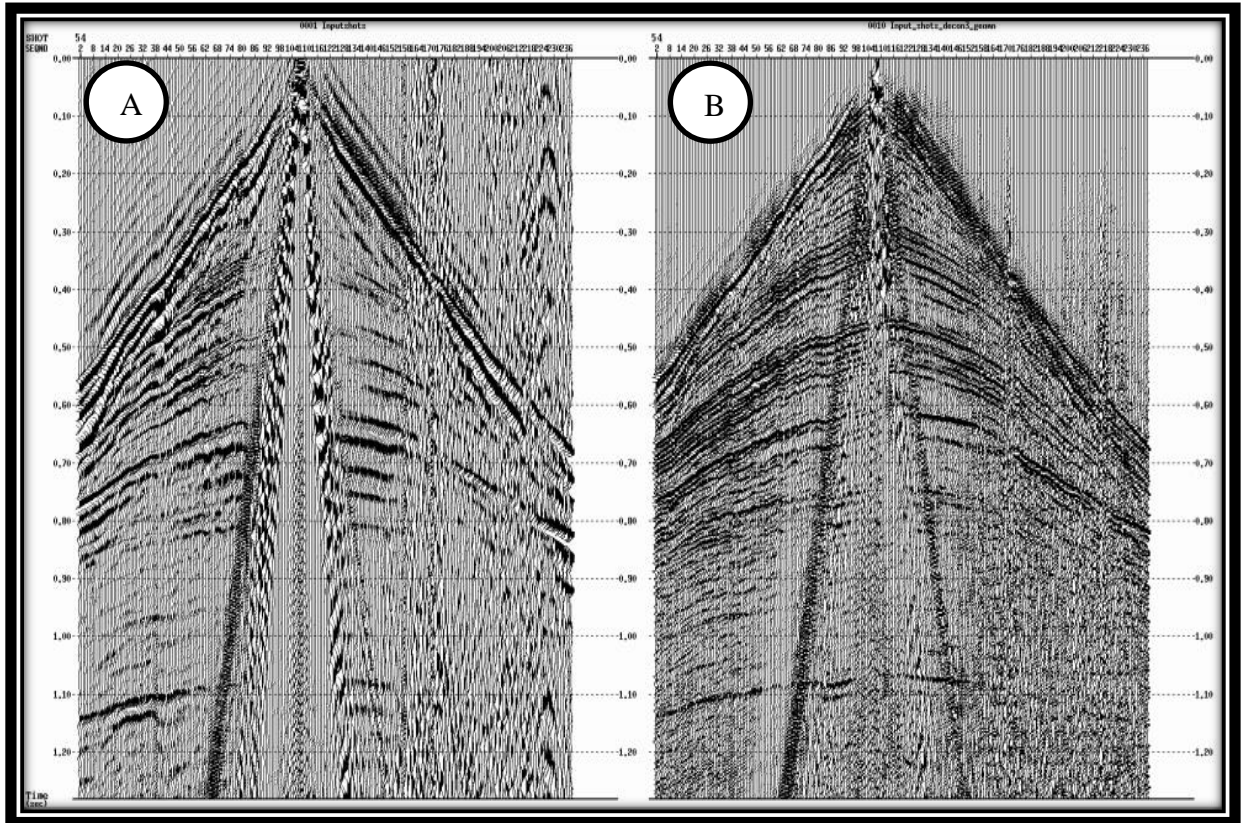


Figure 4.7: (A) Original shot gather from monitoring line (H-2000), while (B) is for the same shot after deconvolution. The pump-jack noise and ground-roll noise that masked reflectors at the central and eastern part of the shot gather are partially attenuated after deconvolution. Notice the continuity of reflectors at the middle and east sides of the shot gather after deconvolution.

### 4.3.3 Noise attenuation by modelling

In Figure (4.7b), we have seen that the five component surface-consistent deconvolution has partially removed some of the noise. Our ultimate goal is to attenuate as much noise as possible while leaving reflection signals and their frequency contents intact. The ground-roll and air blast noises have specific dip characteristics, velocities, and frequency contents. Therefore, noise attenuation is a procedure to model and subtract noise from the original data, resulting in a noise attenuated shot gather.

The procedure for noise attenuation by modelling work as follows:

- Design an ON-mute zone that starts from the top of the gather, which includes characteristic dipping noise.
- Design an OFF-mute zone that starts from the bottom of the gather, and sometimes the end time of the shot gather.
- The triangle area shown in Figure (4.8) will be the noise train zone, where applicable noise attenuation modules can be used to extract noise. The ON-mute and OFF-mute should be kept on while applying frequency filters to avoid contaminating clean zone of shot gather by noise leakage artifacts, such as aliasing.
- After careful noise testing and modeling, filtered noise train will then be subtracted from original shot gathers, resulting in noise-attenuated shot gathers.

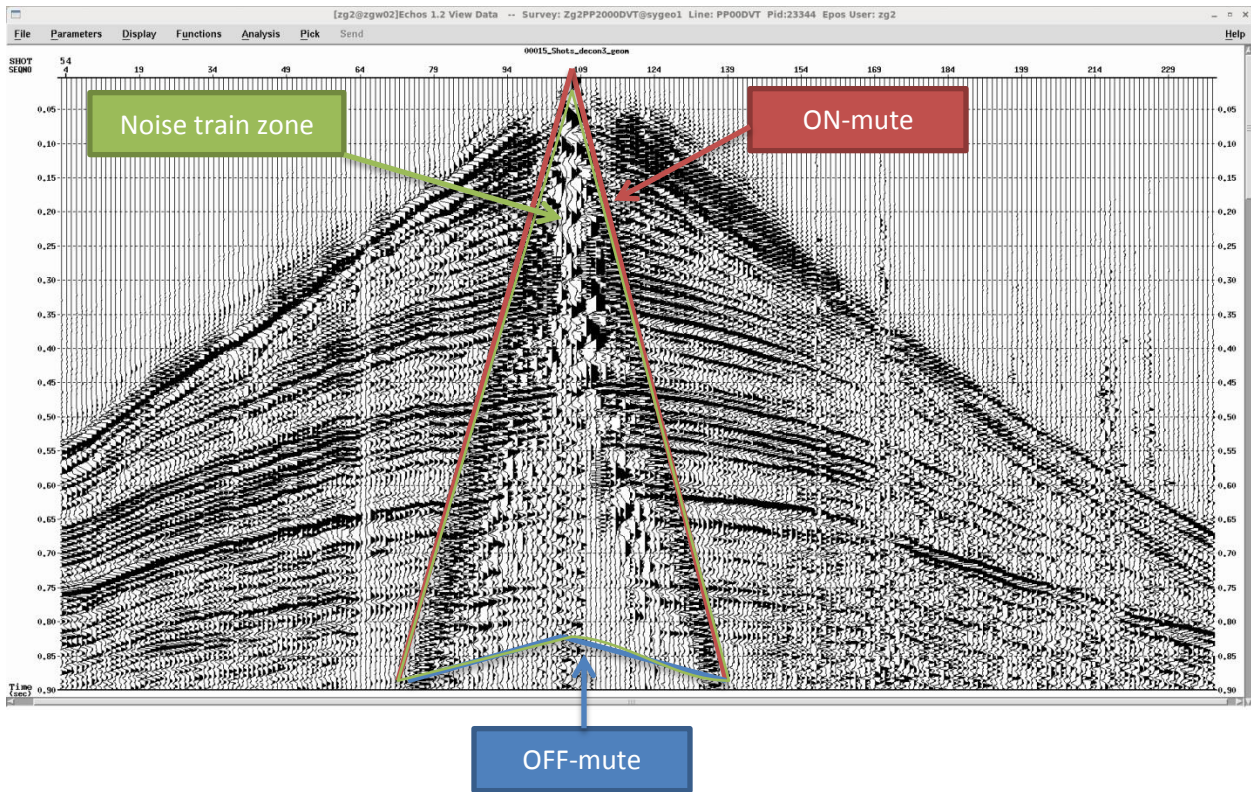


Figure 4.8: A shot gather from the monitor line survey before applying the noise attenuation procedure.

Figure (4.9) shows an application of the noise lifting procedure to the shot gather given in Figure (4.8) to attenuate ground-roll noise and the air blast. Note that ground-roll noises are successfully attenuated while leaving reflectors in the noise train zone intact.

The air blast noise could have been completely removed by the noise lift procedure, but at the expense of nearby reflection signals with a frequency range of 80-100Hz. The air blast and reflectors in the middle of the shot gather have close ranges of frequency content, and by applying a frequency filter, both the noise and reflection signals will be removed. Therefore, a mild frequency filter above 120Hz was applied to raw data of monitor line survey in order to leave reflection signals intact.

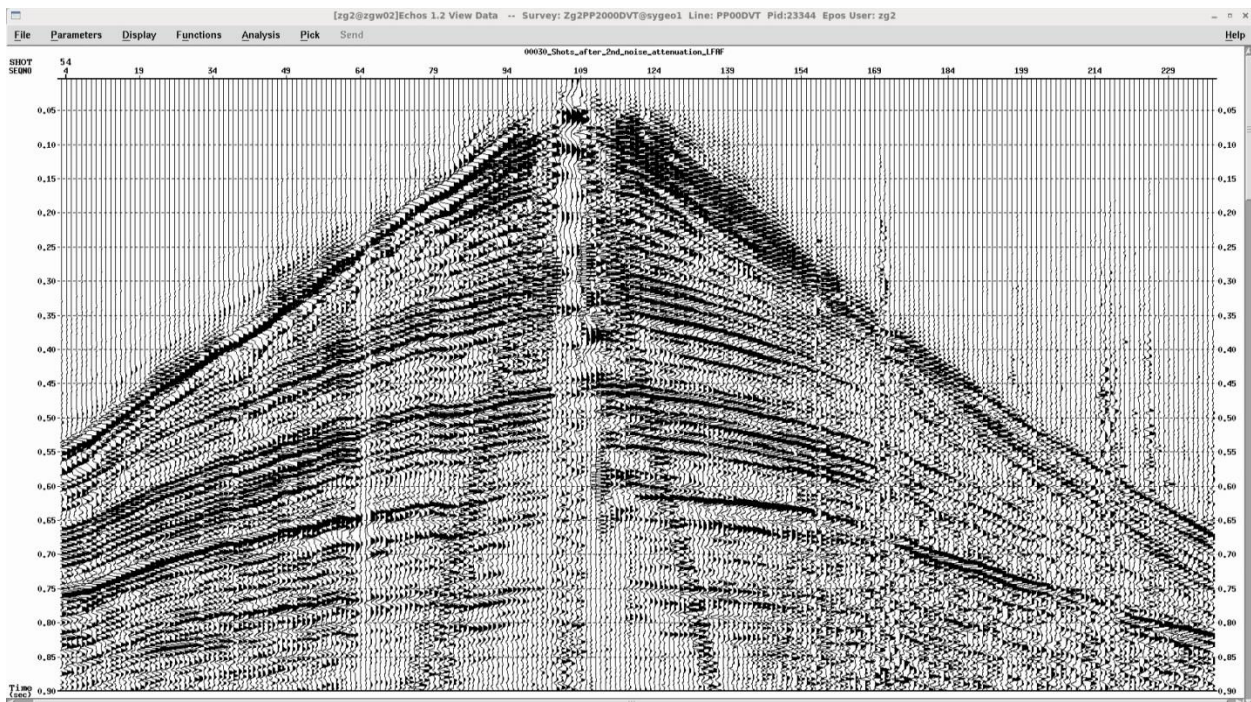


Figure 4.9: A shot gather from the monitor line survey after applying a noise attenuation procedure. The ground-roll noise is successfully removed, while preserving reflection amplitudes. Air blast noises with frequencies above 120Hz are also removed.

#### 4.3.4 Refraction statics calculation and application

Refraction statics were calculated using three main methods. These are, the Generalized Reciprocal Method (GRM), Standard Delay Time (DLT), and Diminishing Residual Matrices (DRM). The optimal choice of a better calculation method for refraction statics was judged by scrutinizing the brute stack as well as continuity and lateral variation of each reflector in the shot gather. Thus, refraction statics calculation using the diminishing residual matrices, DRM, (Gulunay, 1985) was applied. Figure (4.10) shows a shot gather before and after applying refraction static using the DRM method. Notice the improvement and continuity of reflectors in the shot gather after applying refraction statics.

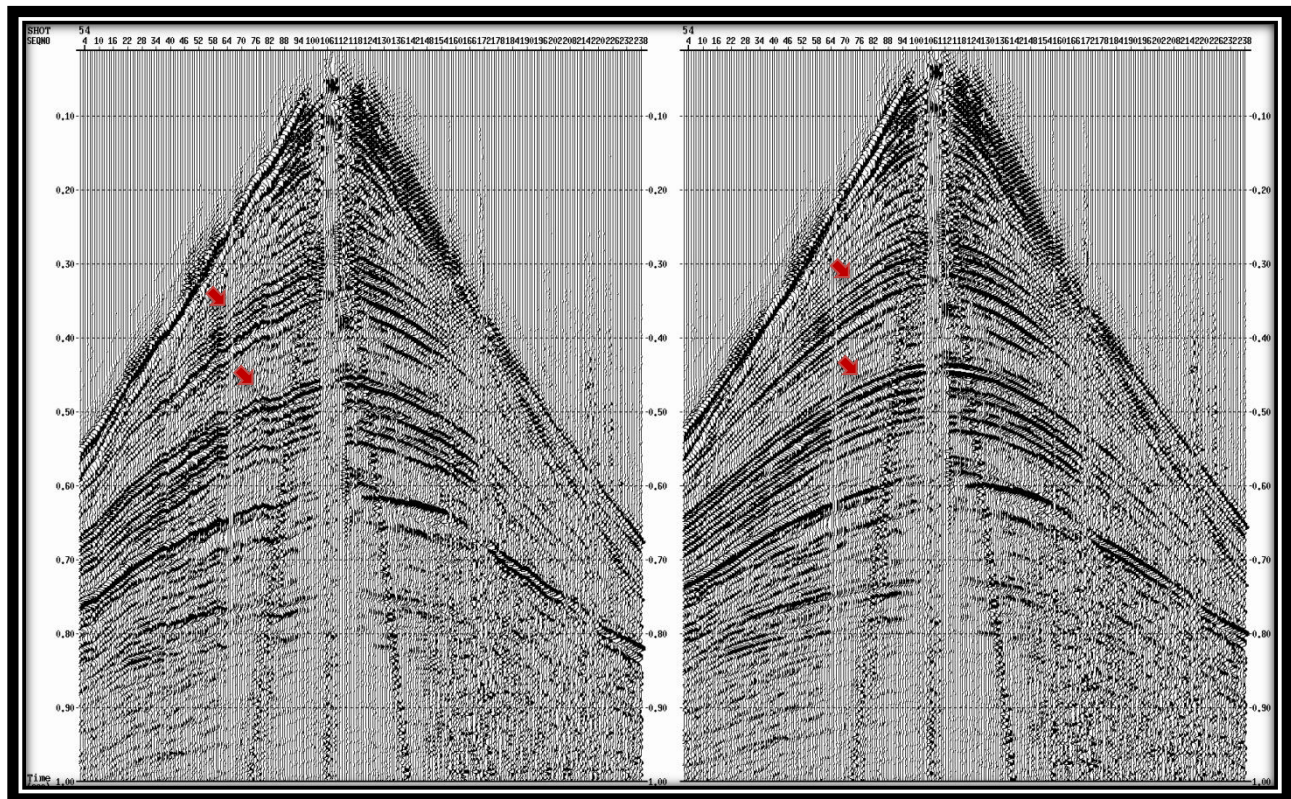


Figure 4.10: A shot gather from the monitor line survey. Left: Shot gather **before** applying refraction statics. Right: Same shot gather **after** applying refraction statics using DRM method.

#### ***4.3.5 Velocity Analysis and seismic imaging***

Velocity analysis includes velocity picking and applying normal move out correction. Velocities picks were guided by plotting interval velocities along the semblance panels. Five stacking panels with 5% velocities changes were also used and they were crucial guides to delineate expected velocity changes at the seam chambers of time-lapse surveys. Figure (4.11a) shows velocity picking for a super CDP gathers from the baseline survey, while Figure (4.11b) shows velocity picking for a super gather from the monitor line survey. Note that, a similar stacking velocity range was assigned in generating velocity semblances in velocity picking tools for both baseline and monitor line.

Note that a single designed mute was used for both time-lapse stack sections of the Pikes Peak seismic data. Two cycles of velocity analyses were performed for time lapse surveys. Surface consistent residual statics with correlation windows of 32msec and 16msec for the first and second cycle respectively are used to compute short-wavelength component of the statics, and applied for structure stack-sections for the time-lapse survey.

The surface consistent residual static corrections were preformed individually, although new emerging 4D processing methods are simultaneously calculating shot-wavelength statics for seismic data vintages. Another option often applied is to use a stack-section of the baseline as a model for trim static of the monitor line for further tuning of the stack section from shot-wavelet time shift effects. Note that trim static is not a surface consistent processing step; hence it was not used for the AVO friendly processing of time-lapse survey of Pikes Peak seismic data.

The corrected static (datum, refraction and residual) gathers were then used as input to a prestack time migration. The phase shift plus interpolation, PSPI, (Gazdag and Sguazzero, 1984) was the migration algorithm used in this research work.

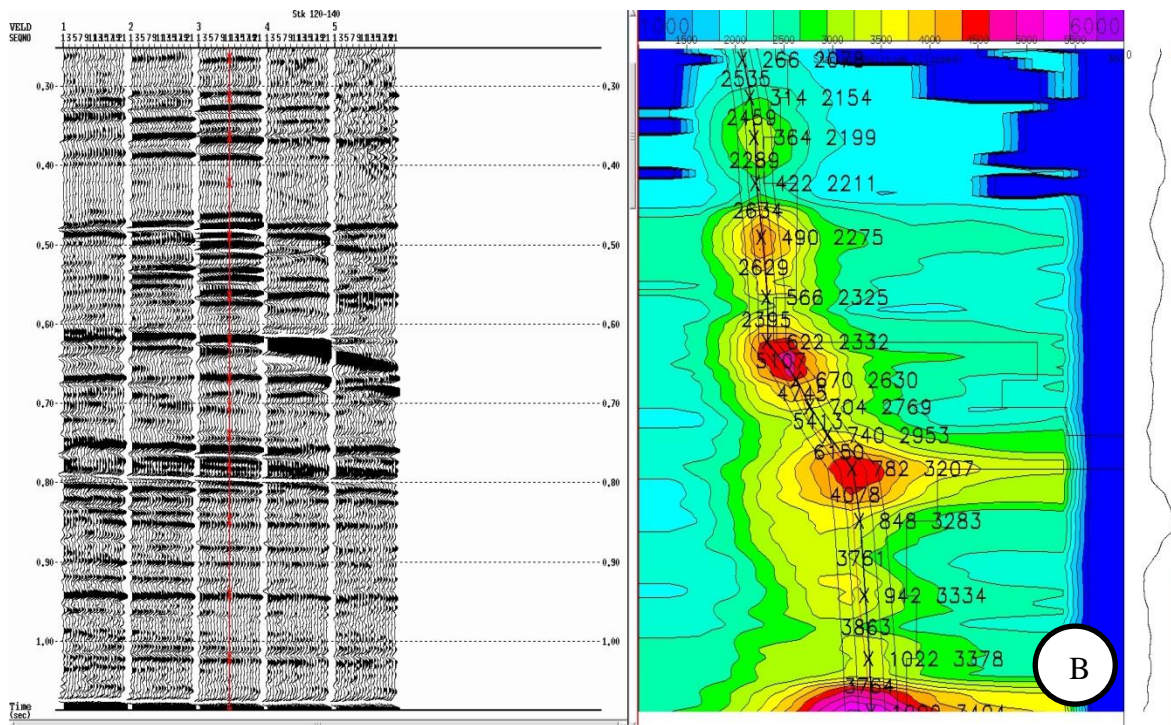
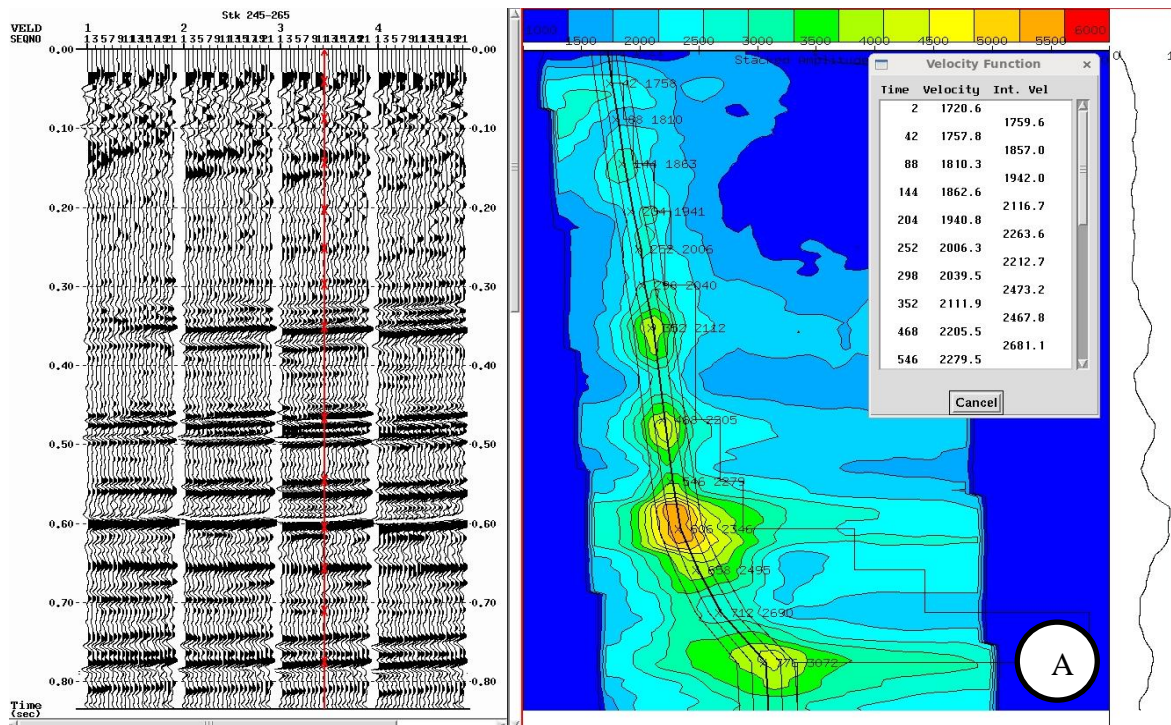


Figure 4.11: Second pass of velocity analysis. (A) for the baseline 1991, while (B) is for the monitor line 2000.

Note that the Kirchhoff migration method was also tested, but the prestack migrated sections did not map the Waseca channel precisely as PSPI migration does. Therefore, results discussed in this thesis will be focused only on the PSPI migrated sections.

The phase-shift plus interpolation migration method is a one-way wave equation downward-extrapolation migration (Gazdag, 1978) that provides better image sections for steep dip (90-degrees) and complex structures. The prestack time migration algorithm by Ng, (1994) is used in seismic imaging of Pikes Peak time-lapse surveys, where the time shifting imaging condition, which replaces downgoing wave of the sources, is used to interpolate in between depth or time steps (Ng 2007). The algorithm adjusts offset binning of input shot gathers and compensates for missing offsets to ensure offset bins are evenly distributed and fully populated with seismic traces.

Migration velocity analyses (MVA) were conducted for both seismic vintages, as prestack time migration needs an accurate velocity model to focus reflections and to position reflectors correctly. Smoothed stacking velocities of 100% were used, and 640 m padding at each side with time padding 20 % of trace length was set. A time step of 5 msec was used to delineate subtle variations in the steam zone.

Figure (4.12) shows both structure-stack and PSPI prestack-migrated sections for the baseline line survey. Note that, the pre-stack migrated section has managed to collapse diffractions at the Pre-Cretaceous/ Top Devonian unconformity (PCU) at 650 msec and elsewhere below the Waseca channel at 480 msec. Furthermore, the migrated section managed to focus reflections at various time depths, and also imaged the Waseca channel precisely. The on-lap features inside the Waseca channel for the PSPI migrated-section of the monitor line (Figure 4.13) are delineated fairly well, compared to the structure section that resulted from applying a second

residual static correction. Notice also that diffraction phenomena at PCU are collapsed in the migrated section. The faulted zones in the top part of the migrated section of monitor line are fully focused, and related diffractions that were shown in structure stack-section are collapsed. The overall PSPI stack-section is better imaged, and reflectors below the Waseca channels are clearly mapped. Figure (4.14) shows time-lapse prestack migrated sections for both baseline and monitor line surveys after applying time-lapse regularization for the monitor line to match the baseline in terms of length, CDP fold and frequency bandwidth. The induced-amplitude changes at the Waseca channel due to the steam injection are clearly noticeable in the stack-section of the monitor line.

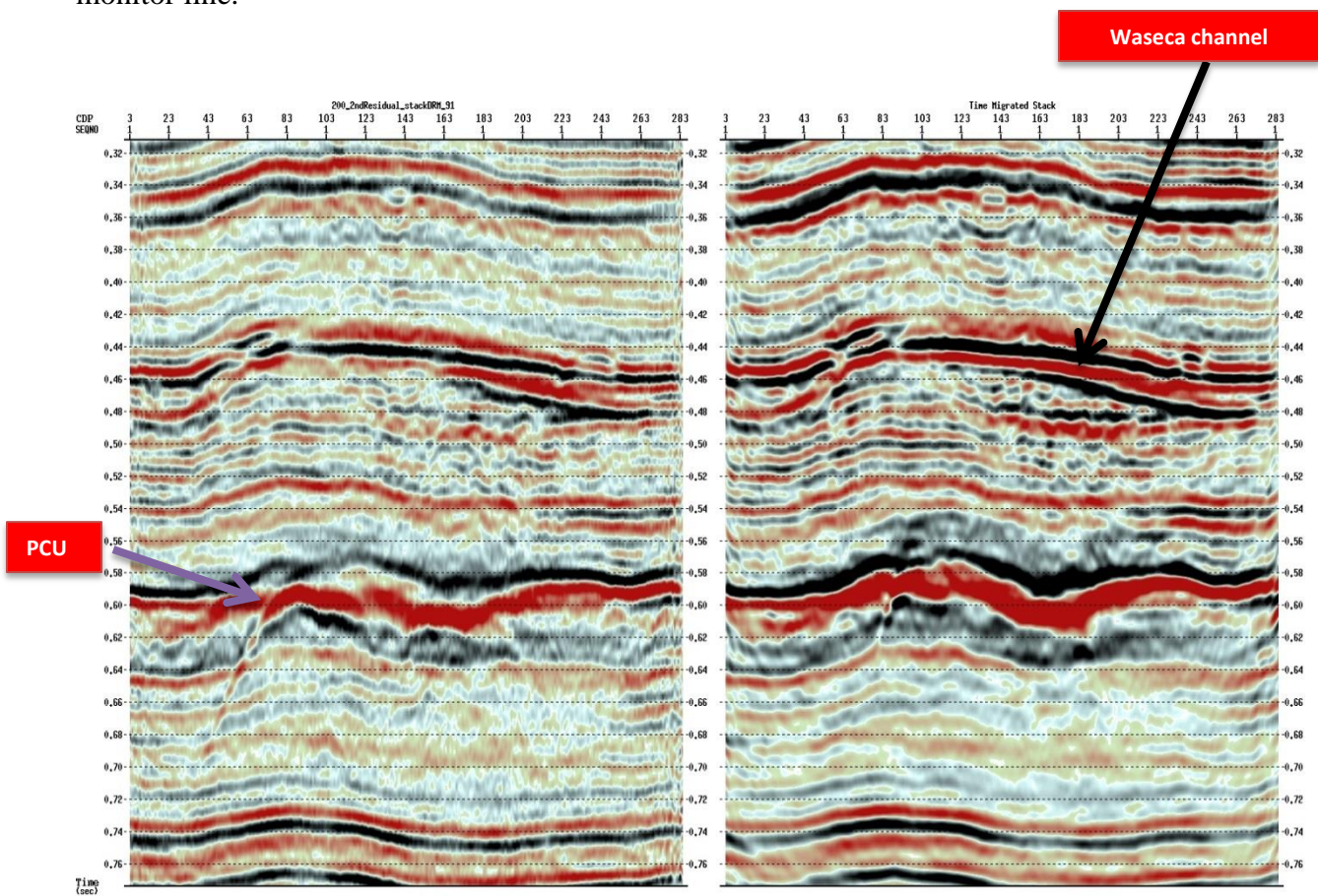


Figure 4.12: Left: Structure stack-section. Right: PSPI migrated stack-section for the 2D baseline (H-1991) survey of Pikes Peak oil field.

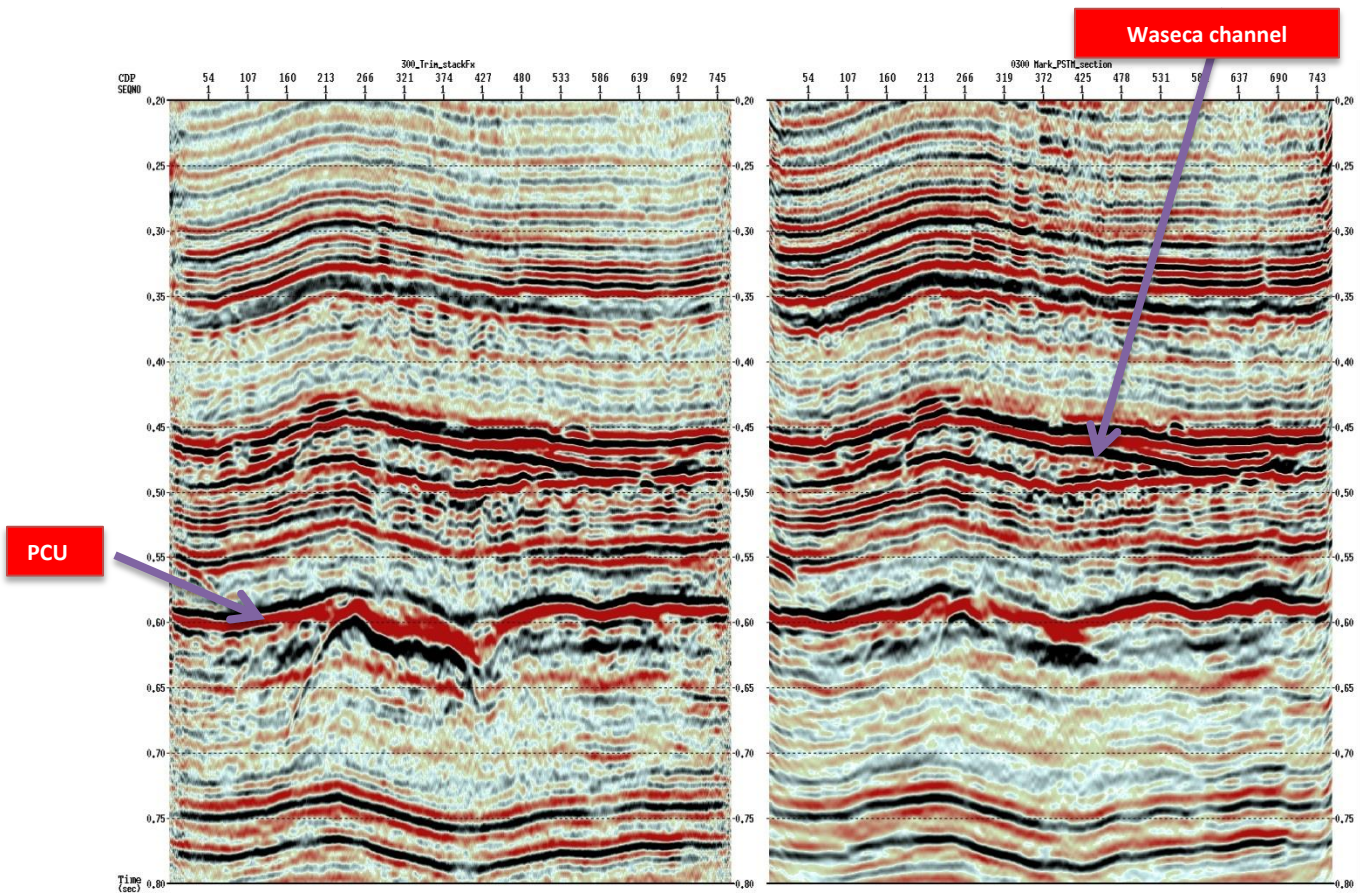


Figure 4.13: Left: Structure stack-section. Right: PSPI migrated stack-section for the 2D monitor line (H-2000) survey of Pikes Peak oil field.

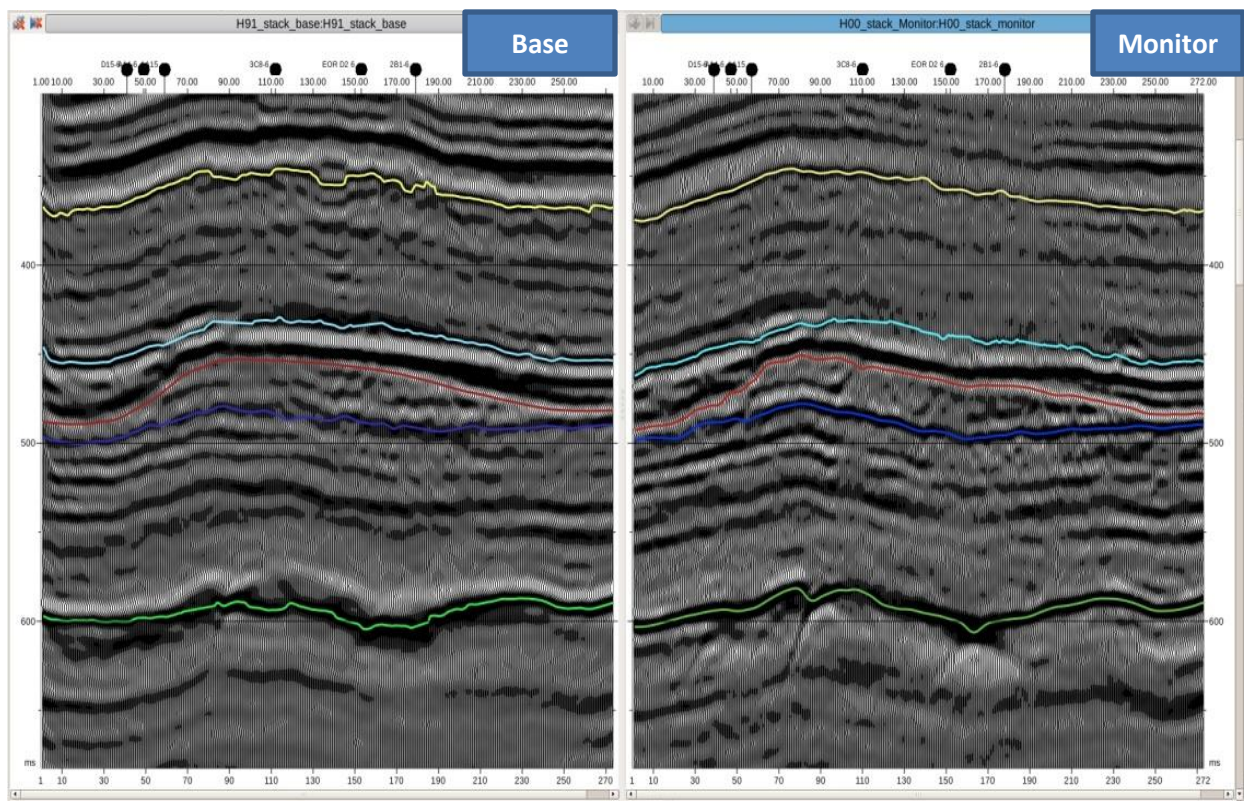


Figure 4.14: PSPI migrated stack-sections for the 2D time-lapse survey of Pikes Peak oil field. Left: Baseline (H-1991) survey. Right: monitor line (H-2000) survey. Time horizons: yellow for BFS, cyan for Colony, red for Top Waseca, blue for Sparky and green for PCU. Note the change in amplitude at the Waseca channel, and below Formations due to steam injection effect.

#### 4.4 Conclusions

The main objective of time-lapse seismic monitoring is to track production related changes in the reservoir and to image the movement of hydrocarbon fluids. The time-lapse processing and imaging flow designed for seismic data vintages of Pikes Peak oil field has overcome many difficulties related to differences in acquisition parameters, environmental changes and noise, and managed to delineate expected time-lapse response. Using a robust migration algorithm, and careful testing of processing parameters, allowed us to image areas where production effects are likely to have occurred.

## Chapter Five: **QUANTITATIVE INTERPRETATION OF THE PIKES PEAK TIME-LAPSE SEISMIC SURVEYS**

### **5.1 Introduction**

The objectives of time-lapse seismic surveys at the Pikes Peak heavy oil field is to track production related changes at the Waseca reservoir and steam movements in heavy oil reservoirs. In terms of geophysical and reservoir engineering perspectives, several efforts have been made to improve interpretations (Watson and Lines, 2001; Wong et al, 2003; Zou et al., 2005) of the Pikes Peak time-lapse seismic surveys.

Husky Energy has placed the west part of the Pikes Peak heavy oil block under CSS process and exploited most of that side before the end of 1987 (Wang et al., 2003). Therefore, the east side of the Pikes Peak oil field where survey lines reside is the ideal location for a time-lapse study.

The information provided by Husky Company about the wells status and history shows that many of the wells in the survey area have undergone several phase changes from steam injection to production over time. The reservoir pressure measured at these wells has also show large variation as the status of these wells changed (Wong et. el., 2003). In the following sections, several quantitative analytical techniques are used to study the effect of steam injection and the production process on the seismic responses as well as changes of the elastic attributes at the reservoir at Pikes Peak heavy oil field over elapsed time.

## 5.2 Interpretation of time-lapse seismic data

As a first step in the interpretation, the well-seismic tie and wavelet extraction process require generating synthetic gathers to be correlated with seismic gathers in order to produce time-depth relation, well logs and markers in the time domain and an estimated wavelet at each well. The well-seismic tie and estimated wavelet at Well 1A15 is displayed in Figure (5.1). A good well to seismic tie with an overall correlation coefficient of  $> 0.72$  between synthetic and seismic gathers is maintained.

The time-lapse stack sections of the baseline and monitor line given in Figure (5.2) show amplitude changes not only at the steam chamber (Waseca reservoir) zone, but also above and below the reservoir zones. The amplitude changes give motivation to explore different interpretation tools to gain a better understanding of the changes of elastic properties of the reservoir over time. In the following subsections, detailed interpretations using observations from seismic stack sections and seismic differences as well as the time-delay analysis are given.

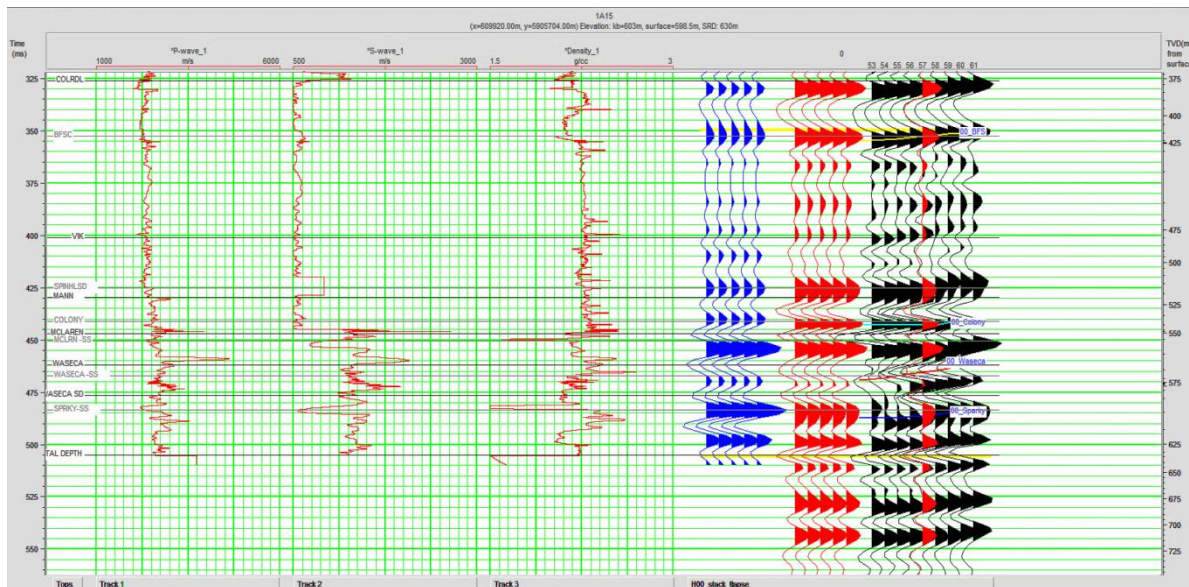


Figure 5.1: Well to seismic tie for dipole sonic well 1A15-6, Pikes Peak oil field.

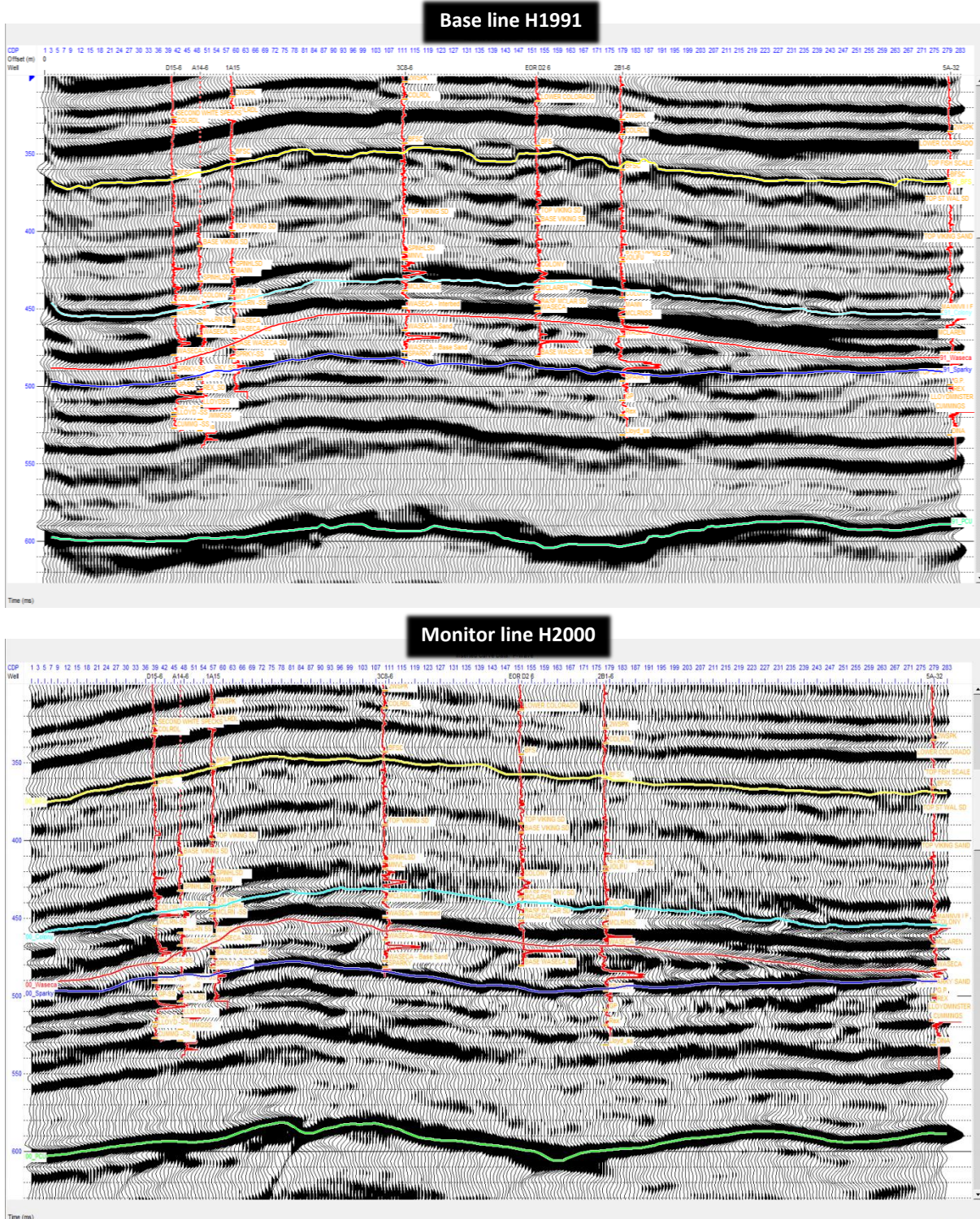


Figure 5.2: Stack sections for the time-lapse survey of Pikes Peak oil field. Top: stack of the baseline H1991. Bottom: stack of the monitor line H2000. Inserted curves are P-wave curve. Note the amplitude build up due to steam injection at the Waseca channel, base of Waseca channel (blue color horizon) and below formations.

### *5.2.1 Analysis of time-lapse seismic differences*

The geometry parameters for time-lapse seismic surveys at Pikes Peak given in Table 4.1 indicate that both seismic lines of vertical components have different survey line lengths, shot intervals, fold coverage, and frequency bandwidth. In order to improve seismic repeatabilities and to eliminate error due to geometry or noise, the monitor line H2000 survey was calibrated to match survey line length, fold and frequency bandwidth of the baseline H1991 survey. Figure (5.3) shows common image gathers, CIG, of the baseline and monitor line surveys for the Pikes Peak, where the effects of cycle steam and production process are evident on the reflector induced-amplitude changes for the gathers of the monitor line survey.

In 4D seismic monitoring, it is understood that a change in the seismic section at the reservoir zone, is due to a combination of elastic impedance changes and time variant shift, while below the reservoir zone, such changes are attributed to the time-variant shift due to velocity change at the reservoir layers. Therefore, the stack sections of the time-lapse survey are then loaded into the Pro4D program of Hampson-Russell in order to perform seismic calibration, and then measure seismic amplitudes differences.

The time-lapse seismic conditioning procedure consists of the following:

- 1- Re-gridding the processing output geometry of the monitor survey to match those of the base line survey.
- 2- Frequency bandwidth matching of the monitor survey to frequency bandwidth content of the baseline survey.
- 3- Constant Phase and bulk time shift where a time-pick is made on the envelope amplitude of the cross-correlation of the base to the monitor survey. The phase shift is determined

by a pick that is made on the instantaneous phase of cross-correlation that corresponds to the time of the envelope maximum (Hirsche et. al., 2002).

- 4- Shaping filter. This step also referred to as matching filter, and is used to match the static time shift, phase, amplitude and frequency content between the surveys by calculating a convolutional shaping filter based on a certain design window (Rickett and Lumley,2001).
- 5- Cross-correlation shallow statics time shift. This step is also referred to as time wrapping that applies a time shift, which is derived from cross correlation analysis, to align mis-positioned events (Rickett and Lumley, 2001). The process is trace by trace operation, and the time-delay map reflects changes in velocity due to steam effect within and below the reservoir formations.
- 6- Time variant shift. This step applies to match data above, within and below reservoir, and then the calibrated data sets are subtracted to obtain the amplitude differences.

Prior to seismic subtraction, several tests were conducted using different time windows; one above the reservoir (100-430 ms) and another one within the reservoir zone (300-550 ms). The above steps were applied to obtain an optimal wavelet shaping filter that can be used to calibrate data vintages of the Pikes Peak surveys for amplitude and phase matching, shallow statics time shift and time-variant static. Figure (5.4a) shows seismic differences between the baseline H1991 and monitor line H2000 of the Pikes Peak time-lapse surveys where time windows analysis was chosen to include the reservoir zone (300- 550 ms). In the seismic difference section, while little changes are seen inside the Waseca reservoir, most significant differences in seismic amplitudes are observed above the thickest reservoir zone in the area where production and injection wells are active.

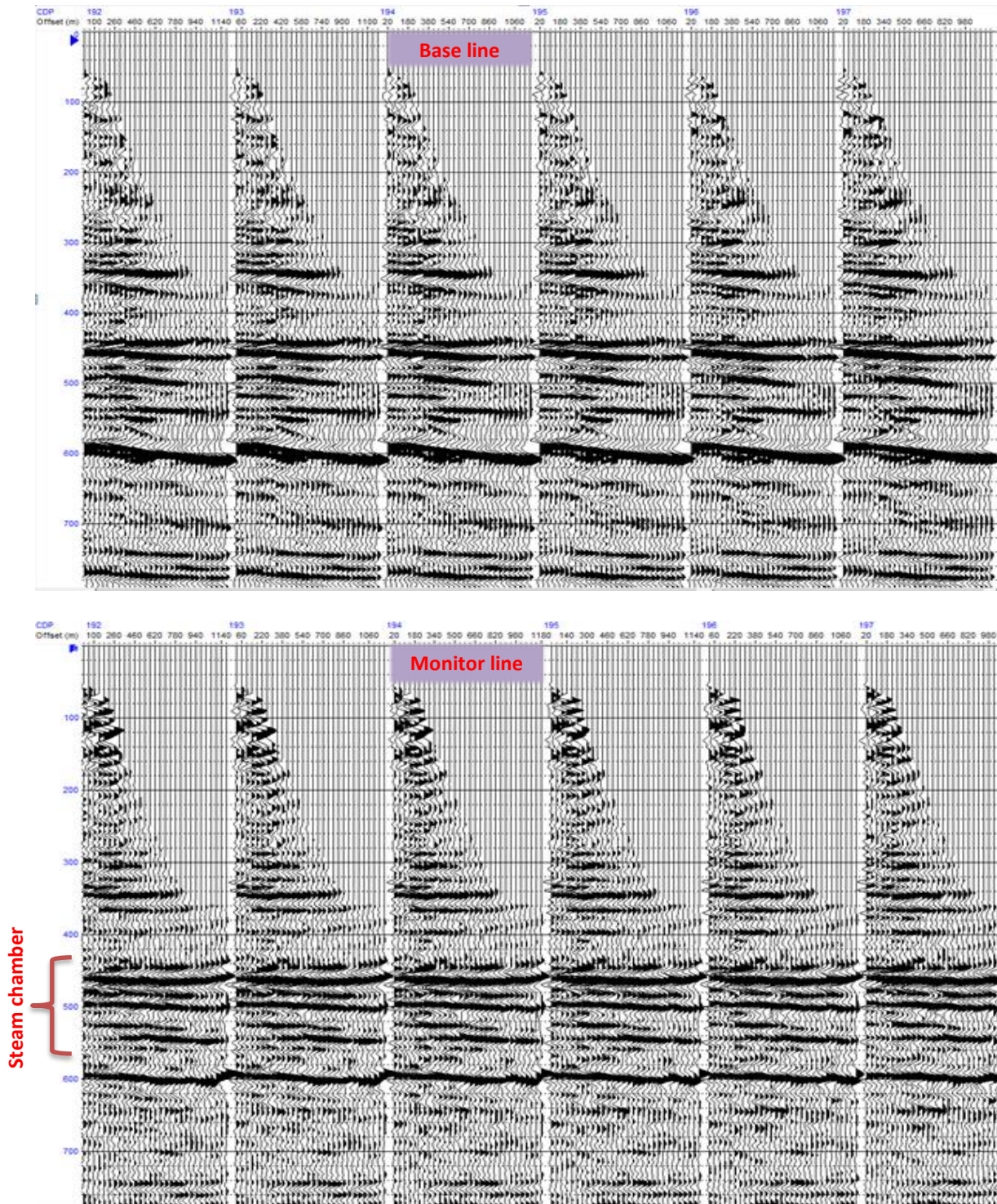


Figure 5.3: Common image gathers of time-lapse survey of Pike's Peak oil field. Top: CIG of the baseline. Bottom: CIG of the monitor line. Note the induced-amplitude changes for the gathers of the monitor line survey due to steam effect at reflectors close to steam chamber (around 450 - 550 ms).

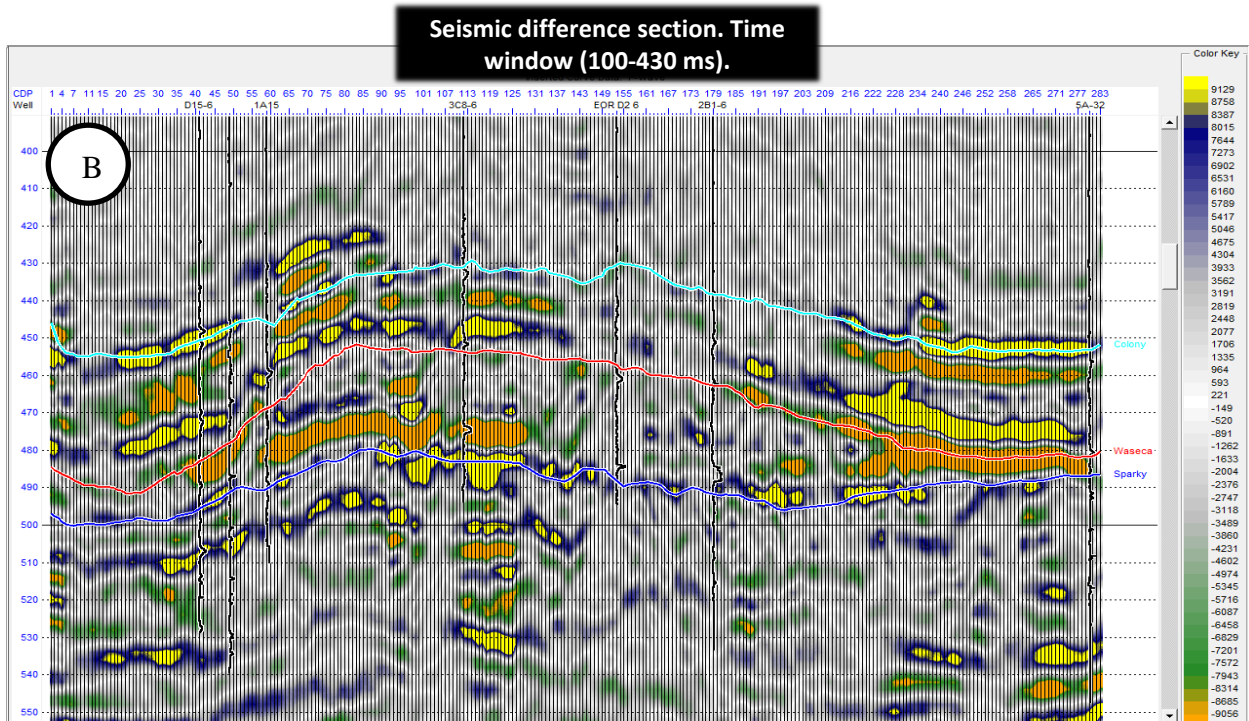
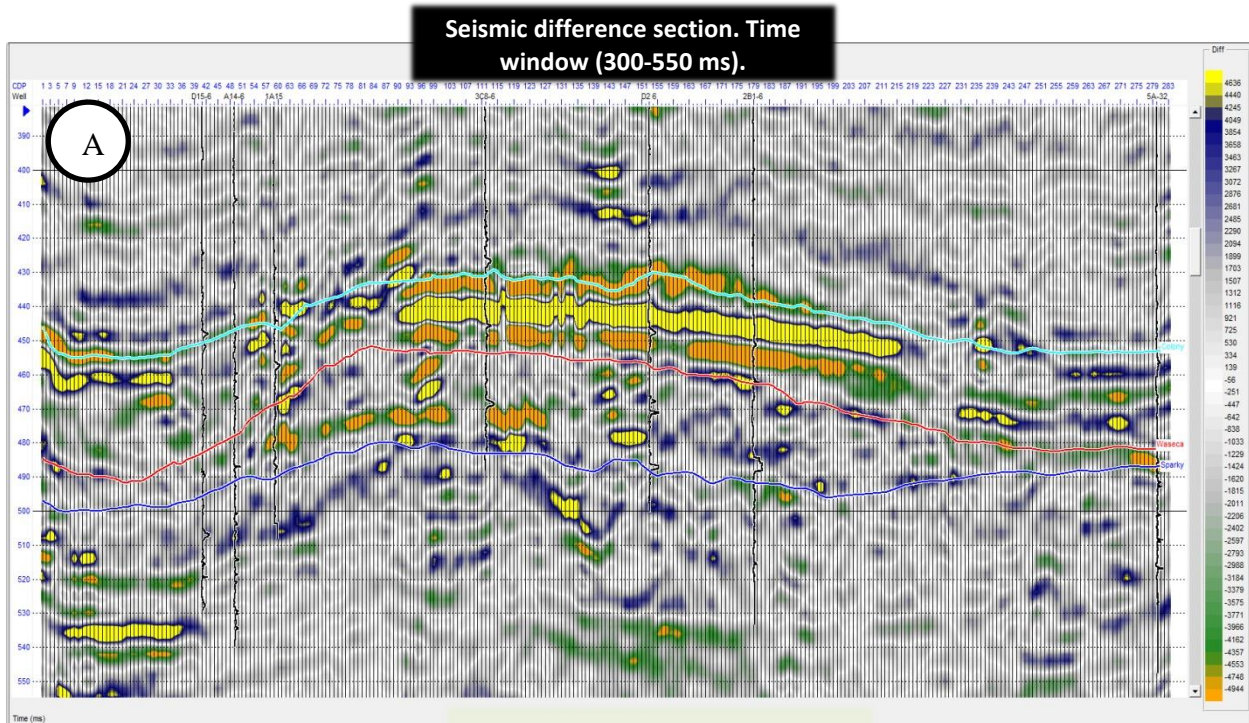


Figure 5.4: Seismic difference between the baseline H1991 and monitor line H2000 of the time-lapse survey of Pikes Peak oil field. A) for time window designed to be above, within and below the Waseca reservoir zone. B) for time window designed to be above the Waseca reservoir zone.

Figure (5.4b) shows seismic differences between the baseline H1991 and monitor line H2000 of the Pikes Peak time-lapse surveys where time windows analysis was chosen to be above the reservoir zone (100- 430 ms). In the seismic difference section, the amplitude differences inside the Waseca reservoir is improved and more changes in amplitude is seen at the bottom of the Waseca channel where sand unit exist. However, significant differences in seismic amplitudes are still observed above the reservoir zone in the area where production and injection wells are active as well as east side of the Waseca zone.

Although the Colony formation is considered as cap rock seal for the Waseca formation at the Pikes Peak oil field, there are weak zones formed from interbedding of shale and coal seams that comprise part of the Colony lithology. The noticeable thick bands correlate with the drop in  $V_p/V_s$  of the dipole sonic log of Well 1A15-6 given in Figure (1.4). The visible cloud of amplitude differences at the Colony formation can be attributed to the hydrocarbon movement through cap rock to overlying formation.

This finding is also in agreement with the crossover of neutron- and density- porosity logs of Well D2-6 (Figure 5.5) nearby the survey lines. The crossover of neutron and density log is indicative of gas accumulations. Thus the excessive steam injection forced the hydrocarbon fluid to move through weak zones in the cap rock to overlying formation. The gas hydrocarbon was formed from evolved solution gas from the oil phase due to relief in pore pressures. The pore pressure measurements at the nearby wells show large variation as Husky Energy did not maintain the original reservoir pressure during the recovery process of heavy oil over lapsed time operations at Pikes Peak oil field. Therefore, pore pressure changes may have contributed to the time-lapse seismic differences.

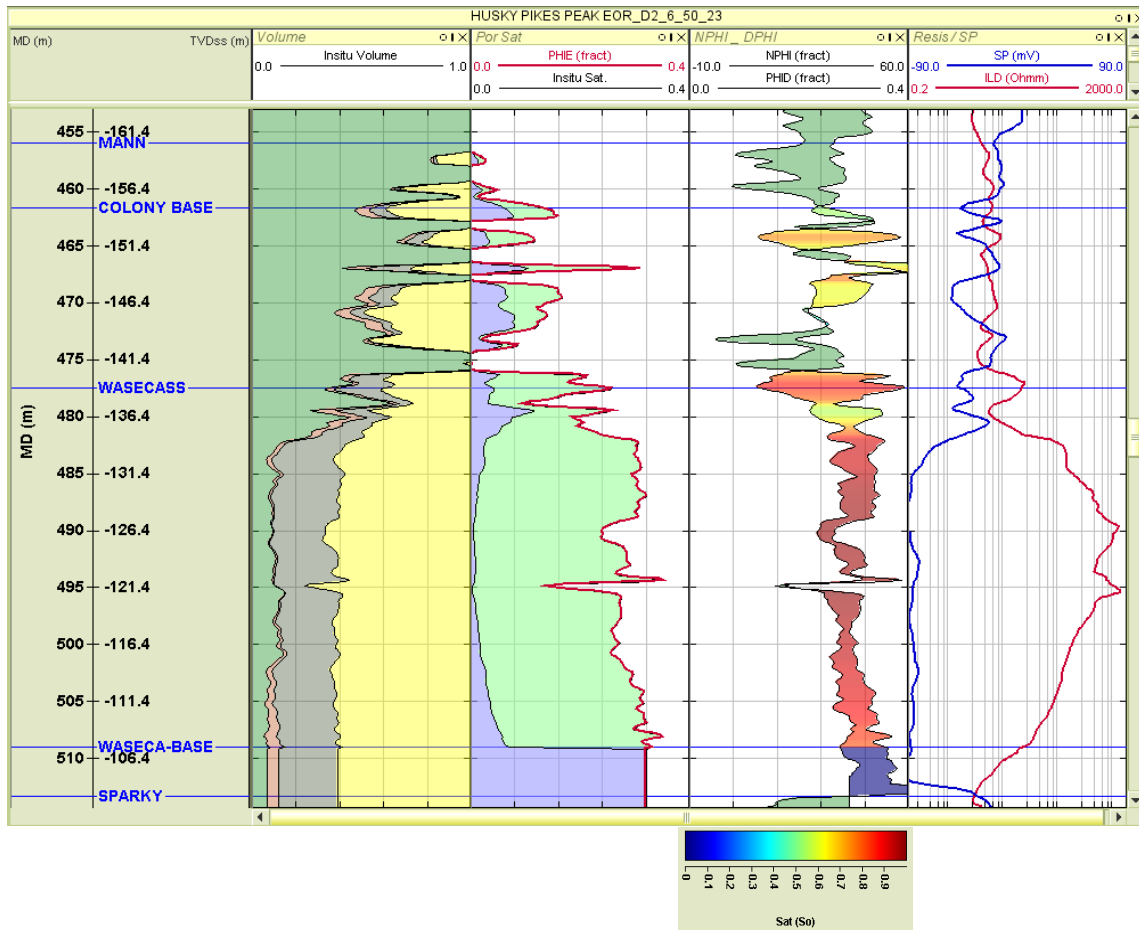


Figure 5.5: Volume, pore saturation, neutron and density porosity and resistivity/SP logs of well D2-6, Pikes Peak oil field. Note the crossover of NPHI and DPHI curves at Colony formation and subsequent formation that are colored by oil saturation ( $S_o$ ).

### 5.2.2 Analysis of Isochron ratio

In time-lapse survey, particularly for heavy oil reservoir, an isochron ratio analysis should have been done after matching overlaying formation directly above the top of the reservoir. This is to ensure that picked time horizons would only reflect correct delay time that is related to reservoir depletion processes, and not affected by time variant static or different processing flows of

seismic data. Thus, the isochron ratio analysis in this study would be considered as a relative analysis. The isochron ratio analysis uses the time interval of the Waseca reservoir from the time-lapse survey to study the effect of steam injection and hydrocarbon recovery process over the reservoir zone. The isochron ratio is calculated using time horizon of the base of reservoir (Sparky horizon) minus time horizon of top of Waseca for the monitor line H2000 divided by the same time horizons of the baseline H1991 survey.

In the previous section, it has been stated that injected steam has decreased the interval velocity of the monitor line H2000, thus increased the travel time through the steam zone and underlying formations. However, if there had been no changes in the reservoir elastic properties over lapsed time, then the isochron ratio would be unity.

In Figure (5.6), where isochron ratios are plotted at each CDP, the positive isochron ratio over CDP range (50-60) has a good correlation with the negative seismic differences patches inside the Waseca reservoir (see Figure 5.4). On the other hand, the negative isochron ratio at CDP 35, close to well D15-6 does not really represent delay time change due to production process, as no steam injection or production has occurred at well D15-6. The isochron ratio over CDP range (100-200) shows noticeable changes with some agreements with the change inside the Waseca reservoir shown in Figure (5.4).

In order to correlate the gas accumulation cloud in the middle of the seismic difference section (Figure 5.4), the time horizons of the reservoir zone was extended to include the Colony formation to act as top of the reservoir, while maintaining the bottom of the reservoir same as in Figure (5.6). The isochron ratio in the middle of Figure (5.7) is consistent with the expected increase in delay time due to the effect of steam injection and residual gas in that zone.

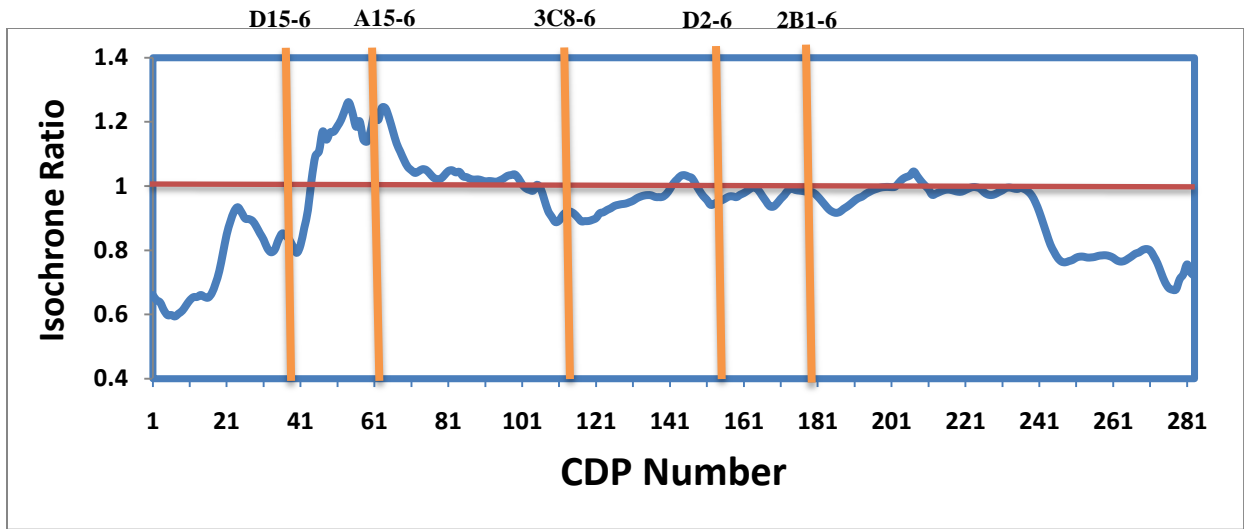


Figure 5.6: Isochron ratio of the Waseca interval travel time, Pikes Peak oil field.

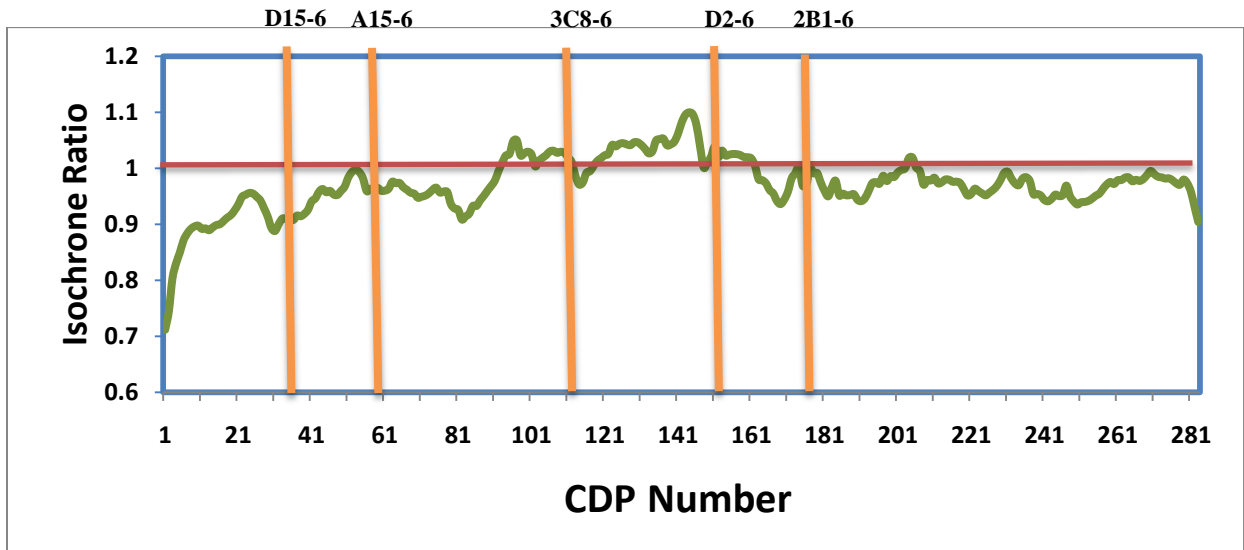


Figure 5.7: Isochron ratio of the extension Waseca interval travel time to start from the Colony formation as top of the reservoir at Pikes Peak oil field.

Note that the interpretation of the relative isochron ratio by relying only on seismic data and production history might not provide a good understanding of the reservoir behavior under the effect of steam and heat. Therefore, geo-thermal as well as geo-pressure studies would have to be incorporated to answer uncertainties of unexpected changes in the isochron ratio.

### **5.3 Interpretation of post-stack impedance inversion**

In seismic inversion we seek to obtain interval rock properties of the earth model by using properties of reflectivity interfaces and information from non-seismic, such as well logs, to constrain the results. The objective in this study is to observe and monitor acoustic impedance (AI) changes between the time-lapse sections as a result of steam injection effects and hydrocarbon recovery processes.

In the seismic inversion, the seismic data is band limited. Therefore, the low frequency of the back ground model is needed to compensate for the low frequency below the field frequency bandwidth. The low frequency background model (Figure 5.8) was built by interpolating P-impedance from well logs along seismic time horizons. The frequency range of 1-8 Hz was chosen to compensate from missing frequency bandwidth of the band-limited stack sections of the time-lapse surveys, as frequency bandwidth of these stack sections are within 8-110 Hz.

In the following subsections, discussions of post stack P-impedance inversion as a result from individual inversion of each survey line as well as from time-lapse post stack impedance inversion are presented.

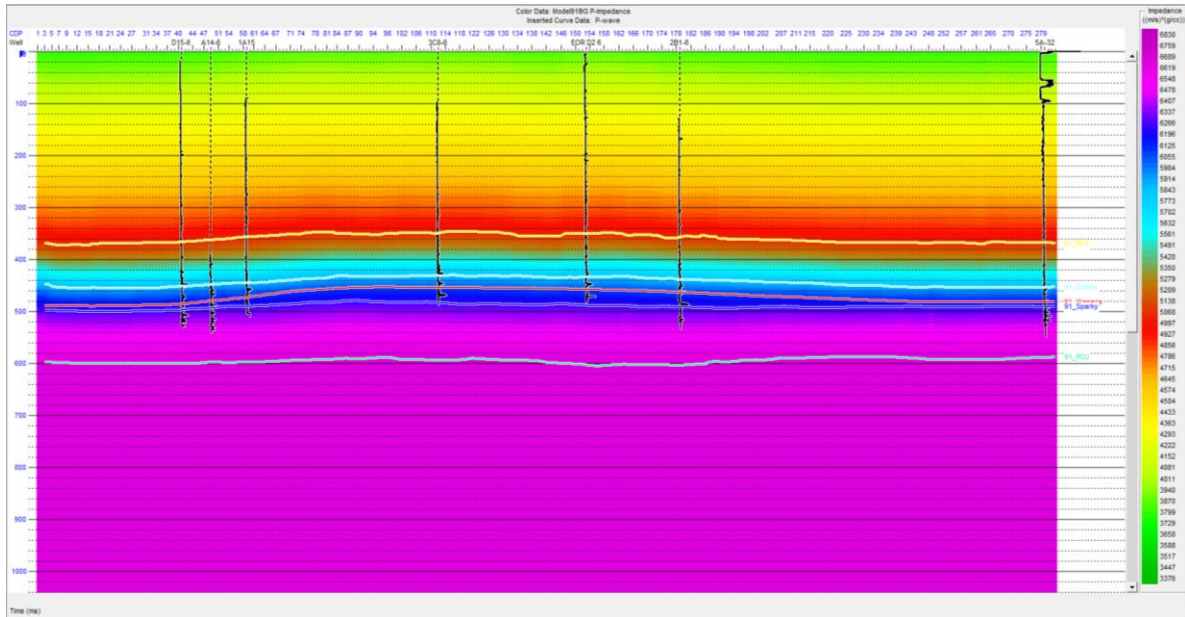


Figure 5.8: The low frequency (1-8 Hz) background model of P-impedance used in the post-stack acoustic impedance inversion of the Pikes Peak time-lapse survey.

### 5.3.1 Post-stack impedance inversion of individual survey line

Figure (5.9) shows the acoustic impedance sections for the baseline H1991 and monitor line H2000 surveys. The impedance inversion was carried out individually using a sparse-spike inversion scheme (Russell, 1988). The P-impedance section of the monitor line shows a decrease in P-impedance values for the large part of the Waseca channel compared to the P-impedance of the baseline survey.

In the CSS process, injected steam leads to an increase in mobility of heavy oil and decrease in density and velocity at the reservoir; thus a decrease in P-impedance section. As expected, the acoustic impedance section of the monitor line H2000 shows a decrease in the P-impedance at the middle of the Waseca channel (the area bounded by the Waseca and Sparky horizons), which represents the steam chamber zone. The cap rock formation above the Waseca channel, which

represents the Colony formation, also shows a drop in P-impedance as sign of possible hydrocarbon accumulations. The decrease in P-velocity, due to steam injection also leads to an increase in travel time in the monitor survey. Therefore, determination of precise changes in P-impedance at the reservoir layer is not feasible by taking the differences between impedance sections, nor would conditioning of post stack impedance sections following 4D conditioning process be practical.

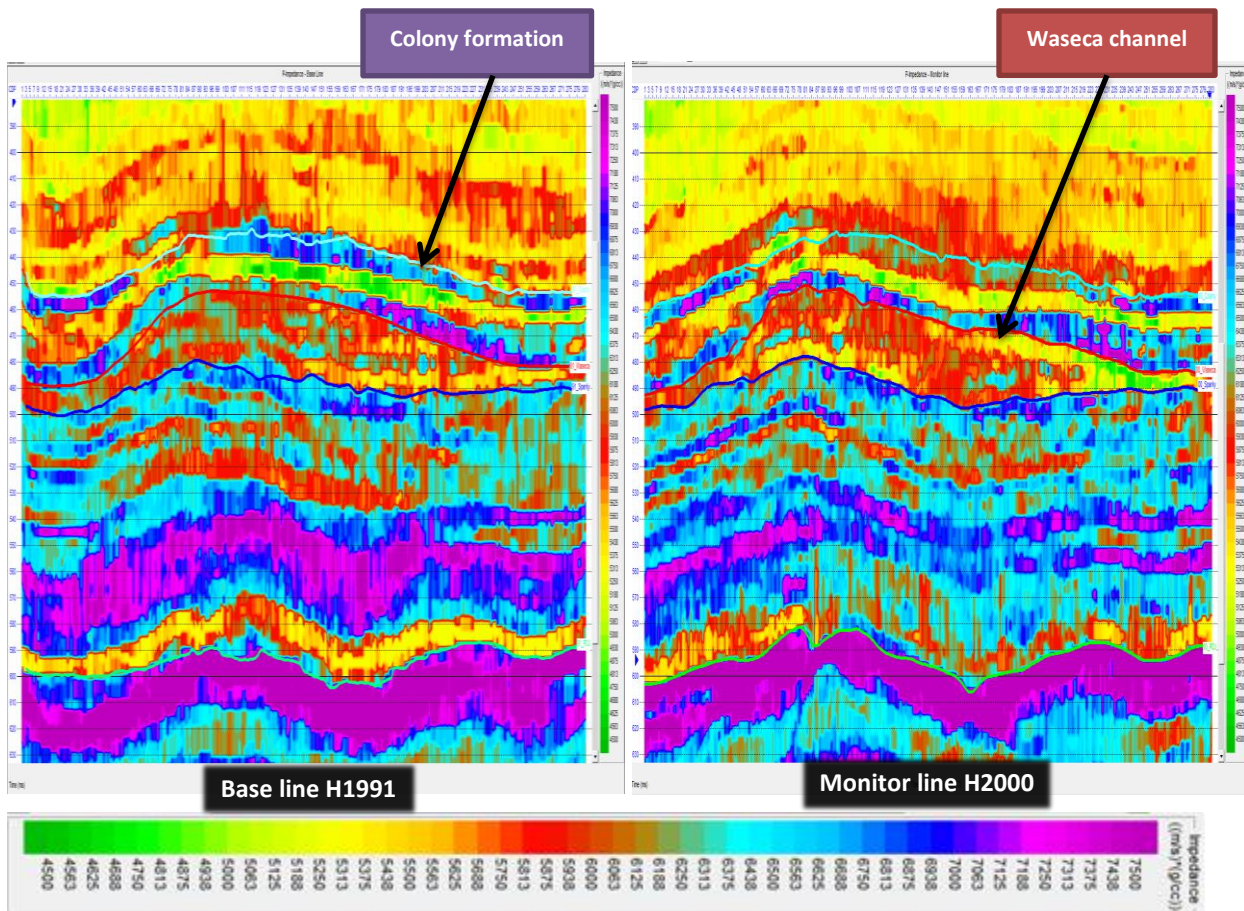


Figure 5.9: The post-stack acoustic impedance (AI) inversion sections of the Pikes Peak oil field from inverting time lapse seismic data individually using a sparse spike impedance inversion scheme. Left: impedance section of the base line H1991. Right: impedance section of the monitor line H2000.

### ***5.3.2 Time-lapse post stack impedance inversion***

It has been stated in a previous section that the differences of impedance sections between baseline and monitor line surveys without a pre-conditioning stack section for 4D processes will be relative and will not reflect precise pore-fluid changes nor be able to track steam movement or a temperature front. Since, the interval time increases at the reservoir and below formation of the monitor line survey, nevertheless, the differences in impedances, without 4D conditioning, will reflect structure and seismic processing changes more than pore fluid changes.

The calibrated stack sections subjected to a 4D conditioning process discussed in Section (5.2.1) are then used for time-lapse post stack acoustic impedance. The low frequency model is also calibrated for the time delay to accommodate changes in velocity that are below the frequency content of the seismic wavelet.

Before embarking on interpreting time-lapse impedance inversion results, recall that the Waseca formation, as shown in Figure (5.10), consists of shale unit, interbedded with silty sand unit and homogenous sand unit (Van Hulten, 1984). The resulting inverted acoustic impedance change between the baseline and monitor survey is shown in Figure (5.11). The impedances differences clearly image areas of impedances changes as a result of steam injection and production processes. Steam effects are most noticeable at the base of the Waseca channel where hydrocarbon moves through sandy homogenous layers.

In order to correlate the impedance difference result in Figure (5.11) with the stack section of the monitor line given in Figure (4.13) of a previous section, notice that there are vertical features in Figure (4.13) that are inconsistent with low angle thrust faults or high angle normal faults. These features could be strike-slip faulting, if the local stress field allows for such a faulting style. Therefore, these features are most likely to represent gas or fluid movement either creating a

vertical fracture or exploiting vertical fault planes. The dimming zones immediately above the sand in Figure (4.13) are possibly related to gas or fluid pocket traps.

The Waseca formation itself has interbedded silty sands that appear to provide a pathway for steam in Figure (5.11) to move vertically, either through a more silt-rich interval or along inclined beds within the sand channel. The high pressure steam/fluids could cause fluid movement through the top seal into the overlying formation which would correlate to the vertical features observed in the seismic section of the monitor line given in Figure (4.13) and also with cloud of amplitude changes in the Colony formation (see Figure 5.4).

The failure (leakage) mechanism could be either tensile failure (fracturing the top seal due to high pore fluid pressure) or through membrane leakage, where the differential pressure of the gas compared to the water phase is enough to drive gas into the water-wet pores within the seal allowing gas to ultimately migrate vertically out of the sand into the overlying formations.

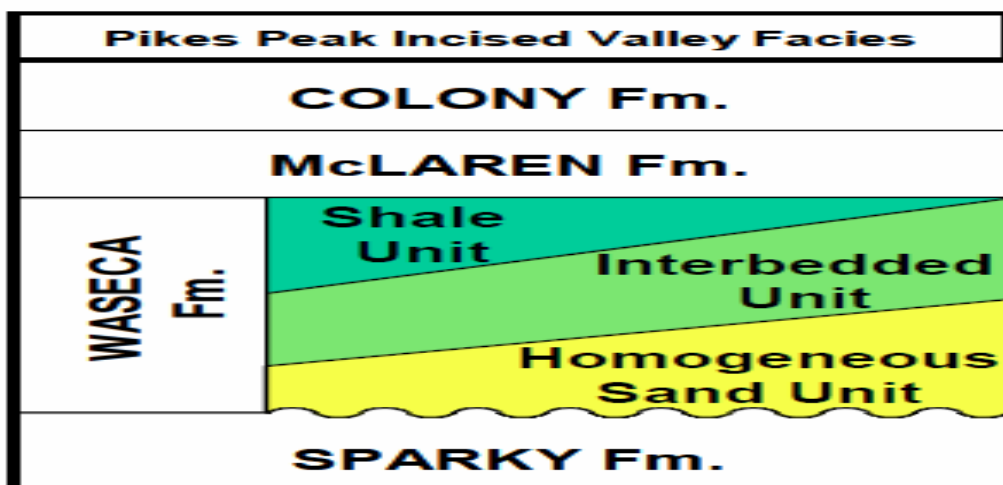


Figure 5.10: Schematic diagram depicting facies of the Waseca incised valley channel at Pikes Peak oil field. The Waseca reservoir is comprised of a shale unit, an interbedded silty sand unit and a homogenous sand unit (after Van Hulst 1984; Watson, 2004).

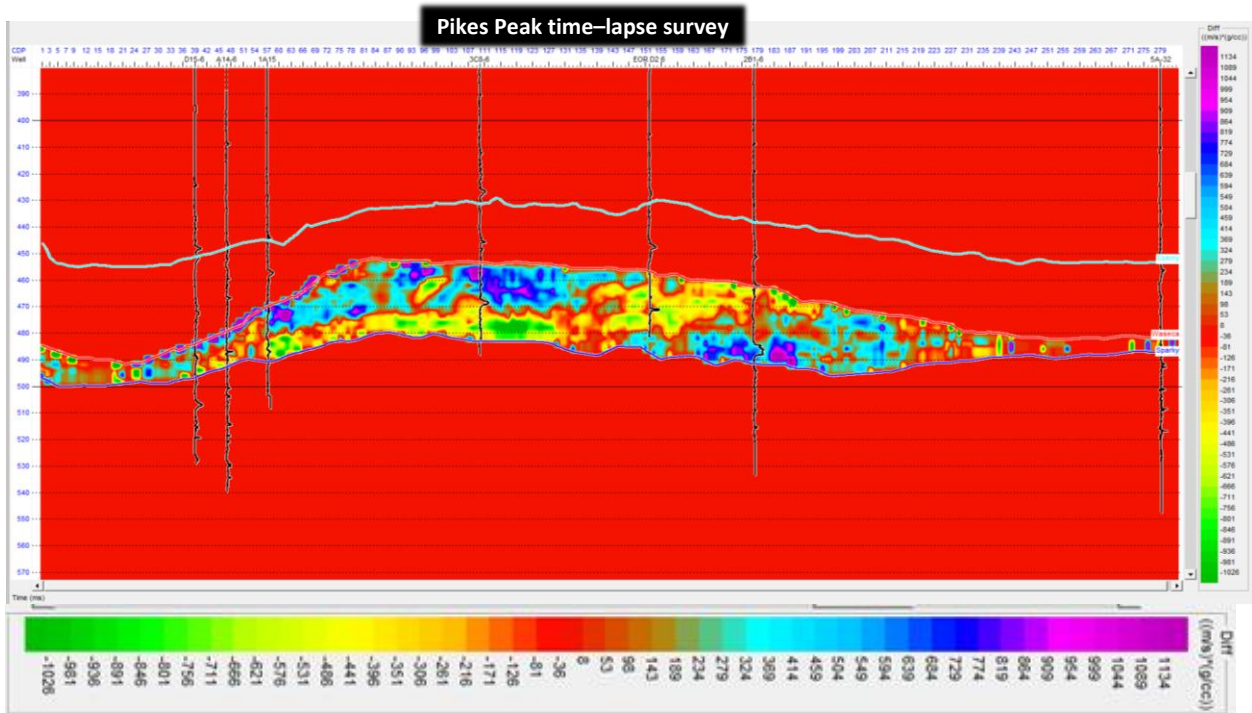


Figure 5.11: The time-lapse P-impedance difference section of the Pikes Peak oil field. The section shows the difference between monitor line and baseline surveys. The negative values in impedance difference section are indicative of impedance decreases due to steam effects.

#### 5.4 AVO inversion of time-lapse survey

The three-term AVO inversion was carried out separately for the baseline H1991 and monitor line H2000 of the Pikes Peak time-lapse surveys using Hampson-Russell software. The AVO inversion is a model based inversion technique, and differs from the band-limited inversion schemes introduced in Chapter Three of this thesis for the time-lapse AVO inversion. The inversion starts from the low frequency model and iterate until the synthetics of the impedances and density are closely matching impedances and density of measured logs. The Angle gathers with associated wavelets were used along with low frequency backgrounds. Blind tests for the

inverted attributes are conducted and QC of inverted elastic attributes (Figure 5.12) around wells shows a total correlation of 0.81 for inverted synthetic is achieved (Figure 5.13).

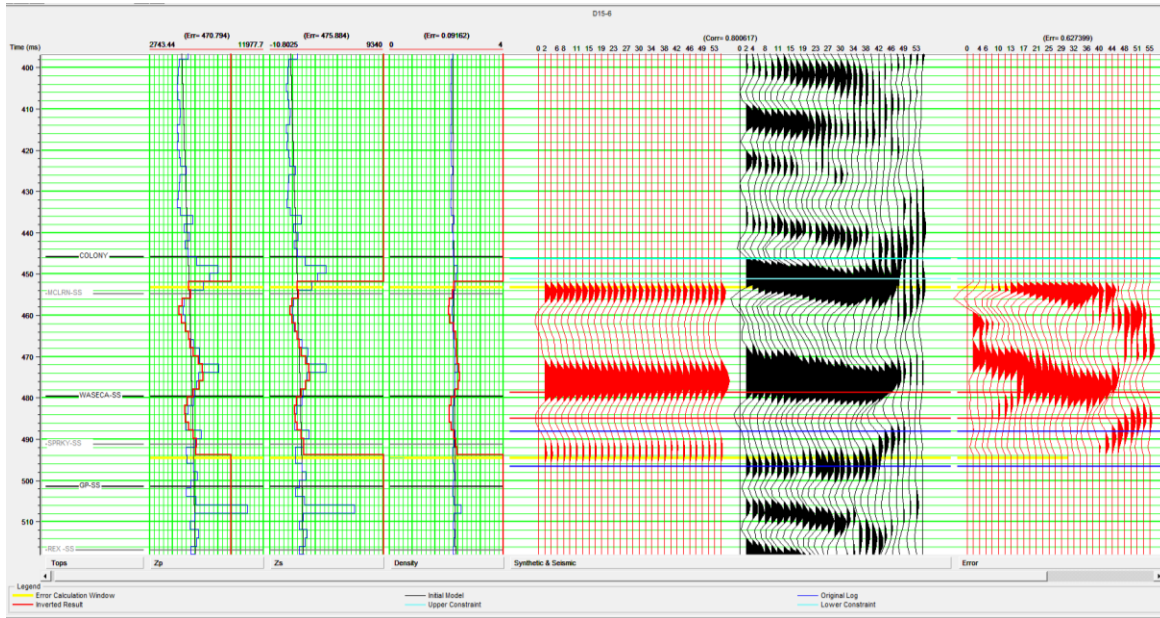


Figure 5.12: Correlating and QC of inverted and actual  $Z_p$ ,  $Z_s$  and density attributes around well D15-6. The second track represents synthetic while the third panel is extracted gathers around the well. The fourth panel shows residual (difference between seismic and synthetic traces).

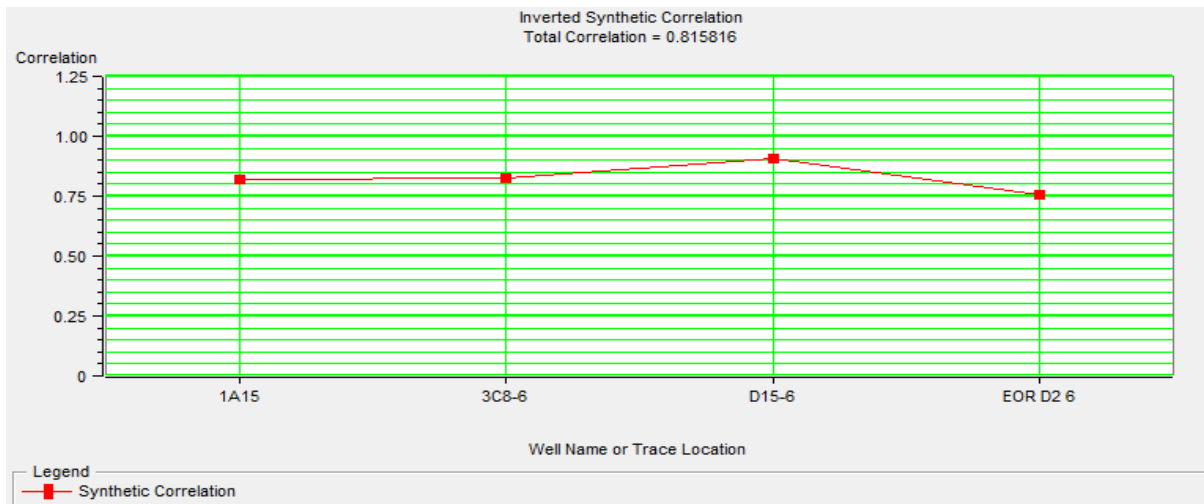


Figure 5.13: Cross-correlation measurement of inverted synthetic along the wells.

In order to establish good correlation between the AVO inverted attributes and the time-lapse post stack P-impedance, the AVO inversion outputs were limited to include only the Waseca reservoir channel.

The acoustic impedance attribute resulting from AVO inversion of the baseline and monitor line (5.14) display apparent changes in terms of P-impedance values. The reservoir channel (which represents the steam chamber) in the monitor line section, shows a decrease in p-impedance covering most of the reservoir channel. The most distinct areas of a P-impedance decrease are at the bottom of the reservoir that is made up of homogenous sand.

The shear impedance in the monitor line (Figure 5.15) survey has also demonstrated a slight decrease in the S-impedance values of the heavy oil bearing layers compared to the shear impedance of the baseline survey. The dark red zones in the shear-impedance sections shown in Figure (5.15) as well as in the density section (Figure 5.16) represent the interbedded silty sand layers of the Waseca reservoir shown in Figure (5.10). The density section of the monitor line survey shows a substantial decrease in density values across the reservoir layer.

In Figure (5.17), the P-wave section of the monitor line survey clearly shows a decrease in P-wave velocity compared to the P-wave velocity from AVO inversion of the baseline survey. The hydrocarbon movement along the base of the P-wave section of the monitor line survey can be tracked easily. On the other hand, in Figure (5.18) of the S-wave velocity section, the interbedded silty sand in the Waseca reservoir provides pathways for the hydrocarbon to move toward the dipping area along the east side of the S-wave section of the monitor line survey.

The  $V_p/V_s$  (Figure 5.19) sections of the baseline and monitor surveys clearly show a drop in the  $V_p/V_s$  ratio of the monitor line survey and map areas that are affected most by the steam injection and hydrocarbon movements.

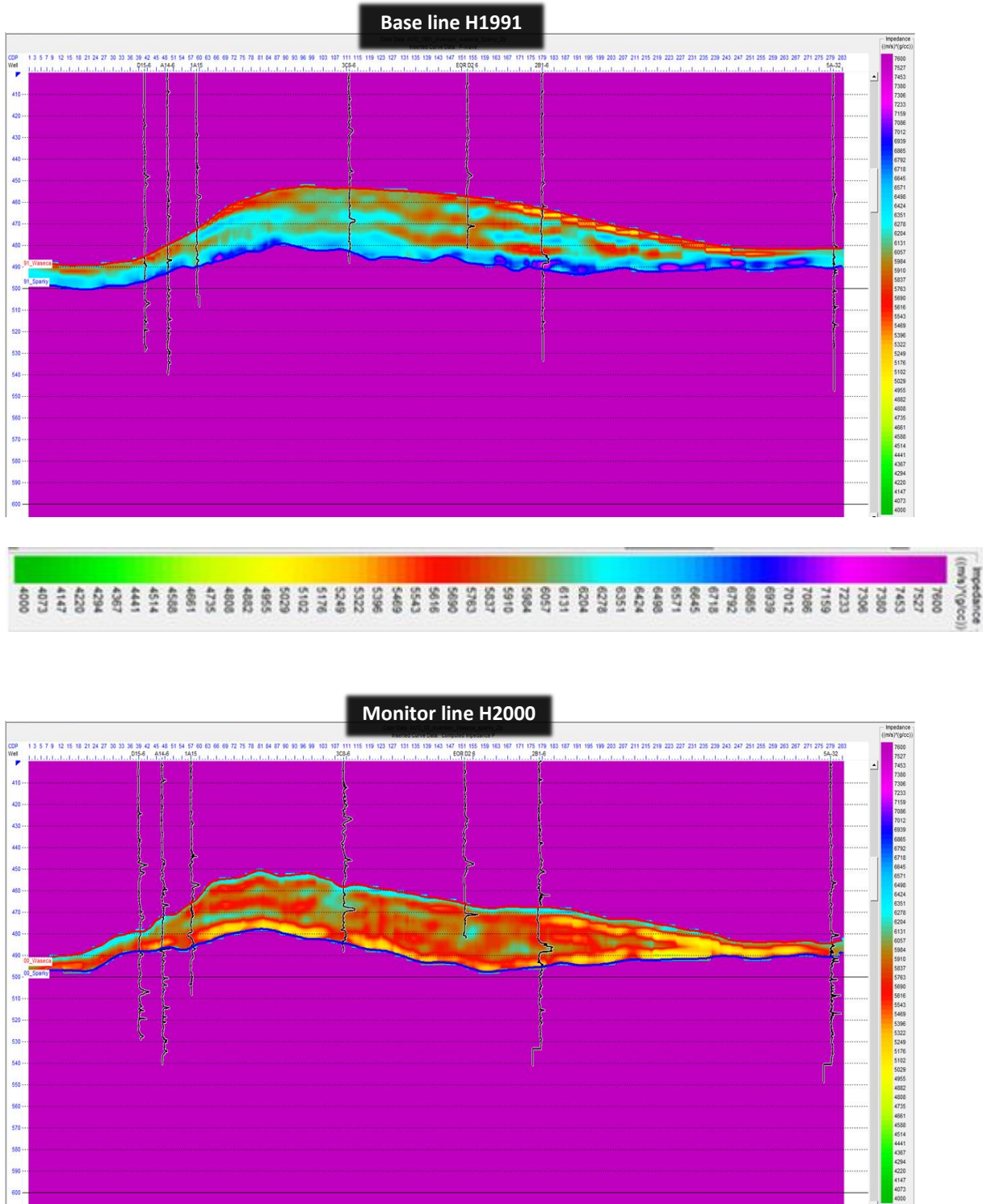


Figure 5.14: P-Impedance sections of the baseline H1991 (top) and monitor line H2000 (bottom) from AVO inversion of the Pikes Peak time-lapse surveys. Inserted curves are AI logs. Color bar for P-impedance is within a range of (4000 – 7600 ((m/s) \*(g/cc))).

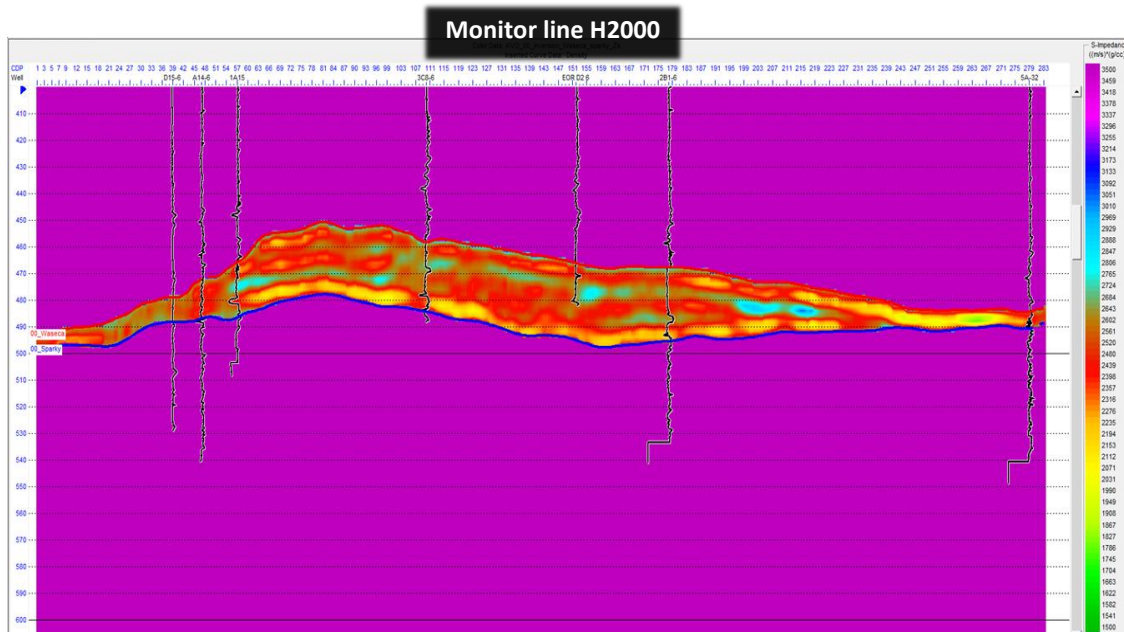
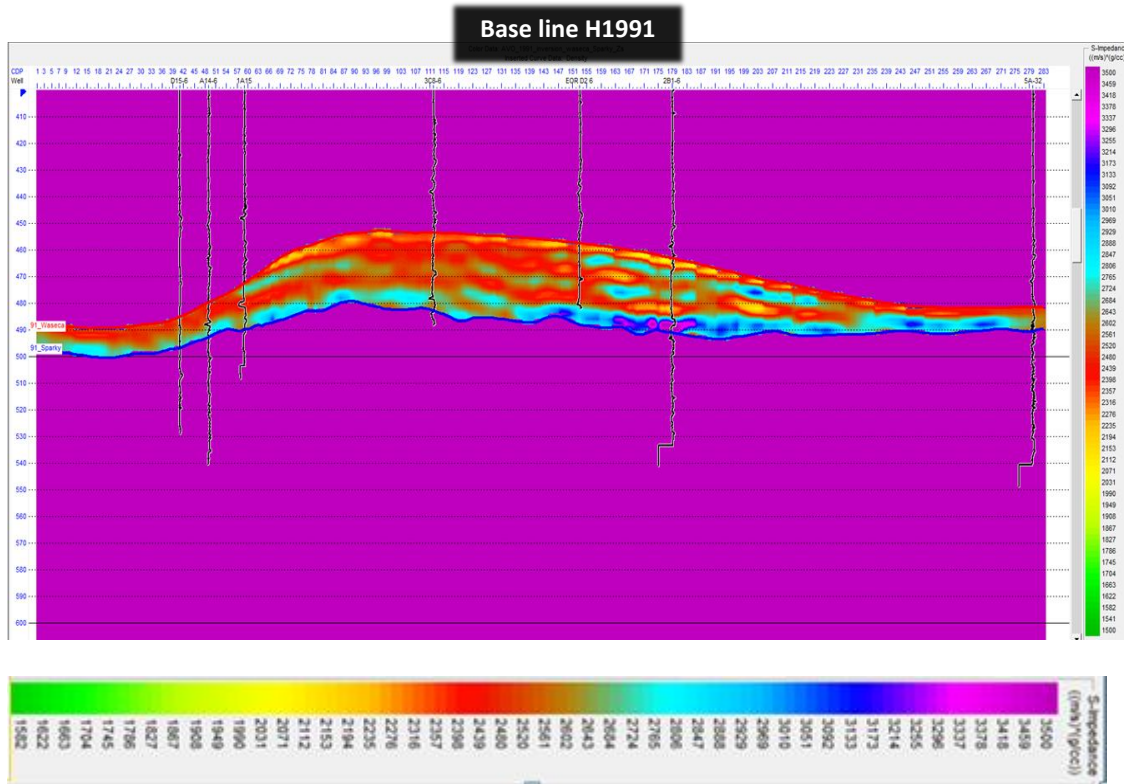


Figure 5.15: S-Impedance sections of the baseline H1991 (top) and monitor line H2000 (bottom) from AVO inversion of the Pikes Peak time-lapse surveys. Inserted curves are density logs. Color bar for S-impedance is within a range of (1500 – 3750 ((m/s)\*(g/cc))).

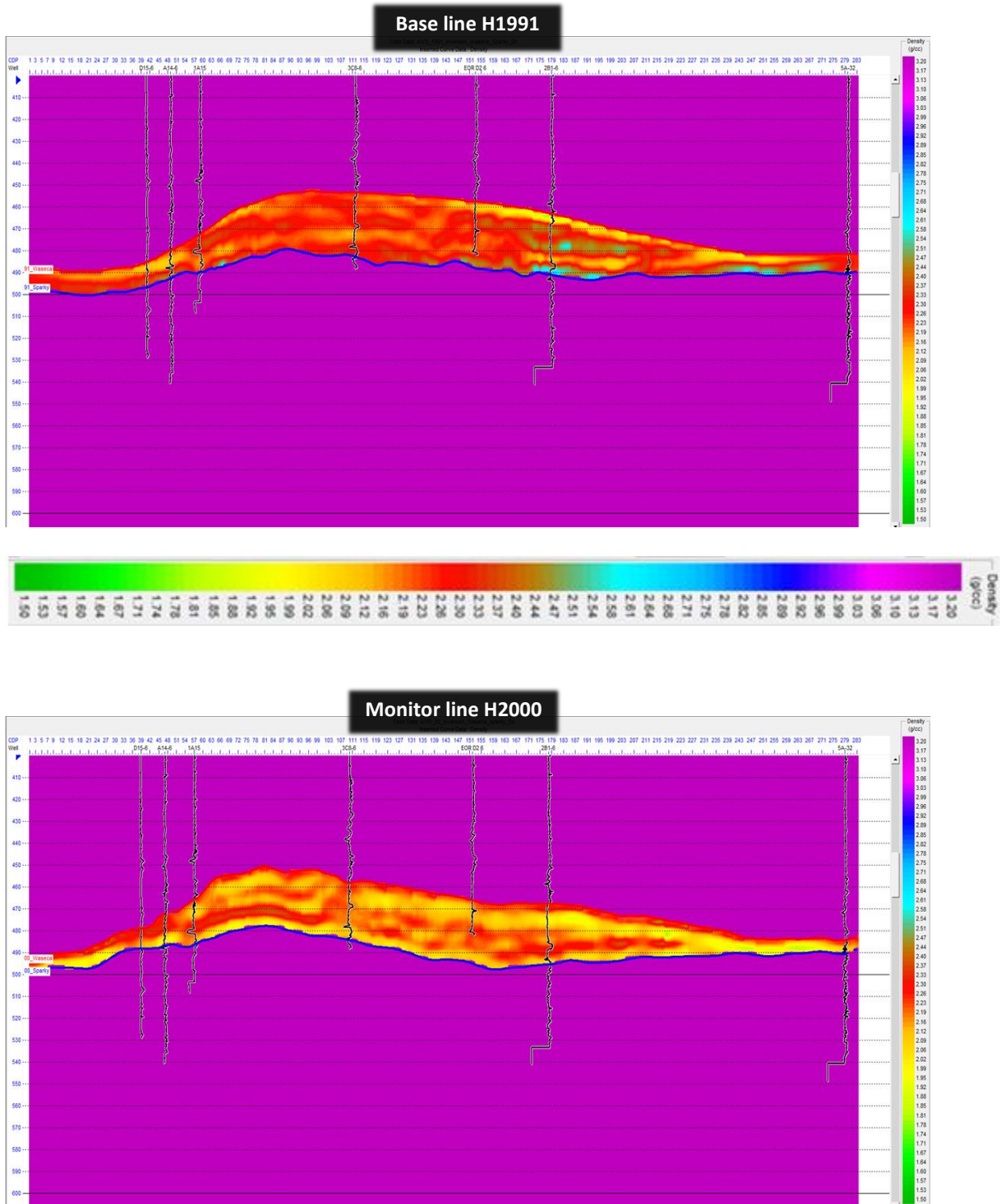


Figure 5.16: Density sections of the baseline H1991 (top) and monitor line H2000 (bottom) from AVO inversion of the Pikes Peak time-lapse surveys. Inserted curves are density logs.

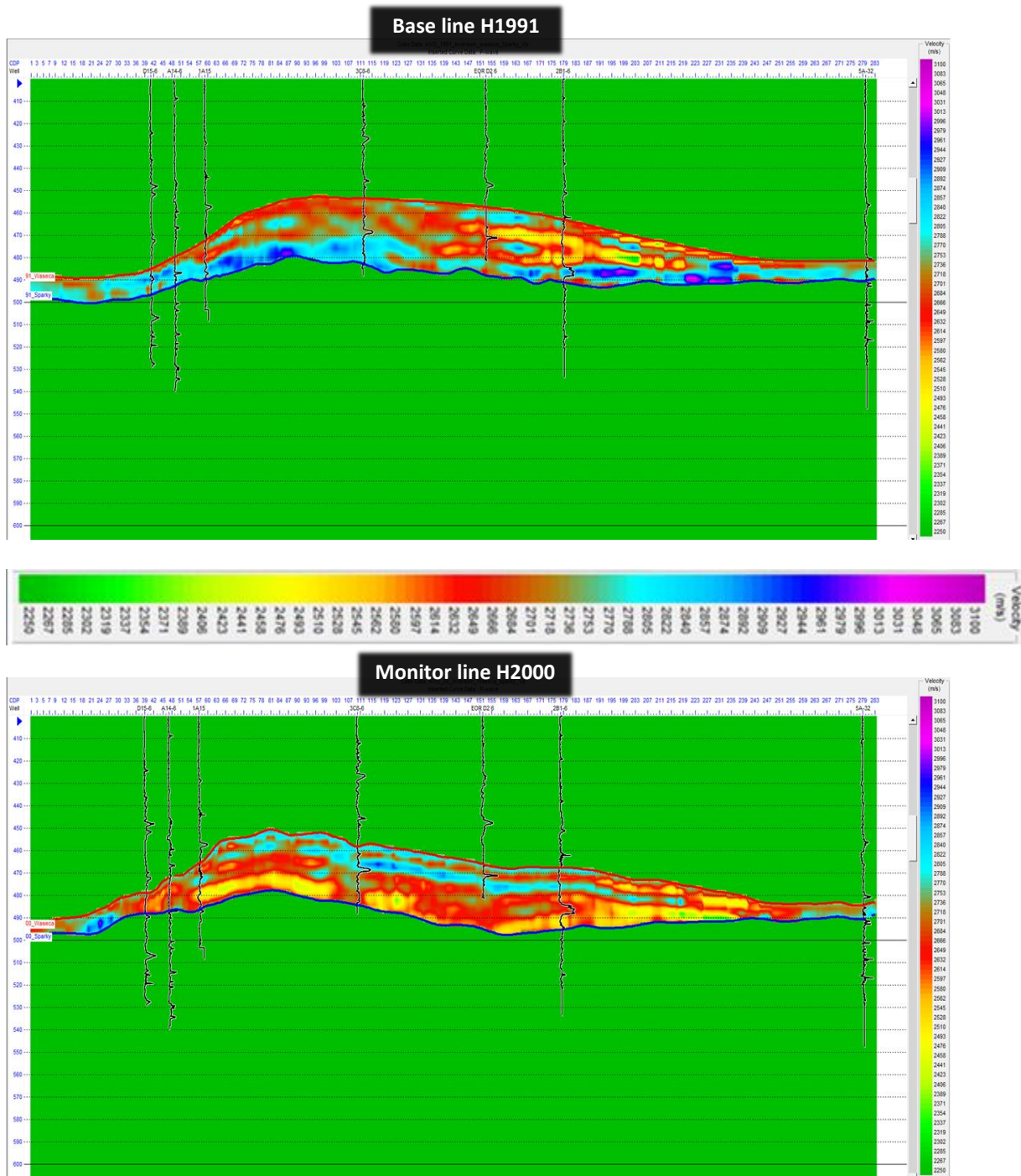


Figure 5.17: P-wave velocity sections of the baseline H1991 (top) and monitor line H2000 (bottom) from AVO inversion of the Pikes Peak time-lapse surveys. Inserted curves are P-wave logs.

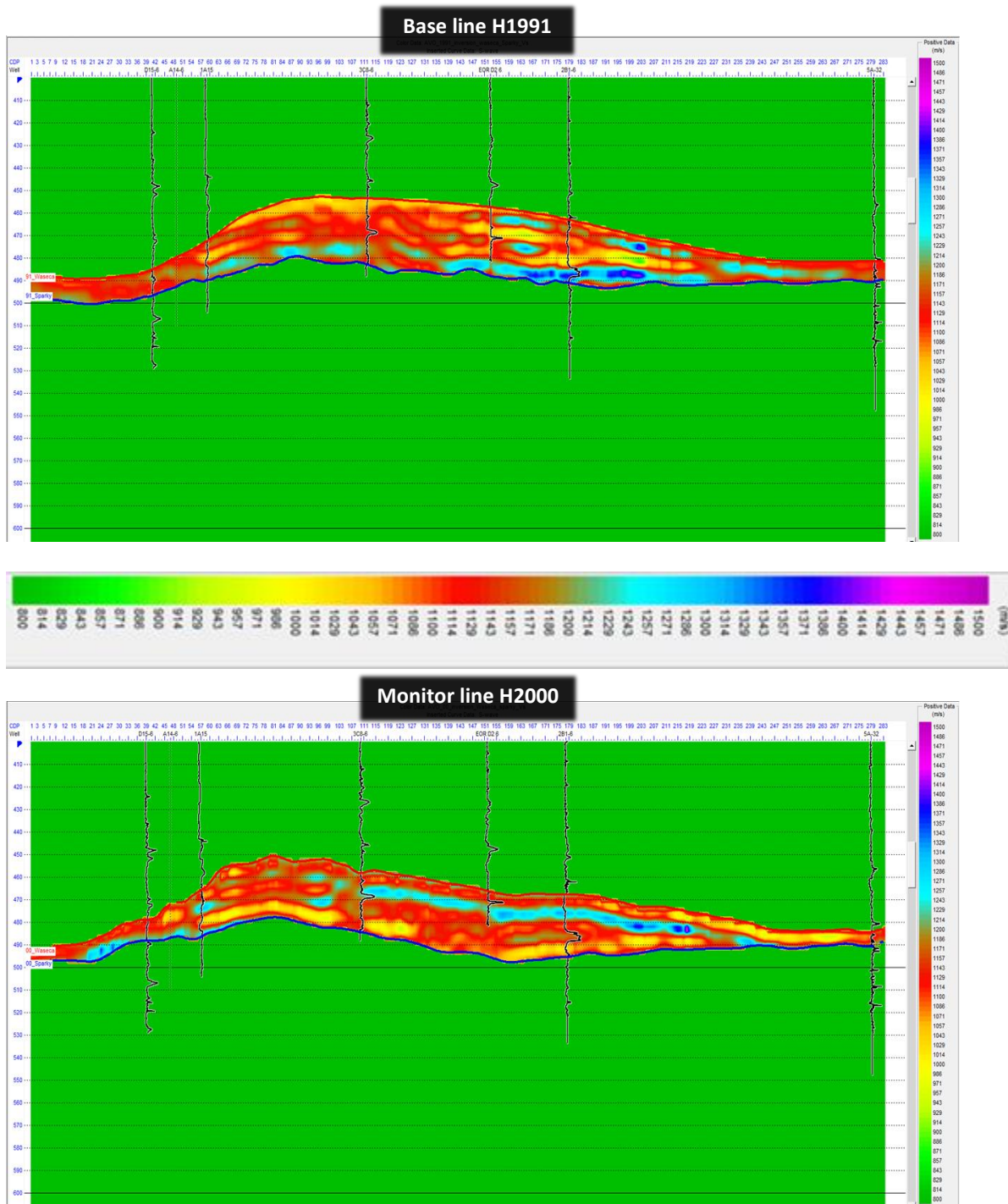


Figure 5.18: S-wave velocity sections of the baseline H1991 (top) and monitor line H2000 (bottom) from AVO inversion of the Pikes Peak time-lapse surveys. Inserted curves are S-wave logs.

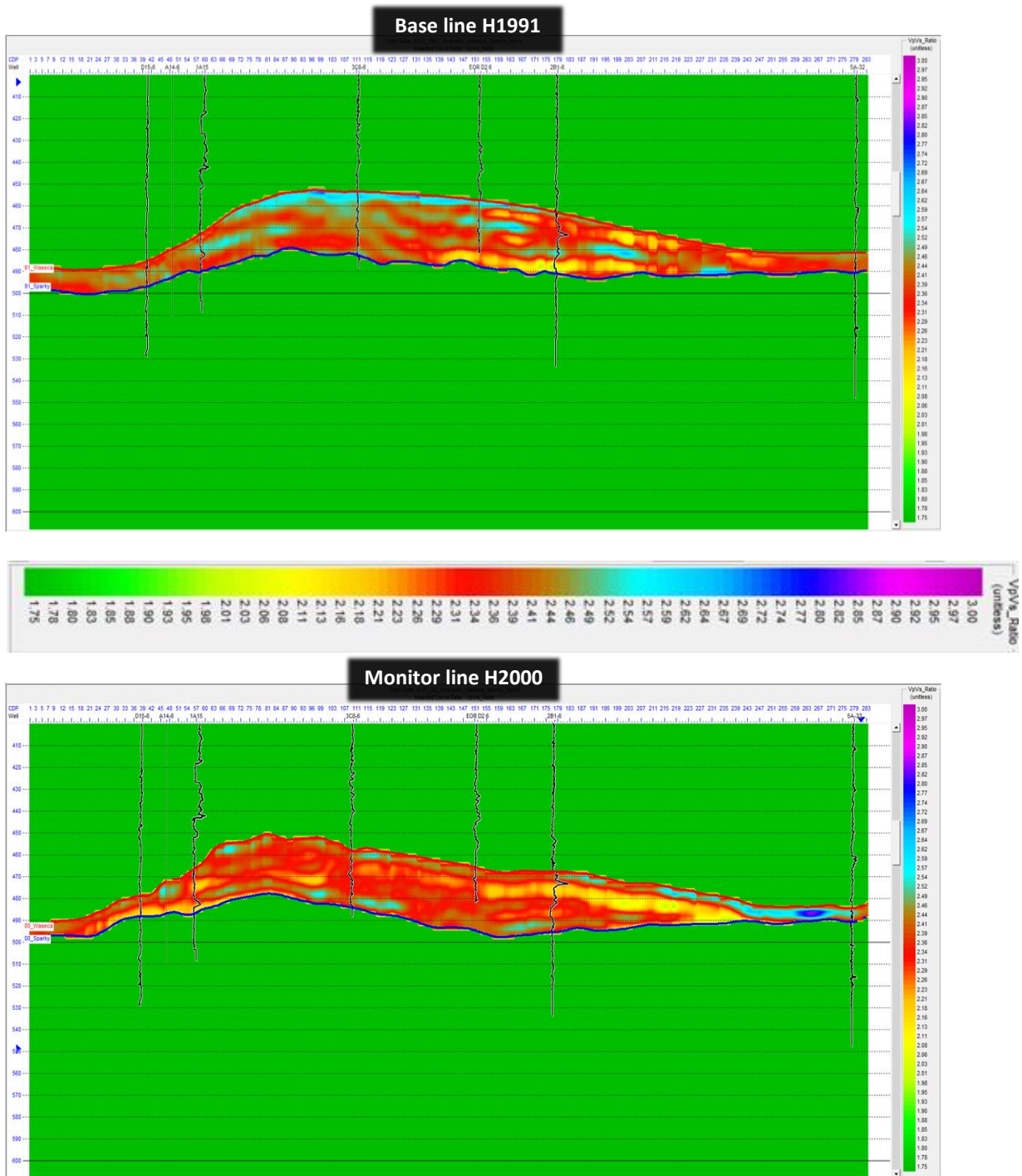


Figure 5.19: Vp/Vs ratio sections of the baseline H1991 (top) and monitor line H2000 (bottom) from AVO inversion of the Pikes Peak time-lapse surveys. Inserted curves are Vp/Vs logs.

As a lithology indicator, the VP/Vs section detects an interbedded silty sand layer, and also maps on-lap features inside the Waseca channel.

In general there is a substantial decrease in the P-wave impedances and velocities shown in monitor line sections, due to the steam injection and reservoir depletion compared to the baseline survey. The shear wave impedances and velocities have also shown some decrease in inverted attributes from the AVO inversion but at small rate compared to the incompressibility attributes.

## **5.5 Conclusions**

The time-lapse stack sections reveal the effect of injected steam on the seismic amplitudes at the Waseca reservoir channel. The heavy oil recovery processes have induced amplitude changes at the Waseca reservoir. The excessive steam pressures have caused fluid movement through the top seal into the overlying formation. This finding correlates with the dimming zones observed in seismic section of the monitor line and also with a cloud of amplitude changes in the Colony formation shown in the amplitude differences section.

The impedance differences show that the interbedded silty sands provide a pathway for steam to move vertically, either through a more silt-rich interval or along inclined beds within the Waseca sand channel. The elastic attributes from the AVO inversion of time-lapse seismic surveys clearly image hydrocarbon movement at the Waseca reservoir channel. The inverted elastic attributes also indicate that incompressibility values are decreasing at a higher rate compared to rigidity attributes of the Waseca reservoir channel of Pikes Peak oil field.

## Chapter Six: **CONCLUSIONS AND FUTURE WORK**

### **6.1 Conclusions**

The research work in this thesis shows number of improvements in the realm of time-lapse AVO inversion. This is accomplished by introducing new method and constraints to predict dipole sonic log, optimized processing flows for seismic repeatabilities and imaging and introducing new computer algorithm schemes for time-lapse AVO inversion to estimate elastic attribute changes of the heavy oil reservoir after depletion.

The first part of the thesis demonstrated the effectiveness of weighted constraints incorporated in the iteratively re-weighted least-squares inversion, IRLS, in improving estimation of intercept and slope of the mudrock relationship used in predicting a shear sonic log. The constraints imposed in the model space have reduced the cycle of calculation iteration needed in re-weighted linear inversion, while constraints incorporated in the data misfit domain have tuned estimated intercept and slope even further, and ensured a smooth convergence of inverse model towards the final solution.

The robust locally weighted smoothing scattering method, LOWESS, used in determining slope and gradient to be used in mudrock relationship, proved to be less affective by outliers that distort the smoothed points in the scattering plot, and proved to be a good interpretive tool to be used in hydrocarbon and lithology discrimination. The proposed computer algorithms for predicting shear sonic have shown to be superior among empirical relations. In terms of residual, the study has found that minimal residuals between measured and predicted shear sonic are accomplished by using the LOWESS method.

In the introductory chapter, it is stated that the aim of this research is to present practical techniques for time-lapse AVO inversion. The developed computer algorithms in this thesis simultaneously invert the baseline and monitor line data from time-lapse surveys to estimate elastic parameters changes of a reservoir as direct inversion attributes. Furthermore, these algorithms are also devised to simultaneously invert the P-P and P-S seismic data to improve resulting shear-wave impedances and density sections. The inverted elastic attributes have shown their robustness in the presence of noise by using constraints in the inverse scheme.

The Pikes Peak oil field is an ideal location for time-lapse monitoring of heavy oil recovery. The processing flow for the time-lapse 2D seismic lines at Pikes Peak have improved repeatability, optimized seismic imaging and minimized errors of seismic data processing. Noise elimination by modelling adopted in this thesis have successfully attenuated ground-roll, pump jack noise and air blast noises leaving reflectivity amplitudes intact. Careful velocity picking and testing of seismic processing parameters along with the use of a phase-shift plus interpolation migration algorithm, allowed to image the Waseca channel fairly well, preserved amplitudes along reflectors, and also assisted in tracking areas of injected steam and production-related effects.

The heavy oil recovery processes have induced amplitude changes at the Waseca reservoir. The dimming zones observed in the stack section of the monitor line, as well as the seismic difference section indicate that excessive steam pressures have caused fluid movement through the top seal into the overlying formation. The impedances differences show that the interbedded silty sand beds provide a pathway for steam to move along inclined beds within the Waseca sand channel. The attributes sections from the AVO inversion of time-lapse seismic surveys imaged

the hydrocarbon movement at the Waseca reservoir channel. The inverted elastic attributes confirm that incompressibility attributes decrease at higher rates compared to rigidity attributes of the Waseca reservoir channel of Pikes Peak oil field.

## **6.2 Future work**

Many research areas related to this study are left to future work. In predicting shear sonic log using P-wave sonic log, a complete log is used without segmenting the log into parts based on lithology. The iteratively re-weighted least-square inversion is then used to refine model parameter estimations. The IRLS would provide more accurate estimation of slope and intercept if the inversion is carried out on segmented logs that are divided based on lithology or facies. Then by incorporating volume log, a multi regression relation is established that ensures contributions from different lithology, such as sand, carbonate and shale are included in predicting shear sonic log. Joint inversion that incorporates multiple logs, such as P-wave sonic, density, temperature and resistivity logs and simultaneously inverts them to predict shear log, should be attempted to improve inverted shear log in the heavy oil reservoir.

The time-lapse algorithms established in this thesis are based on band-limited inversion concept, and uses offset gathers as input. The model based inversion is a standard inversion method used in the industry where several angle gathers/stacks with associated source wavelets are used as inputs for simultaneous AVO inversion. The low frequency model is used as an initial model and the earth model is then updated iteratively until a final solution is found. Since, in the new time-lapse inverse schemes, changes in elastic attributes are obtained as direct inversion

attributes, therefore, modification of these codes are needed to move them from merely academic research work to become standard industry practice for time-lapse AVO inversion. The Robust AVO inversion by incorporating several weighted matrices developed in chapter two should also be tested as it would improve resolution of inverted sections and further stabilize AVO inversion. Furthermore, rock physics of end-member analysis should be considered in future to drive the time-lapse AVO inversion.

In the total difference inversion scheme of time-lapse AVO inversion, the inverse problem is solved as linear inverse problem. Note that equations (3.13 & 3.17) in section 3.4.1 for total inversion of differences are quadratic equations in nature. Therefore, more accurate model parameters are obtained by solving the time-lapse inverse problem in quadratic programming form (Fletcher, 1971).

While the inverted sections given in chapter five from the AVO inversion of the time-lapse survey at Pikes Peak are absolute attributes, the comparisons between attributes of data vintages were made visually. Therefore, further conditioning of offset gathers to account for 4D effects, such as time shift, phase and time wrapping (Hale, 2006) are required in order to obtain exact differences in AVO inverted attributes of the time-lapse surveys that reflect pore fluid changes. After conditioning seismic data from 4D effect, the proposed time-lapse AVO inversion schemes of section 3.4.1 in chapter four can be extended further to calculate pore pressure and saturation changes (Landrø, 2001).

## References

- Acar, R., and Vogel, C. R., 1994, Analysis of total variation penalty methods: Inverse Problems, 10, 1217–1229.
- Ajo-Franklin, J.B., Minsley B.J. and Daley T.M., 2007, Applying compactness constraints to differential travel time tomography: Geophysics, **72**, 67-75.
- Aki, K., and Richards P.G., 1980, Quantitative seismology: theory and methods: W.H. Freeman and Co.
- Allen, J.L., and Peddy, C.P., 1993, Amplitude variation with offset / Gulf Coast Case histories: Soc. Expl. Geophys.
- Altan, S., 1997, Time-lapse seismic monitoring: Repeatability processing tests: 67<sup>th</sup> SEG Annual Meeting, Expanded Abstracts, 866–867.
- Aster, R.C., Borchers, B. and Thurber, C.H., 2005, Parameters estimation and inverse problem : Elsevier Academic Press.
- Avseth, P., Mukerji, T., and Mavko, G., 2005, Quantitative seismic interpretation: Applying Rock Physics Tools to Reduce Interpretation Risk: Cambridge University Press.
- Boulianger, O., and Chouteau, M., 2001, Constraints in 3D gravity inversion: Geophysical Prospecting. **49**, 265-280.
- Bube, K.P., and Langan, R.T., 1997, Hybrid  $\lambda_1/\lambda_2$  minimization with application to tomography: Geophysics, **62**, 1183-1195.
- Calvetti, D. Morigi, S., Reichel, L., and Sgallari, F., 2000, Tikhonov regularization and the L-curve for large, discrete ill-posed problems: J. Comp. Appl. Math., **123**, 423-446.

Carcione, J. M., and Gangi, A. F., 2000, Gas generation and overpressure: Effects on seismic attributes: *Geophysics*, **65**, 1769-1779.

Cary, P. W. and Lorentz, G. A., 1993, Four-component surface consistent deconvolution: *Geophysics*, **58**, 383 - 392.

Castagna, J. P. Batzle, M.L. and Eastwood, R.L., 1985, Relationships between compressional-wave and shear-wave velocities in elastic silicate rocks: *Geophysics*, **50**, 571-581.

Castagna, J. P., and Swan, H. W., 1997, Principles of AVO crossplotting: *The Leading Edge*, **16**, 337-342.

Claerbout, J.F. and Muir, F., 1973, Robust modeling with erratic data: *Geophysics*, **38**, 826-844.

Cleveland, W.S., 1979, Robust locally weighted regression and smoothing scatterplots: *Journal of the American Statistical Assoc.*, **74**, 829-836.

Connolly, P., 1999, Elastic impedance: *The Leading Edge*, **18**, 438-452.

Constable, S.C., Parker, R.L., and Constable, C.G., 1987, Occam's inversion: A practical algorithm for generating smooth models from electromagnetic sounding data: *Geophysics*, **52**, 289-300.

Darche, G., 1989, Iterative  $L_1$  deconvolution: *SEP-Report*, 61, 281-301.

deGroot-Hedlin, and Constable, 1990, Occam's inversion to generate smooth, two-dimensional models from magnetotelluric data: *Geophysics*, **55**, 1613-1624.

Downton, J. and Lines, L., 2000, Preliminary results of the AVO analysis at Pike's Peak: *CREWES Report*, **12**.

Downton, J.E., 2005, Seismic parameter estimation from AVO inversion: **Ph.D.** thesis, Univ. of Calgary.

Eastwood, J., 1993, Temperature-dependent propagation of P- and S- waves in Cold Lake oil sands: Comparison of theory and experiment: *Geophysics*, **58**, 863–872.

Eastwood, J., P. Lebel, A. Dilay, and S. Blakeslee, 1994, Seismic monitoring of steam-based recovery of bitumen: *The Leading Edge*, **13**, 242–251.

Ellis, D. V., and Singer, J. M., 2008, *Well Logging for Earth Scientists*: Springer Publisher.

Farquharson, C. G., and Oldenburg, D.W., 1998, Non-linear inversion using general measures of data misfit and model structure: *Geophy. J. Int.*, **134**, 213-227.

Ferguson, R. J., Margrave G.F., 1996, A simple algorithm for band-pass impedance inversion: CREWES Research Report, **8**.

Gardner, G.H.F., Gardner, L.W. and Gregory, A.R.. 1974, Formation velocity and density- the diagnostic basis for stratigraphic traps: *Geophysics*, **39**, 770-780.

Gazdag, J. & Sguazzero, P., 1984. Migration of seismic data by phase shift plus interpolation: *Geophysics*, **49**, 124–131.

Gazdag, J., 1978, Wave equation migration with the phase-shift method: *Geophysics*, **43**, 1342-1351.

Goodway, B. and Tessman, D.J.. 2002, Blackfoot 3C/3D test makes the point for VectorSeis : Special Topic: Land seismic: *First Break*, **20**, 116-121.

Goodway, B., Chen, T., and Downton, J., 1997, Improved AVO fluid detection and lithology discrimination using Lamé petrophysical parameters: 67<sup>th</sup> SEG Annual Meeting, Expanded Abstracts, 183-186.

Gray, D., Goodway, B. and Chen, T., 1999, Bridging the gap - using AVO to detect changes in fundamental elastic constants: 61<sup>st</sup> EAGE meeting.

Gray, F. D., 2002. Elastic inversion for Lamé parameters. 72<sup>nd</sup> SEG Annual Meeting, Expanded abstracts, 213–216.

Greenberg, M. L. and Castagna, J. P., 1992, Shear-wave velocity estimation in porous rocks: Theoretical formulation, preliminary verification and applications: Geophysical. Prospecting, **40**, 195-210.

Gulunay, N., 1985, A new method for the surface consistent decomposition of statics using diminishing residual matrices (DRM): 55<sup>th</sup> SEG Annual Meeting, Expanded Abstracts.

Hammond, A.L., 1974, Bright Spot: Better seismological indicators of gas and oil: Science, **185**, 515-517

Han, D. and Nur, A., and Morgan, D., 1986, Effects of porosity and clay content on wave velocities in sandstones: Geophysics, **51**, 2093-2107.

Han, D. Liu, J., and Batzle, M., 2008, Velocity and Dispersion of Heavy Oils: 78<sup>th</sup> SEG Annual Meeting, Expanded Abstracts, 1690–1693.

Hansen, P. C., 1994, Regularization tools: A MATLAB package for analysis and solution of discrete ill-posed problems: Numerical Algorithm, **6**, 1-35.

Hansen, P. C., and O’Leary, D. P., 1993, The use of L-curve in regularization of discrete ill-posed problems: SAIM J. Sci. comput., **14**, 1487-1503.

Hedlin, K., Mewhort, L. and Margrave, G., 2001, Delineation of steam flood using seismic attenuation: 71<sup>st</sup> SEG Annual Meeting, Expanded Abstract, 1572-1575.

Hilterman, F., 1989, Is AVO the seismic signature of rock properties?: 59<sup>th</sup> SEG Annual Meeting Expanded Abstracts.

Hirsche, K., N. Pullin, and L. Matthews, 2002, The GLISP 4D monitoring project — a lesson in how to avoid a successful failure: 64th EAGE meeting, Extended Abstracts, A-27.

Hoffe, B. H., Bertram, M. B., Bland, H. C., Gallant, E. V., Lines, L. R., and Mewhort, L. E., 2000, Acquisition and processing of the Pikes Peak 3C-2D seismic survey: CREWES Report, **12**.

Holland, P. W., and Welsch, R. E., 1977, Robust regression using iteratively reweighted least squares: *Comm. Statist.*, **A6**, 813-827.

Hong, X., and Chen, S., 2005, M-estimator and D-optimality model construction using orthogonal forward regression: *IEEE Transaction on systems, Man, and Cybernetics- Part B, Cybernetics*, **35**, 155-162.

Huber, P. J., 1981, *Robust statistics*: J. Wiley, New York Publisher.

Johnston, D. H., McKenny, R. S., Verbeek, J., and Almond, J., 1998, Time-lapse seismic analysis of Fulmar Field: *The Leading Edge*, **17**, 1420 -1428.

Kendall, R., Winarsky, R., Davis, T. and, Benson R., 9C, 4D Seismic Processing For the Weyburn CO2 Flood, Saskatchewan, Canada: *RECORDER*, **10**, 40-44.

Landrø, M., 2001, Discrimination between pressure and fluid saturation changes from time-lapse seismic data: *Geophysics*, **66**, 836-844.

Larsen, J., Margrave, G., and Lu, H. -X., 1999, AVO analysis by simultaneous P-P and P-S weighted stacking applied to 3-C 3-D seismic data: 69<sup>th</sup> SEG Annual Meeting, Expanded Abstracts, 721-724.

Larsen, J.A., 1999, AVO Inversion by Simultaneous P-P and P-S Inversion: **M.Sc.** thesis, Univ. of Calgary.

Last, B.J., and Kubik, K., 1983, Compact gravity inversion: *Geophysics*, **48**, 713-721.

Lawton, D.C., and Howell, T.C., 1992, P-P and P-S synthetic stacks: 62<sup>nd</sup> SEG Annual Meeting, Expanded Abstract, 1344-1347.

- Levenberg, K., 1963. A method of the solution of certain nonlinear problems in least-squares: Quarterly of applied mathematics, **2**,164-168.
- Li, S.Z., 1996, Robustizing robust M-estimation using deterministic annealing: Pattern Recognition, **29**, 159-166.
- Li, Y., and D.W. Oldenburg, 1996, 3-D inversion of magnetic data: Geophysics, **61**, 394-408.
- Li, Y., Downton, J.E., and Xu, Y., 2007, Practical aspects of AVO modeling: The leading Edge, **26**, 295-311.
- Li, Y., Goodway, B., and Downton, J., 2003, Recent applications of AVO to carbonate reservoirs in the Western Canadian Sedimentary Basin: The Leading Edge, **22**, 670-674.
- Li, Y.G., and D.W. Oldenburg, 2000, Incorporating geological dip in formation into geophysical inversions: Geophysics, **65**, 148-157.
- Lindseth, R. O., 1979, Synthetic sonic logs - A process for stratigraphic interpretation: Geophysics, **44**, 3-26.
- Lines, L.R. and Treitel., 1984. Tutorial: A review of least-squares inversion and its application to geophysical problems: Geophysical Prospecting **32**, 159-186.
- Lumley, D., M. Meadows, S. Cole, and D. Adams, 2003, 4D seismic data processing issues and examples: 73<sup>rd</sup> SEG Annual Meeting, Expanded Abstracts.
- Lumley, D.E., 1995, Seismic time-lapse monitoring of subsurface fluid flow: **Ph.D.** thesis, Stanford University.
- Ma, J., Gao, L., and Morozov, I. B., 2009, Time-Lapse Repeatability in 3C-3D Dataset from Weyburn CO2 Sequestration Project: CSPG/CSEG/CWLS Convention.
- Mahmoudian, F. 2006, Linear AVO Inversion of Multi-component Surface Seismic and VSP Data: **M.Sc.**, thesis, Univ. of Calgary.

Margrave, G.F., and Foltinek D.F., 1995, Synthetic P-P and P-S cross sections: CREWES report, **7**, 1-14.

Margrave, G.F., Lawton, D.C., and Stewart, R.R., 1998, Interpreting Channel Sand with 3C-3D Seismic Data: The Leading Edge, **17**, 509-513.

Mavko, G., Mukerji, T., and Dvorkin, J., 1998, The rock physics handbook: Cambridge University Press.

Minsley, B.J., 2007, Modeling and inversion of self-potential data: **Ph.D.**, thesis, MIT.

Ng, M., 1994, Prestack migration of shot records using phase shift plus interpolation: Canadian Journal of Exploration Geophysics **30**, 11-27.

Ng, M., 2007, Using time-shift imaging condition for seismic migration interpolation: 77<sup>th</sup> SEG Annual Meeting, Expanded Abstracts, 2378-2382.

Oldenburg, D. W., Scheuer, T. and Levy, S., 1983, Recovery of the acoustic impedance from reflection seismograms: Geophysics, **48**, 1318-1337.

Oraintara, S., Karl, W.C. , Castanon, D.A., and T.Q. Nguyen, 2000, A method for choosing the regularization parameter in linear inverse problems: IEEE- ICIP on Trans. Image Processing.

Ostrander, W. J., 1982, Plane wave reflection coefficients for gas sands at non normal angles of incidence: 52<sup>nd</sup> SEG Annual Meeting, Expanded Abstracts.

Ostrander, W. J., 1984, Plane-wave reflection coefficients for gas sands at non normal angles-of-incidence: Geophysics, **49**, 1637-1648.

Pendrel, J., Stewart, R.R., Dufour, J., Goodway, B., and Van Riel, P., 1999, Offset Inversion of the Blackfoot P-wave Data and Discrimination of Sandstone and Shales: CSEG Annual Meeting, Expanded Abstract, 289-300.

Portniaguine, O., and Zhdanov, M. S., 1999, Focusing geophysical inversion images: *Geophysics*, **67**, 874-887.

Pullin, N., L. W. Matthews, and K. Hirsche, 1987, Techniques applied to obtain very high resolution 3D seismic imaging at an Athabasca tar sands thermal pilot: *The Leading Edge*, **6**, 10–15.

Reginska, T., 1996, A regularization parameter in discrete ill-posed problems: *SIAM J. Sci. Comput.*, **17**, 740–749.

Rickett, J.E., Lumley, D.E., 2001, Crossequalization data processing for time-lapse seismic reservoir monitoring: A case study from the Gulf of Mexico: *Geophysics*, **66**, 1015-1025.

Ronholt, G., Korsmo, Ø., Hoerber, H., Smith, A., Hughes, P., and Øygaren, M., 2010, PP/PS PSDM, AVO and Joint Inversion Applied to a Virgin Exploration Area in the North Sea. 72<sup>nd</sup> EAGE Annual Meeting incorporating SPE EUROPEC 2010.

Rücker, C. & Günther, T., 2006, A general approach for introducing structural information - From constraints to joint inversion: EAGE Near Surface Geophysics Meeting.

Rudin, L. I., Osher, S., and Fatemi, E., 1992, Nonlinear total variation based noise removal algorithms: *Physica D*, **60**, 259–268.

Ruger, A., 2002, Reflection coefficients and azimuthal AVO Analysis in anisotropic media: SEG geophysical monograph series number **10**: Soc. Expl. Geophys.

Russell, B., Hampson, D., Hirsche, K., and Peron, J., 2005, Joint simultaneous inversion of PP and PS angle gathers: CREWES Report, **17**.

Russell, B., Hedlin K., Hilterman, F., and Lines, L., 2003, Fluid-property discrimination with AVO: A Biot-Gassmann perspective: *Geophysics*, **68**, 29-39.

Russell, B.H., 1988, Introduction to seismic inversion methods: SEG Continuing Education Course Note Series, Vol. **2**, Soc. Expl. Geophys.

Russell, B.H., Lines, L.R., and Hampson, D.P., 2004, A case study in the local estimation of shear-wave logs: CREWES report, **16**.

Rutherford, S.,R., and Williams, R.,H., 1989, Amplitude-versus-offset variations in gas sands: Geophysics, **54**, 680-688.

Saeed, A.N., Lines, L.R., and Margrave, G.F., 2010a, Iteratively re-weighted least squares inversion for the estimation of density from well logs: part one: CREWES report, **22**.

Saeed, A.N., Lines, L.R., and Margrave, G.F., 2010b, Iteratively re-weighted least squares inversion for the estimation of density from well logs: part two: CREWES report, **22**.

Saeed, A.N., Lines, L.R., and Margrave, G.F., 2010c, Mud-rock line estimation via robust locally weighted scattering smoothing method: CREWES report, **22**.

Saeed, A.N., Lines, L.R., and Margrave, G.F., 2012, Prediction of shear-wave log in Western Canadian Sedimentary Basin (WCSB): CREWES report, **24**.

Saeed, A.N., Lines, L.R., and Margrave, G.F., 2013a, Time-lapse AVO inversion: CSEG Annual Meeting., Calgary, Alberta.

Saeed, A.N., Lines, L.R., and Margrave, G.F., 2013b, Practical techniques for time-lapse AVO inversion: 83<sup>rd</sup> SEG Annual Meeting, Expanded Abstracts, 442-446.

Scales, J.A., Gersztenkorn, A., and Treitel, S.,1988, Fast Lp Solution of Large, Sparse, Linear-Systems - Application to Seismic Travel Time Tomography: J. Comput. Phys., **75**, 314-333.

Sheppard, G.L., Wong, F.Y. and Love, D., 1998, Husky's success at the Pikes Peak Thermal Project: Unitar Conference, Beijing, China, Expanded Abstracts.

Sheriff, R. E., Geldart, L. P., (1995), *Exploration Seismology: 2nd Edition*: Cambridge University Press.

Shuey, R., T., 1985, A simplification of the Zoepritz equations: *Geophysics*, **50**, 609-614.

Silva, J.B.C., Medeiros, W.E., and Barbosa, V.C.F, 2001, Potential-field inversion: Choosing the appropriate technique to solve a geologic problem: *Geophysics*, **66**, 511-520.

Smith, G., C., and Gidlow, P.M., 1987, Weighted stacking for rock property estimation and detection of gas: *Geophysical Prospecting*, **35**, 993-1014.

Soubotcheva, N. 2006, Reservoir property prediction from well-logs, VSP and multicomponent seismic data: Pikes Peak heavy oilfield, Saskatchewan: **M.Sc.**, thesis, Univ. of Calgary.

Stewart, R.R., 1990, Joint P and P-SV inversion: CREWES Report, **2**.

Tarantola, A., 1987, *Inverse Problem Theory: Methods for Data Fitting and Model Parameter estimation*: Elsevier Publisher.

Thomsen, L., 1986, Weak elastic anisotropy: *Geophysics*, **51**, 1954-1966.

Thomsen, L., 1988, Reflection seismology over azimuthally anisotropic media: *Geophysics*, **53**, 304-313.

Tikhonov, A.N., and Arsenin, V.Y., 1977, *Solutions of ill-posed problems*: Wiley, New York Publisher.

Tsvankin, I., 2001, *Seismic signatures and analysis of reflection data in anisotropic media*: Elsevier Science Publishers.

Tura, A. C. and Lumley, D., 1999, Estimating pressure and saturation changes from time-lapse AVO data: 69<sup>th</sup> SEG Annual Meeting, Expanded Abstract, 1655-1658.

Ursin, B., 1990, Offset-dependent geometrical spreading in a layered medium: *Geophysics*, **55**, 492-496.

Van Hulten, F.F.N., 1984, Petroleum geology of Pikes Peak heavy oil field, Waseca Formation, Lower Cretaceous, Saskatchewan: Canadian Society of Petroleum Geologists, Memoir **9**, 441-454.

Varga, R.S., 1962. Matrix iterative analysis: Prentice Hill Publisher.

Verm, R. and Hilterman, F., 1995, Lithology color-coded seismic sections: The calibration of AVO crossplotting to rock properties: The Leading Edge, **14**, 847-853.

Wahba, G., 1977, Practical approximate solutions to linear operator equations when the data are noisy: SIAM Journal of numerical analysis, **14**, 651-667.

Waite, M.W., and Sigit, R., 1997, Seismic monitoring of the Duri steamflood: Application to reservoir management: The Leading Edge, **16**, 1275–1278.

Wang, X, Chaney, A., Martin, M. and Perz, M., 2000, Surface consistent deconvolution on seismic data with surface consistent noise: CSEG Annual Meeting, Calgary, Alberta.

Wang, X., 1992, Five-component adaptive surface consistent deconvolution: CSEG Annual Meeting, Calgary, Alberta.

Watson, I.A. and Lines, L.R., 2001, Time-lapse seismic monitoring at Pikes Peak, Saskatchewan: CSEG Annual Meeting, Calgary, Alberta.

Watson, I.A., 2004, Integrated geological and geophysical analysis of a heavy-oil reservoir at Pikes Peak, Saskatchewan: **M.Sc.**, thesis, Univ. of Calgary.

Whitcombe, D.N., P.A. Connolly, R.L. Reagan, and T.C. Redshaw, 2002, Extended elastic impedance for fluid and lithology prediction: Geophysics, **67**, 63-67.

Wolke, R., and Schwetlick, H., 1988, Iteratively re-weighted least squares algorithms, convergence analysis, and numerical comparisons: SIAM Journal of Scientific and statistical computation, **9**, 907-921.

- Wong, F. Y., Anderson, D. B., O'Rourke, J. C., Rea, H. Q. and Scheidt, K. A., 2003, Meeting the challenge to extend success at the Pikes Peak steam project to areas with bottom water: **SPE84776**.
- Wood, J.M., and Hopkins, J.C., 1992, Traps associated with paleo-valleys and interfluves in an unconformity bounded sequence: Lower Cretaceous Glauconitic Member, Southern Alberta, Canada: The American Association of Petroleum Geologists Bulletin, **76**, 904-926.
- Xu, Y., 1999, AVO developments applied to Blackfoot 3C-2D broadband line: **M.Sc.**, thesis, Univ. of Calgary.
- Xu, Y., 2012, Rock physics and seismic methods for characterizing the heterogeneity of oil sands reservoirs in the Western Canadian Sedimentary Basin: **Ph.D.**, thesis, Univ. of Calgary.
- Xu, Y., and Bancroft, J. C., 1997, Joint AVO analysis of PP and PS seismic data inversion: CREWES Report, **9**.
- Zhang, H., 2003, Interpretive PP and PS joint inversion: **M.Sc.**, thesis, Univ. of Calgary.
- Zhdanov, M., and Tolstaya, E., 2004, Minimum support nonlinear parameterization in the solution of a 3D magnetotelluric inverse problem: Inverse Problems, **20**, 937-952.
- Zoeppritz, Karl (1919). Erdbebenwellen VII. VIIb. Über Reflexion und Durchgang seismischer Wellen durch Unstetigkeitsflächen. Nachrichten von der Königlichen Gesellschaft der Wissenschaften zu Göttingen, Mathematisch-physikalische Klasse, 66-84.
- Zou, Y., 2005, Integration of Seismic Methods with Reservoir Simulation, Pikes Peak Heavy Oil Field, Saskatchewan. **Ph.D.**, thesis, Univ. of Calgary.
- Zou, Y., Bentley, L.R., and Lines, L.R, D., 2006, Integration of seismic methods with reservoir simulation, Pikes Peak heavy-oil field, Saskatchewan: The leading Edge, **25**, 764-781.